
Lagrangian Statistics in High and Low *Re* Number Flows: From Filaments in Fully Developed Turbulence to Tracers in Bacterial Suspensions

A thesis

submitted to the
Tata Institute of Fundamental Research, Mumbai
for the degree of
Doctor of Philosophy
in
Physics

by
Rahul Kumar Singh

International Centre for Theoretical Sciences,
Tata Institute of Fundamental Research,
Bengaluru, Karnataka.

June, 2022

Declaration

This thesis is a presentation of my original research work. Wherever contributions of others are involved, every effort is made to indicate this clearly, with due reference to the literature, and acknowledgement of collaborative research and discussions.

The work was done under the guidance of Professor Samridhhi Sankar Ray, at the International Centre for Theoretical Sciences, Tata Institute of Fundamental Research, Bengaluru.



Rahul Kumar Singh

In my capacity as supervisor of the candidate's thesis, I certify that the above statements are true to the best of my knowledge.



Samridhhi Sankar Ray

Date: **9 June 2022**

Acknowledgements

The road to my PhD has been paved with the guidance and assistance of a number of people who have contributed in this journey in their own ways and capacities. I shall make my best efforts to lend my gratitude to all of them.

It gives me immense pleasure to begin with thanking my advisor Professor *Samriddhi Sankar Ray*. I am extremely grateful and greatly indebted to Samriddhi for not only being an advisor but also a mentor in the true sense of the word. He took me under his wings at a time when I was all but lost. I cannot emphasize enough my gratitude towards him for his constant support and unending patience in handling me as a student. He has very often walked the extra mile and done beyond what is necessary to help me out in my academic and non-academic endeavours. Samriddhi has been a reservoir of knowledge and learning, both academically and otherwise. I envy his infectious energy and enthusiasm which do not diminish in the slightest even after a long, hard day's work. The one quality that I admire the most in him is his empathy towards students and his willingness to discuss with them any and all problems under the sun. I have tried to imbibe, though with little success, his clarity of thought and expression, and his ease in communicating ideas. He has been a lesson in professionalism and adopting a measured approach. Needless to say, all my training in turbulence comes from him. And just so that this doesn't turn into an unending thankyou note to Samriddhi, I conclude my statement of reverence for him in the words of the 14th century mystic and poet *Amir Khusrau* describing his dedication towards his teacher (*Hazrat*) *Nizamuddin Auliya*:

khusro nizaam ke bal bal jaiye!

My initiation into the turbulence group was marked by interactions with *Mohit Gupta* and *Jason R. Picardo*, whom I must thank for guiding me in my initial ordeals with numerical simulations. It has since been a learning experience working with Jason on multiple projects and he remains a collaborator till date. My whole-hearted thanks to Professor *Dario Vincenzi* as well who has always lent his help and support without any second thoughts.

Towards the later half of my doctoral stint, I had the joy of working with Dr. *Siddhartha Mukherjee*. My interactions with him, particularly the non-academic ones, have been super fun given both of us hail from similar parts of the country. It has been a learning and a humbling experience seeing the artist in him at work. His love for photography, music, art, and literature have been like a breath of fresh air during the pandemic times. And I have also often been able to reap delicious benefits off his culinary skills. It has also been a pleasure collaborating with *Martin James* and *Sugan D. Murugan* in the past few months. *Sharath Jose* has been very encouraging and a good company during these last days of my stay at ICTS.

Of late, I have had interactions with a jovial bunch of juniors. Thanks to *Divya*, *Aditya* and *Aditya* for being a part of the randomly generated pseudo-quiz group, alongside Siddhartha. *Udepta* has been great fun both as a fellow officemate and as a badminton partner.

My thanks to the Scientific and Technical, and the Administrative staff at ICTS who have been very efficient in their business and always quick to help. *Jeeva M.* used to be the go to person for all academic concerns during the initial years. *Mohammad Irshad* must be thanked for his very patient assistance with IT issues. *Madhulika Singh* has always been readily approachable and very helpful with the financial queries. I make it a note to thank *Suresh R.* and *Basavaraj S. Patil* for making numerous travel and logistical arrangements, especially when the pandemic forced ICTS to shutdown. I also thank the sports complex and canteen staff, both of where I have been a regular. My sincerest gratitudes to the cleaning and the security staff for making the stay at ICTS pleasant. It would be a great amiss to not thank *Hemanta Kumar G.* for his continuous support with the HPC clusters *Mowgli*, *Mario*, *Tetris* and *Contra* which played an integral part in bringing up this thesis.

My stay in Bangalore has been enjoyable in part due to my friends from engineering days to whom I could turn to anytime and whose place I was always welcome. They were the perfect getaway when things got monotonous and boring. The fun time and trips with *Himanshu*, *Saket*, *Ratan* and *Narendra* will be missed. I have been friends with *Himanshu* since we became room mates in college and I must thank him for always being supportive, no matter what the situation. Alongside *Himanshu*, *Saket* has been one of the closest friends since day one of college. *Purnesh* has been a great teacher in disguise over the years and has never shied away from lending an honest opinion. Lastly, I cannot emphasise enough my gratitude towards *Saurabh Singh* for his help and guidance which were instrumental in me opting for a career in academia and joining ICTS for my graduate studies.

While at ICTS, I have made friends with a few people who have all not only been great characters in their own right but have also been crucial as a support group. *Jagannath Sutradhar* has been a driving force behind many a trekking trips. *Ganga Prasath* was always a great help, both on the badminton court and off it. Most importantly, I am extremely thankful to the creatures who were the absolute embodiment of fun and joy and who turned out to be the perfect set of friends: *Mukesh Singh Raghav*, *Pushkal Shrivastava*, *Anugu Sumith Reddy* and *Chandan Kumar Jana*. They have always and everywhere been the partners in crime, be it the trips, late night parties, the badminton court or the ever lasting debates and discussions. The badminton rallies are especially and sorely missed.

Ultimately, I dedicate this thesis to my family to whom no amount of acknowledgment can be just. I thank my elder brother *Rajan Kumar Singh* for all his support and his unwavering belief in me for as long as I can remember. My doting mother *Smt. Chanda Singh* has always been very proud of even the smallest of my achievements and, though at times doubtful, is finally relieved as I finish writing this thesis. I am honoured in thanking my father *Shri Arun Kumar Singh*, who has always been silently in the act behind the scenes and from whom I gather my initial inclinations towards physics.

List of publications relevant to the thesis

1. *Sedimenting Elastic Filaments in Turbulent Flows*
Rahul Kumar Singh, J. R. Picardo and S. S. Ray.
[ArXiv: 2101.00385](#) (under review in *Phys. Rev. Fluids*).
2. *Lagrangian Manifestation of Anomalies in Active Turbulence*
Rahul Kumar Singh, S. Mukherjee and S. S. Ray.
Phys. Rev. Fluids **7**, 033101 (2022).
3. *Anomalous Diffusion and Lévy Walks Distinguish Active from Inertial Turbulence*
S. Mukherjee, **Rahul Kumar Singh**, M. James and S. S. Ray.
Phys. Rev. Lett. **127**, 118001 (2021) [Editors' Suggestion].
Featured in Physics: [Physics **14**, s116 (2021)] *Bacteria That Shove Harder, Move Further*
4. *Elastoinertial Chains in a Two-dimensional Turbulent Flow*
Rahul Kumar Singh, M. Gupta, J. R. Picardo, D. Vincenzi and S. S. Ray.
Phys. Rev. E **101**, 053105 (2020).
5. *Dynamics of a Long Chain in Turbulent Flows: Impact of Vortices*
J. R. Picardo, **Rahul Kumar Singh**, S. S. Ray and D. Vincenzi.
Phil. Trans. R. Soc. A. **378**, 20190405 (2020).

Contents

Declaration	i
Acknowledgements	ii
List of Figures	ix
1 Introduction	1
1.1 Turbulence	1
1.1.1 Three-dimensional Turbulence	5
1.1.2 Two-dimensional Turbulence	14
1.2 Filaments in Turbulence	18
1.2.1 Modelling a Filament	20
1.3 Active Matter and Active Turbulence	23
1.3.1 The Continuum Model: TTSH Theory	25
2 Elasto-inertial Chains in a Two-dimensional Turbulent Flow	41
2.1 Introduction	41
2.2 Modelling	42
2.3 Simulations	45
2.4 Preferential Sampling	46
2.5 Chain Lengths	50
2.6 Conclusions	52
3 Dynamics of Inertialess Filaments in Three-dimensional Turbulence	56
3.1 Introduction	56
3.2 Extensible chain	58
3.3 Inextensible chain	65
3.4 Inflexible chain	66
3.5 Conclusions	70
4 Sedimenting Elastic Filaments in Turbulent Flows	74
4.1 Introduction	74

4.2	The Elasto-inertial Chain: a minimal model for filaments	76
4.3	Simulations	78
4.4	Characterising Inertial Filaments	79
4.4.1	Filament Lengths	79
4.4.2	Shape of the Filaments	80
4.4.3	Preferential Sampling	81
4.4.4	Chaotic Trajectories and Lyapunov Exponents	83
4.5	Fluctuating Settling Velocity	86
4.6	Tumbling: A Poisson Process	90
4.7	Stiff Filaments	93
4.8	Conclusions	95
5	Lagrangian Manifestation of Anomalies in Active Turbulence	102
5.1	Introduction	102
5.2	Simulations	104
5.3	Quantifying Trajectories	105
5.4	Fast and Slow Trajectories and The Role of Emergent Flow Structures	106
5.5	First Passage Problem and Dynamical Heterogeneity	109
5.6	Pair-Dispersion	114
5.7	Conclusions	116
6	Anomalous diffusion and Lévy walks distinguish active turbulence	123
6.1	Introduction	123
6.2	Generalised Hydrodynamics	125
6.3	Simulations	126
6.4	Anomalous Diffusion at High Activity	126
6.5	Quantifying Trajectories	127
6.6	Lévy Walks in Active Turbulence	129
6.7	Emergent Streaks	131
6.8	Conclusions	132
7	Conclusions and Outlook	141
A	Variance of the Settling Velocity	145
B	First Passage Time Distribution	147
C	The Adams-Bashforth Method	149
D	Algorithm for the Eulerian Code	150

E Lagrangian Particle Tracking**153**

List of Figures

1.1	A Three-dimensional Turbulent Flow on a 2π -periodic Cube	6
1.2	Two-dimensional Turbulence on a 2π -periodic Square	13
1.3	A Model Filament	19
1.4	Non-Universal Energy Spectrum in Active Turbulence	25
2.1	Particles versus Filaments in 2D Turbulence	45
2.2	Preferential Sampling by Filaments in 2D Turbulence	47
2.3	Preferential Sampling and Chain Lengths	49
2.4	Lengths of Filament Springs in 2D Turbulence	51
3.1	Vortex Tubes in 3D Turbulence	61
3.2	Teardrops in 3D Turbulence	62
3.3	Vortex Stretching and Preferential Sampling in 3D	63
3.4	Optimal Lengths for Preferential Sampling	64
3.5	Preferential Sampling by Inextensible Filaments	66
3.6	Inextensible (and Inflexible)Filaments in 2D Turbulence	68
3.7	Preferential Sampling by Inextensible Filaments in 3D	69
4.1	Inertial Filaments in 3D Turbulence	78
4.2	Filament Lengths in 3D	79
4.3	Distribution of Hinge Angles	81
4.4	Preferential Sampling in 3D by Inertial Filaments	82
4.5	Chaoticity in Trajectories of Inertial Filaments	86
4.6	Enhanced Settling of Filaments	87
4.7	Scaling of Variance in Settling Velocity	88
4.8	Tumbling Filaments	90
4.9	Tumbling Rates of Inertial Filaments in 3D Turbulence	91
4.10	Normalized variance and Tumbling for Inflexible Filaments	95
5.1	Diffusive and Persistent Trajectories in Active Turbulence	106
5.2	Streaky Influence	107
5.3	Streaks facilitate Coherent Motion of Tracers	110
5.4	First Passage Distributions show Anomalous Scaling	113

5.5	Richardson Dispersion of Tracers in Active Turbulence	115
6.1	Anomalous Diffusion in Active Turbulence	125
6.2	Distribution of turning angles.	128
6.3	Anomalous Diffusion is manifested via Lévy Walks	130
6.4	Vorticity Fields and Emergent Streaks	130
6.5	Streaks dominate the Vorticity Field at High Activity	133
6.6	Probability Distribution of Vorticity.	134

To Bhaiya, Mummy and Papa . . .

Chapter 1

Introduction

This thesis addresses problems in both high and low Re number turbulence with the aid of Lagrangian techniques. Therefore, in this introductory chapter we give a brief description of classical, inertial turbulence (both in two and three dimensions) as well as the model that we use to construct the filaments that we study in such flows. We then discuss active matter systems that exhibit turbulence-like states and describe how a generalized Navier-Stokes equation is used to model such low Re number flows.

1.1 Turbulence

Inertial turbulence in fluids, such as water, air, and gases, is extremely common in nature and its ubiquity across length scales that span various orders of magnitude makes it an important problem across disciplines like physics, engineering, mathematics and biology. Fluid turbulence is observed at large astrophysical scales such as in stars, and formation of planets, intermediate planetary scales such as atmospheric and oceanic circulations and at terrestrial scales as volcanic eruptions, cloud formation, river flows, and flows past objects like windmills, aeroplanes, marine vessels and vehicles on land. Turbulence is intricately involved in processes that impact life on this planet directly such as the dynamics of cloud formation, transport of sediments by rivers and oceans, planktons in turbulent ocean waters, spread of volcanic ash, industrial pollutants, and oil spills among many others. This clearly demands a detailed understanding of turbulence and its applications.

While it is clear that turbulent flows themselves come in myriad forms, in this thesis the focus will be on the classical paradigm of homogeneous and isotropic turbulence. We begin by asking the question: When is a flow said to be turbulent? While it is difficult to give an exact definition of what qualifies as a turbulent flow, it can be described, in a broad sense, as one being chaotic, unpredictable, irregular, intermittent, irreversible,

and comprising of flow structures, that are often swirling and “vortical”, with an enormous variation in length and time-scales [1–4]. A flow can turn turbulent for a variety of reasons. These could be due to instabilities which arise from perturbations due to obstacles. Examples include flow past a car or through a mesh grid commonly used in wind tunnel experiments [5–9]. Another way could be due to external forcing that can stir up a flow. Indeed, flows tend to be unstable and turn turbulent when their characteristic speeds are high and the (kinematic) viscosity is small. However, there is no exact prescription for how large a velocity or how small a viscosity will cause a flow to transition to a homogeneous, isotropic turbulent state [1, 3]. But what we do have is the prescription for how a fluid evolves. This is given by the Navier-Stokes equation:

$$\frac{\partial \mathbf{u}}{\partial t} + \mathbf{u} \cdot \nabla \mathbf{u} = -\frac{1}{\rho} \nabla p + \nu \nabla^2 \mathbf{u} \quad (1.1)$$

where \mathbf{u} is the fluid velocity field, ρ is the density, p is the pressure, and ν is the kinematic viscosity. For flows with low Mach numbers, i.e. when $|\mathbf{u}| \ll c$, with c being the speed of sound, the velocity field is divergenceless: $\nabla \cdot \mathbf{u} = 0$. This, in turn, asserts that the flow is of constant density via the continuity equation (which is just the mass conservation written in the differential form):

$$\frac{\partial \rho}{\partial t} + \nabla \cdot (\rho \mathbf{u}) = 0 \quad (1.2)$$

It is easily seen that a constant density flow yields via Eq. (1.2) the divergenceless or the incompressibility condition and, thus, allows us to work in units where $\rho = 1$. Recasting this equation in a non-dimensional form by redefining the independent variables as $\mathbf{x} = \tilde{\mathbf{x}}L$ and $t = (L/U)\tilde{t}$, (yielding $\mathbf{u} = \tilde{\mathbf{u}}U$, $p = \tilde{p}U^2/\rho$) gives us:

$$\frac{\partial \tilde{\mathbf{u}}}{\partial \tilde{t}} + \tilde{\mathbf{u}} \cdot \tilde{\nabla} \tilde{\mathbf{u}} = -\tilde{\nabla} \tilde{p} + \frac{\nu}{LU} \nabla^2 \tilde{\mathbf{u}} \quad (1.3)$$

The only non-dimensional parameter that appears in this equation is the *Reynolds* number $Re = LU/\nu$ which is an indicator of whether or not the flow is turbulent: A flow becomes turbulent typically at large Re numbers (or small ν) and most theories of homogeneous, isotropic turbulence are in the limit $Re \rightarrow \infty$ [1–3, 10, 11]. The non-dimensionalised Navier-Stokes equation. (1.3) exhibits a Re number similarity: Systems with the same Re are statistically similar despite having different velocities, length scales and viscosities [1].

Any flow that is described by Eq. (1.1), turbulent or otherwise, slowly loses energy due to viscous dissipation ($\nu \nabla^2 \mathbf{u}$). This means that a turbulence in a flow will be freely

decaying and all the energy shall be spent as heat because of viscosity. In order to keep turbulence from decaying, the flow is required to be continuously forced such that viscous dissipation of energy is balanced by the energy being injected. This external forcing is taken care of by adding a forcing term \mathbf{f} in the Navier-Stokes equation:

$$\frac{\partial \mathbf{u}}{\partial t} + \mathbf{u} \cdot \nabla \mathbf{u} = -\nabla p + \nu \nabla^2 \mathbf{u} + \mathbf{f} \quad (1.4)$$

In a statistically steady state, i.e. when energy injection is balanced by viscous dissipation, the energy of the flow $E = \langle \mathbf{u}^2 \rangle / 2$ fluctuates about a mean in time and $\langle \cdot \rangle$ denotes the average computed over the flow domain [1–3]. The average of any scalar θ is given as: $\langle \theta \rangle = \frac{1}{V} \int_V \theta d^d r$, with V being the d -dimensional system volume. The evolution of energy is then simply obtained by dotting Eq. (1.4) with \mathbf{u} and averaging over the volume:

$$\frac{\partial}{\partial t} \langle \mathbf{u}^2 / 2 \rangle + \langle \mathbf{u} \cdot [(\mathbf{u} \cdot \nabla)] \mathbf{u} \rangle = -\langle \mathbf{u} \cdot \nabla p \rangle + \nu \langle \mathbf{u} \cdot \nabla^2 \mathbf{u} \rangle + \langle \mathbf{f} \cdot \mathbf{u} \rangle \quad (1.5a)$$

$$\frac{\partial E}{\partial t} = -\epsilon_\nu + \epsilon_f \quad (1.5b)$$

where $\epsilon_f = \langle \mathbf{f} \cdot \mathbf{u} \rangle$ and $\epsilon_\nu = -\nu \langle \mathbf{u} \cdot \nabla^2 \mathbf{u} \rangle = \nu \langle (\nabla \times \mathbf{u})^2 \rangle$ are, respectively, the rates at which energy is injected into and dissipated out of the system. In the statistically stationary case, energy injection is balanced by dissipation, i.e., $\epsilon_\nu = \epsilon_f$, making the total energy E statistically steady in time. For the case of freely decaying turbulence, the energy evolution:

$$\frac{\partial E}{\partial t} = -\nu \langle (\nabla \times \mathbf{u})^2 \rangle \quad (1.6)$$

shows that energy is continuously dissipated out by viscosity and it decays in the absence of any external forcing¹. This way of looking at the averaged quantities (or statistics) in turbulence helps in restoring some *order out of chaos* from a flow that is otherwise unpredictable and random [1, 3, 12]. In this thesis, we consider only those turbulent flows that are statistically stationary, homogeneous, and isotropic: The statistics of turbulence are invariant under time translations, space translations and rotations. Such a scenario is realised physically when turbulence is observed far away from any system boundaries, and obstacles which may induce statistical inhomogeneities or anisotropies. Stationarity can be ensured by having a constant source of energy that drives turbulence. In numerical simulations, stationarity is imposed by a forcing term (see Eq. (1.4)) and isotropy and homogeneity are taken care of by

¹One of the many grand challenges in fully developed turbulence is the *dissipative anomaly*: Turbulent flows seem to have a limiting, finite energy dissipation even in the limit $\nu \rightarrow 0$.

imposing periodic boundary conditions in all directions. This results in a further simplification: The total derivative terms have zero contribution in the statistics when considering homogeneous, isotropic turbulence.

The statistical approach to turbulence proves to be particularly useful given its chaotic and unpredictable nature. Different realisations of a (turbulent) flow differ completely in their details. So, it helps to adopt a probabilistic approach to make sense out of the random, chaotic nature of a turbulent flow [1, 4]: We compute statistics to have a picture of how various quantities behave on the average, for instance energy E in Eq. (1.5).

The statistics of (turbulent) fluid flows and that of the objects they transport can be captured using variables that are defined either with respect to fixed points in space or that co-move with the fluid elements themselves. The latter description, where the observer co-moves with the particles (fluid or otherwise), captures the time evolution of the dynamics along the trajectories being followed. Referred to as the *Lagrangian description*, this method of obtaining particle statistics along their trajectories is fundamental to understanding various aspects of turbulence, especially transport or aggregation of particulates [13, 14]. This was recognised by Taylor very early in his 1921 work where he employed the Lagrangian approach to study single-particle diffusion in turbulence [15]. Richardson used the Lagrangian approach to investigate pair-particle dispersion in turbulent flows [16] which was formalised and extended to a field of particles by Batchelor [17]. Kraichnan made use of the analytical Lagrangian methods to understand statistical properties of turbulence by means of a field theory [18, 19]. Lagrangian tools have been used to study turbulent entrainment of fluid particles [20], to obtain statistics of material lines, vorticity, and strain [21, 22], velocity statistics [23–26], velocity autocorrelations and gradients [27], and statistics of acceleration [27–32] and pair particle dispersion [33]. The use of Lagrangian stochastic modelling of turbulence has led to better understanding of velocity gradient evolution [34–36], particle collisions in turbulence [37], fluid particle velocity, acceleration, and dissipation statistics [38, 39], and the relative dispersion of particles [40] in turbulence. Lagrangian methods have additionally been employed to investigate geometrical aspects of turbulence such as the study of coherent structures in two- and three-dimensional turbulence [41–46], the link between intermittency and statistically conserved structures [47–49], statistical geometry of turbulence [34, 35, 50, 51], geometry of pair particle dispersion [50]. Lagrangian tools used to improve subgrid-scale modelling in large eddy simulation [52–54];

The Lagrangian description of the flow involves an observer following the trajectories of particles in (turbulent) fluid flows and obtaining measurements along those trajectories

as they evolve in time. For example, the velocity of a fluid particle at any time is just the fluid velocity at the particle position. Thus, if the instantaneous position of the particle is given by $\mathbf{x}(t)$, then the particle velocity $\mathbf{v}(t)$ and acceleration \mathbf{a} are given simply as:

$$\mathbf{v}(t) = \frac{d}{dt}\mathbf{x}(t) = \mathbf{u}(\mathbf{x}(t), t); \quad \mathbf{a} = \frac{d}{dt}\mathbf{v}(t) \quad (1.7)$$

However, for (spherical) *inertial* particles which have a finite radius $a \ll \eta$ and mass density ρ_p , the dynamics is controlled, to a first approximation, by the linear Stokes drag model:

$$\begin{aligned} \mathbf{v} &= \frac{d\mathbf{x}}{dt}; \\ \frac{d\mathbf{v}(t)}{dt} &= -\frac{1}{\tau_p}[\mathbf{v}(t) - \mathbf{u}(\mathbf{x}(t), t)] \end{aligned} \quad (1.8)$$

where the Stokes time τ_p is a measure of how quickly the particles relax to the underlying carrier flow velocity \mathbf{u} . Equation (1.8) is obtained from the Maxey-Riley equation in the case where the particles are small and the sub-leading corrections to the dominant physics is neglected [55]. In the limit of $\tau_p = 0$, we recover our usual tracer dynamics. In this thesis, we will be using these Lagrangian techniques extensively both in the study of filaments as well as in problems of active turbulence.

With the statistical recipe for turbulence set-up, we move on to the phenomenology three- and two-dimensional turbulence.

1.1.1 Three-dimensional Turbulence

Three-dimensional (3D) turbulent flows are a common occurrence in nature and dominate the dynamics of fluid motion across a wide range of scales. Common examples include turbulence in river and oceanic flows, smoke emissions from industries, volcanic eruptions, flows past objects such as cars and aeroplanes, turbulent fluid motion in stars, formation of planets and stars and many others.

The vorticity field $\boldsymbol{\omega}(\mathbf{x}, t) = \nabla \times \mathbf{u}(\mathbf{x}, t)$ is a measure of the local rate of rotation in a flow governed by the Navier-Stokes equation. The rate of energy dissipation is, thus, determined by the mean-squared vorticity or enstrophy $\Omega = (1/2)\langle \boldsymbol{\omega}^2 \rangle$:

$$\frac{\partial E(t)}{\partial t} + 2\nu\Omega = 0 \quad (1.9)$$

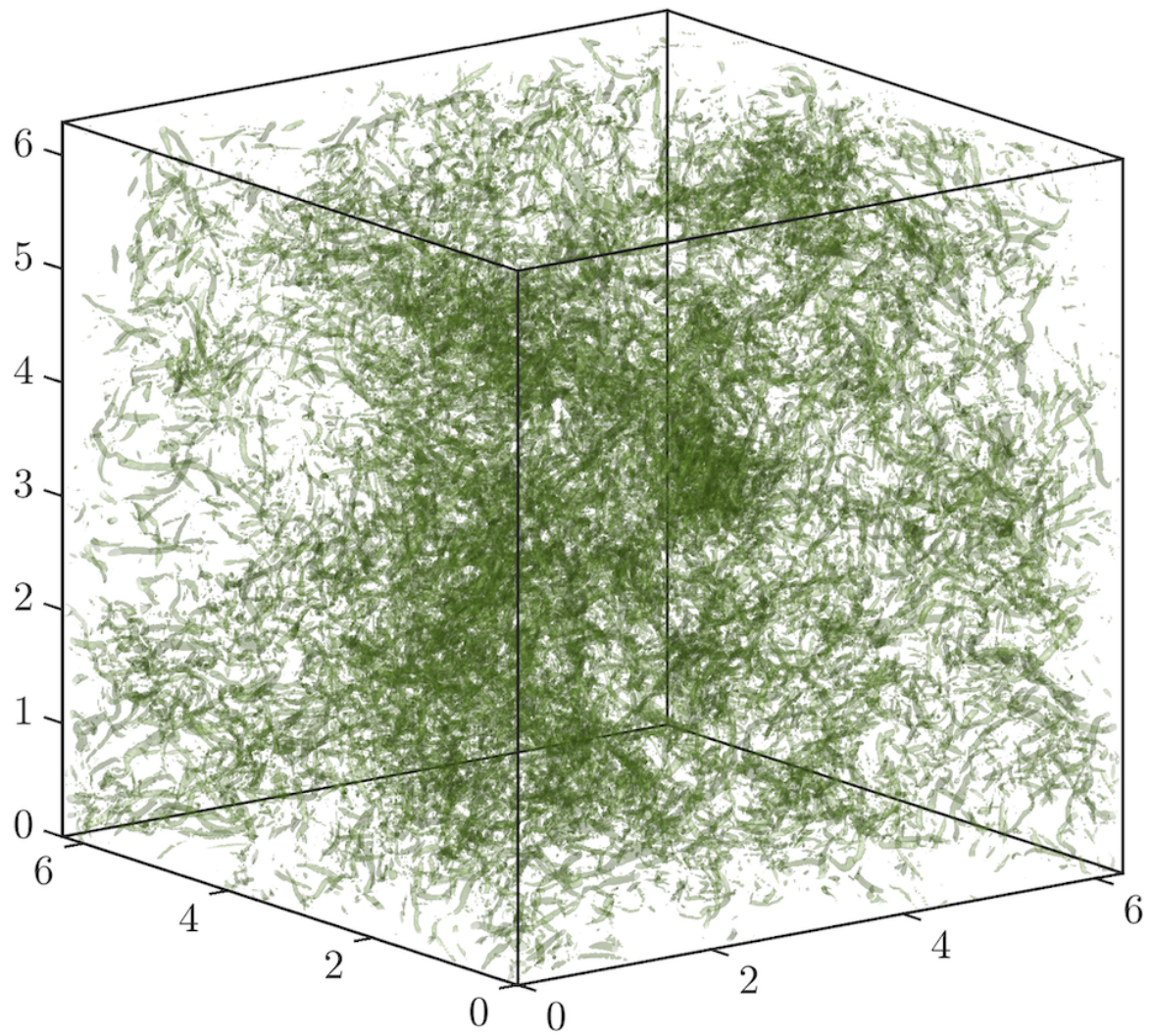


FIGURE 1.1: Tubes of vorticity in 3D turbulence simulated on a $2\pi \times 2\pi \times 2\pi$ periodic box with 256^3 grid points.

The evolution of the vorticity field $\boldsymbol{\omega}(\mathbf{x}, t)$ is obtained by taking the curl of Eq. (1.1):

$$\frac{\partial \boldsymbol{\omega}}{\partial t} + \mathbf{u} \cdot \nabla \boldsymbol{\omega} = \boldsymbol{\omega} \cdot \nabla \mathbf{u} + \nu \nabla^2 \boldsymbol{\omega} \quad (1.10)$$

where we have an additional non-linear term $\boldsymbol{\omega} \cdot \nabla \mathbf{u}$ apart from the usual advection term $\mathbf{u} \cdot \nabla \boldsymbol{\omega}$. The presence of this term ensures that unlike energy $E = (1/2)\langle \mathbf{u}^2 \rangle$, enstrophy $\Omega = (1/2)\langle \boldsymbol{\omega}^2 \rangle$ is not conserved in 3D turbulence. This is easily seen by taking a dot product of Eq. (1.10) with $\boldsymbol{\omega}$ and averaging:

$$\frac{\partial \Omega}{\partial t} = \frac{\partial}{\partial t} \langle \boldsymbol{\omega}^2 / 2 \rangle = \langle \boldsymbol{\omega} \cdot (\boldsymbol{\omega} \cdot \nabla \mathbf{u}) \rangle - \nu \langle (\nabla \times \boldsymbol{\omega})^2 \rangle \quad (1.11)$$

The presence of $\boldsymbol{\omega} \cdot \nabla \mathbf{u}$ in Eq. (1.10), which is a measure of the rate of vortex stretching by the action of local velocity gradients, means that enstrophy in Eq (1.11) is not bounded by from above. Thus, enstrophy is not an invariant of motion in the inviscid ($\nu = 0$) limit. However, 3D turbulence conserves the *helicity* $H = \langle \mathbf{u} \cdot \boldsymbol{\omega} \rangle / 2$ of the flow. Helicity is the measure of the knottedness of the vortex lines in a flow [1–3]. The dissipation of helicity is obtained by dotting Eq. (1.1) with $\boldsymbol{\omega}$ and Eq (1.10) with \mathbf{u} , adding and averaging:

$$\frac{\partial}{\partial t} \langle \mathbf{u} \cdot \boldsymbol{\omega} \rangle + \langle \mathbf{u} \cdot \nabla (\boldsymbol{\omega} \cdot \mathbf{u}) \rangle = -\langle \boldsymbol{\omega} \cdot \nabla p \rangle + \langle \mathbf{u} \cdot (\boldsymbol{\omega} \cdot \nabla \mathbf{u}) \rangle + 2\nu \langle \boldsymbol{\omega} \cdot \nabla^2 \mathbf{u} \rangle$$

Periodic boundary conditions and incompressibility mean that we only have the terms:

$$\frac{\partial}{\partial t} \langle (\mathbf{u} \cdot \boldsymbol{\omega}) / 2 \rangle = \nu \langle \boldsymbol{\omega} \cdot \nabla^2 \mathbf{u} \rangle$$

which can be recast as:

$$\frac{\partial H}{\partial t} = -\nu \langle \boldsymbol{\omega} \cdot \nabla \times \boldsymbol{\omega} \rangle \quad (1.12)$$

Thus, H is an invariant of motion in the inviscid limit. However, all real fluids have non-zero viscosity hence both E and H decay with time.

In order to keep turbulence from decaying, an external forcing is applied at a large scale L that continuously injects energy into the flow. The energy injected at large scale L is transferred to smaller scales via the non-linear interactions (given by the non-linear term $\mathbf{u} \cdot \nabla \mathbf{u}$ in Eq. (1.1)) until being finally dissipated away by viscosity [1, 3, 56]. The dissipation scale, commonly denoted by η , is much smaller compared to the injection scale ($\eta \ll L$) when the flow is turbulent, i.e $Re \gg 1$. This can be seen from Eq. (1.3) where the coefficient of the Laplacian term (which is Re^{-1}) $\nu \ll 1$, thus making its contribution significant only at very small scales. Thus, the injection scale L and the

dissipation scale η are well separated whenever the flow is turbulent ($Re \gg 1$). So, the only relevant parameters at the dissipation scale are the viscosity ν and the energy dissipation rate ϵ . Thus, all the dissipation scale quantities depend only on ν and ϵ . This helps in estimating the typical length, time and velocity at the dissipation (Kolmogorov) scales via simple dimensional analysis [1–3, 10, 12]:

$$\eta \sim \sqrt[4]{\nu^3/\epsilon}, \quad \tau_\eta \sim \sqrt{\nu/\epsilon}, \quad u_\eta \sim \sqrt[4]{\nu\epsilon} \quad (1.13)$$

where τ_η is the typical life-time of structures of size $\sim \eta$ and u_η is their typical velocity. It is straight forward to see that at the dissipation scale, we have $Re_\eta \equiv \eta u_\eta / \nu = 1$, i.e., the flow is smooth at such small scales. The dissipation of energy at a very small scale η means that energy is continually transferred from the large forcing scales to the small dissipation scales. This transfer of energy from large to small scales was seen by Richardson as a continuous process of breaking of eddies into smaller eddies resulting in a transfer of energy from larger to smaller scales before being dissipated at the Kolmogorov scale η [56]. The largest eddies are created by the external forcing/instabilities in the mean flow and broken into smaller ones by inertial instabilities. The smaller eddies are themselves unstable and rapidly break-up into even smaller ones thereby passing on their energy to yet smaller scales. This *cascade* of energy from large forcing scale to small scales is driven by inertial forces and remains unaffected by viscosity until the size of eddies becomes small enough that the Re number at that scale is ~ 1 . At this scale, viscosity starts to play a role and dissipates energy out [1, 3]. The rate of energy transfer down the cascade from the large scales $\Pi \sim U^2/(L/U) = U^3/L$ in a statistically stationary, homogeneous, isotropic turbulent state is balanced by the dissipation rate at viscous scales:

$$\Pi \sim \frac{U^3}{L} \sim \epsilon \sim \nu \frac{u_\eta^2}{\eta^2} \sim \nu \frac{1}{\tau_\eta^2} \quad (1.14)$$

which again leads us to the Kolmogorov scale quantities in Eq. 1.13 and verifies that $Re_\eta \sim 1$.

The fact that $Re_\eta \sim 1$ guarantees that the flow is smooth at the Kolmogorov scale η . However, at scales $r \gg \eta$ the flow is turbulent with $Re > 1$ making it rough and unpredictable. But at any scale r that is well separated from the injection and dissipation, i.e. $\eta \ll r \ll L$ and is referred to as the *inertial range of scales*, the only relevant parameter is the energy dissipation rate ϵ and the scale r . Turbulence statistics in inertial range of scales should then depend only on the scale r and energy transfer rate ϵ . This is, in fact, the basis of the well known Kolmogorov's similarity hypotheses presented in his seminal 1941 work (and which is commonly referred to as

K41) [10]. The similarity hypotheses are stated as [3]:

1. For large Re and $r \ll L$, the statistics of the velocity differences $\delta u(r)$ are determined uniquely by the mean energy dissipation rate ϵ , viscosity ν and their separation r .
2. For large Re and $\eta \ll r \ll L$, the statistics of the velocity differences $\delta u(r)$ are determined uniquely by ϵ and r alone and do not depend on ν .

One of the most commonly studied statistical quantities in turbulence are the *velocity structure function*, defined more precisely later and the *energy spectrum* $E(k)$ (which we discuss later in this section). The order p structure functions $S^{(p)}$ describe how the velocity differences, on average, between any two points depend on their separation \mathbf{r} . Velocity increments when considered longitudinally, i.e. $\delta u_r \equiv [\mathbf{u}(\mathbf{x} + \mathbf{r}) - \mathbf{u}(\mathbf{x})] \cdot \hat{\mathbf{r}}$, yield the longitudinal velocity structure functions $S^{(p)}(\mathbf{r}) = \langle |[\mathbf{u}(\mathbf{x} + \mathbf{r}) - \mathbf{u}(\mathbf{x})] \cdot \hat{\mathbf{r}}|^p \rangle$ [1, 3, 10]. When turbulence is statistically stationary, homogeneous, and isotropic, $S^{(p)}$ can only depend on the magnitude of separation r . Thus, $S^{(p)}(\mathbf{r}) = S^{(p)}(r)$ in our case. The assumption of similarity hypotheses then leads directly to the following expressions for second- and third-order structure functions.

$$S^{(2)}(r) \equiv \langle |\delta u_r|^2 \rangle = C_2 \epsilon^{2/3} r^{2/3} \quad ; \quad \text{Kolmogorov's two-third's law} \quad (1.15)$$

$$S^{(3)}(r) \equiv \langle |\delta u_r|^3 \rangle = -\frac{4}{5} \epsilon r \quad ; \quad \text{Kolmogorov's four-fifth's's law} \quad (1.16)$$

where $C_2 > 0$ is a universal constant. For any order p within the Kolmogorov framework, $S^{(p)}(r) \sim r^{\zeta_p}$ with $\zeta_p = p/3$. These scaling relations hold true in the inertial range $\eta \ll r \ll L$ of scales in turbulence and the expression for $S^{(3)}$ (Eq. (1.16)) can be derived exactly [1, 3, 10]. Subsequent measurements and simulations show compelling evidence, however, that, except for $p = 3$, $\zeta_p \neq p/3$. Indeed we now know that ζ_p is a convex functions non-decreasing function of p . This is because turbulence is strongly intermittent with fluctuations across length and time-scales [1–3, 57, 58]. Nevertheless, the power-law dependence of the structure functions on r reveals an (approximately) self-similar nature of turbulence in the inertial range. The role of scales is more clearly understood by switching the analysis to the Fourier space where the wave numbers k correspond to different length scales. An immediate consequence of Kolmogorov's theory is that the kinetic energy spectrum, which gives the distribution of energy across modes (or the energy held per mode), $E(k) \sim k^{-5/3}$ with very small corrections to the spectral exponent because of intermittency is directly related to the structure function $S^{(2)}(r)$ by a Fourier transform [3, 59].

Similarly, structure functions in the Lagrangian description correspond to the mean

increment in fluid particle velocity in a given time τ . The m -th order Lagrangian velocity structure function is defined as:

$$D^{(m)}(\tau) = \langle |\mathbf{u}(t + \tau) - \mathbf{u}(t)|^m \rangle \quad (1.17)$$

where $\mathbf{u}(t)$ is the Lagrangian velocity of the fluid particle at time t . Kolmogorov's first similarity hypothesis suggests that at high Re numbers when $\tau \ll \tau_\eta$, velocity differences depend on both ϵ and ν and scale as τ .

$$D^{(2)}(\tau) = a_0 \epsilon^{3/2} \nu^{-1/2} \tau^2 \quad \tau \ll \tau_\eta \quad (1.18)$$

with a_0 is universal constant. The second similarity hypothesis suggests the differences depend only upon ϵ when $\tau \gg \tau_\eta$

$$D^{(2)}(\tau) = C_0 \epsilon \tau \quad \tau_\eta \ll \tau \ll T_L \quad (1.19)$$

where T_L is the Lagrangian integral time-scale and C_0 is a universal constant [4].

It is often useful to look at the Fourier space representation of Navier-Stokes equation for a better understanding of scales. By using the Fourier transform for velocity $\mathbf{u}(\mathbf{x}, t) = \sum \tilde{\mathbf{u}}(\mathbf{k}, t) e^{i\mathbf{k} \cdot \mathbf{x}}$ in the unforced Navier-Stokes along with incompressibility (following Einstein summation convention) condition gives [11]:

$$\frac{\partial \tilde{u}_i(\mathbf{k}, t)}{\partial t} + ik_j \sum_{\mathbf{p}+\mathbf{q}=\mathbf{k}} \tilde{u}_j(\mathbf{q}, t) \tilde{u}_i(\mathbf{p}, t) = -ik_i \tilde{p}(\mathbf{k}, t) - \nu k^2 \tilde{u}_i(\mathbf{k}, t) ; \quad k_i \tilde{u}_i(\mathbf{k}, t) = 0 \quad (1.20)$$

where $k = |\mathbf{k}|$. The pressure term can be replaced by using incompressibility:

$$\tilde{p}(\mathbf{k}, t) = -\frac{k_i k_j}{k^2} \sum_{\mathbf{p}+\mathbf{q}=\mathbf{k}} \tilde{u}_i(\mathbf{p}, t) \tilde{u}_j(\mathbf{q}, t) \quad (1.21)$$

We thus have:

$$\left(\frac{\partial}{\partial t} + \nu k^2 \right) \tilde{u}_i(\mathbf{k}, t) = -ik_j \sum_{\mathbf{p}+\mathbf{q}=\mathbf{k}} \tilde{u}_j(\mathbf{p}, t) \tilde{u}_i(\mathbf{q}, t) + \frac{ik_i k_l k_m}{k^2} \sum_{\mathbf{p}+\mathbf{q}=\mathbf{k}} \tilde{u}_l(\mathbf{p}, t) \tilde{u}_m(\mathbf{q}, t) \quad (1.22a)$$

$$\Rightarrow \left(\frac{\partial}{\partial t} + \nu k^2 \right) \tilde{u}_i(\mathbf{k}) = -ik_j \left(\delta_{il} - \frac{k_i k_l}{k^2} \right) \sum_{\mathbf{p}+\mathbf{q}=\mathbf{k}} \tilde{u}_j(\mathbf{p}) \tilde{u}_l(\mathbf{q}) = M_{ijl}(\mathbf{k}) \sum_{\mathbf{p}+\mathbf{q}=\mathbf{k}} \tilde{u}_j(\mathbf{p}) \tilde{u}_l(\mathbf{q}) \quad (1.22b)$$

with $M_{ijl}(\mathbf{k}) = -ik_j (\delta_{il} - k_i k_l / k^2)$ and t being omitted in the last line. The energy

per mode $E(k, t) = 4\pi k^2 U(k)$ with $(2\pi/L)^3 U(k) = \frac{1}{2} \langle |\mathbf{u}(\mathbf{k})|^2 \rangle$ for the case when $L \rightarrow \infty$ which is necessary for isotropy. The kinetic energy is then $\int_0^\infty E(k) dk$. With the flow domain size L being large, the 3-dimensional volume element in k -space, $V_k = (2\pi/L)^3 \rightarrow 0$ and hence one can transition from discrete set of modes to a space of continuous ones as: $V_k \sum_{\mathbf{p}} \rightarrow \int d\mathbf{p}$ [11, 60, 61]. To obtain the evolution of k -th mode energy, multiply both sides by $\tilde{u}_i^*(\mathbf{k}) (= \tilde{u}_i(-\mathbf{k}))$, sum over i and add the Hermitian conjugate equation and take ensemble averages:

$$\begin{aligned} \left(\frac{\partial}{\partial t} + 2\nu k^2 \right) \langle \tilde{u}_i(\mathbf{k}) \tilde{u}_i^*(\mathbf{k}) \rangle &= M_{ijl}(\mathbf{k}) \sum_{\mathbf{p}} \langle \tilde{u}_j(\mathbf{p}) \tilde{u}_l(\mathbf{k} - \mathbf{p}) \tilde{u}_i^*(\mathbf{k}) \rangle \\ &+ M_{ijl}^*(\mathbf{k}) \sum_{\mathbf{p}} \langle \tilde{u}_j(-\mathbf{p}) \tilde{u}_l(-\mathbf{k} + \mathbf{p}) \tilde{u}_i(\mathbf{k}) \rangle \end{aligned} \quad (1.23a)$$

$$\begin{aligned} &= M_{ijl}(\mathbf{k}) \sum_{\mathbf{p}} Q_{ijl}(-\mathbf{k}, \mathbf{p}, \mathbf{k} - \mathbf{p}) - M_{ijl}(\mathbf{k}) \sum_{\mathbf{p}} Q_{ijl}(\mathbf{k}, \mathbf{p}, -\mathbf{k} - \mathbf{p}) \end{aligned} \quad (1.23b)$$

where we have used $M_{ijl}^*(\mathbf{k}) = -M_{ijl}(\mathbf{k})$ and $Q_{ijl}(\mathbf{p}, \mathbf{r}, \mathbf{s}) = \langle \tilde{u}_i(\mathbf{p}) \tilde{u}_j(\mathbf{r}) \tilde{u}_l(\mathbf{s}) \rangle$. In the continuum limit (infinite volume), we have:

$$\left(\frac{\partial}{\partial t} + 2\nu k^2 \right) U(k, t) = M_{ijl}(\mathbf{k}) \int d\mathbf{p} Q_{ijl}(-\mathbf{k}, \mathbf{p}, \mathbf{k} - \mathbf{p}) - M_{ijl}(\mathbf{k}) \int d\mathbf{p} Q_{ijl}(\mathbf{k}, \mathbf{p}, -\mathbf{k} - \mathbf{p}) \quad (1.24)$$

The energy equation is obtained by multiplying both sides by $2\pi k^2$:

$$\left(\frac{\partial}{\partial t} + 2\nu k^2 \right) E(k, t) = T(k) = 2\pi k^2 M_{ijl}(\mathbf{k}) \int d\mathbf{p} [Q_{ijl}(-\mathbf{k}, \mathbf{p}, \mathbf{k} - \mathbf{p}) - Q_{ijl}(\mathbf{k}, \mathbf{p}, -\mathbf{k} - \mathbf{p})] \quad (1.25)$$

The non-linear term $T(k)$ conserves energy and serves only to redistribute energy across modes. This is easily seen by considering the integral:

$$\begin{aligned} I &= \int_0^\infty 2\pi k^2 T(k) dk \\ &= \int d\mathbf{k} M_{ijl}(\mathbf{k}) \int d\mathbf{p} [Q_{ijl}(-\mathbf{k}, \mathbf{p}, \mathbf{k} - \mathbf{p}) - Q_{ijl}(\mathbf{k}, \mathbf{p}, -\mathbf{k} - \mathbf{p})] \\ &\stackrel{\mathbf{k} \leftrightarrow -\mathbf{k}}{=} \int d\mathbf{k} M_{ijl}(\mathbf{k}) \int d\mathbf{p} [Q_{ijl}(\mathbf{k}, \mathbf{p}, -\mathbf{k} - \mathbf{p}) - Q_{ijl}(-\mathbf{k}, \mathbf{p}, \mathbf{k} - \mathbf{p})] = -I \end{aligned}$$

where we have used that $M_{ijl}(-\mathbf{k}) = -M_{ijl}(\mathbf{k})$. Thus,

$$I = \int_0^\infty 2\pi k^2 T(k) dk = 0 \quad (1.26)$$

The Eq. (1.25) can be rewritten in terms of energy flux $\Pi(k)$ through every mode k as:

$$\frac{\partial E}{\partial t} = T(k) - 2\nu k^2 E \quad (1.27a)$$

$$\frac{\partial E}{\partial t} = -\partial_k \Pi - 2\nu k^2 E \quad (1.27b)$$

where the energy flux $\Pi(k, t) = -\int_0^k T(k)dk = \int_k^\infty T(k)dk$ gives the net energy transfer from wave numbers less than k to those larger than k . $T(k)$ is positive for small k (energy removal from large scales) and positive for large k (inertial transfer to small scales). $\Pi(k)$, on the other hand, is positive as energy is transferred to small scales. In the steady state, $\partial_t E$ and $2\nu k^2 E$ are negligible in the inertial range so that $T = 0$ and $\Pi = \epsilon$. We, thus, have by integrating Eq. (1.27) over \mathbf{k} (in the absence of external forcing):

$$\frac{d}{dt} E(t) = \frac{d}{dt} \int_0^\infty E(k)dk = -2\nu \int_0^\infty k^2 E(k)dk = -\epsilon \quad (1.28)$$

It is immediately clear from above that energy is being dissipated out by viscous term (νk^2) in the Navier-Stokes equation at large k (corresponding to the small scales in real space). The viscous term acts only at large k while the energy injected at small k is transferred to higher modes by the non-linear interactions which is captured by $T(k)$. Invoking Kolmogorov's first similarity hypothesis, we have that statistics at large enough wave numbers can only depend upon ν, ϵ and k . This gives for the energy spectrum at large k using dimensional analysis [62]:

$$E(k) = C' \nu^{\frac{3a+5}{4}} \epsilon^{\frac{-a+1}{4}} k^a \quad (1.29)$$

where C' is some universal constant and $a \in \mathbb{R}^+$. The second similarity hypothesis states that at large Re , $E(k)$ should become independent of ν for $1/L \ll k \ll 1/\eta$, yielding $a = -5/3$. Thus, we have in the inertial range of wave numbers:

$$E(k) = C \epsilon^{2/3} k^{-5/3} \quad (1.30)$$

We would like to refer the reader to a newer, simpler treatment of the Navier-Stokes equations to obtain energy equations, mode-to-mode energy transfer and the subsequent energy cascade relations discussed in [63, 64].

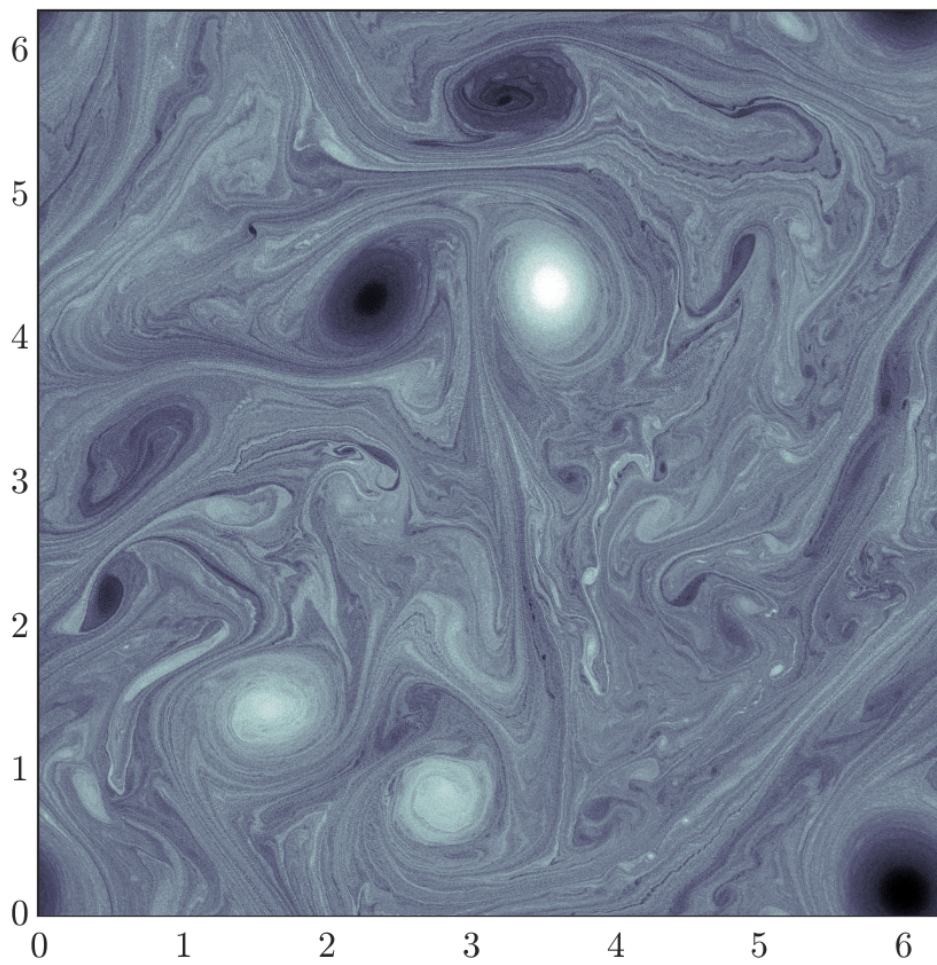


FIGURE 1.2: Vorticity field of a two-dimensional turbulence simulated on a $2\pi \times 2\pi$ periodic box with 1024^2 grid points.

1.1.2 Two-dimensional Turbulence

What is two-dimensional (2D) turbulence? A two-dimensional turbulent flow can be thought of as the limiting case of a three-dimensional turbulent flow with a high aspect ratio, i.e. the ratio of lateral to vertical length scales of the system is large. Fig. 1.2 shows a snapshot of a 2D turbulent obtained from numerical simulations. Common examples include soap film flows, oil on water, and large scale atmospheric circulations. However, any 2D turbulent flow is always embedded in a 3D world and there is always some aspect of motion that is non-planar [3]. Additionally, 2D turbulent flows are always interacting with their surroundings resulting in a frictional drag which dissipates energy out at large scales [65]. This external frictional contribution is taken care of by adding an Ekman friction term $\alpha \mathbf{u}$ in Navier-Stokes equation as [66]:

$$\frac{\partial \mathbf{u}}{\partial t} + \mathbf{u} \cdot \nabla \mathbf{u} = -\nabla p + \nu \nabla^2 \mathbf{u} - \alpha \mathbf{u} + \mathbf{f} \quad (1.31)$$

which yields the following evolution of the pseudo-scalar vorticity $\omega = \nabla \times \mathbf{u}$:

$$\frac{\partial \omega}{\partial t} + \mathbf{u} \cdot \nabla \omega = \nu \nabla^2 \omega - \alpha \omega + f_\omega \quad (1.32)$$

where $f_\omega = \nabla \times \mathbf{f}$. The energy and enstrophy equations (similar to Eqs. (1.9), (1.11) in 3D) can be obtained as below:

$$\frac{\partial E}{\partial t} = -\epsilon_\nu - \epsilon_\alpha + \epsilon_f \quad (1.33a)$$

$$\frac{\partial \Omega}{\partial t} = -\eta_\nu - \eta_\alpha + \eta_f \quad (1.33b)$$

where $\epsilon_\nu = \nu \langle (\nabla \mathbf{u})^2 \rangle$, $\epsilon_\alpha = \alpha \langle \mathbf{u}^2 \rangle$, $\epsilon_f = \langle \mathbf{u} \cdot \mathbf{f} \rangle$ and similarly $\eta_\nu = \langle (\nabla \omega)^2 \rangle$, $\eta_\alpha = \alpha \langle \omega^2 \rangle$ and $\eta_f = \langle \omega f_\omega \rangle$. Thus, in the inviscid ($\nu = 0$), unforced ($\mathbf{f} = 0$) limit with no friction ($\alpha = 0$), both energy $E = \langle \mathbf{u}^2 \rangle / 2$ and enstrophy $\Omega = \langle \omega^2 \rangle / 2$ are invariants of a 2D turbulent flow [3, 65]. However, real, physical flows always have a finite viscosity so that:

$$\frac{\partial E}{\partial t} = \frac{\partial}{\partial t} \langle \mathbf{u}^2 / 2 \rangle = -\epsilon_\nu(t) = -2\nu \Omega \quad (1.34a)$$

$$\frac{\partial \Omega}{\partial t} = \frac{\partial}{\partial t} \langle \omega^2 / 2 \rangle = -\eta_\nu(t) = -2\nu P \quad (1.34b)$$

where $P = \frac{1}{2} \langle (\nabla \omega)^2 \rangle$ is the palinstrophy in two-dimensions. As the flow evolves, $\langle \omega^2 \rangle$ decreases monotonically as P is a positive quantity (equation 1.34b) and, thus, Ω is bounded from above by its initial value. This, in turn, implies that $\epsilon_\nu \rightarrow 0$ in the limit of vanishing viscosity, $\nu \rightarrow 0$ and almost all of the energy in 2D turbulence is dissipated

not by viscosity (which acts at small scales) but is transferred to large scales where it is removed by the Ekman friction term. This transfer of energy to larger scales in fully developed 2D turbulence is referred to as ‘inverse cascade’ [3, 19, 65, 67, 68]. There is, however, no bound on palinstrophy and enstrophy is expected to have a direct (forward) cascade. A finite viscosity results in a non-zero dissipation and a statistically stationary state ($\partial_t E = 0$) can only be obtained by forcing the flow at some scale ℓ_f . Turbulent fluctuations are then dynamically transferred to large scales by the *inverse energy cascade* and to small scales by the *forward enstrophy cascade* where they are destroyed by friction at large scales $\ell_\alpha \gg \ell_f$ and by viscosity at very small scales $\ell_\nu \ll \ell_f$. In the stationary state, the forcing energy is dissipated out by friction and viscosity (refer to equation (1.33)):

$$\epsilon_f = \epsilon_\nu + \epsilon_\alpha ; \quad \eta_f = \eta_\nu + \eta_\alpha \quad (1.35)$$

The forcing energy scale obeys the relation $\ell_f^2 \simeq \epsilon_f/\eta_f$. The characteristic length scales associated with friction and viscosity are obtained similarly as:

$$\ell_\alpha^2 \simeq \epsilon_\alpha/\eta_\alpha ; \quad \ell_\nu^2 \simeq \epsilon_\nu/\eta_\nu$$

which, using Eq. (1.35), leads directly to the relations [65]:

$$\frac{\epsilon_\alpha}{\epsilon_\nu} = \frac{1 - \ell_\nu^2/\ell_f^2}{\ell_\nu^2/\ell_f^2 - \ell_\nu^2/\ell_\alpha^2} = \left(\frac{\ell_\alpha^2}{\ell_\nu^2} \right) \frac{1 - (\ell_\nu/\ell_f)^2}{(\ell_\alpha/\ell_f)^2 - 1} \quad (1.36a)$$

$$\frac{\eta_\alpha}{\eta_\nu} = \frac{1 - (\ell_\nu/\ell_f)^2}{(\ell_\alpha/\ell_f)^2 - 1} \quad (1.36b)$$

With $\ell_\alpha \gg \ell_f \gg \ell_\nu$, we have

1. $\epsilon_\alpha \gg \epsilon_\nu$, indicating that large scale friction dissipates out the energy.
2. $\eta_\alpha \ll \eta_\nu$, indicating that viscosity dissipates out the enstrophy at small scales.

Thus, energy cascades in an ‘‘inverse’’ manner opposite to that in 3D turbulence while enstrophy is transferred to smaller scales in a ‘‘forward cascade’’. This means that large vortices are continuously converted into finer structures before being ultimately destroyed by viscosity. In the stationary case, i.e. when injection is balanced by viscous and frictional damping, the two intermediate ranges of scales, given by $\ell_f \ll \ell \ll \ell_\alpha$ and $\ell_\nu \ll \ell \ll \ell_f$, then yield turbulence statistics that are self-similar (scale-independent). In other words, these (inertial) ranges are well separated from scales at which either friction or viscosity act and, hence, flow properties in these ranges are dependent only on the transfer rates η or ϵ . The dual cascade nature of 2D turbulence then leads to the prediction of two scaling forms for structure functions: The inverse

cascade relation is $S_I^{(2)}(r) = C_2 \epsilon^{2/3} r^{2/3}$ while that for the direct cascade is $S_D^{(2)}(r) \sim \eta^{2/3} r^2$. Similarly, relations for the third-order longitudinal structure functions $S_{I,D}^{(3)}$ are guaranteed by constant energy and enstrophy fluxes in the respective inertial ranges [1, 65, 69–71]:

$$S_I^{(3)}(r) \equiv \langle [\delta u_{\parallel}(r)]^3 \rangle = \frac{3}{2} \epsilon r \quad (1.37)$$

which is the 2D equivalent of the 4/5th law in 3D turbulence. Similar prediction for the direct cascade gives:

$$S_D^{(3)}(r) = \frac{1}{8} \eta r^3 \quad (1.38)$$

The dual nature of cascades and the role of associated length-scales is better understood by switching to the Fourier space. We begin by stating the Fourier space analogues of the energy and enstrophy equations which can be obtained in the same way as Eq. (1.27) for 3D turbulence [65]:

$$\frac{\partial E(k)}{\partial t} = T(k) + F(k) - \nu k^2 E(k) - \alpha E(k) \quad (1.39a)$$

$$\frac{\partial \Omega(k)}{\partial t} = k^2 T(k) + k^2 F(k) - \nu k^2 \Omega(k) - \alpha \Omega(k) \quad (1.39b)$$

with $F(k)$ being the contribution due to the forcing term, $T(k)$ is rate of energy transfer due to non-linear interactions and the two remaining terms correspond to dissipation. The enstrophy equation (1.39b) can be obtained by recognising that $\Omega(k) = k^2 E(k)$.

The rate of energy transfer across modes is described by flux relations for both energy and enstrophy. The non-linear interaction term is responsible for energy transfer across scales and, hence, are related to energy and enstrophy fluxes as [65, 68]:

$$\Pi(k) = \int_k^\infty T(k') dk' ; \quad Z(k) = 2 \int_k^\infty k'^2 T(k') dk' \quad (1.40)$$

where the fluxes $\Pi(k)$, $Z(k)$ give the rate of transfer (of energy and enstrophy respectively) from wave numbers $< k$ to those $> k$. The existence of inertial ranges for energy and enstrophy suggests self-similar, scale independent behaviour suggests that the respective transfer rates are independent of the wave-number k [68]. The transfer rates in Eq. (1.40) can be represented as [60, 67, 68]:

$$\Pi(k) = \frac{1}{2} \int_k^\infty dk' \int_0^k \int_0^k T(k', p, q) dp dq - \frac{1}{2} \int_0^k k' dk' \int_k^\infty \int_k^\infty T(k', p, q) dp dq \quad (1.41a)$$

$$Z(k) = \int_k^\infty k'^2 dk' \int_0^k \int_0^k T(k', p, q) dp dq - \int_0^k k'^2 dk' \int_k^\infty \int_k^\infty T(k', p, q) dp dq \quad (1.41b)$$

We again refer the reader to a simpler derivation of these flux relations and the rate of energy transfer across modes [63, 64]. The following detailed energy and enstrophy conservation laws for triads:

$$T(k, p, q) + T(p, q, k) + T(q, k, p) = 0 \quad (1.42a)$$

$$k^2 T(k, p, q) + p^2 T(p, q, k) + q^2 T(q, k, p) = 0 \quad (1.42b)$$

also imply the overall conservation laws $\int_0^\infty T(k) dk = \int_0^\infty k^2 T(k) dk = 0$. We, thus, have the following relations between the transfer terms [60, 61, 67, 68]:

$$\begin{aligned} T(p, q, k)/T(k, p, q) &= (q^2 - k^2)/(p^2 - q^2); & T(q, k, p)/T(p, q, k) &= (k^2 - p^2)/(q^2 - k^2); \\ T(k, p, q)/T(q, k, p) &= (p^2 - q^2)/(k^2 - p^2) \end{aligned} \quad (1.43)$$

In order to have self-similar solutions, we must have for modes k, p, q lying in the inertial range [60, 68]:

$$E(ak)/E(k) = a^{-n}; \quad \frac{T(ak, ap, aq)}{T(k, p, q)} = a^{-(1+3n)/2} \quad (1.44)$$

with a being an arbitrary scaling factor and n is yet to be determined. It can be shown using the relations (1.44) and (1.43) in Eqns (1.41a) and (1.41b) that [60]:

$$\Pi(k) \propto k^{(5-3n)/2}; \quad Z(k) \propto k^{(9-3n)/2} \quad (1.45)$$

Thus, $n = 5/3$ yields a scale independent energy cascade while $n = 3$ yields a scale-independent enstrophy cascade giving $\Pi(k) = \epsilon$ in the inverse cascade inertial range and $Z(k) = \eta$ in the direct cascade inertial range, with ϵ and η assumed to be k -independent [60]. Hence, we have in the respective inertial ranges:

$$E(k) = C\epsilon^{2/3}k^{-5/3} \quad (1.46a)$$

$$E(k) = C'\eta^{2/3}k^{-3} \quad (1.46b)$$

So, now we not only have the two cascade regimes, but also the directions of the respective cascades from the preceding discussion in real position space [67]. However, a close

inspection reveals that Eq. (1.46b) gives a logarithmically divergent total enstrophy:

$$\Omega = \int_{k_{min}}^{\infty} k^2 E(k) dk = C' \eta^{2/3} \int_{k_{min}}^{\infty} \frac{dk}{k} \quad (1.47)$$

suggesting a logarithmic-factor correction. This factor can be motivated by observing that $\Pi(k)$ should be proportional to the energy held in the modes $\sim k$, $kE(k)$, assuming locality of interactions in the k -space and to the effective rate of shear ω_k which distorts the structures of scale $\sim 1/k$:

$$\Pi(k) \sim \omega_k k E(k) \quad (1.48)$$

where ω_k is estimated as $\omega_k^2 \sim \int_0^k p^2 E(p) dp$ because all wave numbers up to $\sim k$ contribute to the effective mean shear distorting structures of wave-number $\sim k$ while the effects of wave-numbers $\gg k$ average out on scales $\sim k$ and characteristic distortion times $\sim \omega_k^{-1}$ [60, 65]. Assuming such a form also ensures that $\Pi(k)$ can take a constant scale-invariant value ϵ . Accordingly, the major contribution to ω_k comes from wave-numbers $\sim k$ which is consistent with Kolmogorov's assumptions. A similar line of reasoning applied to enstrophy transfer yields:

$$Z(k) \sim \omega_k k^3 E(k) \quad (1.49)$$

where $k^3 E(k)$ is the total enstrophy in wave-numbers $\sim k$. Using Eq. (1.46b) yields $\omega_k^2 \propto \ln(k/k_{min})$ where k_{min} is the wave-number that marks the end of k^{-3} range from below. The divergence of ω_k^2 at the lower limit implies $Z(k)$ increases with k as per Eq. (1.49). This dependence on k can be resolved and a constant $Z(k)$ can be restored by assuming a correction as $E(k) = C' \eta^{2/3} k^{-3} [\ln(k/k_{min})]^{-n}$. Using this expression for $E(k)$ gives a scale-independent transfer rate $Z(k)$ when $n = 1/3$, i.e.,

$$E(k) = C' \eta^{2/3} k^{-3} [\ln(k/k_{min})]^{-1/3} \quad ; \quad \omega_k^2 = \eta^{2/3} [\ln(k/k_{min})]^{2/3} \quad (1.50)$$

where η is k -independent. However, the contribution to $E(k)$ in Eq. (1.50) is dominated by wave numbers in the range $k \ll k$ which means the degree of localness is no the same as the inverse cascade range (where $E(k) \sim k^{-5/3}$). So, the dominant straining motion comes from much larger scales than the structures being strained [65, 67].

1.2 Filaments in Turbulence

Turbulent flows, in nature or otherwise, are often *multiphase*: they are laden with particles and objects of varying sizes, shapes and internal degrees of freedom. The

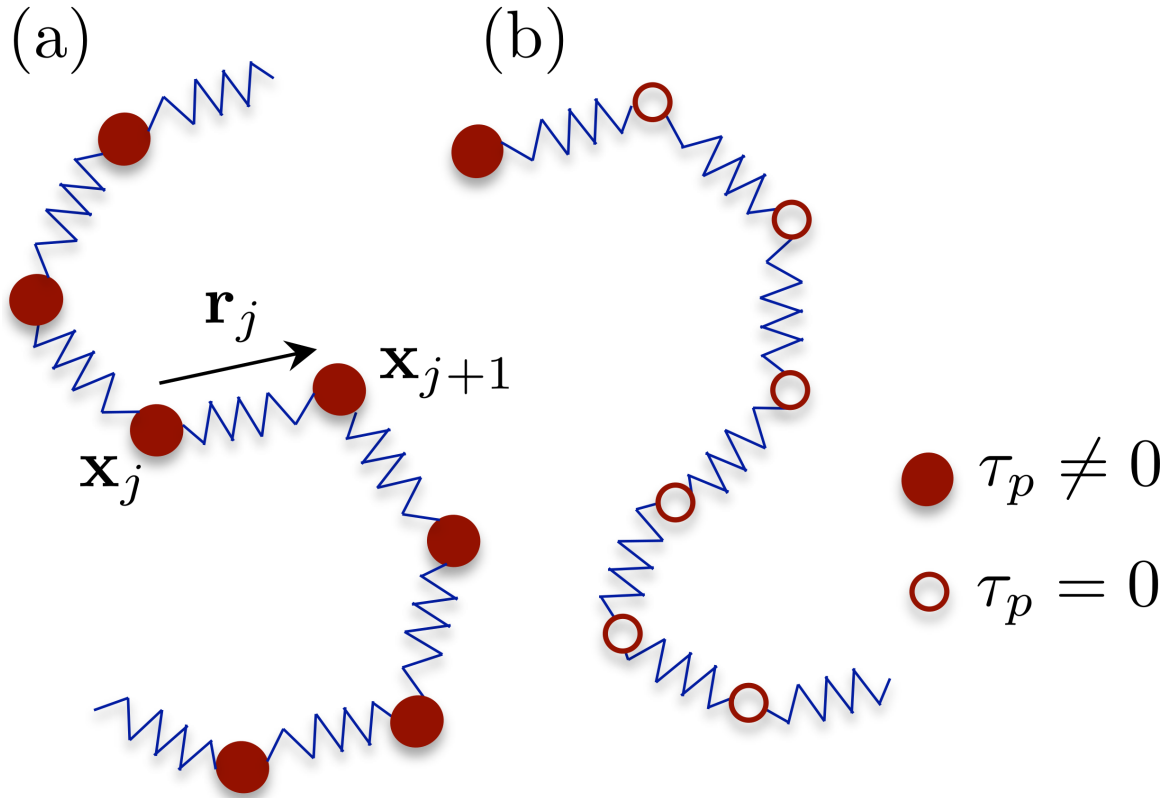


FIGURE 1.3: A schematic of (a) a uniformly-inertial and (b) a heavy-headed filament. A filament of tracers will have $\tau_p = 0$ for all the beads.

ubiquity of such multiphase turbulent flows, of which some common examples include the spread of volcanic ash, pollutant emissions from industries and vehicles, formation of water drops and ice crystals in clouds, and sediment transport by rivers and oceans, demands the study of the transport properties of such objects in a turbulent background. The transport of spherical particles in turbulent flows is very well studied in terms of their distribution, preferential concentration [72–84], dispersion [85–87], acceleration statistics [88], collision rates [89], settling under gravity [90, 91], diffusion [92] and velocity correlations [93]. The dynamics of small anisotropic particles (with additional internal degrees of freedom such as rotation) in turbulent backgrounds [94–97] has been quantified in terms of their rotation [98–100], tumbling [101], orientation [102, 103], and settling [104, 105]. More importantly, a common theme of these previous studies has been the small size of the particles being transported: They are smaller than the dissipative Kolmogorov scale η of the turbulent carrier flow.

However, equally common are multiphase turbulent flows where the object size is larger than η and that may have additional degrees of freedom beyond rotation (for small anisotropic particles) such as torsion, flexibility, and extensibility. In order to model and to study the dynamics of such flexible, extensible objects in turbulent flows, we adopt the bead-spring model of polymers as suggested by experiments [106, 107].

The dynamics of these filaments become complicated and significantly different from that of the free, spherical, point-like particles as shown in Chapters 2 to 4. In this introductory chapter, we discuss how such filaments are modelled.

1.2.1 Modelling a Filament

We model a filament (see Fig. 1.3) as a sequence of N_b identical inertial beads, with a radius $a \ll \eta$, connected to their nearest neighbours via elastic links with the two freely hanging end beads being connected to just one neighbour each. All the beads are characterised by a Stokesian relaxation time-scale $\tau_p = \frac{2\rho a^2}{9\rho_f \nu}$, where $\rho = m/(4\pi a^3/3)$ is the density, m is the mass and a is the radius of the spherical beads, and ρ_f and ν are the density and kinematic viscosity of the turbulent carrier fluid. In this thesis, we examine separately the problems related to filaments where $\tau_p = 0$ in Chapter 3 and $\tau_p \neq 0$ in Chapters 2 and 4. We denote by $\mathbf{x}_1, \dots, \mathbf{x}_{N_b}$ denote the positions of the beads and by $\mathbf{r}_i = \mathbf{x}_{i+1} - \mathbf{x}_i, i = 1, \dots, N_b - 1$ the separation vectors between the i th and $(i+1)$ th bead. The equation of motion for the beads which make up such filament is then given by:

$$m\ddot{\mathbf{x}}_i(t) = -\gamma [\dot{\mathbf{x}}_i - \mathbf{u}(\mathbf{x}_i)] + A\eta_i + (F_i\mathbf{r}_i - F_{i-1}\mathbf{r}_{i-1}) \quad (1.51)$$

where $\gamma = 6\pi\rho_f\nu a$ is the Stokes drag coefficient of the bead advected by a (turbulent) velocity field $\mathbf{u}(\mathbf{x}, t)$ of a constant density ρ and viscosity ν which is obtained from a simultaneous solution of the Navier-Stokes equation (1.4) (see Appendix B for details of numerical simulations). White Gaussian noises η_i account for thermal fluctuations on the beads which sets the equilibrium length $|\mathbf{r}_i| = r_0$. Lastly, the spring forces acting on the beads are incorporated by using the Finitely Extensible Non-linear Elastic (FENE) model with the spring constants F_i being given by the *Warner force law* [108, 109]:

$$F_i = \frac{3kT/r_0^2}{[1 - (r_i/r_m)^2]} = \frac{H_0}{[1 - (r_i/r_m)^2]} = H_0 f_i \quad (1.52)$$

where k is the Boltzmann constant, T is the temperature, r_0, r_m are the equilibrium and maximum length of the springs, and $r = |\mathbf{r}|$. Hence, by dividing Eq. (1.51) by γ throughout, we have :

$$\tau_p \ddot{\mathbf{x}}_i(t) = -[\dot{\mathbf{x}}_i - \mathbf{u}(\mathbf{x}_i)] + \frac{A}{\gamma}\eta_i + \frac{H_0}{\gamma}(f_i\mathbf{r}_i - f_{i-1}\mathbf{r}_{i-1}) \quad (1.53)$$

where $\tau_p = m/\gamma$ is the Stokes relaxation time of the beads. The equation of motion for the filament is then simply obtained in terms of the separation (spring) vectors \mathbf{r}_i

where $i = 1, 2, \dots, N_b - 1$ as:

$$\tau_p \ddot{\mathbf{r}}_i(t) = -[\dot{\mathbf{r}}_i + \mathbf{u}(\mathbf{x}_i) - \mathbf{u}(\mathbf{x}_{i+1})] + \frac{A}{\gamma} [\eta_{i+1} - \eta_i] + \frac{H_0}{\gamma} [f_{i+1} \mathbf{r}_{i+1} - 2f_i \mathbf{r}_i + f_{i-1} \mathbf{r}_{i-1}] \quad (1.54)$$

We now redefine the constants:

$$H_0/\gamma = 3kT/\gamma r_0^2 = 1/4\tau_E, \quad \text{so that} \quad A/\gamma = \sqrt{2kT/\gamma} = \sqrt{r_0^2/6\tau_E}$$

where τ_E is the relaxation time associated with the springs. The dynamics of the filaments are then completely described by the equations of motion for the individual links:

$$\tau_p \ddot{\mathbf{r}}_i(t) = [\mathbf{u}(\mathbf{x}_{i+1}) - \mathbf{u}(\mathbf{x}_i) - \dot{\mathbf{r}}_i] + \frac{1}{4\tau_E} [f_{i+1} \mathbf{r}_{i+1} - 2f_i \mathbf{r}_i + f_{i-1} \mathbf{r}_{i-1}] + \sqrt{\frac{r_0^2}{6\tau_E}} [\eta(\mathbf{r}_{i+1}) - \eta(\mathbf{r}_i)] \quad (1.55)$$

and that of the centre of mass:

$$\tau_p \ddot{\mathbf{X}}_c(t) = -\dot{\mathbf{X}}_c + \frac{1}{N_b} \sum_{i=1}^{N_b} \left[\sqrt{\frac{r_0^2}{6\tau_E}} \eta(\mathbf{x}_i) + \mathbf{u}(\mathbf{x}_i) \right] \quad (1.56)$$

The relaxation time-scale τ_E for the individual springs yields an effective elasticity $\tau_{eff} = \frac{\tau_E N_b (N_b + 1)}{6}$ for the filament [110, 111] which is quantified by the Weissenberg number $Wi = \tau_{eff}/\tau_\eta$. The entire filament has equilibrium and maximum end-to-end extensions of $R = r_0 \sqrt{N_b - 1}$ and $L = r_m (N_b - 1)$ respectively [108].

Real filaments, however, are never fully flexible and there is always some associated resistance to bending. Such filaments with bending stiffness have an energy cost associated with bending, which manifests as an additional force on the beads of the chain. The bending energy is defined using the angles (via the dot product) between successive link vectors, such that a relatively inflexible filament has a larger bending cost and so is more likely to remain in a rod-like configuration. If S is the measure of bending stiffness, then the resulting force acting on the j -th bead is given as [112]:

$$\mathbf{f}_j^B = \frac{S}{r_0} \left[\frac{\alpha_{j-2}}{r_{j-1}} \hat{\mathbf{r}}_{j-2} - \left(\frac{\alpha_{j-2}}{r_{j-1}} \hat{\mathbf{r}}_{j-2} \cdot \hat{\mathbf{r}}_{j-1} + \frac{\alpha_{j-1}}{r_j} + \frac{\alpha_{j-1}}{r_{j-1}} \hat{\mathbf{r}}_{j-1} \cdot \hat{\mathbf{r}}_j \right) \hat{\mathbf{r}}_{j-1} \right] \quad (1.57)$$

$$+ \left(\frac{\alpha_{j-1}}{r_j} \hat{\mathbf{r}}_{j-1} \cdot \hat{\mathbf{r}}_j + \frac{\alpha_{j-1}}{r_{j-1}} + \frac{\alpha_j}{r_j} \hat{\mathbf{r}}_j \cdot \hat{\mathbf{r}}_{j+1} \right) \hat{\mathbf{r}}_j - \frac{\alpha_j}{r_j} \hat{\mathbf{r}}_{j+1} \right] \quad (1.58)$$

with

$$\alpha_j = \begin{cases} 0 & \text{if } j \leq 0 \text{ or } j = N_b \\ 1 & \text{otherwise.} \end{cases} \quad (1.59)$$

The characteristic-time associated with the bending force is $\tau_B = \zeta r_0^3 / S$ where ζ is the Stokes drag on the beads and r_0 is the equilibrium length of the elastic links. Similar to the Weissenberg number, we define a dimensionless measure of bending stiffness as the bending Weissenberg number $Wi_B = \tau_B / \tau_\eta$. The filaments become inflexible for small Wi_B , while the limit of fully flexible filaments is attained for large Wi_B .

The equation of motion for the links [Eq. (1.55)] now includes the additional term $\frac{1}{\zeta} (\mathbf{f}_{j+1}^B - \mathbf{f}_j^B)$ on the right hand side to account for bending stiffness. However, because these bending forces are internal to the filaments, they do not affect the motion of the center-of-mass explicitly and so its equation of motion remains identical to that of fully flexible filaments [Eq. (1.56)].

It must also be noted that objects transported by turbulent flows experience a “turbulent” drag force apart from the usual viscous Stokes’ drag. However, for particles of size smaller than the Kolmogorov dissipation scale such as our inertial beads, the local flow is laminar rather than turbulent ($Re = 1$ at the Kolmogorov dissipation scale η). Thus, such particles experience negligible turbulent drag [113]. This can also be seen by comparing the turbulent and the Stokes’ drag force contributions on an object in a turbulent flow. The turbulent drag force F_D is given by the equation: $F_D = \frac{1}{2} C_D \rho (\mathbf{v} - \mathbf{u})^2 A$, where C_D is the drag coefficient, ρ is the fluid density, \mathbf{v} is the object velocity, \mathbf{u} is the local fluid velocity, and A is the object cross-sectional area. This can be easily compared to the viscous Stokes’ drag force on the object which in our case is a spherical bead. For a sphere, we have the Stokes’ drag given by $F_\nu = 6\pi\rho\nu a |\mathbf{v} - \mathbf{u}|$, where ν is the kinematic viscosity of the fluid and a is the radius of the sphere. The ratio of the magnitude of the two drag forces can, thus, be estimated as:

$$\frac{F_D}{F_\nu} = \frac{1}{12} \frac{C_D |\mathbf{v} - \mathbf{u}| a}{\nu} \sim \frac{1}{12} \frac{C_D |\mathbf{v} - \mathbf{u}| a}{\eta^{4/3} \epsilon^{1/3}}$$

where we have used the fact that $A = \pi a^2$ and $\eta \sim (\nu^3 / \epsilon)^{1/4}$ is used, with ϵ being the turbulent energy dissipation rate. In our model of the bead-spring chains, the beads are considered to be of much smaller size than the Kolmogorov length scale, i.e. $a \ll \eta$. We already know that for small Re numbers, $C_D \approx 1$. The fact that $a \ll \eta$ along with the $1/12$ factor makes the turbulent drag force contribution very small compared to the

Stokes' drag. This small contribution from the turbulent drag force is, thus, unlikely to alter the dynamics of our filaments. However, as the particle (bead) size grows beyond η significantly, the turbulent drag will have a significant contribution and can no longer be neglected.

The relevance of our bead-spring model of a chain is easily underlined by the fact that very simple modifications render it useful for various real-life applications. Our filament model can easily be tweaked to make the mass-distribution non-uniform (see Chapter 2) which can prove suitable for modelling marine organisms that comprise a heavy-head followed by a long tail and often dwell in turbulent waters (such as tadpoles) or even viruses (such as tailed bacteriophages) [114] and sperm cells. The ability of such living entities to move in a preferred direction can also be easily accounted for within our model using an additional active force term acting on the beads. Similarly, the motion of (long, filamentary) micro-organisms is often governed by the search for nutrients (chemotaxis) and an active force can easily be incorporated on the head bead of our filaments to mimic a drive based on the concentration gradient of nutrients.

A uniformly weighted, flexible filament finds its applications in the study of fiber dynamics in turbulent flows: Examples include fibre suspensions encountered in paper making and textile industries, passive marine pollutants such as marine debris, broken fishing gear, and microplastics. In order to obtain a uniform mass distribution within the bead-spring model, one must include a large number of beads in a filament accompanied by suitable elasticity and bending rigidity of the connecting springs. At smaller length scales and very small inertia, these filaments, of course, are used to model polymers and can also serve as models for DNA chains (which are polynucleotide chains with four types of beads: A, C, G and T) [115]. The non-flexible, rigid rod limit of our filaments can be utilised to model surfactant chain molecules (which can be treated as rigid rods with relatively heavy heads) [116].

1.3 Active Matter and Active Turbulence

Living matter, ranging from large bird flocks to bacterial suspensions at small scales, displays complex, dynamical behaviour and pattern formation that bear resemblances to non-living systems. Referred to as *active matter*, these systems exhibit an intriguing class of non-equilibrium phenomena [117–119] which originates in the ability of these systems to be active: They are driven at the level of individual units, e.g. the motility of organisms, cells and particles. Energy is thus injected only at the scale of individuals yet these systems exhibit long range order and collective dynamics,

rich pattern formation and self-similar behaviour across several length scales making these low Reynolds number systems particularly fascinating [117, 118, 120, 121]. Examples of these systems can be as diverse as bacterial colonies [122, 123], suspensions of microtubules and molecular motors [124–126], or schools of fish [127] and bird flocks [117, 128, 129]. In dense active systems, typically those involving microscopic entities, the interactions between individual agents lead to unorganized, often vortical, dynamics with self-similar distribution of energy across several length scales. This last aspect, namely the *appearance* of the flow field and the power-laws which emerge in measurements of the kinetic energy across Fourier modes [122, 130–132], lead to such states being called *active turbulence* in analogy with similar traits of high Reynolds number inertial turbulence [132].

The study of active matter systems was sparked by the evidence of long-range ordering in a study by Vicsek (1995) where particles with random initial distribution and orientations move with a velocity \mathbf{v} of constant magnitude $|\mathbf{v}(t)| = v$ and whose direction is determined by that of its neighbours [133]. The evolution of i -th particle is given by:

$$\mathbf{x}_i(t + \Delta t) = \mathbf{x}_i(t) + \mathbf{v}_i(t)\Delta t \quad (1.60)$$

$$\theta_i(t + \Delta t) = \langle \theta(t) \rangle_r + \eta(t) \quad (1.61)$$

where the velocity $\mathbf{v}_i(t + \Delta t)$ at each step has the absolute value v and a direction $\theta(t + \Delta t)$ with $\langle \theta(t) \rangle_r$ being the mean orientation of all the particles velocities within a radius r of the i -th particle and η is a zero mean white Gaussian noise. Such dynamics result in particles spontaneously breaking the rotational symmetry and display correlated motion resulting in a transition from an ordered phase ($\langle \mathbf{v} \rangle \neq 0$) to a disordered phase ($\langle \mathbf{v} \rangle = 0$) when the noise strength is increased.

Collective motion and long range correlations are a general feature of systems that are comprised of a large number of driven individual units for e.g. bird flocks [117, 128, 129], schools of fish [127], bacterial colonies [122, 123] and even suspensions of microtubules and molecular motors [124–126]. Even non-living systems as self-propelled particles (SPPs) with their short range interactions display polar ordering, form vortex arrays and generate turbulent states [134]. Similarly, an assembly of self-propelled rods (SPRs), which have been used to model bacteria, display rich pattern formation as vortex arrays, polar ordering, laning and turbulence-like states [122, 135].

This problem of spontaneous symmetry breaking in active matter systems was tackled analytically first by Toner and Tu (1995) who proposed a continuum hydrodynamic theory that describes long-range ordering and collective motion of a group, such as a

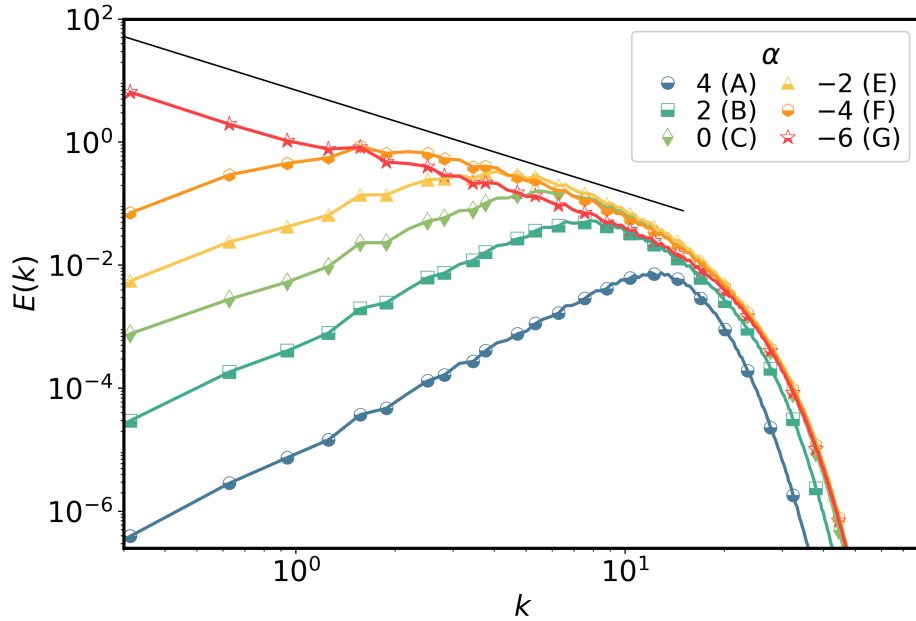


FIGURE 1.4: The energy spectrum in two-dimensional active turbulence shows (non-universal) power-law scalings which change with the degree of activity α .

flock of birds [120, 136, 137]. The problem of pattern formation was dealt with by Swift and Hohenberg (1977) by studying fluctuating instabilities via higher order derivatives [138]. The Toner-Tu model alongwith the Swift-Hohenberg theory (TTSH) has been used to model the collective behaviour of dense bacterial suspensions [123, 139–142] which exhibit a wide variety of spatio-temporal chaotic patterns [122, 143, 144]. The TTSH theory, which essentially is a generalization of the Navier-Stokes equation (see Eq. (1.67)), has led to a better understanding of *turbulence in bacterial suspensions* (which are essentially low- Re flows) and is reminiscent of classical turbulence resulting from the Navier-Stokes equation (1.1). Numerical simulations of the generalized hydrodynamic equation (1.67) have revealed the existence of a range of phases in dense suspensions of active matter, *viz.* active turbulence [143, 144], active vortex lattices, square lattices, and parameter dependent phase-transitions [144]. Active turbulent flows exhibit non-Gaussian velocity (and vorticity) distributions as a function of activity which has been observed both in simulations [145–147] and experiments [122, 123]. Energy spectrum in active turbulence, unlike classical inertial turbulence, shows non-universal scaling [122, 131, 132, 143, 146, 148, 149] and is a function of the activity [148] (see Fig. 1.4).

1.3.1 The Continuum Model: TTSH Theory

A system comprising a large number of individual units is simpler to handle as a field or as a collective of individuals rather than taking care of all the units separately. This

amounts to coarse graining at some level which greatly reduces complexity but incurs a cost: information about the smallest scales (or very large Fourier modes) is lost. However, we are only concerned with patterns and collective motion of a large group of individuals where the detailed physics of smallest scales becomes irrelevant. To that end, a continuum description of a system that exhibits collective motion (flocking) and pattern formation can be motivated simply by considering a scalar order parameter field $\phi(\mathbf{x}, t)$. An equation of the Landau-Ginzburg form describes a transition from a disordered to an ordered state:

$$\frac{\partial\phi(\mathbf{x}, t)}{\partial t} = a\phi + b\phi^3 + \dots \quad (1.62)$$

where globally ordered state $\phi_c = \sqrt{-a/b}$ is obtained when $a > 0, b < 0$ while $a, b < 0$ yields a trivial fixed point $\phi = 0$ corresponding to the disordered state.

For the order parameter field $\phi(\mathbf{x}, t)$ to exhibit pattern formation and correlations over a certain length scale, it helps to consider an equation for the \mathbf{k} -th Fourier mode $\tilde{\phi}_{\mathbf{k}}$ [150]:

$$\frac{\partial\tilde{\phi}_{\mathbf{k}}}{\partial t} = (ck^2 + dk^4 + \dots)\tilde{\phi}_{\mathbf{k}}; \quad k = |\mathbf{k}| \quad (1.63)$$

An equation of the form (1.63), considering only the two leading terms in the expansion, yields a fastest growing mode $|\mathbf{k}_f| = k_f = \sqrt{-c/2d}$, for $a > 0$, and $b < 0$ ensures that higher modes decay. Combining eqns. (1.63), (1.62) yields the following equation in the position space:

$$\frac{\partial\phi(\mathbf{x}, t)}{\partial t} = \alpha\phi + \beta\phi^3 + \Gamma_0\nabla^2\phi + \Gamma_2\nabla^4\phi \quad (1.64)$$

The (α, β) -terms correspond to the Toner-Tu drive while the Laplacian and the bi-Laplacian terms are the Swift-Hohenberg terms responsible for pattern formation [150].

However, a coarse grained bacterial fluid velocity $\mathbf{u}(\mathbf{x}, t)$ is a vector field and thus a continuum description must include terms from the Navier-Stokes equation (1.1) and equation (1.64). We start by assuming, as was the case for classical turbulence, that the bacterial fluid is incompressible which is a good approximation for very dense suspensions: $\nabla \cdot \mathbf{u} = \partial_i u_i = 0$. Polar ordering in dense bacterial suspensions can be accounted for by choosing a quartic Landau potential for the velocity field similar to the scalar theory [151]:

$$U(\mathbf{u}) = \frac{\alpha}{2}|\mathbf{u}|^2 + \frac{\beta}{4}|\mathbf{u}|^4 \quad (1.65)$$

that exhibits a phase transition from a disordered isotropic state $\mathbf{u} = 0$ for $\alpha, \beta > 0$ to a flocking phase $\mathbf{u} = \sqrt{-\alpha/\beta}$ with arbitrary orientations for $\alpha < 0$ while $\beta > 0$ always. However, bacterial suspensions exhibit not global but only local polar ordering which suggests that the system must be destabilised which can be achieved by incorporating contributions from a stress term. For this, a symmetric and traceless rate-of-strain tensor S has been postulated [122, 151]:

$$S_{ij} = \lambda' \left(u_i u_j - \frac{\delta_{ij}}{d} |\mathbf{u}|^2 \right) - \Gamma_0 (\partial_i u_j + \partial_j u_i) - \Gamma_2 \nabla^2 (\partial_i u_j + \partial_j u_i) \quad (1.66)$$

where d is the dimensionality. The first term represents active stress contributions [152, 153] and the coefficient λ' signals the type of bacteria constituting the flow: $\lambda' > 0$ (< 0) for puller (pusher) type bacteria. The Γ_0 -term ascertains that Navier-Stokes equation is recovered as a limit while the Γ_2 -term is dictated by stability considerations as Γ_0 can become positive in dense bacterial suspensions [122, 123]. Reduction in viscosity been substantiated by experiments [117, 128, 139, 140, 154–157] and analytically [134, 141, 142]. Writing down a generalized Navier-Stokes equation using (1.65), (1.66): and

$$\frac{\partial \mathbf{u}}{\partial t} + \mathbf{u} \cdot \nabla \mathbf{u} = -\nabla p' - \alpha \mathbf{u} - \beta \mathbf{u}^3 + \nabla \cdot S$$

where the pressure p' is a Lagrange multiplier enforcing the incompressibility constraint. Substituting the expression for the strain rate S and redefining parameters as $\lambda = 1 - \lambda'$, $\lambda_1 = -\lambda'/d$, $p = p' - \lambda_1 \nabla \cdot \mathbf{u}^2$ yields the generalized hydrodynamic model:

$$\frac{\partial \mathbf{u}}{\partial t} + \lambda \mathbf{u} \cdot \nabla \mathbf{u} = -\nabla p - \alpha \mathbf{u} - \beta \mathbf{u}^3 - \Gamma_0 \nabla^2 \mathbf{u} - \Gamma_2 \nabla^4 \mathbf{u} \quad (1.67)$$

The Navier-Stokes equation for a classical, passive fluid is recovered in the limit $\lambda' = \alpha = \beta = \Gamma_2 = 0$ and $\Gamma_0 < 0$. Equation (1.67) reduces to the incompressible Toner-Tu model when $\Gamma_0 < 0, \Gamma_2 = 0$ [136, 137]. The two higher order derivatives, which constitute the Swift-Hohenberg term, give rise to quasi-chaotic flow patterns along with the convective derivative.

References

- [1] U. Frisch, *Turbulence: The Legacy of A. N. Kolmogorov*. Cambridge University Press, 1995, [10.1017/CBO9781139170666](https://doi.org/10.1017/CBO9781139170666).
- [2] M. Lesieur, *Turbulence in Fluids*. Springer Netherlands, 2008, [10.1007/978-1-4020-6435-7](https://doi.org/10.1007/978-1-4020-6435-7).
- [3] P. A. Davidson, *Turbulence: an introduction for scientists and engineers*. Oxford university press, 2015, [10.1093/acprof:oso/9780198722588.001.0001](https://doi.org/10.1093/acprof:oso/9780198722588.001.0001).
- [4] A. Monin and A. Yaglom, *Statistical Fluid Mechanics, Volume 2: Mechanics of Turbulence*. 01, 2007.
- [5] A. L. Kistler and T. Vrebalovich, *Grid turbulence at large reynolds numbers*, *Journal of Fluid Mechanics* **26** (1966) 37–47.
- [6] L. Mydlarski and Z. Warhaft, *Passive scalar statistics in high-péclet-number grid turbulence*, *Journal of Fluid Mechanics* **358** (1998) 135–175.
- [7] H. S. Kang, S. Chester and C. Meneveau, *Decaying turbulence in an active-grid-generated flow and comparisons with large-eddy simulation*, *Journal of Fluid Mechanics* **480** (2003) 129–160.
- [8] P. Krogstad and P. A. Davidson, *Is grid turbulence saffman turbulence?*, *Journal of Fluid Mechanics* **642** (2010) 373–394.
- [9] K. Nagata, T. Saiki, Y. Sakai, Y. Ito and K. Iwano, *Effects of grid geometry on non-equilibrium dissipation in grid turbulence*, *Physics of Fluids* **29** (2017) 015102.
- [10] A. N. Kolmogorov, V. Levin, J. C. R. Hunt, O. M. Phillips and D. Williams, *The local structure of turbulence in incompressible viscous fluid for very large reynolds numbers*, *Proceedings of the Royal Society of London. Series A: Mathematical and Physical Sciences* **434** (1991) 9–13.
- [11] S. A. Orszag, *Analytical theories of turbulence*, *Journal of Fluid Mechanics* **41** (1970) 363–386.

-
- [12] G. K. Batchelor, *The theory of homogeneous turbulence*. Cambridge university press, 1953.
- [13] P. K. Yeung, *Lagrangian investigations of turbulence*, *Annual Review of Fluid Mechanics* **34** (2002) 115–142.
- [14] F. Toschi and E. Bodenschatz, *Lagrangian properties of particles in turbulence*, *Annual Review of Fluid Mechanics* **41** (2009) 375–404.
- [15] G. I. Taylor, *Diffusion by continuous movements*, *Proceedings of the London Mathematical Society* **s2-20** (1922) 196–212.
- [16] L. F. Richardson and G. T. Walker, *Atmospheric diffusion shown on a distance-neighbour graph*, *Proceedings of the Royal Society of London. Series A, Containing Papers of a Mathematical and Physical Character* **110** (1926) 709–737.
- [17] G. K. Batchelor, *Diffusion in a field of homogeneous turbulence: Ii. the relative motion of particles*, *Mathematical Proceedings of the Cambridge Philosophical Society* **48** (1952) 345–362.
- [18] R. H. Kraichnan, *Lagrangian-history closure approximation for turbulence*, *The Physics of Fluids* **8** (1965) 575–598.
- [19] R. H. Kraichnan, *Isotropic turbulence and inertial-range structure*, *The Physics of Fluids* **9** (1966) 1728–1752.
- [20] M. Holzner, A. Liberzon, N. Nikitin, B. Lüthi, W. Kinzelbach and A. Tsinober, *A lagrangian investigation of the small-scale features of turbulent entrainment through particle tracking and direct numerical simulation*, *Journal of Fluid Mechanics* **598** (2008) 465–475.
- [21] B. Lüthi, A. Tsinober and W. Kinzelbach, *Lagrangian measurement of vorticity dynamics in turbulent flow*, *Journal of Fluid Mechanics* **528** (2005) 87–118.
- [22] K. Hoyer, M. Holzner, B. Lüthi, M. Guala, A. Liberzon and W. Kinzelbach, *3d scanning particle tracking velocimetry*, *Experiments in Fluids* **39** (2005) 923.
- [23] N. Mordant, P. Metz, O. Michel and J.-F. Pinton, *Measurement of lagrangian velocity in fully developed turbulence*, *Phys. Rev. Lett.* **87** (Nov, 2001) 214501.
- [24] L. Chevillard, S. G. Roux, E. Levêque, N. Mordant, J.-F. Pinton and A. Arneodo, *Lagrangian velocity statistics in turbulent flows: Effects of dissipation*, *Phys. Rev. Lett.* **91** (Nov, 2003) 214502.

-
- [25] N. Mordant, E. Lévêque and J.-F. Pinton, *Experimental and numerical study of the lagrangian dynamics of high reynolds turbulence*, *New Journal of Physics* **6** (sep, 2004) 116–116.
- [26] INTERNATIONAL COLLABORATION FOR TURBULENCE RESEARCH collaboration, H. Xu, M. Bourgoïn, N. T. Ouellette and E. Bodenschatz, *High order lagrangian velocity statistics in turbulence*, *Phys. Rev. Lett.* **96** (Jan, 2006) 024503.
- [27] P. K. Yeung and S. B. Pope, *Lagrangian statistics from direct numerical simulations of isotropic turbulence*, *Journal of Fluid Mechanics* **207** (1989) 531–586.
- [28] A. La Porta, G. A. Voth, A. M. Crawford, J. Alexander and E. Bodenschatz, *Fluid particle accelerations in fully developed turbulence*, *Nature* **409** (Feb, 2001) 1017–1019.
- [29] C. Beck, *Lagrangian acceleration statistics in turbulent flows*, *Europhysics Letters (EPL)* **64** (oct, 2003) 151–157.
- [30] N. Mordant, A. M. Crawford and E. Bodenschatz, *Three-dimensional structure of the lagrangian acceleration in turbulent flows*, *Phys. Rev. Lett.* **93** (Nov, 2004) 214501.
- [31] L. Biferale, G. Boffetta, A. Celani, B. J. Devenish, A. Lanotte and F. Toschi, *Multifractal statistics of lagrangian velocity and acceleration in turbulence*, *Phys. Rev. Lett.* **93** (Aug, 2004) 064502.
- [32] N. Mordant, A. Crawford and E. Bodenschatz, *Experimental lagrangian acceleration probability density function measurement*, *Physica D: Nonlinear Phenomena* **193** (2004) 245–251.
- [33] L. Biferale, G. Boffetta, A. Celani, B. J. Devenish, A. Lanotte and F. Toschi, *Lagrangian statistics of particle pairs in homogeneous isotropic turbulence*, *Physics of Fluids* **17** (2005) 115101.
- [34] M. Chertkov, A. Pumir and B. I. Shraiman, *Lagrangian tetrad dynamics and the phenomenology of turbulence*, *Physics of Fluids* **11** (1999) 2394–2410.
- [35] L. Chevillard and C. Meneveau, *Lagrangian dynamics and statistical geometric structure of turbulence*, *Phys. Rev. Lett.* **97** (Oct, 2006) 174501.
- [36] C. Meneveau, *Lagrangian dynamics and models of the velocity gradient tensor in turbulent flows*, *Annual Review of Fluid Mechanics* **43** (2011) 219–245.

- [37] M. Sommerfeld, *Validation of a stochastic lagrangian modelling approach for inter-particle collisions in homogeneous isotropic turbulence*, *International Journal of Multiphase Flow* **27** (2001) 1829–1858.
- [38] S. B. Pope, *On the relationship between stochastic lagrangian models of turbulence and second-moment closures*, *Physics of Fluids* **6** (1994) 973–985.
- [39] S. B. Pope, *Lagrangian pdf methods for turbulent flows*, *Annual Review of Fluid Mechanics* **26** (1994) 23–63.
- [40] B. Sawford, *Turbulent relative dispersion*, *Annual Review of Fluid Mechanics* **33** (2001) 289–317.
- [41] G. Haller and G. Yuan, *Lagrangian coherent structures and mixing in two-dimensional turbulence*, *Physica D: Nonlinear Phenomena* **147** (2000) 352–370.
- [42] G. Haller, *Lagrangian structures and the rate of strain in a partition of two-dimensional turbulence*, *Physics of Fluids* **13** (2001) 3365–3385.
- [43] G. Haller, *Lagrangian coherent structures from approximate velocity data*, *Physics of Fluids* **14** (2002) 1851–1861.
- [44] M. Mathur, G. Haller, T. Peacock, J. E. Ruppert-Felsot and H. L. Swinney, *Uncovering the lagrangian skeleton of turbulence*, *Phys. Rev. Lett.* **98** (Apr, 2007) 144502.
- [45] M. A. Green, C. W. Rowley and G. Haller, *Detection of lagrangian coherent structures in three-dimensional turbulence*, *Journal of Fluid Mechanics* **572** (2007) 111–120.
- [46] G. Haller and F. J. Beron-Vera, *Coherent lagrangian vortices: the black holes of turbulence*, *Journal of Fluid Mechanics* **731** (2013) R4.
- [47] A. Celani and M. Vergassola, *Statistical geometry in scalar turbulence*, *Phys. Rev. Lett.* **86** (Jan, 2001) 424–427.
- [48] P. Castiglione and A. Pumir, *Evolution of triangles in a two-dimensional turbulent flow*, *Phys. Rev. E* **64** (Oct, 2001) 056303.
- [49] G. Falkovich, K. Gawędzki and M. Vergassola, *Particles and fields in fluid turbulence*, *Rev. Mod. Phys.* **73** (Nov, 2001) 913–975.
- [50] A. Pumir, B. I. Shraiman and M. Chertkov, *Geometry of lagrangian dispersion in turbulence*, *Phys. Rev. Lett.* **85** (Dec, 2000) 5324–5327.

- [51] A. Pumir, B. I. Shraiman and M. Chertkov, *The lagrangian view of energy transfer in turbulent flow*, *Europhysics Letters (EPL)* **56** (nov, 2001) 379–385.
- [52] C. Meneveau, T. S. Lund and W. H. Cabot, *A lagrangian dynamic subgrid-scale model of turbulence*, *Journal of Fluid Mechanics* **319** (1996) 353–385.
- [53] E. Bou-Zeid, C. Meneveau and M. Parlange, *A scale-dependent lagrangian dynamic model for large eddy simulation of complex turbulent flows*, *Physics of Fluids* **17** (2005) 025105.
- [54] S. B. Pope, *Ten questions concerning the large-eddy simulation of turbulent flows*, *New Journal of Physics* **6** (mar, 2004) 35–35.
- [55] M. R. Maxey and J. J. Riley, *Equation of motion for a small rigid sphere in a nonuniform flow*, *The Physics of Fluids* **26** (1983) 883–889.
- [56] L. F. Richardson and P. Lynch, *Weather Prediction by Numerical Process*. Cambridge Mathematical Library. Cambridge University Press, 2 ed., 2007, [10.1017/CBO9780511618291](https://doi.org/10.1017/CBO9780511618291).
- [57] U. Frisch, *Fully developed turbulence and intermittency*, *Annals of the New York Academy of Sciences* **357** (1980) 359–367.
- [58] E. D. Siggia, *Numerical study of small-scale intermittency in three-dimensional turbulence*, *Journal of Fluid Mechanics* **107** (1981) 375–406.
- [59] R. Pandit, P. Perlekar and S. S. Ray, *Statistical properties of turbulence: An overview*, *Pramana* **73** (Oct, 2009) 157.
- [60] R. H. Kraichnan, *Inertial ranges in two-dimensional turbulence*, *The Physics of Fluids* **10** (1967) 1417–1423.
- [61] C. E. Leith and R. H. Kraichnan, *Predictability of turbulent flows*, *Journal of Atmospheric Sciences* **29** (1972) 1041 – 1058.
- [62] W. D. McComb, *The physics of fluid turbulence*. 1990.
- [63] M. K. Verma, *Statistical theory of magnetohydrodynamic turbulence: recent results*, *Physics Reports* **401** (2004) 229–380.
- [64] M. K. Verma, *Energy Transfers in Fluid Flows: Multiscale and Spectral Perspectives*. Cambridge University Press, 2019, [10.1017/9781316810019](https://doi.org/10.1017/9781316810019).
- [65] G. Boffetta and R. E. Ecke, *Two-dimensional turbulence*, *Annual Review of Fluid Mechanics* **44** (2012) 427–451.

- [66] M. Rivera and X. L. Wu, *External dissipation in driven two-dimensional turbulence*, *Phys. Rev. Lett.* **85** (Jul, 2000) 976–979.
- [67] R. H. Kraichnan, *Inertial-range transfer in two- and three-dimensional turbulence*, *Journal of Fluid Mechanics* **47** (1971) 525–535.
- [68] R. H. Kraichnan and D. Montgomery, *Two-dimensional turbulence*, *Reports on Progress in Physics* **43** (may, 1980) 547–619.
- [69] D. Bernard, *Three-point velocity correlation functions in two-dimensional forced turbulence*, *Phys. Rev. E* **60** (Nov, 1999) 6184–6187.
- [70] E. Lindborg, *Can the atmospheric kinetic energy spectrum be explained by two-dimensional turbulence?*, *Journal of Fluid Mechanics* **388** (1999) 259–288.
- [71] V. Yakhot, *Two-dimensional turbulence in the inverse cascade range*, *Phys. Rev. E* **60** (Nov, 1999) 5544–5551.
- [72] V. Armenio and V. Fiorotto, *The importance of the forces acting on particles in turbulent flows*, *Physics of Fluids* **13** (2001) 2437–2440.
- [73] E. Balkovsky, G. Falkovich and A. Fouxon, *Intermittent distribution of inertial particles in turbulent flows*, *Phys. Rev. Lett.* **86** (Mar, 2001) 2790–2793.
- [74] G. Falkovich and A. Pumir, *Intermittent distribution of heavy particles in a turbulent flow*, *Physics of Fluids* **16** (2004) L47–L50.
- [75] J. Bec, *Fractal clustering of inertial particles in random flows*, *Physics of Fluids* **15** (2003) L81–L84.
- [76] J. Bec, L. Biferale, M. Cencini, A. Lanotte, S. Musacchio and F. Toschi, *Heavy particle concentration in turbulence at dissipative and inertial scales*, *Phys. Rev. Lett.* **98** (Feb, 2007) 084502.
- [77] G. Boffetta, F. De Lillo and A. Gamba, *Large scale inhomogeneity of inertial particles in turbulent flows*, *Physics of Fluids* **16** (2004) L20–L23.
- [78] J. Bec, L. Biferale, G. Boffetta, M. Cencini, S. Musacchio and F. Toschi, *Lyapunov exponents of heavy particles in turbulence*, *Physics of Fluids* **18** (2006) 091702.
- [79] M. Cencini, J. Bec, L. Biferale, G. Boffetta, A. Celani, A. S. Lanotte et al., *Dynamics and statistics of heavy particles in turbulent flows*, *Journal of Turbulence* **7** (2006) N36.

- [80] L. Chen, S. Goto and J. C. Vassilicos, *Turbulent clustering of stagnation points and inertial particles*, *Journal of Fluid Mechanics* **553** (2006) 143–154.
- [81] A. Guha, *Transport and deposition of particles in turbulent and laminar flow*, *Annual Review of Fluid Mechanics* **40** (2008) 311–341.
- [82] R. Monchaux, M. Bourgoin and A. Cartellier, *Analyzing preferential concentration and clustering of inertial particles in turbulence*, *Int. J. Multiph. Flow* **40** (2012) 1 – 18.
- [83] S. Goto and J. C. Vassilicos, *Self-similar clustering of inertial particles and zero-acceleration points in fully developed two-dimensional turbulence*, *Physics of Fluids* **18** (2006) 115103.
- [84] H. Yoshimoto and S. Goto, *Self-similar clustering of inertial particles in homogeneous turbulence*, *Journal of Fluid Mechanics* **577** (2007) 275–286.
- [85] M. W. Reeks, *On a kinetic equation for the transport of particles in turbulent flows*, *Physics of Fluids A: Fluid Dynamics* **3** (1991) 446–456.
- [86] L.-P. Wang and D. E. Stock, *Dispersion of heavy particles by turbulent motion*, *Journal of Atmospheric Sciences* **50** (1993) 1897 – 1913.
- [87] J. Bec, L. Biferale, A. S. Lanotte, A. Scagliarini and F. Toschi, *Turbulent pair dispersion of inertial particles*, *Journal of Fluid Mechanics* **645** (2010) 497–528.
- [88] N. M. Qureshi, U. Arrieta, C. Baudet, A. Cartellier, Y. Gagne and M. Bourgoin, *Acceleration statistics of inertial particles in turbulent flow*, *The European Physical Journal B* **66** (Dec, 2008) 531–536.
- [89] L.-P. Wang, A. S. Wexler and Y. Zhou, *Statistical mechanical description and modelling of turbulent collision of inertial particles*, *Journal of Fluid Mechanics* **415** (2000) 117–153.
- [90] J. Bec, H. Homann and S. S. Ray, *Gravity-driven enhancement of heavy particle clustering in turbulent flow*, *Phys. Rev. Lett.* **112** (May, 2014) 184501.
- [91] G. H. Good, P. J. Ireland, G. P. Bewley, E. Bodenschatz, L. R. Collins and Z. Warhaft, *Settling regimes of inertial particles in isotropic turbulence*, *J. Fluid Mech.* **759** (2014) R3.
- [92] T. Elperin, N. Kleorin and I. Rogachevskii, *Turbulent thermal diffusion of small inertial particles*, *Phys. Rev. Lett.* **76** (Jan, 1996) 224–227.

- [93] W. H. Snyder and J. L. Lumley, *Some measurements of particle velocity autocorrelation functions in a turbulent flow*, *Journal of Fluid Mechanics* **48** (1971) 41–71.
- [94] G. A. Voth and A. Soldati, *Anisotropic particles in turbulence*, *Annual Review of Fluid Mechanics* **49** (2017) 249–276.
- [95] V. Raman and R. O. Fox, *Modeling of fine-particle formation in turbulent flames*, *Annual Review of Fluid Mechanics* **48** (2016) 159–190.
- [96] M. Mandø and L. Rosendahl, *On the motion of non-spherical particles at high reynolds number*, *Powder Technology* **202** (2010) 1–13.
- [97] D. Njobuenwu and M. Fairweather, *Dynamics of single, non-spherical ellipsoidal particles in a turbulent channel flow*, *Chemical Engineering Science* **123** (2015) 265–282.
- [98] M. Byron, J. Einarsson, K. Gustavsson, G. Voth, B. Mehlig and E. Variano, *Shape-dependence of particle rotation in isotropic turbulence*, *Physics of Fluids* **27** (2015) 035101.
- [99] S. Parsa, E. Calzavarini, F. Toschi and G. A. Voth, *Rotation rate of rods in turbulent fluid flow*, *Phys. Rev. Lett.* **109** (Sep, 2012) 134501.
- [100] S. Kramel, G. A. Voth, S. Timpel and F. Toschi, *Preferential rotation of chiral dipoles in isotropic turbulence*, *Phys. Rev. Lett.* **117** (Oct, 2016) 154501.
- [101] K. Gustavsson, J. Einarsson and B. Mehlig, *Tumbling of small axisymmetric particles in random and turbulent flows*, *Phys. Rev. Lett.* **112** (Jan, 2014) 014501.
- [102] L. Chevillard and C. Meneveau, *Orientation dynamics of small, triaxial-ellipsoidal particles in isotropic turbulence*, *Journal of Fluid Mechanics* **737** (2013) 571–596.
- [103] R. Ni, N. T. Ouellette and G. A. Voth, *Alignment of vorticity and rods with lagrangian fluid stretching in turbulence*, *Journal of Fluid Mechanics* **743** (2014) R3.
- [104] C. Siewert, R. Kunnen, M. Meinke and W. Schröder, *Orientation statistics and settling velocity of ellipsoids in decaying turbulence*, *Atmospheric Research* **142** (2014) 45–56.

- [105] H. Zhang, G. Ahmadi, F.-G. Fan and J. B. McLaughlin, *Ellipsoidal particles transport and deposition in turbulent channel flows*, *International Journal of Multiphase Flow* **27** (2001) 971–1009.
- [106] G. Verhille and A. Bartoli, *3d conformation of a flexible fiber in a turbulent flow*, *Exp. Fluids* **57** (Jun, 2016) 117.
- [107] M. E. Rosti, A. A. Banaei, L. Brandt and A. Mazzino, *Flexible fiber reveals the two-point statistical properties of turbulence*, *Phys. Rev. Lett.* **121** (Jul, 2018) 044501.
- [108] R. B. Bird, C. F. Curtiss, R. C. Armstrong and O. Hassager, *Dynamics of Polymeric Liquids*. John Wiley and Sons, New York, 1977, [10.1002/pol.1978.130160210](https://doi.org/10.1002/pol.1978.130160210).
- [109] H. C. Öttinger, *Stochastic Processes in Polymeric Fluids*. Springer Berlin Heidelberg, 1996, [10.1007/978-3-642-58290-5](https://doi.org/10.1007/978-3-642-58290-5).
- [110] S. Jin and L. R. Collins, *Dynamics of dissolved polymer chains in isotropic turbulence*, *New Journal of Physics* **9** (oct, 2007) 360–360.
- [111] J. R. Picardo, D. Vincenzi, N. Pal and S. S. Ray, *Preferential sampling of elastic chains in turbulent flows*, *Phys. Rev. Lett.* **121** (Dec, 2018) 244501.
- [112] E. Gauger and H. Stark, *Numerical study of a microscopic artificial swimmer*, *Phys. Rev. E* **74** (Aug, 2006) 021907.
- [113] M. K. Verma, *Introduction to mechanics*. Universities Press, 2008.
- [114] F. L. Nobrega, M. Vlot, P. A. de Jonge, L. L. Dreesens, H. J. E. Beaumont, R. Lavigne et al., *Targeting mechanisms of tailed bacteriophages*, *Nature Reviews Microbiology* **16** (Dec, 2018) 760–773.
- [115] P. Vesely, *Molecular biology of the cell*. by bruce alberts, alexander johnson, julian lewis, martin raff, keith roberts and peter walter. isbn 0-8153-3218-1; hardback; 1,616 pages; \$110.00 garland science inc., new york, 2002, *Scanning* **26** (2004) 153–153, [<https://onlinelibrary.wiley.com/doi/pdf/10.1002/sca.4950260309>].
- [116] S. B. Opps, B. G. Nickel, C. G. Gray and D. E. Sullivan, *The ground-state phase behavior of model langmuir monolayers*, *The Journal of Chemical Physics* **113** (2000) 339–348.

- [117] M. C. Marchetti, J. F. Joanny, S. Ramaswamy, T. B. Liverpool, J. Prost, M. Rao et al., *Hydrodynamics of soft active matter*, *Rev. Mod. Phys.* **85** (Jul, 2013) 1143–1189.
- [118] S. Ramaswamy, *Active matter*, *Journal of Statistical Mechanics: Theory and Experiment* **2017** (may, 2017) 054002.
- [119] A. Doostmohammadi, J. Ignés-Mullol, J. M. Yeomans and F. Sagués, *Active nematics*, *Nature communications* **9** (2018) 1–13.
- [120] J. Toner, Y. Tu and S. Ramaswamy, *Hydrodynamics and phases of flocks*, *Annals of Physics* **318** (2005) 170–244.
- [121] J. M. Yeomans, *Playful topology*, *Nature Materials* **13** (2014) 1004–1005.
- [122] H. H. Wensink, J. Dunkel, S. Heidenreich, K. Drescher, R. E. Goldstein, H. Löwen et al., *Meso-scale turbulence in living fluids*, *Proceedings of the National Academy of Sciences* **109** (2012) 14308–14313.
- [123] J. Dunkel, S. Heidenreich, K. Drescher, H. H. Wensink, M. Bär and R. E. Goldstein, *Fluid dynamics of bacterial turbulence*, *Physical review letters* **110** (2013) 228102.
- [124] K.-T. Wu, J. B. Hishamunda, D. T. Chen, S. J. DeCamp, Y.-W. Chang, A. Fernández-Nieves et al., *Transition from turbulent to coherent flows in confined three-dimensional active fluids*, *Science* **355** (2017) .
- [125] T. Sanchez, D. T. N. Chen, S. J. DeCamp, M. Heymann and Z. Dogic, *Spontaneous motion in hierarchically assembled active matter*, *Nature* **491** (Nov, 2012) 431–434.
- [126] Y. Sumino, K. H. Nagai, Y. Shitaka, D. Tanaka, K. Yoshikawa, H. Chaté et al., *Large-scale vortex lattice emerging from collectively moving microtubules*, *Nature* **483** (Mar, 2012) 448–452.
- [127] Y. Katz, K. Tunstrøm, C. C. Ioannou, C. Huepe and I. D. Couzin, *Inferring the structure and dynamics of interactions in schooling fish*, *Proceedings of the National Academy of Sciences* **108** (2011) 18720–18725.
- [128] S. Ramaswamy, *The mechanics and statistics of active matter*, *Annual Review of Condensed Matter Physics* **1** (2010) 323–345.
- [129] A. Cavagna, A. Cimarelli, I. Giardina, G. Parisi, R. Santagati, F. Stefanini et al., *Scale-free correlations in starling flocks*, *Proceedings of the National Academy of Sciences* **107** (2010) 11865–11870.

- [130] L. Giomi, L. Mahadevan, B. Chakraborty and M. F. Hagan, *Banding, excitability and chaos in active nematic suspensions*, *Nonlinearity* **25** (Jul, 2012) 2245–2269.
- [131] R. Alert, J.-F. Joanny and J. Casademunt, *Universal scaling of active nematic turbulence*, *Nature Physics* **16** (Jun, 2020) 682–688.
- [132] R. Alert, J. Casademunt and J.-F. Joanny, *Active turbulence*, *Annual Review of Condensed Matter Physics* **13** (2022) null.
- [133] T. Vicsek, A. Czirók, E. Ben-Jacob, I. Cohen and O. Shochet, *Novel type of phase transition in a system of self-driven particles*, *Phys. Rev. Lett.* **75** (Aug, 1995) 1226–1229.
- [134] R. Großmann, P. Romanczuk, M. Bär and L. Schimansky-Geier, *Vortex arrays and mesoscale turbulence of self-propelled particles*, *Phys. Rev. Lett.* **113** (Dec, 2014) 258104.
- [135] M. Bär, R. Grossmann, S. Heidenreich and F. Peruani, *Self-propelled rods: Insights and perspectives for active matter*, *Annual Review of Condensed Matter Physics* **11** (2020) 441–466.
- [136] J. Toner and Y. Tu, *Long-range order in a two-dimensional dynamical XY model: How birds fly together*, *Phys. Rev. Lett.* **75** (Dec, 1995) 4326–4329.
- [137] J. Toner and Y. Tu, *Flocks, herds, and schools: A quantitative theory of flocking*, *Phys. Rev. E* **58** (Oct, 1998) 4828–4858.
- [138] J. Swift and P. C. Hohenberg, *Hydrodynamic fluctuations at the convective instability*, *Physical Review A* **15** (1977) 319.
- [139] Y. Hatwalne, S. Ramaswamy, M. Rao and R. A. Simha, *Rheology of active-particle suspensions*, *Phys. Rev. Lett.* **92** (Mar, 2004) 118101.
- [140] L. Giomi, T. B. Liverpool and M. C. Marchetti, *Sheared active fluids: Thickening, thinning, and vanishing viscosity*, *Phys. Rev. E* **81** (May, 2010) 051908.
- [141] S. Heidenreich, J. Dunkel, S. H. Klapp and M. Bär, *Hydrodynamic length-scale selection in microswimmer suspensions*, *Physical Review E* **94** (2016) 020601.
- [142] H. Reinken, S. H. Klapp, M. Bär and S. Heidenreich, *Derivation of a hydrodynamic theory for mesoscale dynamics in microswimmer suspensions*, *Physical Review E* **97** (2018) 022613.

- [143] M. James, W. J. Bos and M. Wilczek, *Turbulence and turbulent pattern formation in a minimal model for active fluids*, *Physical Review Fluids* **3** (2018) 061101.
- [144] M. James, D. A. Suchla, J. Dunkel and M. Wilczek, *Emergence and melting of active vortex crystals*, *Nature Communications* **12** (Sep, 2021) 5630.
- [145] M. James and M. Wilczek, *Vortex dynamics and lagrangian statistics in a model for active turbulence*, *The European Physical Journal E* **41** (2018) 1–6.
- [146] S. Mukherjee, R. K. Singh, M. James and S. S. Ray, *Anomalous diffusion and lévy walks distinguish active from inertial turbulence*, *Phys. Rev. Lett.* **127** (Sep, 2021) 118001.
- [147] J. Urzay, A. Doostmohammadi and J. M. Yeomans, *Multi-scale statistics of turbulence motorized by active matter*, *Journal of Fluid Mechanics* **822** (2017) 762–773.
- [148] V. Bratanov, F. Jenko and E. Frey, *New class of turbulence in active fluids*, *Proceedings of the National Academy of Sciences* **112** (2015) 15048–15053.
- [149] S. C.P. and A. Joy, *Friction scaling laws for transport in active turbulence*, *Physical Review Fluids* **5** (2020) 024302.
- [150] A. U. Oza, S. Heidenreich and J. Dunkel, *Generalized swift-hohenberg models for dense active suspensions*, *The European Physical Journal E* **39** (Oct, 2016) 97.
- [151] J. Dunkel, S. Heidenreich, M. Bär and R. E. Goldstein, *Minimal continuum theories of structure formation in dense active fluids*, *New Journal of Physics* **15** (apr, 2013) 045016.
- [152] A. Baskaran and M. C. Marchetti, *Hydrodynamics of self-propelled hard rods*, *Phys. Rev. E* **77** (Jan, 2008) 011920.
- [153] R. A. Simha and S. Ramaswamy, *Hydrodynamic fluctuations and instabilities in ordered suspensions of self-propelled particles*, *Physical review letters* **89** (2002) 058101.
- [154] A. Sokolov and I. S. Aranson, *Reduction of viscosity in suspension of swimming bacteria*, *Phys. Rev. Lett.* **103** (Sep, 2009) 148101.
- [155] J. Gachelin, G. Miño, H. Berthet, A. Lindner, A. Rousselet and E. Clément, *Non-newtonian viscosity of escherichia coli suspensions*, *Phys. Rev. Lett.* **110** (Jun, 2013) 268103.

-
- [156] H. M. López, J. Gachelin, C. Douarche, H. Auradou and E. Clément, *Turning bacteria suspensions into superfluids*, *Phys. Rev. Lett.* **115** (Jul, 2015) 028301.
- [157] D. Saintillan, *Rheology of active fluids*, *Annual Review of Fluid Mechanics* **50** (2018) 563–592.

Chapter 2

Elasto-inertial Chains in a Two-dimensional Turbulent Flow

*The interplay of inertia and elasticity is shown to have a significant impact on the transport of filamentary objects, modelled by bead-spring chains, in a two-dimensional turbulent flow. We show how elastic interactions amongst inertial beads result in a non-trivial sampling of the flow, ranging from entrapment within vortices to preferential sampling of straining regions. This behavior is quantified as a function of inertia and elasticity and is shown to be very different from free, non-interacting heavy particles, as well as inertialess chains [Picardo et al., Phys. Rev. Lett. **121**, 244501 (2018)]. In addition, by considering two limiting cases, of a heavy-headed and a uniformly-inertial chain, we illustrate the critical role played by the mass distribution of such extended objects in their turbulent transport.*

This chapter closely follows the work [Singh et al., Phys. Rev. E **101** (2020)].

2.1 Introduction

The study of the dynamics of a long filamentary object in a turbulent flow is fairly recent. In particular, studies on the deformation [1–4] and buckling [5] of fibers, as well as on their usefulness as a probe for the statistical properties of a turbulent flow [6, 7], have led to the development of new ideas in the area of turbulent transport which go beyond the spherical point-particle approximation.

The dynamics of such filamentary objects becomes particularly intriguing when their length extends beyond the dissipation scale of the turbulent flow; the mean flow velocity sampled by the object is then dependent on its instantaneous shape, and this couples translation to flow-induced deformation. (The situation is considerably simpler for a sub-dissipation scale object, as its center of mass behaves like a tracer, independently of its internal dynamics.) Recently, the work of Picardo et al. [8], which studied

long elastic chains consisting of inertialess tracers linked by springs, revealed a new mechanism by which such objects preferentially sample the flow: unlike a collection of non-interacting tracers, which distribute homogeneously, these chains selectively occupy the vortical regions of a two-dimensional turbulent flow, with a non-trivial dependence on the elasticity (quantified by the Weissenberg number Wi) and typical inter-bead separations in the chain.

This behavior of elastic chains is in contrast to the well-known preferential sampling of straining regions exhibited by non-interacting, heavy particles (whose inertia is measured through the Stokes number St). More popularly known as “preferential concentration”, this phenomenon has been the subject of extensive research in the last decade [9–16], motivated by its relevance to a diverse range of physical processes, from transport in particle-laden sprays [17] to collision-driven growth of droplets in warm clouds [18, 19].

It is critical to appreciate that the mechanisms of preferential sampling by the elastic inertia-less chains and the non-interacting, inertial particles are fundamentally different. In the former, it is the elasticity of the links which allows such chains to extend, coil up and be trapped in vortices, whereas for the latter the dissipative dynamics and centrifugal expulsion from vortices lead to particles concentrating in straining regions. This contrast naturally leads us to investigate the dynamics of a heavy elastic chain, which serves as a model for an extensible filamentary object that possesses both inertia and elasticity, as is the case in most physical situations. In addition, by varying the masses of the particles that compose a chain, we can study the effect of an inhomogeneous mass distribution along the chain itself.

Therefore, such a chain provides a simple way to account for the simultaneous effects of inertia, elasticity, and fluid drag in models of filamentary objects, such as algae in marine environments [20], bio-filaments (actin and microtubules, for instance) [21], and swimming microorganisms [22–24]. Of course, such applications would require the consideration of additional effects, such as an active swimming velocity and inter-chain interactions. Nevertheless, the basic ideas elucidated below, in particular the competing effects of inertia and elasticity on preferential sampling, should remain relevant and help pave the way for future studies.

2.2 Modelling

Towards this end, we consider an *elasto-inertial chain*, *i.e.* a sequence of heavy spherical particles—henceforth called beads—which are connected to their nearest neighbours through elastic (phantom) links [see Fig. 1.3(a)] with an associated time scale

τ_E . The N_b beads that compose the chain have positions \mathbf{x}_j , $1 \leq j \leq N_b$, and each bead is characterized by the inertial relaxation time τ_p (defined precisely later) with which its velocity would relax to that of the fluid in the absence of elastic interactions with the neighboring beads. By incorporating the drag stemming from the advecting fluid velocity field \mathbf{u} and the elastic forces on each bead, we obtain the equations of motion for the inter-bead separation vectors $\mathbf{r}_j = \mathbf{x}_{j+1} - \mathbf{x}_j$ with $1 \leq j \leq N_b - 1$ [see Fig. 1.3(a)]:

$$\tau_p \ddot{\mathbf{r}}_j = [\mathbf{u}(\mathbf{x}_{j+1}, t) - \mathbf{u}(\mathbf{x}_j, t) - \dot{\mathbf{r}}_j] - \frac{1}{4\tau_E} (2f_j \mathbf{r}_j - f_{j-1} \mathbf{r}_{j-1} - f_{j+1} \mathbf{r}_{j+1}) + \sqrt{\frac{r_0^2}{2\tau_E}} [\boldsymbol{\xi}_{j+1}(t) - \boldsymbol{\xi}_j(t)]. \quad (2.1)$$

Here, the “link velocity” is denoted as $\dot{\mathbf{r}}_j = \dot{\mathbf{x}}_{j+1} - \dot{\mathbf{x}}_j$ and the “link acceleration” as $\ddot{\mathbf{r}}_j$. We use the FENE (finitely extensible nonlinear elastic) interaction $f_j = (1 - |\mathbf{r}_j|^2 / r_m^2)^{-1}$, where r_m is the maximum inter-bead length, commonly used in polymer physics [25]. We also consider independent white noises $\boldsymbol{\xi}_j(t)$ acting on each bead, in order to set the equilibrium link-length, proportional to r_0 , thereby preventing the chain from collapsing to a point object. Alternatively, this could be achieved without including fluctuations, by incorporating r_0 directly into the elastic forces, *i.e.*, by replacing $-f_j \mathbf{r}_j$ with $-f_j \mathbf{r}_j (1 - r_0 / |\mathbf{r}_j|)$ in Eq. (2.1). We have checked that the two formulations lead to similar sampling behaviours. The equation of motion for the center of mass \mathbf{x}_c is given by

$$\tau_p \ddot{\mathbf{r}}_c = \left(\frac{1}{N_b} \sum_{j=1}^{N_b} \mathbf{u}(\mathbf{x}_j, t) - \dot{\mathbf{r}}_c \right) + \frac{1}{N_b} \sqrt{\frac{r_0^2}{2\tau_E}} \sum_{j=1}^{N_b} \boldsymbol{\xi}_j(t). \quad (2.2)$$

While in Eq. (2.1) the noise term is needed to set a nonzero equilibrium size, it has a negligible effect on the trajectory of the center of mass and only produces a small correction to its turbulent eddy diffusivity.

In Eqs. (2.1) and (2.2), we have taken τ_p , τ_E , and r_0 to be identical for all beads and links. Thus we obtain a uniformly-inertial chain, which will be the main focus of our study. However, to explore the role of the mass-distribution of the chain, we also consider a second case, in which all the inertia is concentrated in a single heavy end-bead ($j = 1$), with the remainder of the chain composed of $N_b - 1$ inertia-less beads, as illustrated in Fig. 1.3(b). Such a “heavy-headed chain” pits the inertia of the head-bead against the elasticity of its tail and serves as an ideal candidate to illustrate the effects of these competing forces. The equations of motion for the inter-bead links of such a heavy-headed chain are a specific instance of Eqs. (2.1) and (2.2) and are given by:

$$\dot{\mathbf{r}}_j = \mathbf{u}(\mathbf{x}_{j+1}, t) - \mathbf{u}(\mathbf{x}_j, t) - \frac{1}{4\tau_E} (2f_j \mathbf{r}_j - f_{j-1} \mathbf{r}_{j-1} - f_{j+1} \mathbf{r}_{j+1}) + \sqrt{\frac{r_0^2}{2\tau_E}} [\boldsymbol{\xi}_{j+1}(t) - \boldsymbol{\xi}_j(t)] \quad \forall j \neq 1 \quad (2.3)$$

and for $j = 1$:

$$\dot{\mathbf{r}}_1 = \mathbf{u}(\mathbf{x}_2, t) + \frac{1}{4\tau_E} (f_2 \mathbf{r}_2 - f_1 \mathbf{r}_1) + \sqrt{\frac{r_0^2}{2\tau_E}} \boldsymbol{\xi}_2(t) - \dot{\mathbf{x}}_1. \quad (2.4)$$

The center of mass, which coincides with the head bead, obeys:

$$\tau_p \ddot{\mathbf{r}}_1 = (\mathbf{u}(\mathbf{x}_1, t) - \dot{\mathbf{x}}_1) + \frac{1}{4\tau_E} f_1 \mathbf{r}_1 + \sqrt{\frac{r_0^2}{2\tau_E}} \boldsymbol{\xi}_1(t). \quad (2.5)$$

Equations (2.1) to (2.5) complete the description of the dynamics of our two types of elasto-inertial chains. This, of course, is a *minimal* description because, in order to keep the model as simple as possible, we have neglected certain effects that are not essential to our study. Hydrodynamic and excluded-volume interactions between the segments of a chain, although present in a real filament, are not expected to modify the dynamics qualitatively. As was shown in Ref. [8] for an inertia-less chain and will be further demonstrated below for elasto-inertial chains, preferential sampling in two-dimensional turbulence results from a dramatic difference in the configuration of the chain in straining and vortical regions (for instance, inertia-less chains are highly stretched in the former and coiled up in the latter [8]). This essential qualitative behavior would be affected only marginally by the aforementioned interactions. Collisions and hydrodynamic interactions between different chains as well as the back reaction of the chain dynamics on the flow would be relevant to the study of a suspension of chains, but less so to the present study, in which we focus on how a single chain samples a turbulent flow. Finally, our elastic links do not offer any resistance to bending, which ought to be important in any realistic modelling of an elastic filament [26]. The reason for disregarding it here is that, for an extended object advected by a turbulent flow, little is known even about just the interplay between its elasticity and inertia. Thus, the goal of our study is to understand this issue by considering a minimal model of an elastic filament that allows us to isolate the competing roles of inertia and elasticity. Refinements of the model, aimed at a more realistic description of an elastic filament, will naturally have to consider its bending stiffness as an additional feature of the dynamics.

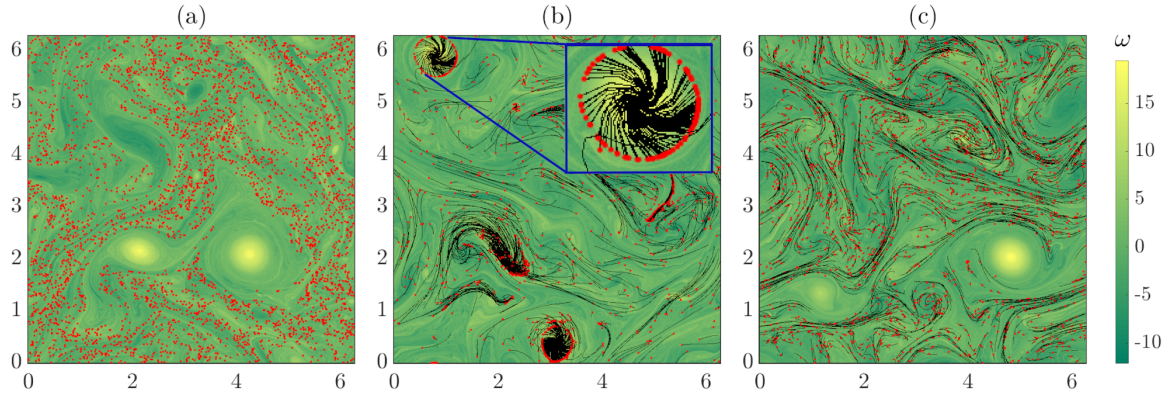


FIGURE 2.1: Representative snapshots of a randomly chosen subset of (a) non-interacting inertial particles, as well as (b) heavy-headed chains and (c) uniformly-inertial chains overlaid on the vorticity field. The center-of-mass of the chains are shown by red dots [like the free particles in panel (a)] and the chain itself by black lines. The inset in panel (b) shows a zoomed-in view of the vortex located near the top-left corner of this panel. We show results for $St = 0.14$ and $Wi = 1.38$ [for panels (b) and (c)].

2.3 Simulations

We immerse the elasto-inertial filament in a two-dimensional, homogeneous, isotropic turbulent velocity field \mathbf{u} , which is obtained through direct numerical simulations (DNSs) of the incompressible ($\nabla \cdot \mathbf{r} = 0$) Navier-Stokes equation:

$$\partial_t \mathbf{u} + (\mathbf{u} \cdot \nabla) \mathbf{u} = -\nabla p + \nu \nabla^2 \mathbf{u} + \mathbf{f} - \mu \mathbf{u}. \quad (2.6)$$

Two-dimensional flows are particularly useful for investigating the competing effects of elasticity and inertia because of long-lived, coherent vortical structures, as we shall see later. We use a standard pseudo-spectral method (see Appendix D) to solve Eq. (2.6) on a 2π square periodic domain with $N^2 = 1024^2$ collocation points. We drive the flow to a turbulent, statistically steady state with an external forcing $\mathbf{f} = -F_0 \sin(k_f x) \mathbf{e}_y$, where F_0 is the forcing amplitude and k_f sets the energy-injection and typical vortex scale $l_f = 2\pi k_f^{-1}$. The energy at large scales (due to an inverse cascade) is damped out by using an Ekman term [27, 28] with the coefficient of friction $\mu = 10^{-2}$. The flow is characterized by the large eddy-turn-over time scale $\tau_f = l_f / \sqrt{2E}$ and the short time scale $\tau_\eta = 1 / \sqrt{2\langle \omega^2 \rangle}$ associated with enstrophy dissipation, where E is the mean kinetic energy of the flow and $\langle \omega^2 \rangle$ is the mean enstrophy (averaged spatially over the domain and temporally over the statistically steady state). We set the coefficient of kinematic viscosity $\nu = 1 \times 10^{-6}$, $k_f = 5$, and $F_0 = 0.2$, giving $\tau_f = 1.45$ and $\tau_\eta = 0.35$. We obtain fluid velocities at the offgrid locations using bilinear interpolation (see Appendix E).

2.4 Preferential Sampling

As mentioned earlier, we study the dynamics of a single chain and its preferential sampling of the flow. However, we evolve 5×10^4 chains simultaneously with the purpose of illustrating preferential sampling visually as well as achieving high accuracy in the statistics of chain deformation and translation. The dynamics of the chains is determined by Eqs. (2.1) and (2.2) or (2.3) to (2.5). These are numerically integrated by a second-order Runge-Kutta scheme. Each chain consists of $N_b = 10$ beads and has a maximum length of $L_m = (N_b - 1)r_m = 1.25$ (comparable to the forcing scale l_f) as well as an equilibrium length proportional to $\sqrt{(N_b - 1)r_0} = 0.04$. The dynamics of the chain is controlled entirely by its elasticity and inertia, described respectively by the Weissenberg number $Wi = \tau_{\text{chain}}/\tau_f$, where $\tau_{\text{chain}} = 6\tau_E/(N_b(N_b + 1))$ provides an estimate of the effective relaxation time of the entire chain [29], and the Stokes number $St = \tau_p/\tau_\eta$. The inertial relaxation time $\tau_p = 2\rho_p a^2/9\rho_f \nu$, where ρ_p and ρ_f are the particle and the fluid densities, respectively; a is the radius of the spherical particle. We use several values of Wi and St to explore the different regimes in the behavior of our elasto-inertial chains. We note that the time-scales of the elasticity of the links and the inertia of the beads are independent of each other.

We begin our study by asking: (i) are elasto-inertial chains really different from non-interacting inertial particles and (ii) does the use of inertial beads, instead of tracer ones as in Ref. [8], modify the dynamics qualitatively? We answer these questions first in the context of the heavy-headed chains [Eqs. (2.3)–(2.5)], where the competing influences of elasticity and inertia are most easily illustrated.

In Figs. 2.1(a) and 2.1(b), we show representative snapshots of (a) non-interacting inertial particles and (b) heavy-headed chains (the inertial head bead is shown in red, while the inertia-less tail is in black) in a two-dimensional turbulent flow. The underlying vorticity fields, on which for clarity only a random subset of particles or chains is overlaid, are different realizations of the same statistically steady flow. As expected, the inertial non-interacting particles preferentially concentrate in the straining zones of the flow. The behavior of the heavy-headed chains, though, is in stark contrast to this, and also differs from the dynamics of the inertia-less elastic chains studied in Ref. [8]. Indeed, in the absence of inertia, elastic chains coil up into vortices and shrink down to tracer-like objects, which then continue to reside inside vortices, whereas in straining regions they are rapidly stretched out until they depart from the underlying straining flow and encounter a vortex. Thus, inertia-less chains get preferentially trapped inside vortices, and snapshots such as those in Fig. 2.1 would show them to be located well inside the core of vortices [8].

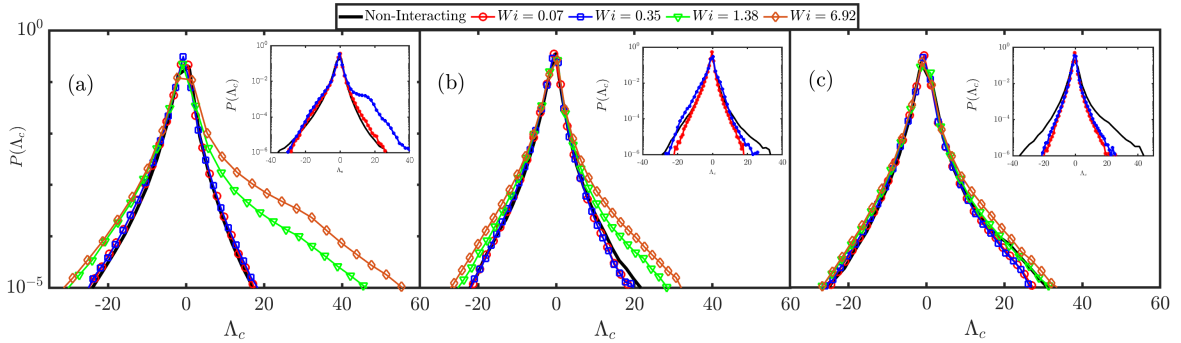


FIGURE 2.2: PDFs of Λ_c measured for uniformly-inertial chains with (a) $St = 0.14$, (b) $St = 0.85$ and (c) $St = 2.84$. Curves are plotted for different degrees of elasticity of the chains, as well as for non-interacting inertial particles (see legend). The insets of panels (b) and (c) show the same distributions for the heavy-headed chains, but for only two values of Wi .

Returning to the snapshot of the heavy-headed chains in Fig. 2.1(b), we see that a majority of them overlap with vortical regions, while, however, remaining elongated, unlike inertia-less chains. The head beads, which are inertial, live on the periphery of the vortices, while their inertia-less elastic tails are pinned to the vortex cores, tracing out a Ferris-wheel pattern. This is especially clear when we look at the arrangement of the chains in and around the vortex visible in the top left corner of Fig. 2.1(b) (the inset shows a zoomed-in view of this vortex). The elasticity of the tail, which keeps it pinned to the core of the vortex (through the mechanism identified in Ref. [8]), competes with the centrifugal force that pushes the head inertial bead out of the vortex. It is this competition between the two effects which manifests itself in the head beads encircling the edge of the vortices.

These results show that combining an inertial particle with an elastic tail gives rise to dynamics which are very different from that of either a free inertial particle or a purely elastic chain. Such a competition between inertia and elasticity, which dictates the behaviour of a heavy-headed chain, also impacts the dynamics of a uniformly-inertial chain [Eqs. (2.1) and (2.2)], but in a less obvious manner. In Fig. 2.1(c), which presents a snapshot of uniformly-inertial chains, the core of the strongest vortices are evacuated because of centrifugal forces, while the weaker vortices are still occupied by partially coiled inertial chains. The stark difference between panels (b) and (c) of Fig. 2.1 provides a vivid illustration of the importance of the mass distribution of such long objects. For a better appreciation of these effects, we now turn to a more quantitative measurement of the sampling behavior of elasto-inertial chains.

A natural way to quantify the relative sampling of vortical and straining regions is to measure the (Lagrangian) Okubo-Weiss parameter

$$\Lambda_c = \frac{\omega_c^2 - \sigma_c^2}{4\langle\omega^2\rangle} \quad (2.7)$$

at the center of mass of the chains along their trajectories. The vorticity ω_c and the strain rate σ_c are measured at the center of mass and normalized by the mean enstrophy $\langle\omega^2\rangle$ of the flow. The sign of this parameter is a signature of the local geometry of the flow: $\Lambda_c > 0$ implies that the center of mass lies in a vortical region, while $\Lambda_c < 0$ is indicative of a straining zone. As is obvious from the definition of Λ_c , extremely small values correspond to regions with comparable amounts of vorticity and straining. As an alternative to Λ_c , one could measure the values of the Okubo-Weiss parameter averaged over all the beads of each chain. We have verified, especially for large Wi , that the two measurements give similar results and lead to the same conclusions.

In Fig. 2.2, we show the plots of the probability distribution function (PDF) of Λ_c for non-interacting inertial particles and uniformly-inertial chains. We consider four values of Wi (0.07, 0.35, 1.38, 6.92) for each of three Stokes numbers: (a) $St = 0.14$, (b) $St = 0.85$, and (c) $St = 2.84$.

For small, but still nonzero Stokes numbers [see Fig. 2.2(a)], non-interacting inertial particles have a distribution of Λ_c which is negatively skewed, indicating a preferential sampling of straining regions [30]. (Note that uniformly distributed non-interacting *tracers* would show a positively skewed PDF of Λ_c owing to the presence of intense coherent vortices in the flow [27, 31].) However, for a chain of inertial beads with the same Stokes number, the effect of the elasticity draws the chain (defined by its center of mass) towards more vortical regions. This is clearly seen in the widening of the right tails of the PDF as Wi increases [Fig. 2.2(a)].

This effect of elasticity persists, qualitatively, as St is increased to intermediate values, but is considerably weaker [Fig. 2.2(b)]. On the one hand, the increasing centrifugal forces acting on the chains counteract the tendency of elasticity to entrap them in vortices, causing the large- Wi PDFs to show less positively-skewed tails. On the other hand, the non-interacting inertial particles begin to decorrelate from the flow and start to distribute more uniformly, which causes the corresponding PDFs of Λ_c to become more positively skewed. The net result is that the effect of Wi weakens, and eventually for large St the PDFs of Λ_c become nearly independent of elasticity [Fig. 2.2(c)].

Along with the preferential sampling of vortices, increasing Wi also causes a relatively mild over-sampling of strong straining regions in comparison with non-interacting particles. This effect is more prominent at small St , as seen in the negative tails of

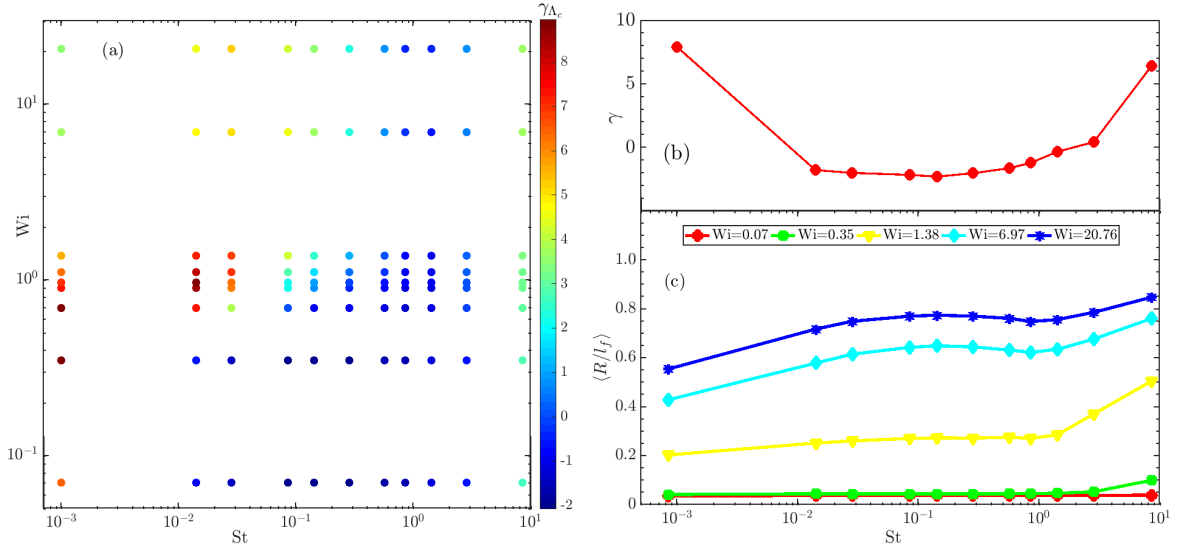


FIGURE 2.3: (a) Pseudo-color plots of the skewness γ of the distribution of Λ_c , in the $St - Wi$ plane, for uniformly-inertial chains. For comparison, the same skewness obtained for non-interacting particles is shown in panel (b). We also show, in panel (c), the average normalized length of the inertial chains as a function of St for a few representative values of Wi .

Fig. 2.2(a). The strong straining regions in two-dimensional turbulence are saddle-like, with a stable direction along which the flow enters and an unstable one along which the flow departs. An inertial point-particle in such a saddle region would quickly depart along either branch of the unstable direction. A chain, in contrast, cannot depart as easily: it gets stretched-out and oriented along the unstable direction, with the fluid drag at one end of the chain counter-acting that at the other. The consequence is that an inertial chain spends more time in strong straining zones compared to an inertial point particle. This effect is lost at larger St , as the motion of the chain decorrelates from the instantaneous underlying flow field [Fig. 2.2(c)].

We now turn to the sampling behaviour of a heavy-headed chain. The corresponding PDFs of Λ_c , measured at the head bead, which coincides with the centre of mass, are shown in the insets of Fig. 2.2. For clarity, we only present representative results in each case, for $Wi = 0.07$ and 0.35 . For small St [inset of panel (a)], the effect of Wi is qualitatively similar to that for a uniformly-inertial chain. For larger St , however, the PDFs are quite different. While the elastic tail gets entrapped inside vortices, centrifugal forces push the heavy head bead to their periphery, where the flow is neither intensely vortical nor strongly straining. Consequently, the corresponding PDFs have relatively narrow tails, for both positive and negative values of Λ_c [insets of panels (b) and (c)].

A convenient way of further quantifying the complex dependence of preferential sampling on the inertia and elasticity of a chain is to calculate the skewness of the PDFs

of Λ_c ,

$$\gamma = \frac{\langle (\Lambda_c - \bar{\Lambda}_c)^3 \rangle}{\langle (\Lambda_c - \bar{\Lambda}_c)^2 \rangle^{3/2}}, \quad (2.8)$$

where $\bar{\Lambda}_c$ is the average value of Λ_c , as a function of both the Stokes and Weissenberg numbers. For comparison, let us first consider the plot of γ vs St for non-interacting inertial particles shown in Fig. 2.3(b). Here, γ is negative over intermediate values of St , where there is evidence of preferential concentration (e.g., Ref. [12]), whereas for $St \rightarrow 0$ or $St \gg 1$, the homogeneous distribution of these particles ensures that γ is positive (as is the case for tracers).

In Fig. 2.3(a), we show a pseudo-color plot of the skewness γ in the $St - Wi$ plane for a uniformly-inertial chain. We see that when the chain stretches marginally, *i.e.*, for $Wi \ll 1$, γ shows qualitatively the same dependence on St as for non-interacting particles [Fig. 2.3(b)]. However, when $Wi \gtrsim 1$, the chains are elongated and get trapped by vortices, thereby increasing both the value of γ and the range of St for which $\gamma > 0$.

The difference between a uniformly-inertial chain and an inertial-less one [8] can be appreciated by comparing the behavior of γ vs Wi for St around unity with the case of $St \rightarrow 0$, in Fig. 2.3(a). Indeed, for nonzero Stokes numbers, there is a reversal in the sampling behaviour, with γ going from negative to positive values with increasing Wi . In contrast, when $St \rightarrow 0$, γ remains strictly positive while showing a non-monotonic dependence on Wi , as has been shown in Ref. [8] and is further discussed below. In the opposite limit of very large St , γ is nearly independent of Wi , in accordance with the PDFs of Λ_c shown in Fig. 2.2(c).

2.5 Chain Lengths

Our arguments, so far, are largely based on the stretching of the chain. It is, therefore, essential to check if stretching indeed happens in the way we suggest. In Fig. 2.3(c) we show representative plots of the average length of the chain $\langle R \rangle$, normalized by l_f , as a function of St , and for different values of Wi . For a negligible Wi , there is hardly any evidence of stretching. However, as soon as Wi is nonzero, the chain starts stretching much more, in a manner that depends non-trivially on the inertia of the beads.

The variation of the chain length with St occurs in two distinct regimes, which are most clearly visible for the large- Wi case in Fig. 2.3(c). For $St \lesssim 1$, an inertial chain preferentially samples straining regions of the flow more than an inertial-less one and, therefore, is stretched out more. As St approaches unity, however, the heavy chains begin to decorrelate from the flow and the degree of sampling of straining regions

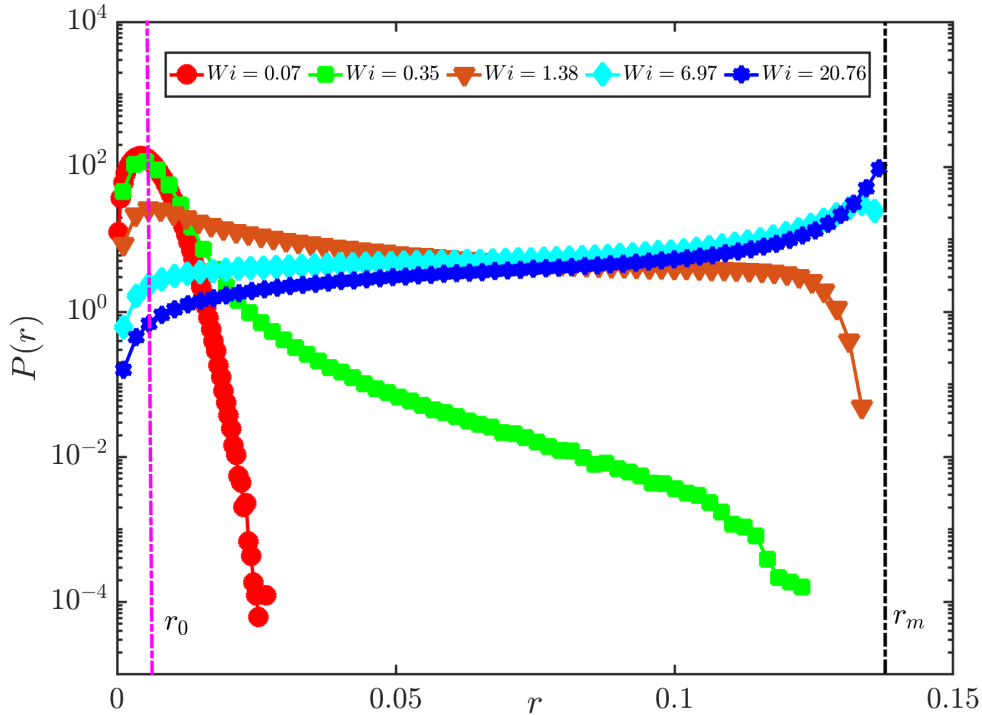


FIGURE 2.4: PDF $P(r)$ of the inter-bead separation r for uniformly-inertial ($St = 0.14$) chains, for different values of Wi (see legend). The solid (black) vertical line corresponds to the maximum link length r_m and the dashed-dot (magenta) line corresponds to r_0 which sets the equilibrium link-length. With increasing elasticity, we see the distributions develop broader tails and eventually, at large values of Wi , peak near r_m .

reduces [the same is seen for non-interacting particles in Fig. 2.3(b)]. This is why the chain lengths, especially for large Wi , show a weak local maximum for intermediate values of $St \approx 0.1$, where the preferential sampling is strong [see Fig. 2.3(b)]. In the second regime, of $St > 1$, the chain lengths again show an increasing trend. This is because, unlike small- St beads, which are well correlated with the flow, the velocity differences between large- St beads do not scale with their separation—even beads that are close to each other can have very different velocities. Therefore, it is more difficult for the elastic links to keep such heavy inertial beads together, and the chain elongates as St increases.

The stretching of the chain is, of course, rooted in the distribution of the lengths of individual links. In Fig. 2.4, we show a representative plot of this PDF for $St = 0.14$ and for different values of Wi . When Wi is very small, the PDF is narrow with a peak, as expected, near the equilibrium length scale r_0 . With increasing Wi , the PDF initially develops broader tails, but which, for $Wi \lesssim 1$, are still far from the cut-off r_m imposed in our model. As Wi increases beyond unity, however, the distribution starts getting flatter and eventually peaks near to $r = r_m$. For such large- Wi chains, the typical inter-bead separation is of the order of the vortex size; this limits the ability

of the chains to coil into vortices, as successive beads can no longer simultaneously encounter the same vortex (finite N_b acts a restriction on deformability) [8]. This is the reason why γ , for $St \rightarrow 0$, shows a peak for $Wi \approx 1$ and gradually decreases at large values of Wi [Fig. 2.3(a)]. For $St \gtrsim 0.1$, however, the centrifugal forces acting on the beads prevent excessive entrapment of chains into vortices, thus eliminating the local maximum in γ and resulting in a more gradual and monotonic increase with Wi .

2.6 Conclusions

Inertia and elasticity are two fundamental properties of extended objects. While the former causes expulsion from vortical regions, as seen for inertial particles, the latter leads to entrapment within vortices, as observed for inertia-less chains. This work has shown, in the context of a model elasto-inertial chain, that these competing features interact and result in a non-trivial sampling of a turbulent flow. Moreover, the dynamics of a heavy-headed chain, and its contrast with that of a uniformly inertial one, has shown that a non-homogeneous mass distribution can lead to a persistent orientation which keeps the heavier portion of an elastic filament away from vortical regions. Given this, our work, based on model elastic filaments with inertia, serves as a building block for future experimental and numerical studies of the dynamics of extended objects in turbulent flows.

References

- [1] C. Brouzet, G. Verhille and P. Le Gal, *Flexible fiber in a turbulent flow: A macroscopic polymer*, *Phys. Rev. Lett.* **112** (2014) 074501.
- [2] G. Verhille and A. Bartoli, *3d conformation of a flexible fiber in a turbulent flow*, *Exp. in Fluids* **57** (2016) 117.
- [3] A. Gay, B. Favier and G. Verhille, *Characterisation of flexible fibre deformations in turbulence*, *Europhys. Lett.* **123** (2018) 24001.
- [4] D. Dotto and C. Marchioli, *Orientation, distribution, and deformation of inertial flexible fibers in turbulent channel flow*, *Acta Mechanica* **230** (2019) 597–621.
- [5] S. Allende, C. Henry and J. Bec, *Stretching and buckling of small elastic fibers in turbulence*, *Phys. Rev. Lett.* **121** (2018) 154501.
- [6] M. E. Rosti, A. A. Banaei, L. Brandt and A. Mazzino, *Flexible fiber reveals the two-point statistical properties of turbulence*, *Phys. Rev. Lett.* **121** (2018) 044501.
- [7] M. E. Rosti, S. Olivieri, A. A. Banaei, L. Brandt and A. Mazzino, *Flowing fibers as a proxy of turbulence statistics*, *Meccanica* **55** (2020) 357–370.
- [8] J. R. Picardo, D. Vincenzi, N. Pal and S. S. Ray, *Preferential sampling of elastic chains in turbulent flows*, *Phys. Rev. Lett.* **121** (2018) 244501.
- [9] J. Bec, *Fractal clustering of inertial particles in random flows*, *Phys. of Fluids* **15** (2003) L81–L84.
- [10] J. Bec, A. Celani, M. Cencini and S. Musacchio, *Clustering and collisions of heavy particles in random smooth flows*, *Phys. of Fluids* **17** (2005) 073301.
- [11] J. Chun, D. L. Koch, S. L. Rani, A. Ahluwalia and L. R. Collins, *Clustering of aerosol particles in isotropic turbulence*, *J. Fluid Mech.* **536** (2005) 219–251.
- [12] J. Bec, L. Biferale, M. Cencini, A. Lanotte, S. Musacchio and F. Toschi, *Heavy particle concentration in turbulence at dissipative and inertial scales*, *Phys. Rev. Lett.* **98** (2007) 084502.

- [13] R. Monchaux, M. Bourgoïn and A. Cartellier, *Analyzing preferential concentration and clustering of inertial particles in turbulence*, *Int. J. Multiph. Flow* **40** (2012) 1 – 18.
- [14] K. Gustavsson and B. Mehlig, *Statistical models for spatial patterns of heavy particles in turbulence*, *Adv. in Phys.* **65** (2016) 1–57.
- [15] J. Bec, H. Homann and S. S. Ray, *Gravity-driven enhancement of heavy particle clustering in turbulent flow*, *Phys. Rev. Lett.* **112** (2014) 184501.
- [16] G. H. Good, P. J. Ireland, G. P. Bewley, E. Bodenschatz, L. R. Collins and Z. Warhaft, *Settling regimes of inertial particles in isotropic turbulence*, *J. Fluid Mech.* **759** (2014) R3.
- [17] S. Sahu, Y. Hardalupas and A. M. K. P. Taylor, *Droplet–turbulence interaction in a confined polydispersed spray: effect of turbulence on droplet dispersion*, *J. Fluid Mech.* **794** (2016) 267–309.
- [18] W. W. Grabowski and L.-P. Wang, *Growth of cloud droplets in a turbulent environment*, *Annual Review of Fluid Mechanics* **45** (2013) 293–324.
- [19] J. Bec, S. S. Ray, E. W. Saw and H. Homann, *Abrupt growth of large aggregates by correlated coalescences in turbulent flow*, *Phys. Rev. E* **93** (2016) 031102.
- [20] R. E. Goldstein, *Green algae as model organisms for biological fluid dynamics*, *Annual Review of Fluid Mechanics* **47** (2015) 343–375.
- [21] F. Gittes, B. Mickey, J. Nettleton and J. Howard, *Flexural rigidity of microtubules and actin filaments measured from thermal fluctuations in shape.*, *Journal of Cell Biology* **120** (1993) 923–934.
- [22] A. Choudhary, D. Venkataraman and S. S. Ray, *Effect of inertia on model flocks in a turbulent environment*, *Europhys. Lett.* **112** (2015) 24005.
- [23] A. Gupta, A. Roy, A. Saha and S. S. Ray, *Flocking of active particles in a turbulent flow*, *Phys. Rev. Fluids* **5** (2020) 052601.
- [24] R. E. Breier, C. C. Lalescu, D. Waas, M. Wilczek and M. G. Mazza, *Emergence of phytoplankton patchiness at small scales in mild turbulence*, *Proc. Nat. Acad. Sci. USA* **115** (2018) 12112–12117.
- [25] R. B. Bird, C. F. Curtiss, R. C. Armstrong and O. Hassager, *Dynamics of Polymeric Liquids*. John Wiley and Sons, New York, 1977, 10.1002/pol.1978.130160210.

-
- [26] A recent study [?] shows that including bending stiffness in elastic chains with massless (tracer) beads has little effect on the nature of their preferential sampling of a three-dimensional turbulent flow.
- [27] P. Perlekar and R. Pandit, *Statistically steady turbulence in thin films: direct numerical simulations with ekman friction*, *New Journal of Physics* **11** (2009) 073003.
- [28] G. Boffetta and R. E. Ecke, *Two-dimensional turbulence*, *Annual Review of Fluid Mechanics* **44** (2012) 427–451.
- [29] S. Jin and L. R. Collins, *Dynamics of dissolved polymer chains in isotropic turbulence*, *New Journal of Physics* **9** (2007) 360–360.
- [30] D. Mitra and P. Perlekar, *Topology of two-dimensional turbulent flows of dust and gas*, *Phys. Rev. Fluids* **3** (2018) 044303.
- [31] A. Gupta, P. Perlekar and R. Pandit, *Two-dimensional homogeneous isotropic fluid turbulence with polymer additives*, *Phys. Rev. E* **91** (2015) 033013.

Chapter 3

Dynamics of Inertialess Filaments in Three-dimensional Turbulence

We show and explain how a long bead-spring chain, immersed in a homogeneous isotropic turbulent flow, preferentially samples vortical flow structures. We begin with an elastic, extensible chain which is stretched out by the flow, up to inertial-range scales. This filamentary object, which is known to preferentially sample the circular coherent vortices of two-dimensional (2D) turbulence, is shown here to also preferentially sample the intense, tubular, vortex filaments of 3D turbulence. In the 2D case, the chain collapses into a tracer inside vortices. In 3D, on the contrary, the chain is extended even in vortical regions, which suggests that the chain follows axially-stretched tubular vortices by aligning with their axes. This physical picture is confirmed by examining the relative sampling behaviour of the individual beads, and by additional studies on an inextensible chain with adjustable bending-stiffness. A highly-flexible, inextensible chain also shows preferential sampling in 3D, provided it is longer than the dissipation scale, but not much longer than the vortex tubes. This is true also for 2D turbulence, where a long inextensible chain can occupy vortices by coiling into them. When the chain is made inflexible, however, coiling is prevented and the extent of preferential sampling in 2D is considerably reduced. In 3D, on the contrary, bending stiffness has no effect, because the chain does not need to coil in order to thread a vortex tube and align with its axis.

This chapter closely follows the work [Picardo *et al.*, Phil. Trans. Roy. Soc. A **378** (2020)].

3.1 Introduction

A three-dimensional (3D) incompressible turbulent flow has a peculiar geometrical structure which distinguishes it from a purely random field. The visualisation of the

isosurfaces of enstrophy and energy dissipation indeed indicates that vorticity concentrates into tubular structures, while regions of intense strain are sheet-like [1] (see Fig. 3.1 for a visualization based on the Q -criterion [2, 3]). Several Lagrangian studies have shown that the dynamics of objects smaller than the viscous-dissipation scale can depend sensitively on the nature of the local velocity gradient. Heavy particles, for instance, are ejected from vortical regions because of centrifugal forces and thus concentrate in strain-dominated ones [4, 5]. In turbulent channel flows, highly stretched polymers are mainly found in the regions of strong biaxial extension that surround the near-wall streamwise vortices [6–8]. Gyrotactic swimmers are trapped into the high-shear zones of a turbulent flow [9], while ellipsoidal swimmers preferentially sample low-vorticity zones [10]. Much less studied, however, is the case of an object whose size lies in the inertial range of turbulence; its translation is coupled to its internal dynamics, which in turn is directly affected by coherent structures of the flow. This situation has only just begun to receive attention, especially in the context of flexible fibers [11–16].

A bead-spring chain is a simple physical system that allows us to investigate the interaction between an extended filamentary object and the geometrical structure of a turbulent flow. Such a system has been widely employed in polymer physics [17] and is here generalised in order to describe a chain longer than the dissipation scale. It consists of a sequence of beads connected by phantom springs. The extensibility of the chain can be tuned by varying the strength and the maximum length of the springs, and its stiffness is controlled by a bending potential that depends on the angle between each neighbouring pair of springs. Even though a bead-spring chain can only be regarded as a very rudimentary model of an elastic filament, it has the basic properties needed to investigate the physical mechanisms that determine the motion of an extensible and flexible object in a turbulent flow. Moreover, its dynamics can be studied in detail with moderate numerical effort.

In [18], an extensible bead-spring chain was studied in a two-dimensional (2D), homogeneous, and isotropic, turbulent flow. It was shown that the centre of mass of the chain preferentially samples the vortical regions. This is because the chain is strongly stretched in high-strain regions and thus becomes unable to follow their evolution. It eventually gets trapped into one of the large-scale vortices that dominate a 2D turbulent flow. Inside the vortex, where straining is absent, it contracts and stays therein. Hence, in 2D turbulence, an extensible chain departs from straining regions but behaves like a tracer inside vortices, whence the preferential sampling of the latter.

Here we study the dynamics of a bead-spring chain in 3D turbulence, where, unlike in 2D, vorticity-stretching leads to the formation of intense vortex tubes [19, 20],

with significant straining along the tube axis. We address the question of whether preferential sampling of vortical regions persists in three dimensions and, if so, how it depends on the extensibility and flexibility of the chain.

3.2 Extensible chain

We consider a chain consisting of N_b identical inertialess beads (see [21] for a study of chains with inertial beads in two-dimensional turbulent flows), each of which has a Stokes drag coefficient ζ . The beads are connected to their nearest neighbours by nonlinear springs, with equilibrium length r_{eq} , maximum length r_m , and spring coefficient κ . The characteristic relaxation time of each spring is thus $\tau_E = \zeta/4\kappa$, which in turn sets the relaxation time of the chain $\tau_E^{\text{chain}} = (N_b + 1)N_b\tau_E/6$ [22]. If \mathbf{x}_i , $1 \leq i \leq N_b$, denote the position vectors of the beads, it is convenient to describe the configuration of the chain in terms of the position of its centre of mass, $\mathbf{X}_c = (\sum_{i=1}^{N_b} \mathbf{x}_i)/N_b$, and the interbead separations $\mathbf{r}_j = \mathbf{x}_{j+1} - \mathbf{x}_j$, $1 \leq j \leq N_b - 1$.

We first consider a freely-jointed (the links do not oppose resistance to bending), extensible chain, as in [18]. The equations of motion for such a chain are:

$$\dot{\mathbf{X}}_c = \frac{1}{N_b} \sum_{i=1}^{N_b} \mathbf{u}(\mathbf{x}_i, t) + \frac{1}{N_b} \sqrt{\frac{r_{\text{eq}}^2}{6\tau_E}} \sum_{i=1}^{N_b} \boldsymbol{\xi}_i(t), \quad (3.1a)$$

$$\dot{\mathbf{r}}_j = \mathbf{u}(\mathbf{x}_{j+1}, t) - \mathbf{u}(\mathbf{x}_j, t) + \frac{1}{\zeta} (\mathbf{f}_{j+1}^E - \mathbf{f}_j^E) + \sqrt{\frac{r_{\text{eq}}^2}{6\tau_E}} [\boldsymbol{\xi}_{j+1}(t) - \boldsymbol{\xi}_j(t)], \quad (1 \leq j \leq N_b - 1). \quad (3.1b)$$

The elastic force on the j -th bead, \mathbf{f}_j^E , takes the form:

$$\mathbf{f}_j^E = \kappa \alpha_j \hat{\mathbf{r}}_j \frac{r_j}{1 - r_j^2/r_m^2} - \kappa \alpha_{j-1} \hat{\mathbf{r}}_{j-1} \frac{r_{j-1}}{1 - r_{j-1}^2/r_m^2}, \quad (3.2)$$

with $r_j = |\mathbf{r}_j|$, $\hat{\mathbf{r}}_j = \mathbf{r}_j/r_j$ and

$$\alpha_j = \begin{cases} 0 & \text{if } j \leq 0 \text{ or } j = N_b \\ 1 & \text{otherwise.} \end{cases} \quad (3.3)$$

The divergence of the force at $r = r_m$ ensures that the length of the chain, $R = \sum_{j=1}^{N_b-1} r_j$, stays smaller than the maximum value $L_m = (N_b - 1)r_m$. The vectors $\boldsymbol{\xi}_j(t)$, $1 \leq j \leq N_b$, are independent multi-dimensional white noises; they serve the purpose of modeling the collisions between the beads and the molecules of the fluid, thereby setting the equilibrium end-to-end length of the chain to $r_{\text{eq}}\sqrt{N_b - 1}$. Equations (3.1)

generalise the well-known Rouse model of polymer physics [17] in such a way as to account for the nonlinearity of the velocity field. Indeed, in the original Rouse model the velocity differences between the beads are replaced by their first-order Taylor expansion in the separation vectors, because polymers are assumed to be much shorter than the smallest scale of the velocity field. Here the full velocity differences are retained, since the chain is allowed to extend into the inertial range of turbulence. An analogous generalisation was applied in [23–26] to the elastic dumbbell model ($N_b = 2$). Finally, the velocity field $\mathbf{u}(\mathbf{x}, t)$ describes the motion of the fluid and is the solution of the incompressible Navier–Stokes equations,

$$\partial_t \mathbf{u} + \mathbf{u} \cdot \nabla \mathbf{u} = -\nabla p + \nu \Delta \mathbf{u} + \mathbf{F}, \quad \nabla \cdot \mathbf{u} = 0, \quad (3.4)$$

where p is pressure, ν the kinematic viscosity of the fluid, and $\mathbf{F}(\mathbf{x}, t)$ is a large-scale body forcing which maintains a homogeneous, isotropic, and statistically stationary turbulent flow. We perform direct numerical simulations (DNS) on a 2π -periodic domain, using a standard de-aliased pseudo-spectral method. For 3D simulations, we use a $N^3 = 512^3$ spatial grid and a second order Adams-Bashforth time-integration scheme (for details see Appendix C). The body-forcing $\mathbf{F}(\mathbf{x}, t)$ injects a constant amount of energy—equalling the mean dissipation rate ϵ —into the first two wave-number shells. The Kolmogorov dissipation time and length scales are given by $\tau_\eta = (\nu/\epsilon)^{1/2}$ and $\eta = (\nu^3/\epsilon)^{1/4} \approx 1.7 k_{\max}$ (where $k_{\max} = \sqrt{2}N/3$ is the maximum resolved wavenumber). The results presented below correspond to a flow with Taylor-Reynolds number $Re_\lambda = 2E\sqrt{5/(3\nu\epsilon)} = 196$ (where E is the mean kinetic energy), which is sufficiently large for a clear inertial range (albeit less than a decade) to emerge in the energy spectrum and for the formation of distinct vortex tubes (cf. Fig. 3.1). We have checked that the sampling behaviour we describe persists even for smaller Re_λ of 123 and 64 as well, though it does intensify with Re_λ over this limited range.

While our primary focus is on chains in a 3D turbulent flow, it is helpful to compare their 3D dynamics with that in a 2D turbulent flow, especially when addressing the effects of extensibility and flexibility. For 2D flow simulations, a $N^2 = 1024^2$ spatial grid and a second order Runge-Kutta time-integration scheme is used, as in Ref. [18]. A constant-in-time forcing $\mathbf{F} = F_0 \sin(k_f x) \mathbf{e}_y$ is applied, where F_0 is the forcing amplitude and $k_f = 5$ is the forcing wavenumber, which sets the scale of the large coherent vortices, $2\pi k_f^{-1}$. An Ekman friction term [27, 28] with coefficient $\mu = 10^{-2}$ is included in (3.4) to damp out the energy at the large scales (due to an inverse cascade).

After the flow (3D or 2D) attains a stationary state, we introduce a large number of chains, of order 10^4 , each with $N_b = 20$ beads. We evolve many chains simultaneously

only to obtain good statistics; the dynamics we study are of a single chain in the flow. The chains are given a small initial length, close to the no-flow equilibrium value. They are then allowed to be stretched out by the flow and attain a steady-state distribution before we begin recording statistics. The equations governing the dynamics of the centre of mass and separation vectors of the chain are integrated using a second-order Runge-Kutta scheme, augmented by a rejection algorithm [29] that prevents the nonlinear spring force from diverging as $|\mathbf{r}|$ approaches r_m . The chains are evolved with a time step $\Delta t_{\text{chain}} = \Delta t_f / N_{\text{sub}}$, where Δt_f is the time-step of the fluid flow solver and N_{sub} is the number of sub-steps taken by the chain solver for every step of the fluid solver. The flow is assumed to be unchanging over the duration of the sub-steps. While N_{sub} is set to unity for the freely-jointed chain, used in this section, we use up to $N_{\text{sub}} = 10^3$ for accurately resolving the numerically-stiff dynamics of inextensible and inflexible chains, to be introduced later in § 3.3 and 3.4.

The influence of elasticity on the dynamics of the chain is described in terms of the elastic Weissenberg number $Wi_E = \tau_E^{\text{chain}} / \tau_f$, which is the ratio of the chain relaxation time to the viscous-dissipation time scale of the flow. For 3D turbulence, $\tau_f = \tau_\eta$, whereas for 2D flows we choose the small time scale associated with the dissipation of enstrophy, $\tau_f = \langle 2\omega^2 \rangle^{-1/2}$, where $\langle \omega^2 \rangle$ is the mean enstrophy. For small Wi_E , the chain is in a contracted configuration and acts like a tracer; for large Wi_E , it is stretched out by the flow.

As mentioned in § 3.1, the dynamics of an extensible chain was studied in [18] for a 2D turbulent flow forced at large spatial scales. The equilibrium size of the chain was assumed to be of the order of the dissipation scale, while L_m was much longer and comparable to the scale of the coherent vortices, $2\pi k_f^{-1}$, or even greater than it. When Wi_E was sufficiently large for the typical length of the chain to approach the size of the vortices, then the chain was shown to exhibit a marked preferential sampling of vortical regions. The mechanism that was proposed in [18] to explain this phenomenon, already sketched briefly in § 3.1, can be summarised as follows:

1. Inside a vortex, where stretching is absent, the chain shrinks down to its equilibrium size. Since the equilibrium size of the chain is much smaller than the size of the vortex, the chain essentially behaves as a tracer and follows the vortex during its lifetime.
2. In a region of intense strain, the chain is stretched to the extent that it cannot continue to follow the straining region. The chain eventually encounters a vortex that coils it up and ‘entraps’ it according to the dynamics described above.

The combination of these effects causes an extensible chain to stay inside large vortices

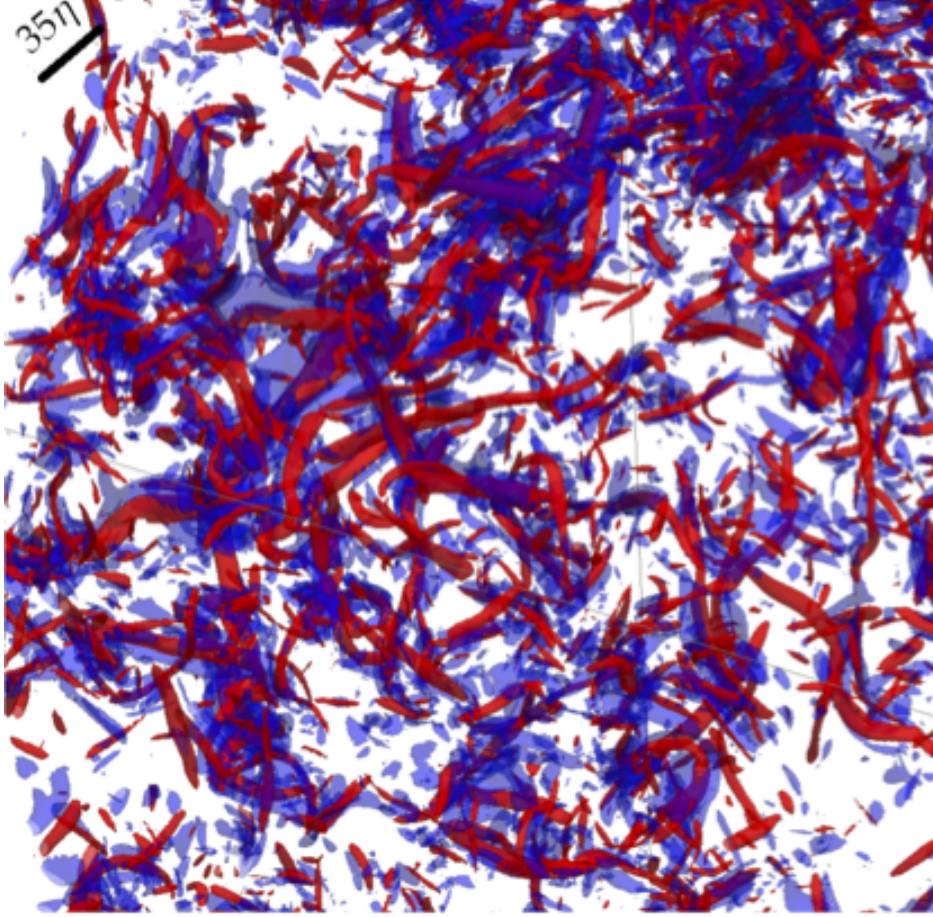


FIGURE 3.1: Contours of Q showing intense, rotational, vortex tubes (red, $Q = +5\sqrt{\langle Q^2 \rangle}$) enveloped by strong straining sheets (blue, $Q = -2\sqrt{\langle Q^2 \rangle}$), in three-dimensional homogeneous isotropic turbulence. The black scale bar at the top-left corner corresponds to a length of 35η .

and leave high-strain regions, which results in a strong preferential sampling of vortices. This phenomenon was quantified in [18] by studying the Okubo-Weiss parameter [30, 31] evaluated at the position of the centre of mass of the chain,

$$\Lambda_c = \frac{\omega_c^2 - \sigma_c^2}{4\langle \omega^2 \rangle}, \quad (3.5)$$

where ω_c and σ_c are the vorticity and the strain rate at the position of the centre of mass, respectively. We recall that positive values of Λ_c correspond to vorticity-dominated regions, whereas negative values indicate strain-dominated regions. For large enough values of Wi_E , the probability of positive values of Λ_c was found to be much higher than for a tracer transported by the same flow [18]. In addition, the joint probability density function (PDF) of the chain length R and Λ_c confirmed that the chain is contracted in vortical regions and extended in straining ones.

The first question we address here is whether or not an extensible chain exhibits

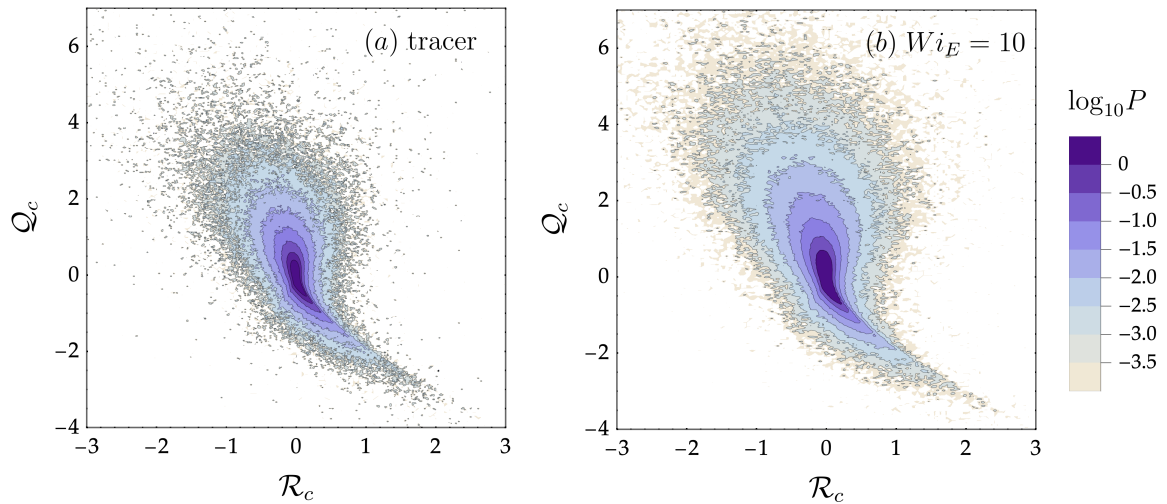


FIGURE 3.2: Joint PDF of \mathcal{R}_c and \mathcal{Q}_c (a) for a tracer and (b) for an inertialess, freely-jointed, extensible chain with $Wi_E = 10$, $L_m = 40\eta$, $r_{eq} = 0.045\eta$.

preferential sampling of vortical regions also in a 3D turbulent flow. A substantial difference indeed exists between 2D and 3D flows. A 2D turbulent flow is characterised by large, long-lived vortices, inside which stretching is weak. In a 3D turbulent flow, vorticity concentrates into intense tubular structures with significant stretching along their axes. The dynamics of the chain in vorticity-dominated regions is therefore expected to be substantially different in the two cases.

In three dimensions, the local nature of the flow can be classified by using the \mathcal{Q} - \mathcal{R} representation of the velocity gradient [32]. If $\mathbf{A}_c = \tau_\eta \nabla \mathbf{u}(\mathbf{X}_c(t), t)$ denotes the rescaled velocity gradient at the position of the centre of mass, let $\mathcal{Q}_c = -\text{tr} \mathbf{A}_c^2 / 2$ and $\mathcal{R}_c = -\det \mathbf{A}_c$ be its second and third invariants. Since \mathcal{Q}_c can be rewritten as

$$\mathcal{Q}_c = \tau_\eta^2 \frac{\omega_c^2 / 2 - \mathbf{S}_c : \mathbf{S}_c}{2}; \quad \mathbf{S}_c = (\mathbf{A}_c + \mathbf{A}_c^T) / 2, \quad (3.6)$$

the sign of \mathcal{Q}_c discriminates between the regions dominated by vorticity ($\mathcal{Q}_c > 0$) and those dominated by strain ($\mathcal{Q}_c < 0$). Thus, \mathcal{Q}_c has a role analogous to that played by Λ_c in a 2D flow. Figure 3.1 presents a snapshot of the iso-surfaces of \mathcal{Q} from our 3D simulation, which clearly reveal sheet-like straining zones (large negative \mathcal{Q} in blue) in close proximity to intense tubular vortices (large positive \mathcal{Q} in red).

Figure 3.2 compares the steady-state joint PDFs of \mathcal{R}_c and \mathcal{Q}_c for a tracer particle (panel a) and for the extensible chain with a large $Wi_E = 10$ (panel b). The chain has an equilibrium size of about 0.4η and a maximum extension $L_m = 40\eta$, so that when the chain is stretched its length R lies in the inertial range and is comparable to the typical size of vortex tubes in our simulations (cf. the vortex tubes and scale

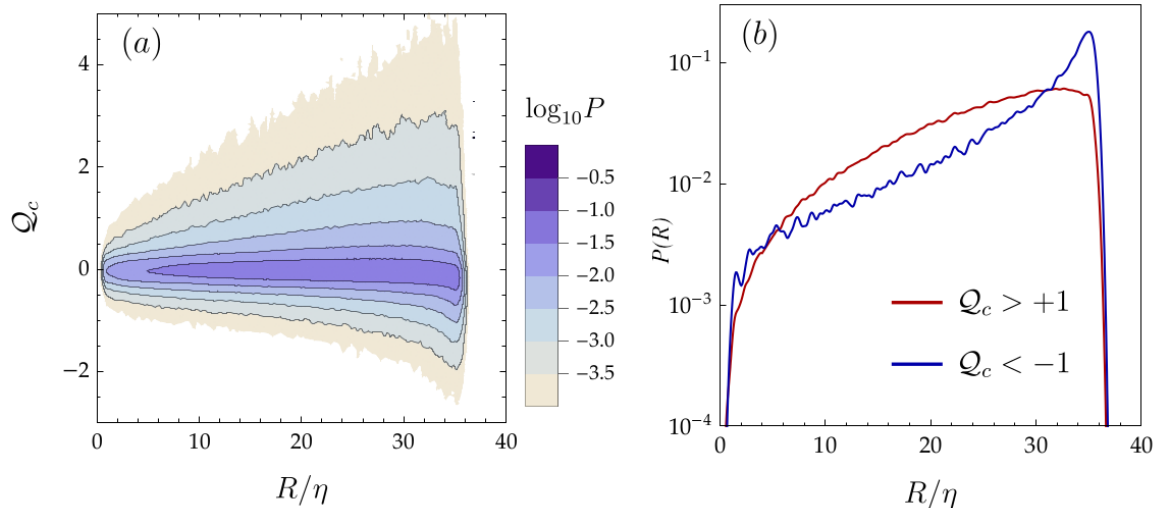


FIGURE 3.3: (a) Joint PDF of the chain length R (rescaled by the dissipation scale η) and Q_c for a freely-jointed inextensible chain. (b) Conditional PDF of R rescaled by η given $Q_c < -1$ (blue curve) and $Q_c > 1$ (red curve). The parameters are $Wi_E = 10$, $L_m = 40\eta$, $r_{eq} = 0.045\eta$ in both panels.

bar in Figure 3.1). The shape of the joint PDF of the chain is similar to that of the tracer. However, the probability of sampling positive Q_c is significantly larger for the chain, than for the tracer. Therefore, we deduce that preferential sampling of vorticity-dominated regions persists in three dimensions.

As mentioned above, however, a major difference exists between the chain dynamics in 2D and 3D turbulence. This is reflected in the conditional PDF of the chain length R given the value of Q_c , presented in figure 3.3b, which shows that contrary to the 2D case the chain is considerably stretched not only in strain-dominated but also in vorticity-dominated regions. This difference is clear from the comparison of the joint PDF of R and Q_c , shown in figure 3.3a, with its 2D analog (see figure 3 in [18]) and has important consequences for preferential sampling. In two dimensions, indeed, the contraction of the chain inside vortices was identified as an essential element of the sampling dynamics [18] (though we shall revisit this idea in section 3.4). In three dimensions, the chain does not collapse into a tracer even when the flow has a strong vortical nature (figure 3.3b). Hence, the mechanism leading to preferential sampling ought to be different from that operating in 2D turbulence.

Now, the only way an elongated chain can remain inside a vortex tube of comparable length, is if it aligns itself along the vortex axis. Given that the majority of vortices are axially stretched (figure 3.2), this scenario is consistent with our observation that the chain is typically stretched out inside a vortex (figure 3.3b). In contrast, it is unlikely that the entire chain can be encapsulated into straining regions, given their less coherent, sheet-like topology. Moreover, the evolution of straining regions is much

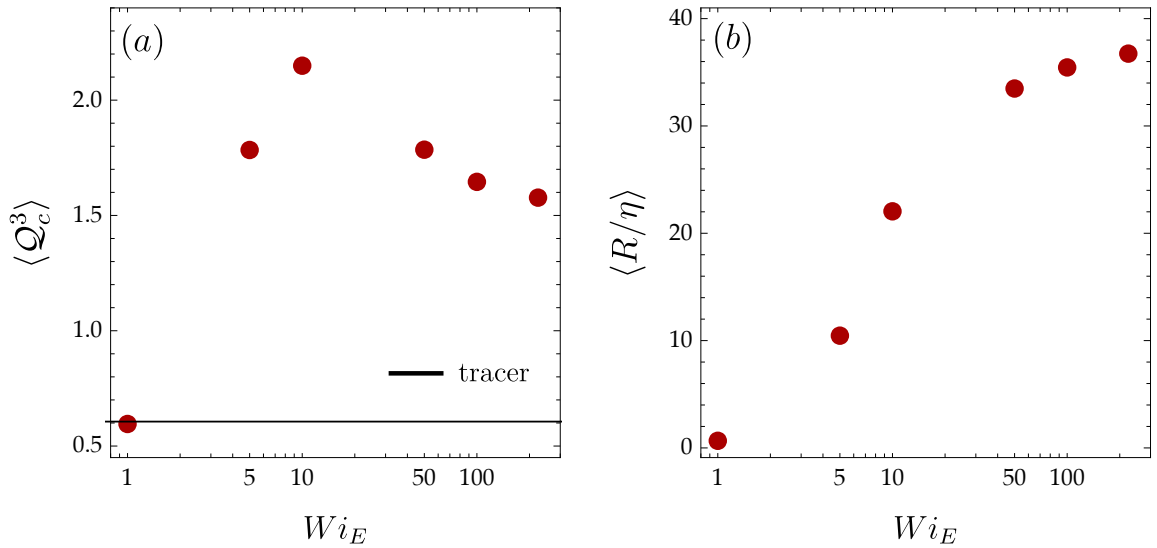


FIGURE 3.4: (a) Third moment of the distribution of Q and (b) the average chain length as a function of Wi_E , for fixed $L_m = 40\eta$ and $r_{eq} = 0.045\eta$. The value of $\langle Q_c^3 \rangle$ for a tracer is shown as a horizontal black line in panel *a*; it is positive due to the presence of intense vortex tubes.

more non-local in nature than that of the vortex tubes [33], which tend to move with the fluid, except for the effects of viscous diffusion (in the inviscid limit the tubes would be ‘frozen’ into the fluid as a consequence of Kelvin’s circulation theorem [20]). Thus, we expect a chain to be able to enter and follow a vortex tube more easily than a straining region.

This explanation implies that there is an ideal chain elasticity for preferential sampling: If Wi_E is too small then the chain acts like a tracer, whereas, if Wi_E is too large then the chain may stretch out beyond the length of the vortex tubes and be unable to reside inside them. This intuition is corroborated by figure 3.4, which shows the effect of Wi_E on preferential sampling (panel *a*), as well as on the mean length of the chain (panel *b*). We find that the third moment of the PDF of Q_c , whose positivity implies a higher probability of positive Q_c , varies non-monotonically with Wi_E , peaking at a value which corresponds to a mean chain length $\langle R \rangle \approx 20\eta$. For larger Wi_E , all the chains approach the maximum chain length $L_m = 40\eta$ and cannot reside within the vortex tubes as effectively (cf. figure 3.1).

We shall present more direct evidence for our explanation of 3D preferential sampling in section 3.4. But first, let us address the question that naturally arises from figure 3.3*a*: Is elasticity essential for preferential sampling, given that the chains are stretched out even inside vortices? The physical picture of chains aligning along vortex tubes would hold even for long chains of a fixed length, and so we would expect such inextensible chains to show preferential sampling as well. We test this idea in the next section.

3.3 Inextensible chain

In order to describe a ‘macroscopic’ inextensible chain, we disregard Brownian fluctuations in (3.1) and replace \mathbf{f}_j^E with

$$\tilde{\mathbf{f}}_j^E = \kappa \alpha_j \hat{\mathbf{r}}_j (r_j - r_{\text{eq}}) - \kappa \alpha_{j-1} \hat{\mathbf{r}}_{j-1} (r_{j-1} - r_{\text{eq}}), \quad (3.7)$$

where r_{eq} still has the meaning of equilibrium length of the springs. Wi_E is set to a very small value to ensure that the chain is in effect inextensible. Its length is then $L = (N_b - 1)r_{\text{eq}}$ (in the simulations, we set $Wi_E = 0.1$, which ensures that $R = \sum_{j=1}^{N_b-1} r_j$ differs from L by 2% at most).

We now consider an inextensible chain having the same length as the maximum length of the extensible chain (with $Wi_E = 10$) considered in § 3.2, *i.e.* we take $L = L_m = 40\eta$. The PDFs of \mathcal{Q}_c for the two cases are compared in figure 3.5a. The absence of extensibility is seen to have only a small effect.

The influence of the length L of the inextensible chain on the level of preferential sampling is depicted in figure 3.5b, in terms of the third moment of \mathcal{Q}_c . Here, we see the same non-monotonic variation of $\langle \mathcal{Q}_c^3 \rangle$ with L , that we saw with Wi_E for the extensible chain (figure 3.4a). Moreover, the value of $\langle \mathcal{Q}_c^3 \rangle$ for $L = 20\eta$ is very close to that of the extensible chain (horizontal line in panel b), which has a mean length $\langle R \rangle \approx 20\eta$ (case of $Wi_E = 10$ in figure 3.4b). These results clearly demonstrate that preferential sampling persists even when the chain is not collapsible. Indeed the only role of extensibility is to allow a chain with a short equilibrium length to be stretched by the flow and reach the appropriate length for staying in a vortex; it does not influence the preferential-sampling dynamics otherwise. This finding supports our intuition regarding the mechanism of preferential sampling whereby the chain resides in intense vortical regions by aligning with the axis of vortex tubes. Such a mechanism, indeed, does not rely on the extensibility of the chain, and is equally applicable to inextensible, but long, chains.

The results in figure 3.5b also confirm our understanding of figure 3.4b, that there is an optimal length for preferential sampling—either attained dynamically by stretching or permanently fixed from the outset—that is comparable to the characteristic linear size of vortex tubes.

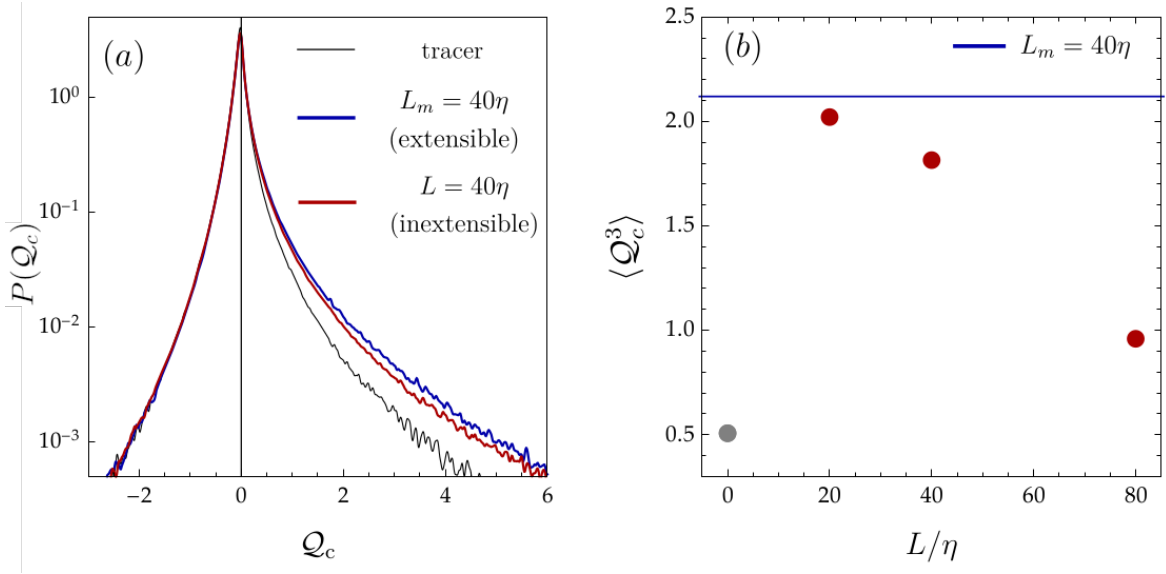


FIGURE 3.5: PDF of Q_c for a tracer (black curve), an extensible chain with $Wi_E = 10$, $r_{\text{eq}} = 0.045\eta$ and $L_m = 40\eta$ (blue curve), and an inextensible chain with $L = L_m$ (red curve). (b) Third moment of the PDF of Q_c for a tracer (grey bullet) and for an inextensible chain with various lengths L (red bullets). The blue line indicates the value of $\langle Q_c^3 \rangle$ for the extensible chain of panel a. The mean length of this extensible chain is close to 20η , as seen in figure 3.4b (case of $Wi_E = 10$).

3.4 Inflexible chain

So far we have considered a chain that does not oppose bending. However, taking the bending stiffness of the chain into account allows us to further understand preferential sampling in 3D turbulence. Specifically, by increasing the stiffness of the chain, we can check whether it is necessary for chains to be able to coil in order to enter vortex tubes. Coiling certainly plays an important role in preferential sampling in 2D turbulence, as demonstrated indirectly in [18], where the deformability of the chain was controlled by changing the number of beads N_b while keeping the maximum length L_m fixed. Here, we directly incorporate the forces arising from bending stiffness into the equations of motion, by assuming that the chain has a bending energy given by [34]

$$E^B = Ar_{\text{eq}}^{-1} \sum_{j=2}^{N_b-1} (1 - \hat{\mathbf{r}}_j \cdot \hat{\mathbf{r}}_{j-1}), \quad (3.8)$$

where $A > 0$ determines the bending stiffness¹. The bending energy generates a force that depends on the angle between two neighbouring links and whose effect is to restore the chain into a rod-like configuration. The form of the force on the j -th bead is [34]

¹Note that our definition of the separation vectors \mathbf{r}_j differs from that used in [34].

$$\begin{aligned} \mathbf{f}_j^B = \frac{A}{r_{eq}} & \left[\frac{\alpha_{j-2}}{r_{j-1}} \hat{\mathbf{r}}_{j-2} - \left(\frac{\alpha_{j-2}}{r_{j-1}} \hat{\mathbf{r}}_{j-2} \cdot \hat{\mathbf{r}}_{j-1} + \frac{\alpha_{j-1}}{r_j} + \frac{\alpha_{j-1}}{r_{j-1}} \hat{\mathbf{r}}_{j-1} \cdot \hat{\mathbf{r}}_j \right) \hat{\mathbf{r}}_{j-1} \right. \\ & \left. + \left(\frac{\alpha_{j-1}}{r_j} \hat{\mathbf{r}}_{j-1} \cdot \hat{\mathbf{r}}_j + \frac{\alpha_{j-1}}{r_{j-1}} + \frac{\alpha_j}{r_j} \hat{\mathbf{r}}_j \cdot \hat{\mathbf{r}}_{j+1} \right) \hat{\mathbf{r}}_j - \frac{\alpha_j}{r_j} \hat{\mathbf{r}}_{j+1} \right], \end{aligned} \quad (3.9)$$

where α_j was defined in (4.17). The characteristic time associated with this force is $\tau_B = \zeta r_{eq}^3/A$, and a dimensionless measure of it is the ‘bending’ Weissenberg number $Wi_B = \tau_B/\tau_\eta$. The chain is inflexible and rod-like for small Wi_B , while the freely-jointed limit is recovered for large Wi_B .

With the addition of the bending stiffness, the evolution equations for an inertialess, inextensible chain become:

$$\dot{\mathbf{X}}_c = \frac{1}{N_b} \sum_{i=1}^{N_b} \mathbf{u}(\mathbf{x}_i, t), \quad (3.10a)$$

$$\dot{\mathbf{r}}_j = \mathbf{u}(\mathbf{x}_{j+1}, t) - \mathbf{u}(\mathbf{x}_j, t) + \frac{1}{\zeta} \left(\tilde{\mathbf{f}}_{j+1}^E - \tilde{\mathbf{f}}_j^E \right) + \frac{1}{\zeta} \left(\mathbf{f}_{j+1}^B - \mathbf{f}_j^B \right) \quad (1 \leq j \leq N_b - 1). \quad (3.10b)$$

We begin by assessing the effect of bending stiffness on preferential sampling in two dimensions. As we already appreciate the importance of coiling in 2D [18], studying the impact of bending stiffness in this case will help us better understand the results in 3D. Moreover, this also provides us with the opportunity to check whether extensibility is crucial for preferential sampling in 2D as suggested in [18], *i.e.*, whether it is essential for a chain inside a vortex to collapse to a tracer, or if it is sufficient for a long chain to simply coil into the vortex.

Figure 3.6 presents snapshots of the inextensible chains overlaid on the vorticity field, for a highly flexible (panel *a*), a moderately flexible (panel *b*), and an inflexible (panel *c*) case. We see that the highly flexible chain is coiled up by the vortices and stays almost entirely within them. The inflexible rod-like chain, however, is unable to coil, and thus while some portions of the chain linger within vortices, the entire chain can never be entrapped by a vortex and preferential sampling weakens considerably. This effect of bending stiffness, which is exactly as anticipated in [18], is shown quantitatively by the PDFs of Λ_c in figure 3.6*d* (see (3.5) for the definition of Λ_c). An analogous behaviour is observed for inextensible, inertialess fibers, described by the local slender-body theory, in a two-dimensional turbulent flow [35].

Figure 3.6*d* also allows us to address the role of extensibility in 2D, by comparing the PDF of Λ_c for an extensible, freely-jointed, chain ($Wi_E = 20$, studied in [18]) with the PDF for the inextensible, highly flexible chain ($Wi_B = 0.4$). The extensible chain has

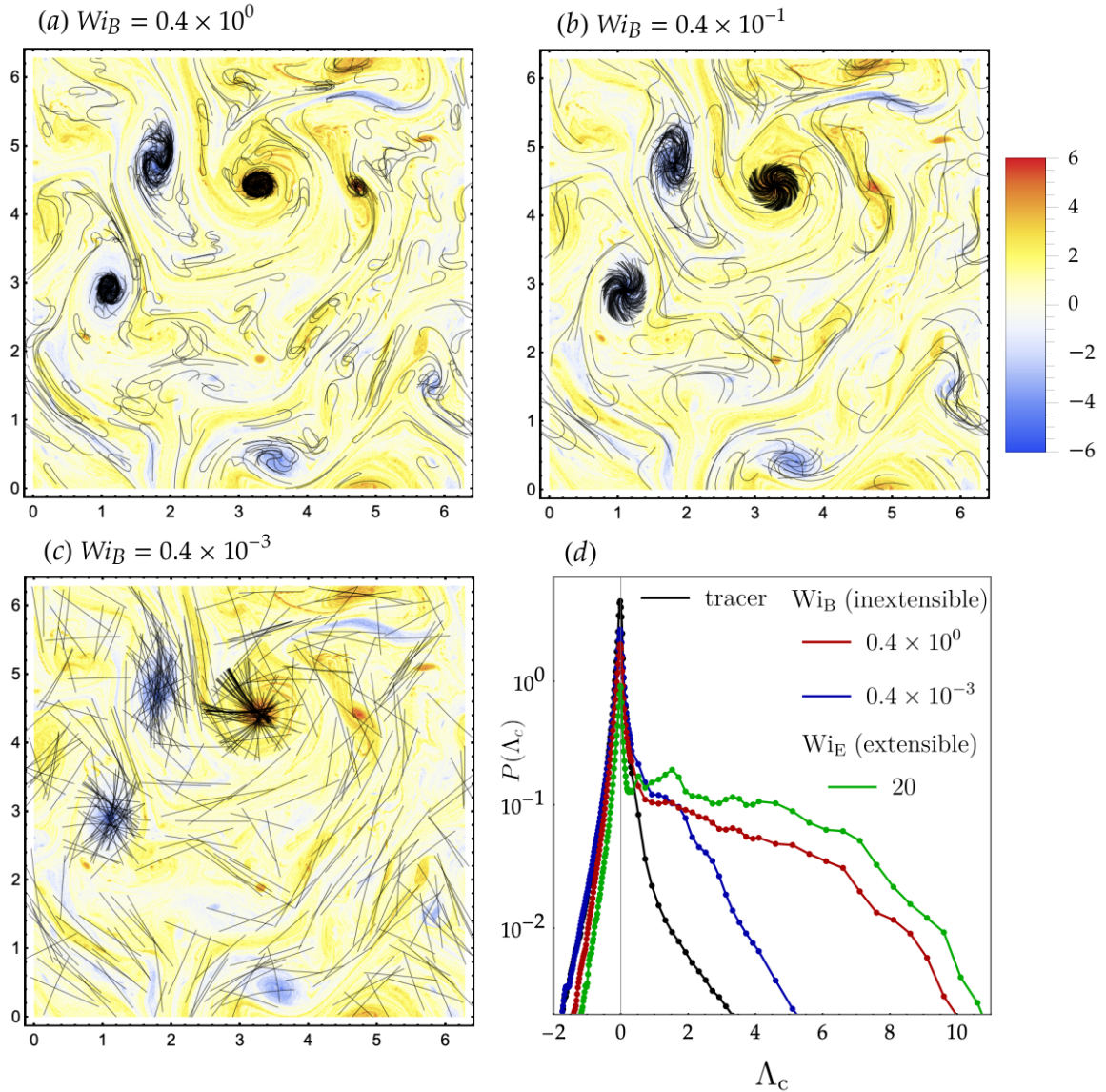


FIGURE 3.6: Snapshots of an ensemble of inextensible chains (black lines) in a 2D turbulent flow, overlaid on the vorticity field, corresponding to (a) $Wi_B = 0.4$ (highly flexible), (b) $Wi_B = 0.4 \times 10^{-2}$ (moderately flexible) and (c) $Wi_B = 0.4 \times 10^{-3}$ (inflexible). It should be noted that several chains are plotted at the same time in order for the reader to visualise the preferential sampling of vortices more easily. There is, however, no interaction between the chains. The length of the chain L is equal to the large vortex scale $2\pi/k_f = 1.25$. (c) PDF of the Okubo–Weiss parameter for the inextensible chain of panels *a* and *c*, along with the PDF for a tracer, as well as that for an extensible chain ($Wi_E = 20$) with equilibrium size of 0.04 and maximum length L_m equal to the length L of the inextensible chain.

a small equilibrium length of 0.04 and a maximum length $L_m = 1.25$, which equals the fixed length L of the inextensible chain. We see that while there is a small reduction of the degree of preferential sampling when the chain is unable to collapse to a tracer-like object, the long inextensible chains are still able to occupy vortices effectively (Figure 3.6*a*), provided of course that they are flexible. Therefore, extensibility is

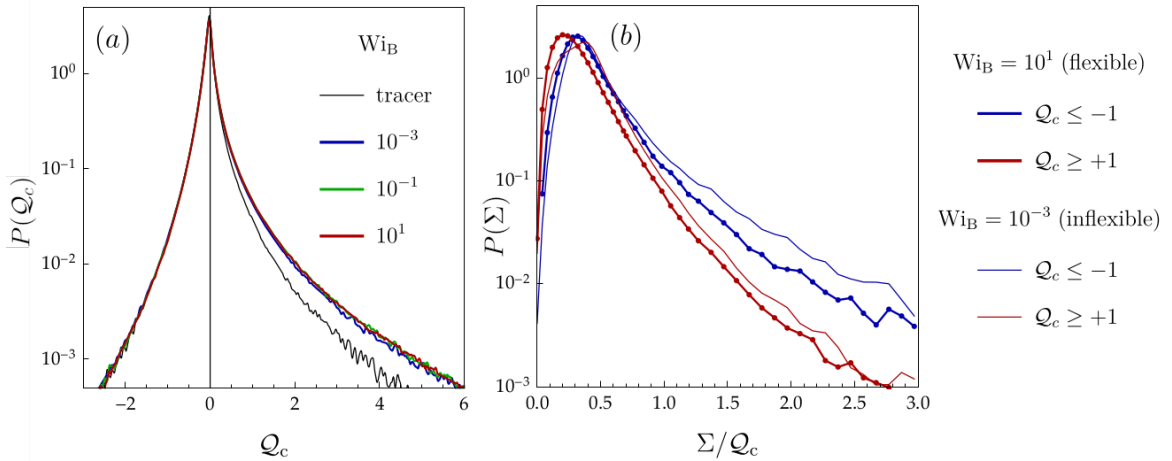


FIGURE 3.7: (a) PDF of Q_c for a tracer and for an inextensible chain ($L = 20\eta$) with bending stiffness varying from that of a highly flexible chain ($Wi_B = 10^1$) to that of a rod-like inflexible one ($Wi_B = 10^{-3}$). (b) PDF of the standard deviation Σ of the values of Q_j sampled by the beads of a chain, conditioned on the center-of-mass being in a vortical ($Q_c \geq +1$) or straining region ($Q_c \leq -1$). Results are shown for the cases of a highly flexible ($Wi_B = 10^1$) and inflexible ($Wi_B = 10^{-3}$) chain of panel a.

not a crucial ingredient for preferential sampling, either in 2D or in 3D (shown in section 3.3). However, it does have a more significant effect in 2D because extensible chains can collapse to tracers inside 2D vortices, whereas this is not possible inside axially-stretched 3D vortex tubes.

Returning to the effect of the bending stiffness, we have shown above that in 2D it strongly affects the preferential sampling of vortical regions because chains must coil in order to enter vortices. We now examine the effect of the bending stiffness in three dimensions. Figure 3.7a shows the PDF of Q_c for a long inextensible chain ($L = 20\eta$) with different values of Wi_B , corresponding to a highly flexible ($Wi_B = 10^1$), a moderately flexible ($Wi_B = 10^{-1}$), and a rod-like inflexible ($Wi_B = 10^{-3}$) chain. The PDF clearly does not vary with Wi_B , which is an unequivocal indication that, in three dimensions, the bending stiffness has no effect on preferential sampling. This fact provides further confirmation of our explanation of preferential sampling of vortical regions in 3D turbulence. If the main mechanism is the alignment of the chain with the axis of the tubular structures on which vorticity concentrates, the chain does not need to coil in order to reach and keep that configuration. It is then natural that the bending stiffness does not affect preferential sampling in three dimensions.

All our results, thus far, point to the ability of chains to thread vortex tubes and follow them by aligning with the vortex axis. In contrast, no such mechanism exists for chains to reside inside straining zones which have a complex geometry and evolve non-locally, as pointed out earlier in section 3.2. Indeed this difference between vortical

and straining regions forms the basis for our explanation of preferential sampling. Therefore, it is important to support this claim with some direct evidence. To this end, we denote by \mathcal{Q}_j the value of \mathcal{Q} at the position of the j -th bead, \mathbf{x}_j . We then consider the mean μ and standard deviation Σ of \mathcal{Q}_j over the N_b beads of the chain:

$$\mu = \langle \mathcal{Q}_j \rangle_b \quad \text{and} \quad \Sigma = \langle (\mathcal{Q}_j - \mu)^2 \rangle_b^{1/2} \quad (3.11)$$

with $\langle \cdot \rangle_b$ denoting the average over $j = 1, \dots, N_b$. Figure 3.7b compares the conditional PDFs of Σ for chains in rotational ($\mathcal{Q}_c \geq +1$) and straining ($\mathcal{Q}_c \leq -1$) regions, for both flexible and inflexible (inextensible) chains. In both cases, we see that Σ is typically greater when the centre of mass of the chain is in a high-strain region. This finding confirms that it is generally easier for a chain, even if it is rod-like, to reside within vortex tubes than within straining regions.

3.5 Conclusions

We have shown that a long bead-spring chain—a simple model for filamentary objects—preferentially samples vortical regions of both 2D and 3D turbulent flows. This behaviour is exhibited by a long inextensible chain, as well as an extensible one that has a small equilibrium length but which is stretched out to inertial-range scales by the flow. The key difference between the underlying mechanisms in 2D and 3D is revealed by the contrasting behaviour of inflexible chains. In 2D, where the chain must coil in order to be trapped within vortices, bending stiffness inhibits preferential sampling. In 3D, however, an inflexible chain exhibits the same sampling behaviour as a fully-flexible one, because the chain follows tubular vortices by aligning with their axes, and neither bending nor extensibility is essential for this to occur.

The extent of preferential sampling is much stronger in 2D than in 3D turbulence (compare the difference between the PDFs for a tracer and the chain in figure 3.6d and figure 3.7a). This is because 2D coherent vortices have much longer lifetimes than 3D vortex tubes, allowing the chain to spend a much larger fraction of time inside the former. On the other hand, the preferential sampling phenomenon is more robust in 3D, as it persists regardless of the extensibility or flexibility of the chain.

Filamentary objects in turbulent flows are encountered in several physical situations, from fibres in the paper industry to micro-plastics and algae in oceanic environments. The understanding of the sampling behaviour of individual chains developed here sets the stage for future studies of the transport, dispersion, and settling of filaments in turbulent suspensions, for which, however, additional physical effects such as intra-chain and inter-chain hydrodynamic interactions must be considered.

References

- [1] J. Schumacher, R. M. Kerr and K. Horiuti, *Structure and Dynamics of Vorticity in Turbulence*, p. 43–86. Cambridge University Press, 2012.
10.1017/CBO9781139032810.003.
- [2] Y. D. † and F. D. ‡, *On coherent-vortex identification in turbulence*, *Journal of Turbulence* **1** (2000) N11.
- [3] J. R. Picardo, L. Agasthya, R. Govindarajan and S. S. Ray, *Flow structures govern particle collisions in turbulence*, *Phys. Rev. Fluids* **4** (2019) 032601.
- [4] M. R. Maxey, *The gravitational settling of aerosol particles in homogeneous turbulence and random flow fields*, *Journal of Fluid Mechanics* **174** (1987) 441–465.
- [5] K. D. Squires and J. K. Eaton, *Preferential concentration of particles by turbulence*, *Physics of Fluids A: Fluid Dynamics* **3** (1991) 1169–1178.
- [6] P. A. Stone and M. D. Graham, *Polymer dynamics in a model of the turbulent buffer layer*, *Physics of Fluids* **15** (2003) 1247–1256.
- [7] V. E. Terrapon, Y. Dubief, P. Moin, E. S. G. Shaqfeh and S. K. Lele, *Simulated polymer stretch in a turbulent flow using brownian dynamics*, *Journal of Fluid Mechanics* **504** (2004) 61–71.
- [8] F. Bagheri, D. Mitra, P. Perlekar and L. Brandt, *Statistics of polymer extensions in turbulent channel flow*, *Phys. Rev. E* **86** (2012) 056314.
- [9] F. Santamaria, F. De Lillo, M. Cencini and G. Boffetta, *Gyrotactic trapping in laminar and turbulent kolmogorov flow*, *Physics of Fluids* **26** (2014) 111901.
- [10] N. Pujara, M. A. R. Koehl and E. A. Variano, *Rotations and accumulation of ellipsoidal microswimmers in isotropic turbulence*, *Journal of Fluid Mechanics* **838** (2018) 356–368.
- [11] C. Brouzet, G. Verhille and P. Le Gal, *Flexible fiber in a turbulent flow: A macroscopic polymer*, *Phys. Rev. Lett.* **112** (2014) 074501.

- [12] G. Verhille and A. Bartoli, *3d conformation of a flexible fiber in a turbulent flow*, *Experiments in Fluids* **57** (2016) 117.
- [13] A. Gay, B. Favier and G. Verhille, *Characterisation of flexible fibre deformations in turbulence*, *Europhys. Lett.* **123** (2018) 24001.
- [14] M. E. Rosti, A. A. Banaei, L. Brandt and A. Mazzino, *Flexible fiber reveals the two-point statistical properties of turbulence*, *Phys. Rev. Lett.* **121** (2018) 044501.
- [15] D. Dotto and C. Marchioli, *Orientation, distribution, and deformation of inertial flexible fibers in turbulent channel flow*, *Acta Mechanica* **230** (2019) 597–621.
- [16] M. E. Rosti, S. Olivieri, A. A. Banaei, L. Brandt and A. Mazzino, *Flowing fibers as a proxy of turbulence statistics*, *Meccanica* **55** (2020) 357–370.
- [17] D. Feldman, *The theory of polymer dynamics*, *Journal of Polymer Science Part C: Polymer Letters* **27** (1989) 239–240.
- [18] J. R. Picardo, D. Vincenzi, N. Pal and S. S. Ray, *Preferential sampling of elastic chains in turbulent flows*, *Phys. Rev. Lett.* **121** (2018) 244501.
- [19] H. K. Moffatt, S. Kida and K. Ohkitani, *Stretched vortices – the sinews of turbulence; large-reynolds-number asymptotics*, *Journal of Fluid Mechanics* **259** (1994) 241–264.
- [20] P. A. Davidson, *Turbulence: an introduction for scientists and engineers*. Oxford university press, 2015, [10.1093/acprof:oso/9780198722588.001.0001](https://doi.org/10.1093/acprof:oso/9780198722588.001.0001).
- [21] R. Singh, M. Gupta, J. R. Picardo, D. Vincenzi and S. S. Ray, *Elastoinertial chains in a two-dimensional turbulent flow*, *Phys. Rev. E* **101** (2020) 053105.
- [22] S. Jin and L. R. Collins, *Dynamics of dissolved polymer chains in isotropic turbulence*, *New Journal of Physics* **9** (2007) 360–360.
- [23] M. D. Lucia, A. Mazzino and A. Vulpiani, *Dumb-bell model for polymer transport in laminar flows*, *Europhys. Lett.* **60** (2002) 181–187.
- [24] M. F. Piva and S. Gabbanelli, *A single dumbbell falling under gravity in a cellular flow field*, *Journal of Physics A: Mathematical and General* **36** (2003) 4291–4306.
- [25] J. Davoudi and J. Schumacher, *Stretching of polymers around the kolmogorov scale in a turbulent shear flow*, *Physics of Fluids* **18** (2006) 025103.
- [26] A. Ahmad and D. Vincenzi, *Polymer stretching in the inertial range of turbulence*, *Phys. Rev. E* **93** (2016) 052605.

-
- [27] P. Perlekar and R. Pandit, *Statistically steady turbulence in thin films: direct numerical simulations with ekman friction*, *New Journal of Physics* **11** (2009) 073003.
- [28] G. Boffetta and R. E. Ecke, *Two-dimensional turbulence*, *Annual Review of Fluid Mechanics* **44** (2012) 427–451.
- [29] H. C. Öttinger, *Stochastic Processes in Polymeric Fluids*. Springer Berlin Heidelberg, 1996, [10.1007/978-3-642-58290-5](https://doi.org/10.1007/978-3-642-58290-5).
- [30] A. Okubo, *Horizontal dispersion of floatable particles in the vicinity of velocity singularities such as convergences*, *Deep Sea Research and Oceanographic Abstracts* **17** (1970) 445–454.
- [31] J. Weiss, *The dynamics of enstrophy transfer in two-dimensional hydrodynamics*, *Physica D: Nonlinear Phenomena* **48** (1991) 273–294.
- [32] H. M. Blackburn, N. N. Mansour and B. J. Cantwell, *Topology of fine-scale motions in turbulent channel flow*, *Journal of Fluid Mechanics* **310** (1996) 269–292.
- [33] A. Tsinober, ed., *An Informal Conceptual Introduction to Turbulence*. Springer Netherlands, 2009, [10.1007/978-90-481-3174-7](https://doi.org/10.1007/978-90-481-3174-7).
- [34] E. Gauger and H. Stark, *Numerical study of a microscopic artificial swimmer*, *Phys. Rev. E* **74** (2006) 021907.
- [35] J. Bec. Private Communication, 2021.

Chapter 4

Sedimenting Elastic Filaments in Turbulent Flows

We investigate the gravitational settling of a long, model elastic filament in homogeneous isotropic turbulence. We show that the flow produces a strongly fluctuating settling velocity, whose mean is moderately enhanced over the still-fluid terminal velocity, and whose variance has a power-law dependence on the filament's weight but is surprisingly unaffected by its elasticity. In contrast, the tumbling of the filament is shown to be closely coupled to its stretching, and manifests as a Poisson process with a tumbling time that increases as a power law with the elastic relaxation time of the filament. Apart from elasticity, inertia, and gravitational acceleration, we have also considered the effect of bending stiffness and found that stiff filaments settle and tumble slower than fully-flexible filaments.

Parts of this chapter closely follows the work [Singh *et al.*, arXiv:2101.00385 (2021)].

4.1 Introduction

Sediments in turbulent flows, commonplace in nature and industry, raise the question of how objects settle under gravity while being buffeted by a turbulent carrier flow. Even for the simplest case of tiny rigid spherical particles, the interaction of these forces is intricate and leads to an enhancement of the settling velocity over its value in a still fluid [1–7]. Recent work has extended our understanding to spheroidal particles, with additional rotational degrees of freedom, and addressed the issue of how they orient themselves while settling [8, 9]. A common feature of these prior studies is that they are limited to rigid particles whose sizes, regardless of their anisotropy, are much smaller than the dissipative Kolmogorov scale η of the flow. These constraints are certainly meaningful for a wide variety of applications, such as understanding the

initiation of rain in warm clouds [10–14] and the radiative properties of cold clouds [15–18], which involve, respectively, turbulent suspensions of spherical water droplets and non-spherical ice crystals.

However, sediments that are both deformable and larger than the Kolmogorov scale are just as ubiquitous. One important example is the sedimentation of long deformable filaments, wherein flow-induced deformation modifies the net drag force experienced by the filament [19], thus coupling the dynamics of conformation to settling. This problem has been recently addressed for low Reynolds number, non-turbulent flows [20, 21]. However, understanding the gravitational settling of filaments when the carrier flow is turbulent remains an important open problem, encountered in diverse settings such as fiber suspensions in industry [22], sedimentation of passive marine pollutants like as plastic debris from fishing gear [23–25], as well as the dynamics of filamentary microorganisms in the field of marine ecology [26–28].

In this Chapter, we address this issue through a combination of scaling analysis and detailed numerical simulations on a model elastic filament in a homogeneous and isotropic turbulent flow. In particular, we show that the turbulent flow produces strong fluctuations in the settling velocity, while moderately enhancing its mean value over the terminal velocity in a still-fluid. We theoretically derive how the normalised variance of the settling velocity scales with the elasticity and inertia (mass) of the filament, as well as with the relative strengths of the accelerations due to gravity and turbulence. Our estimates are then verified through detailed numerical simulations. Furthermore, applying ideas from the persistence problem of non-equilibrium statistical physics, we uncover a close connection between the two internal motions of tumbling and stretching, which accompany the unsteady yet inevitable descent of the filament.

A simple model of a long filament, which retains enough internal structure to exhibit both elasticity and inertia, is a chain of heavy inertial particles connected through elastic springs. Such chains are a macroscopic adaptation of the bead-spring model commonly used to study polymers [29]—a connection suggested by experiments on flexible fibres in turbulent flows [30, 31]. These chains provide a useful framework to understand the intricate interplay between elasticity and turbulent mixing [32–34] and provide insights which complement those obtained from other models with uniformly distributed mass [35, 36], which are optimal for relatively more *rigid* fibers and well suited to studies of buckling, flapping or as probes for two-point Eulerian statistics of the carrier flow. Here, we use the bead-spring chain model, which allows for a natural inclusion of elasticity, stiffness, and inertia, to address issues of gravitational settling which have been neglected in previous studies. In this context, the most striking feature of these filamentary chains is the manner in which they preferentially sample

the geometry of a turbulent flow: in the inertia-less (neutrally buoyant) limit, elastic chains preferentially sample the vortical regions of the flow, in both two and three dimensions (3D) though for different reasons [32, 34]. This prediction, for the case of rigid chains in 3D, was recently confirmed experimentally [37]. The introduction of inertia (without gravity), counter-acts this tendency due to centrifugal expulsion from vortices and decorrelation from the flow, resulting in rather distinct dynamics [33]. Here, we account for gravitational acceleration and investigate the settling dynamics of these *elasto-inertial* chains.

4.2 The Elasto-inertial Chain: a minimal model for filaments

We model a filament of mass M as a chain of N_b spherical beads. Considering ρ to be the mass density of the filament, we distribute the mass uniformly over the beads, each of radius $a \ll \eta$, so that $\frac{4}{3}\pi a^3 \rho N_b = M$. The beads are then characterised by a Stokesian relaxation time $\tau_p = \frac{2\rho a^2}{9\rho_f \nu}$, where ρ_f and ν are the density and kinematic viscosity of the carrier fluid. Each bead, positioned instantaneously at \mathbf{x}_j , is connected to its nearest neighbours through (phantom) elastic links with which we associate a relaxation time scale τ_E (yielding an effective elastic time scale $\tau_E N_b(N_b + 1)/6$ for the filament [32, 38]), thus rendering our elasto-inertial chains extensible (and fully flexible). The dynamics of these model filaments are then completely determined by the coupled equations of motion for the inter-bead separation vectors $\mathbf{r}_j = \mathbf{x}_{j+1} - \mathbf{x}_j$ and the center-of-mass \mathbf{x}_c :

$$\begin{aligned} \tau_p \ddot{\mathbf{r}}_j &= [\mathbf{u}(\mathbf{x}_{j+1}, t) - \mathbf{u}(\mathbf{x}_j, t) - \dot{\mathbf{r}}_j] + A [\boldsymbol{\xi}_{j+1}(t) - \boldsymbol{\xi}_j(t)] \\ &\quad + \frac{1}{4\tau_E} (f_{j-1} \mathbf{r}_{j-1} - 2f_j \mathbf{r}_j + f_{j+1} \mathbf{r}_{j+1}) \end{aligned} \quad (4.1)$$

$$\tau_p \ddot{\mathbf{x}}_c = \left(\frac{1}{N_b} \sum_{j=1}^{N_b} \mathbf{u}(\mathbf{x}_j, t) - \dot{\mathbf{x}}_c \right) + \frac{A}{N_b} \sum_{j=1}^{N_b} \boldsymbol{\xi}_j(t) - \tau_p g \hat{\mathbf{z}}. \quad (4.2)$$

Here, we use the FENE (finitely extensible nonlinear elastic) interaction $f_j = (1 - |\mathbf{r}_j^2|/r_m^2)^{-1}$, with a prescribed maximum inter-bead length r_m , to model the springs. $\boldsymbol{\xi}_j(t)$ are independent white noises which, unlike in the case of polymers, do not represent Brownian forces but rather are introduced as a means to set the equilibrium length r_0 for each segment of our filament (in the absence of flow). The noise amplitude is chosen accordingly as $A^2 = \frac{r_0^2}{6\tau_E}$. The entire chain then has equilibrium and maximum end-to-end extensions of $R_0 = r_0 \sqrt{N_b - 1}$ and $R_m = r_m(N_b - 1)$, respectively. We note

that the precise method of enforcing the equilibrium length is not crucial to our study; in previous work we had omitted the noise and instead set the equilibrium length by using a spring force of $f_j(r_j - r_0)$, without affecting the qualitative dynamics of the chains in flow [34].

We choose a coordinate system such that the acceleration due to gravity g acts along the negative z -axis. Finally, the time-scales τ_p and τ_E , as well as the acceleration due to gravity g , allow us to define non-dimensional numbers in terms of analogous (small-scale) quantities of the carrier turbulent flow, namely the Kolomogorov time $\tau_\eta \equiv \sqrt{\nu/\epsilon}$ and acceleration $a_\eta \equiv (\epsilon^3/\nu)^{1/4}$, where ϵ is the mean energy dissipation rate of the flow. The dynamics of our filaments are thus completely determined by the Stokes number $St \equiv \tau_p/\tau_\eta$ (a measure of the inertia), the Froude number $Fr \equiv a_\eta/g$ (a measure of the force of gravity), and the Weissenberg number $Wi \equiv \frac{N_b(N_b+1)\tau_E}{6\tau_\eta}$ (a measure of elasticity). Here, we have used the mapping proposed by [38] to estimate the effective relaxation time of the entire chain from τ_E (which corresponds to individual links).

Note that this model neglects the feedback of the chains onto the flow. Because we consider the extremely dilute limit of a single chain (we simulate many chains only to obtain good statistics), the motion of the chain does not affect the global flow. However, the chain will certainly modify the local flow field. This in turn would result in one portion of the chain influencing other portions, via the disturbed flow. This effect can be accounted for within the bead-spring framework by including inter-bead hydrodynamic interactions (HI), as has been done in polymer models [39, 40]. However, the effect of HI on chain dynamics is minimal when the chain is stretched out by the flow. We therefore ignore HI for simplicity. Similarly, we also ignore excluded volume interactions. Bending stiffness is also disregarded for now, although we study its effect later in Sec. 4.7. Thus, our chain represents a minimal model of a filament, adopted in order to more clearly reveal the fundamental interplay between elasticity, inertia, and gravitational and turbulent acceleration.

It is also important to point out that other models of filament dynamics, particularly in the context of turbulent transport, are available [30, 31, 35, 36]. However, studies for low Reynolds number flow show [20] that the bead-spring approach to filaments still remains an important framework [41–44] because of the limitations of models based on slender-body theory [45, 46].

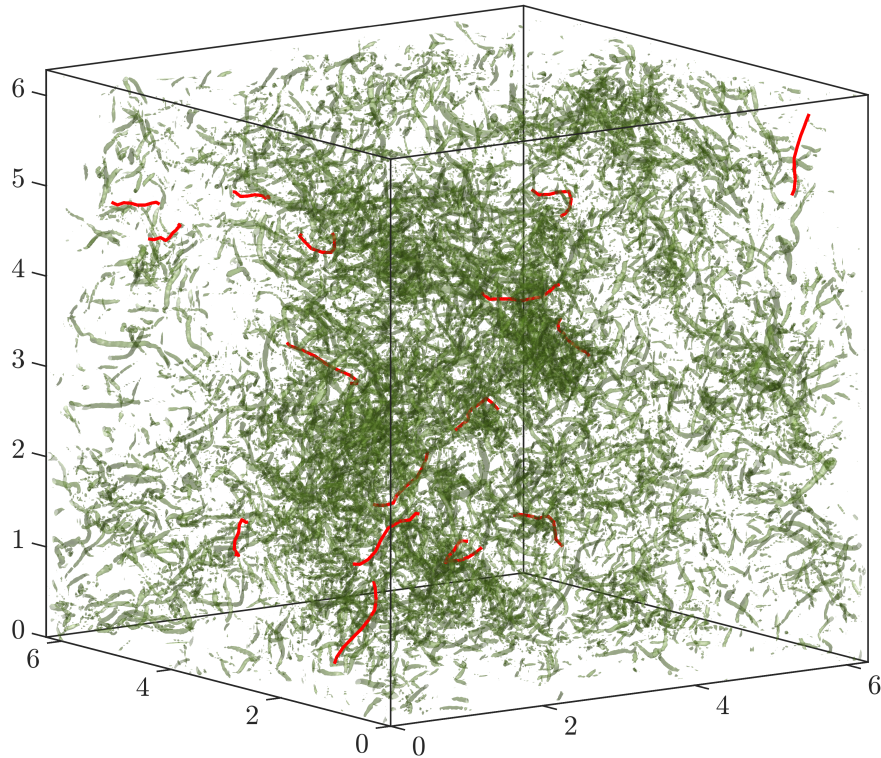


FIGURE 4.1: Representative snapshot of a few elastic filaments (red curves) sedimenting through a turbulent flow. The intense vortex tubes (green contours) of the flow are visualized via iso-surfaces of the Q field ($3\langle Q^2 \rangle^{-1/2}$) [48]. The parameters of the filaments are $Wi = 20$, $St = 2$, and $Fr = 1$.

4.3 Simulations

In our direct numerical simulations, we solve the equations of motion of the filaments, using a second-order Runge-Kutta scheme, together and simultaneously with the three-dimensional, incompressible Navier-Stokes equations, driven to a statistically stationary state by using a constant energy injection scheme. To simulate the carrier flow, we use a de-aliased pseudo-spectral algorithm, spatially discretize the Navier-Stokes equations on a 2π periodic cubic box with $N^3 = 512^3$ collocation points, and use a second-order slaved Adams-Bashforth scheme for time integration [47] (see Appendix C). The fluid velocity $\mathbf{u}(\mathbf{x}, t)$ obtained on the regular periodic grid is interpolated, using trilinear interpolation (which is a generalisation of the bilinear interpolation scheme discussed in Appendix E), to obtain the velocity $\mathbf{u}(\mathbf{x}_j, t)$ at the bead positions. We choose the coefficient of viscosity $\nu = 10^{-3}$ to obtain a Taylor-scale Reynolds number $Re_\lambda \approx 200$. We evolve an ensemble of 10^4 filaments, each with an equilibrium end-to-end extension of $R_0 = 15.2\eta$, a maximum length $L = 270\eta$, and $N_b = 10$ beads (we have checked that our results remain qualitatively unchanged if we use a fewer number of beads, $N_b = 5$), and consider $0.1 \leq St \leq 8.0$, $0.5 \leq Wi \leq 40$ and $0.5 \leq Fr \leq 2.0$.

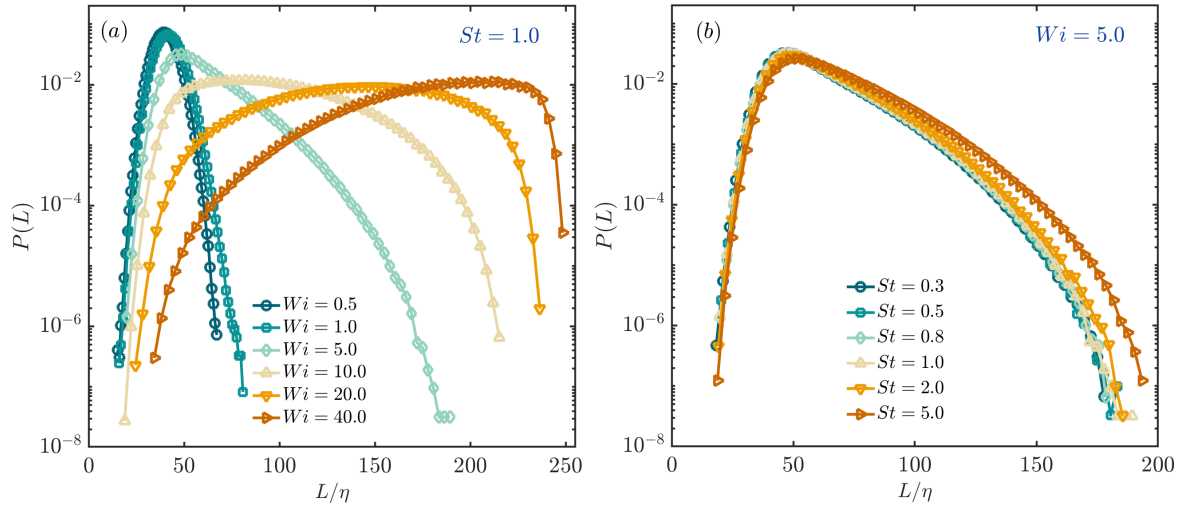


FIGURE 4.2: PDFs of total lengths L (normalised by η) for (a) constant $St = 1.0$ and varying Wi (b) constant $Wi = 5.0$ and varying St .

4.4 Characterising Inertial Filaments

For completeness, before we address the central question of gravitational settling, let us briefly characterise these inertial filaments in terms of how much and where they stretch as well as their (Lagrangian) chaotic behaviour.

4.4.1 Filament Lengths

As we discussed in Chapter 2 for two-dimensional turbulence, the dynamics of inertial, elastic filaments in turbulent flows is greatly complicated by the combined effects of inertia and elasticity. A filament that has its equilibrium length r_0 in the inertial range feels the full roughness of the turbulent carrier flow so that different beads experience completely different fluid drag forces causing the filament to stretch, compress and acquire dynamically varying shapes. Therefore, the total length of a filament $L = \sum_{i=1}^{N_b-1} r_i$, where $r_i = |\mathbf{r}_i|$ is the length of the individual springs, is dynamically varying. A small Wi filament hardly stretches so that its length does not deviate much from the equilibrium value. This is seen in Fig. 4.2(a) where the distribution of the total filament lengths is narrow and sharply peaked at the equilibrium value $R_0 = 15.2\eta$. However, the filaments start to stretch much more as Wi is increased and the distributions start to develop broader tails. For very large Wi , the filaments are maximally stretched and the distribution of lengths starts to develop a peak around the maximum length $L = 270\eta$.

In addition to elasticity, inertia also (mildly) contributes in the stretching of the filaments. A filament with larger inertia offers more resistance to the tendency of the springs to fall back to their equilibrium lengths. Hence, a filament with higher St is

more probable to stay in a stretched configuration causing the right tails of the length PDFs to widen as St is increased (Fig. 4.2(b)).

4.4.2 Shape of the Filaments

The shape of (fully flexible) long filament being advected by a turbulent flow is continuously evolving and changing due to the roughness of the flow. A filament that is fully flexible offers no resistance to bending, so that the angles $\psi_i, i = 2, 3, \dots, N_b - 2$ between successive links (springs) can take values in $[0, 180^\circ]$, where ψ_i is defined as:

$$\cos \psi_i = \frac{\mathbf{r}_{i-1} \cdot \mathbf{r}_i}{|\mathbf{r}_{i-1}| |\mathbf{r}_i|} \quad (4.3)$$

with the end beads being attached to only one spring each. A filament $\psi_i = 180^\circ \forall i$ has an end-to-end length equal to its total length:

$$\left| \sum_{i=1}^{N_b} \mathbf{r}_i \right| = \sum_{i=1}^{N_b} |\mathbf{r}_i| \quad (4.4)$$

A filament in a “straighter” configuration will typically have ψ_i ’s taking larger values while smaller hinge angles ensure that the end-to-end lengths of filaments are much less than their total lengths. Additionally, our filament model has a head-tail symmetry, i.e. it is identical under the transformation $\mathbf{r}_j \rightarrow -\mathbf{r}_j$, implying that any i -th bead (i -th spring) is identical to $(N_b - i + 1)$ -th bead ($(N_b - i)$ -th spring). Thus, the statistics of hinge angles are unique only for the beads $2, 3, \dots, (\lceil N_b/2 \rceil - 1)$. Hence, we show only the statistics of the angles that are unique (Fig. 4.3). The shape of a filament is indirectly dependent on its length: A filament with a small total length spans lesser flow structures and is susceptible to change its shape due to their influence. This means that a smaller filament prefers a more “bent” configuration than a straight one resulting in a distribution of hinge angles that is rather uniform over an intermediate range (Fig. 4.3 inset). However, as the elasticity of the filament increases (Fig. 4.3 main panel), it is stretched out to much longer lengths that span several flow structures. At such long lengths, the shape of the filament can only be affected by flow structures that act in a coordinated way to exert drag forces on the beads so as to make them the filament bend. Such a situation becomes less probable as the lengths have become larger. Thus, larger Wi filaments prefer a “straighter” configuration resulting in the distribution of the hinge angles biased towards larger values as shown in the main panel of Fig 4.3.

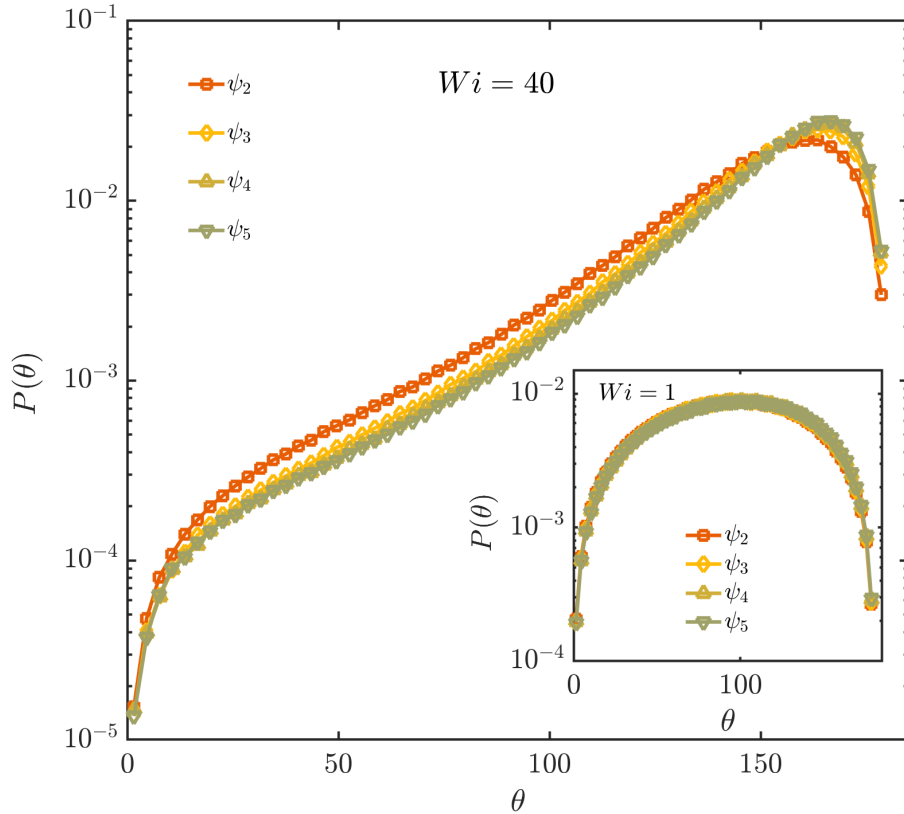


FIGURE 4.3: PDFs of the hinge angles for two different instances of elasticity: $Wi = 40$ (main) and $Wi = 1.0$ (inset).

4.4.3 Preferential Sampling

A filament of tracers preferentially samples the vortical regions of a turbulent flow in both two and three dimensions [32, 34]. However, the underlying reasons for this are subtly different. While in two-dimensional flows, filaments tend to coil up in the vortices [32], in three dimensions, as shown in the previous chapter, while being preferentially trapped, they tend to stretch out in vortex tubes as well as the straining zones. However, the problem of preferential sampling becomes more curious when the filaments comprise of heavy, inertial particles rather than inertialess tracers. The extent of preferential sampling is then governed by the interplay of the inertia of the beads and the elasticity of the springs. In two dimensions, highly elastic filaments preferentially sample the vortical regions of the flow while increase in inertia leads to a preferential sampling of the straining zones [33] (see Chapter 2). But does this observation still hold in three-dimensions?

We answer this question by recording the \mathcal{Q} -values at all the beads of a filament (for all the filaments). The \mathcal{Q} -criterion, like the Okubo-Weiss parameter in 2D, is the indicator of the local geometry of the flow in 3D. If $A = \nabla \mathbf{u}$ is the local velocity gradient of the

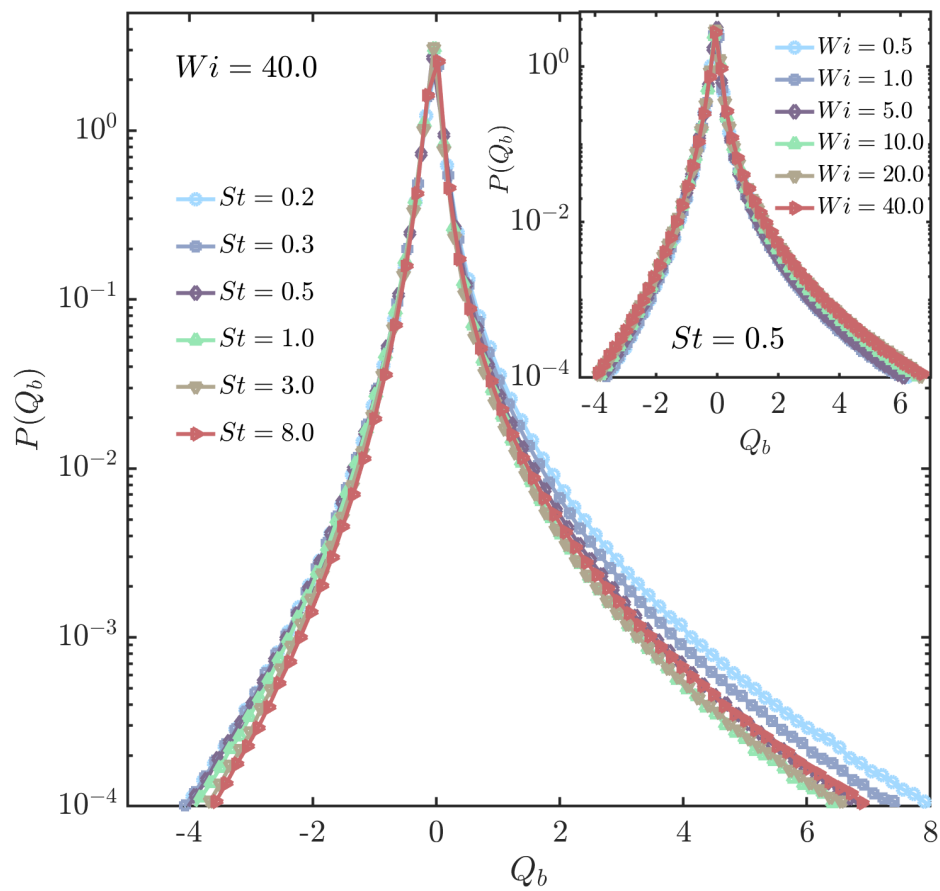


FIGURE 4.4: PDFs of the Q values (Q_b) measured at the beads of a filament for a fixed Wi and varying St (main) and for fixed St and varying Wi (inset).

flow, then the \mathcal{Q} -criterion is defined as:

$$\mathcal{Q} = \tau_\eta^2 \frac{\omega^2 - S : S}{2} ; \quad S = (A + A^\top)/2 \quad (4.5)$$

so that a $\mathcal{Q} > 0 (< 0)$ indicates a vorticity (strain) dominated flow region. We show the PDFs of the \mathcal{Q} values calculated at the bead positions (\mathcal{Q}_b) of the filaments for different instances of St in the main panel of Fig. 4.4. Similar to the 2D case, a small, non-zero inertia results in an under sampling of the vortical regions due to centrifugal expulsion of the filaments from the vortices as compared to a filament of tracers. This is seen in the shrinking of the right tails of the \mathcal{Q} -PDFs. As St is increased, the filaments sample the straining regions even more until $St \simeq 1$ as the left tails become wider. An even further increase in inertia causes the filaments to decorrelate from the flow as the particle relaxation time τ_p has become so large that they are unable to follow the local flow closely. At such large inertia, i.e. $St \gg 1$ the filaments populate the flow more homogeneously and this manifests in the slight widening (and narrowing) of the right (left) tails of the \mathcal{Q}_b distributions for large St ($= 3.0, 8.0$).

The effect of elasticity is, however, to counteract the effect of inertia by drawing the filaments towards vortical regions and resulting in their entrapment inside the vortices. A more stretched out filament is more likely to encounter a vortices due to its larger length. Therefore, the filaments show a preference for sampling the vortical regions more as Wi is increased and is seen in the widening of the right tails of \mathcal{Q} -PDFs (see Fig. 4.4 (inset)). Increase in elasticity also causes a mild oversampling of the straining regions as the longer filaments cannot exit the strong straining regions of the flow as easily and results in the broadening of the left tails of the \mathcal{Q} -PDFs as well.

Thus, the qualitative picture of preferential sampling of a 3D turbulent flow by an inertial, elastic filament is similar to that in 2D. However, the underlying difference is that filaments shrink to smaller lengths when trapped inside the vortices in 2D turbulence [32–34] but are stretched out by the vortices in 3D [34].

This complex interplay of inertia and elasticity in addition to the turbulent background flow contrives to make trajectories followed by the filaments chaotic.

4.4.4 Chaotic Trajectories and Lyapunov Exponents

Chaoticity is one of the defining features of turbulent flows. Chaotic advection in turbulent flows leads to enhanced mixing of passive scalars [49–54]. Similarly, advection of long, extensible filaments in turbulent backgrounds is also chaotic and which also have added complexities of inertia and elasticity. In this section, we examine the impact of

these additional internal degree of freedom of filaments on the chaotic nature of their trajectories in turbulence, which is quantified by the Lagrangian Lyapunov exponents.

We first begin by briefly discussing chaos and Lyapunov exponents, that are a measure of chaos in a system. A chaotic system is characterised by its sensitivity to initial conditions such that small initial perturbations lead to the system attaining a completely different state in a finite time. One way to measure this sensitivity to initial conditions or chaoticity was provided by Lyapunov by comparing the growth rate of perturbations to an exponential by means of a characteristic exponent associated with the evolution of the system, and is referred to as the Lyapunov exponent [55]. The characteristic Lyapunov exponent $\chi[f]$ for any complex valued function $f(t)$ is defined as [56]:

$$\chi[f] = \limsup_{t \rightarrow \infty} \frac{1}{t} \ln |f(t)| \quad (4.6)$$

where $|\cdot|$ denotes the Euclidean norm, \limsup is the supremum limit, and $f(t)$ is defined on the interval $[t_0, \infty)$. For a matrix of functions

$$F(t) = f_{ij}(t), \quad i = 1, \dots, n, \quad j = 1, \dots, m \quad m \leq n \quad (4.7)$$

where $t \in [t_0, \infty)$, the characteristic exponent is defined as:

$$\chi[F] = \max_{ij} \chi[f_{ij}] \quad (4.8)$$

The theory of Lyapunov exponents can be applied directly to the evolution of a material line element (or the evolution of the distance between two initially nearby fluid particles). The Lagrangian evolution of a tracer trajectory is given as:

$$\frac{d\mathbf{X}(t)}{dt} = \mathbf{u}(\mathbf{X}(t), t) \quad (4.9)$$

where $\mathbf{X}(t)$ is the position of the tracer at time t and $\mathbf{u}(\mathbf{X}(t), t)$ is the fluid velocity at \mathbf{X} . The evolution of a material line $\mathbf{D}(t) = \delta\mathbf{X}(t)$ connecting two initially infinitesimally close tracers is then simply given as:

$$\frac{d\mathbf{D}(t)}{dt} = [\nabla\mathbf{u}(\mathbf{X}(t), t)] \mathbf{D}(t) \quad (4.10)$$

where the matrix $[\nabla\mathbf{u}(\mathbf{X}(t), t)]$ is the velocity gradient tensor evaluated at location $\mathbf{X}(t)$ at time t [57, 58]. By setting $\mathbf{D}(t=0) = I_3$, where I_3 is the 3×3 identity matrix, one can quantify the deformations of a unit sphere by the action of the local velocity

gradients [58]. The resulting ellipse from the deformation of the sphere has semi-axes given by the singular values $\sigma_i(\mathbf{X}, t)$ of the deformation tensor $\mathbf{D}(t)$. The exponential growth rate of these singular values gives the Finite Time Lyapunov Exponents (FTLEs) γ_i , $i = 1, 2, 3$:

$$\gamma_i(\mathbf{X}, t) = \frac{1}{t - t_0} \ln \sigma_i(\mathbf{X}, t) \quad (4.11)$$

The Lyapunov exponents (LEs) are the ensemble averaged FTLEs [58]:

$$\lambda_i = \langle \gamma_i \rangle = \frac{1}{t - t_0} \langle \ln \sigma_i \rangle \quad (4.12)$$

The maximal Lyapunov Exponent λ_1 is then an indicator of the chaoticity. As a result of incompressibility, the velocity gradient tensor is traceless and the determinant of the deformation tensor is unity at all times indicating the volume preservation. This means the product $\sigma_1\sigma_2\sigma_3 = 1$ and the sum of LEs $\lambda_1 + \lambda_2 + \lambda_3 = 0$ [58].

The equation 4.10 is used to track the fluid deformations along the tracer trajectories. Each deformation tensor is initialized to δ_{ij} and evolved as:

$$D_{ij}(t + \Delta t) = e^{A_{ik}\Delta t} D_{kj}, \quad A_{ik} = \partial_k u_i \quad (4.13)$$

which is the exact solution for a constant velocity gradient.

For our long filaments, that are not point-like tracers but which are inertial and whose lengths lie deep in the inertial range, we record the velocity gradient tensor at their centres of mass and evolve the deformation tensor as per Eq. 4.13. The maximal Lyapunov exponents, thus obtained, are shown in Fig. 4.5 as a function of St for different choices of Wi . Non-interacting, inertial particles in turbulent flows are ejected from vortical regions into the straining zones which have large stretching rates. This results in increased chaoticity compared to tracers which sample all the regions of the flow homogeneously for $St < 1$. However, for larger St the heavy, inertial particles have a delayed response to the local fluid motion thereby resulting in the weakening of chaoticity [59].

What happens when we introduce elastic interactions between these heavy, inertial particles such as in the case of our filaments. We begin by showing a plot of the maximal Lyapunov exponents (λ_1) in Fig. 4.5. For small values of Wi , the filaments stretch less and stay close to their equilibrium lengths (see Section 4.4.1). Due to their finite but small lengths, these filaments are more likely to spend more time in the same flow region for a longer duration resulting in reduced chaoticity as compared to free, inertial particles. With increasing Wi , however, the filaments are stretched to much

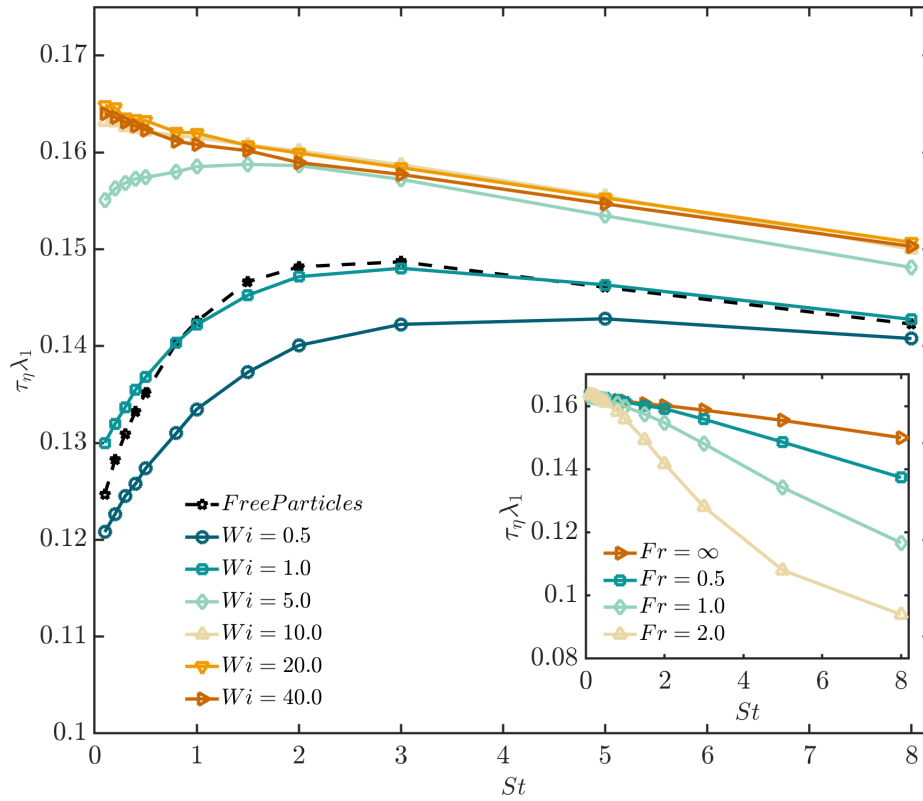


FIGURE 4.5: Maximal Lyapunov exponents for inertial particles (dashed black curve) and filaments (solid lines) in a turbulent flow.

longer lengths that span multiple flow structures. Consequently, the motion of the centre-of-mass, which is the combined effect of the motion of the beads, then becomes more chaotic as the individual beads of a filament experience completely different fluid drag forces at all times. This is seen in the increase in values of Lyapunov exponents which ultimately saturate for extremely large Wi .

Given this complex dynamics of inertial chains in three-dimensional turbulent flows, with and without gravitational forces, let us now return to the question of sediments.

4.5 Fluctuating Settling Velocity

We begin our study by examining the fluctuating settling velocities $v_z \equiv \dot{\mathbf{x}}_c \cdot \hat{\mathbf{z}}$ of the filaments. Let us first consider the mean value $\langle v_z \rangle$, where the angular brackets denote an average over the ensemble of chains and over time in the statistically stationary state. From Eq. (4.2), denoting $a_z \equiv \ddot{\mathbf{x}}_c \cdot \hat{\mathbf{z}}$ as the vertical acceleration in the z direction, the assumption of a mean settling velocity implies, by definition, that $\langle a_z \rangle = 0$. Furthermore, since the noises are independent and of zero-mean, we obtain $\langle v_z \rangle = \langle \bar{u}_z \rangle - \tau_p g$, where $\tau_p g$ is the terminal settling velocity in a still-fluid, and $\bar{u}_z \equiv \frac{1}{N_b} \sum_{j=1}^{N_b} u_z(\mathbf{x}_j, t)$ is

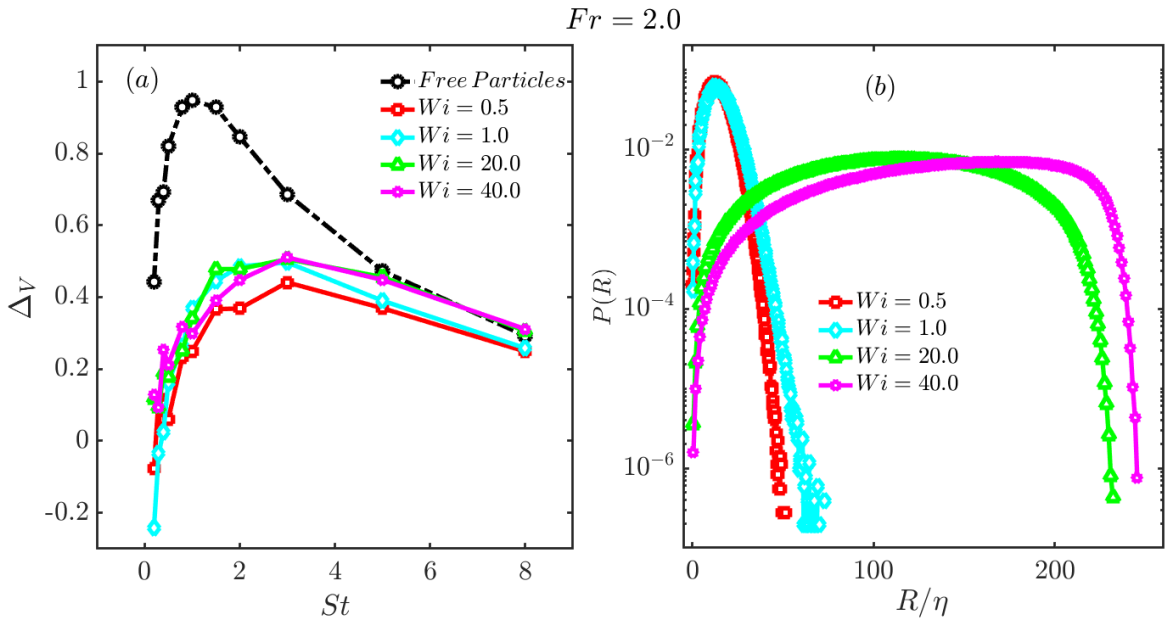


FIGURE 4.6: (a) Plot of the relative enhancement in the mean settling velocity Δ_V , over the still fluid value, as a function of St , for free, inertial, point particles and for filaments with different values of Wi . (b) Probability distribution function of the end-to-end extension of the filament for the same values of Wi as in panel (a). The equilibrium and maximum lengths for all filaments are $R_0 = 15.6\eta$ and $R_{max} = 270\eta$ respectively. In both panels, $Fr = 2$.

the average z -component of the fluid velocity field sampled by the filament. If an object uniformly samples the flow, as tracer particles do, then $\langle \bar{u}_z \rangle = 0$. However, this is typically not the case for non-tracers: Heavy inertial particles (with $St > 0$) are known to exhibit an enhanced mean settling velocity. The magnitude of this effect, which may be quantified through $\Delta_V = \langle v_z \rangle / \tau_p g - 1 = -\langle \bar{u}_z \rangle / \tau_p g$, varies non-monotonically with St as explained in Ref. [7].

Now, as instantiated by our model, a filament can be thought of as a string of elastically-linked, inertial particles. So, how does this internal linking impact the mean settling velocity of filaments? Figure 4.6(a) answers this question by presenting simulation results of Δ_V as a function of St , for filaments with $Fr = 2$ (results for $Fr = 1$ and 0.5 are qualitatively similar but with reduced magnitudes of Δ_V) and various values of Wi , as well as for free inertial particles (whose dynamics are given by Eq. (4.2) with $A = 0$ and $N_b = 1$). Comparing the results for particles and filaments, we see that the elastic links reduce the level of enhancement, but only up to moderate values of St . At large St , the results for chains asymptote to that for free particles.

Let us first consider the case of small to moderate St , for which the enhancement settling for particles is due to a preferential sampling of the downward flowing regions of the flow (i.e., on average the z component of the fluid velocity sampled by the particles $\langle \bar{u}_z \rangle < 0$ and not zero as it would be for tracers) [7]. When these same

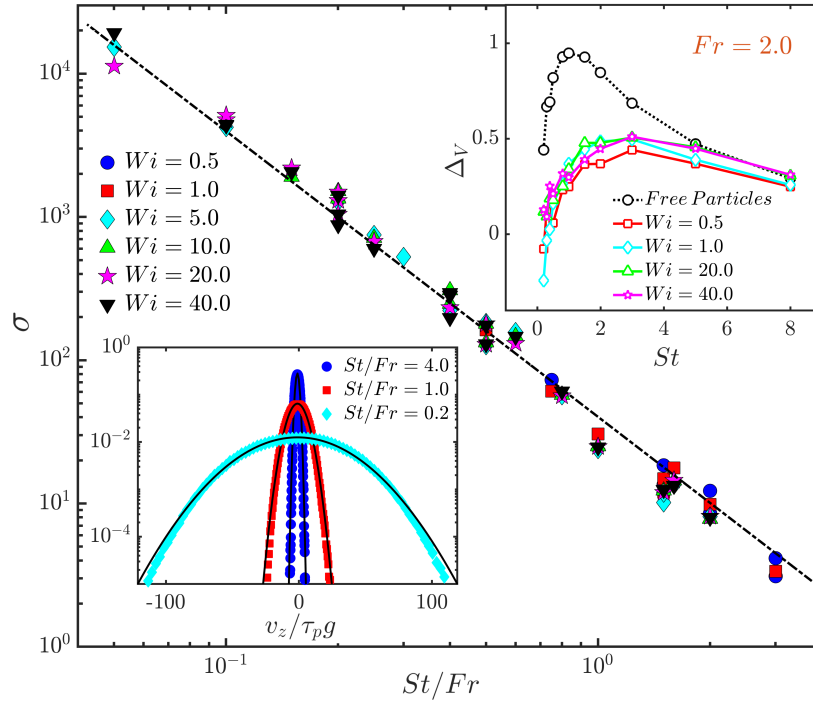


FIGURE 4.7: Loglog plot of the normalised variance σ as a function of St/Fr ; the different symbols correspond to different values of Wi (see legend) with the thick, black dashed line showing $(St/Fr)^{-2}$. (Inset): Representative plots of the pdfs (from which σ is extracted) of the settling speed v_z rescaled by the corresponding $\tau_p g$ for $Wi = 40$ and different values of St/Fr ; the black lines are Gaussian fits.

particles are linked together to form long chains they can no longer remain inside these regions of the flow. The chains in our work have inertial-scale lengths that increase with Wi as the chains are stretched out by the flow, as depicted in Fig. 4.6(b) which shows the probability distribution function of the end-to-end extension. At $Wi = 0.5$ the chains are mostly at the equilibrium extension, while at $Wi = 40$ they are broadly distributed with several near the maximum length. Despite this variation in extension, the value of Δ_V barely changes with Wi . This tells us that even the equilibrium size of approximately 15η is too large for the chains to preferentially sample the down-welling zones of the flow. Further increase in the extension with Wi , thus, has no additional effect on the mean settling velocity.

Turning to the case of large St , we note that both particles and chains decorrelate from the underlying flow when $St \gg 1$. So, preferential sampling is no longer important, and the particles or chains experience the flow as a short-correlated noise [7]. Moreover, at large St , the effect of elasticity weakens relative to that of inertia, so that the chains begin to settle, on average, like a collections of free beads. Thus, we see in Fig. 4.6(a), that Δ_V for the chains asymptotes to the result for free particles as St increases, with the values for larger Wi chains (weaker elastic forces) being closer to the free particle limit.

Next, let us examine how the settling velocity fluctuates about its mean value. The probability distribution function (pdf) of v_z , illustrated in the inset of Fig. 4.7, shows that the turbulent flow can produce strong temporal fluctuations—much greater than Δ_V —which become increasingly large and slightly non-Gaussian (the black lines are Gaussian fits) as St/Fr increases (the relevance of this ratio becomes clear below). The magnitude of these fluctuations is best quantified through the normalised variance $\sigma \equiv \frac{\langle v_z^2 \rangle}{\langle v_z \rangle^2} - 1$ of the distribution. To obtain a theoretical estimate for this variance, we use Eq. (4.2) to calculate the second moment of the settling velocity $\langle v_z^2 \rangle$. Noting that $\sum_{j=1}^{N_b} \sum_{k=1}^{N_b} \langle \xi_{j,z}(t) \xi_{k,z}(t') \rangle = C \delta_{j,k} \delta(t - t')$, where the subscript z denotes the z -components of the noise and C is a constant (which absorbs the N_b factor) with the dimension of inverse time, we obtain $\langle v_z^2 \rangle = \langle \bar{u}_z^2 \rangle + \tau_p^2 g^2 + \tau_p^2 \langle a_z^2 \rangle + CA^2$, which on using $\Delta_V < 1$ leads to the non-dimensional, normalised variance (see Appendix A for a detailed calculation)

$$\sigma \approx \left[\frac{\langle \bar{u}_z^2 \rangle + CA^2}{(a_\eta \tau_\eta)^2} + St^2 \frac{\langle a_z^2 \rangle}{a_\eta^2} \right] \left(\frac{St}{Fr} \right)^{-2}. \quad (4.14)$$

This result is further simplified by the observation, from our simulations, that $\langle \bar{u}_z^2 \rangle \approx (2/3)E$, where E is the mean kinetic energy of the flow. This leads to $\frac{\langle \bar{u}_z^2 \rangle}{(a_\eta \tau_\eta)^2} \sim \sqrt{Re}$, where Re is the large scale Reynolds number. Furthermore, we anticipate that, for finite Fr , $St^2 \frac{\langle a_z^2 \rangle}{a_\eta^2} \ll \sqrt{Re}$ for all St , because for $St \ll 1$, $\langle a_z^2 \rangle \sim a_\eta^2$ (chains follow the flow), while for $St \gg 1$, $\langle a_z^2 \rangle \ll a_\eta^2$ (chains fall with their terminal velocity), and in both cases this term becomes negligibly small. Indeed, we have found from our numerical data that the term $St^2 \frac{\langle a_z^2 \rangle}{a_\eta^2}$ is at least one order of magnitude smaller than $\frac{\langle \bar{u}_z^2 \rangle}{(a_\eta \tau_\eta)^2}$, for all Wi and the ranges of St and Fr that we consider. Finally, the additive contribution of the noise, $CA^2 \propto 1/Wi$, may also be neglected as it is small compared to the variance induced by the turbulent flow. Moreover, as mentioned earlier, the noise has no physical significance other than serving as a means to maintain the equilibrium length r_0 in a still fluid.

It follows, therefore, that to leading order $\sigma \sim (St/Fr)^{-2}$; the variance only depends on a single *settling factor* St/Fr , which is the ratio of the still-fluid terminal settling velocity $\tau_p g$ to the Kolmogorov-scale velocity of the turbulent flow $u_\eta = a_\eta \tau_\eta$.

Motivated by this scaling result, we plot the value of σ obtained from our simulations, carried out by varying Wi , St and Fr *independently* over a range of values, against St/Fr in Fig. 4.7. We see that the leading order behaviour of the variance matches the scaling prediction $\sigma \sim (St/Fr)^{-2}$ (dotted line) to a good approximation (see Fig. 4.7), over a wide range of Wi . Clearly, the extent of elasticity and therefore the stretching of the filament does not appreciably impact the settling velocity statistics.

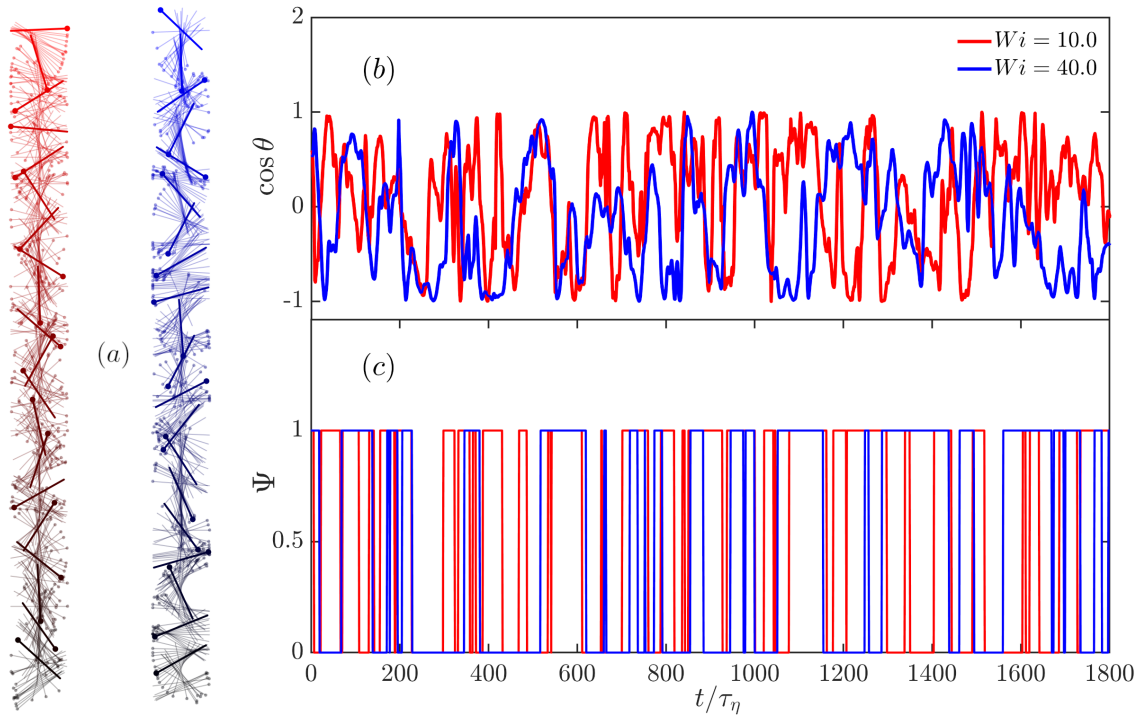


FIGURE 4.8: (a) Representative time-trace of snapshots of the end-to-end vectors \mathbf{R} of two filaments with $Wi = 10$ (red) and 40 (blue) at different times (increasing downwards) as they sediment ($St = 2$, $Fr = 0.5$); the vectors are projected on a two-dimensional plane to illustrate the change in orientation θ with respect to the direction of gravity $-\hat{\mathbf{z}}$. The filaments have been shown in intervals of $3.5\tau_\eta$ and the ones in bolder colors at $68\tau_\eta$. Plots of (b) $\cos \theta$ and (c) Ψ (see text) of the same filaments as a function of non-dimensional (with τ_η) time: $\Psi = 1(0)$ corresponds to an “up” (“down”) state of our filaments.

4.6 Tumbling: A Poisson Process

So far, we have only considered the settling of the filament as a whole. However, unlike for instance spherical particles, these filaments have additional internal degrees of freedom which raise new questions, of which perhaps the most interesting is to understand how the filaments tumble as they descend through the turbulent flow. It is useful to recall that the tumbling of individual polymers—small elastic chains unaffected by inertia or gravity—has been studied in the context of simple shear flows [60, 61].

To study tumbling quantitatively, we consider the dynamics of the end-to-end vector $\mathbf{R} \equiv \sum_{j=1}^{N_b-1} \mathbf{r}_j$. In Fig. 4.8(a), we show typical time traces of the end-to-end vector projected on a two-dimensional plane, for two sedimenting filaments with different Wi (and $St = 2$, $Fr = 0.5$). Clearly the filaments undergo complicated *rotational* dynamics accompanied by tumbling events. This behaviour is quantified through the cosine of the angle made by \mathbf{R} with the z -axis, via $\mathbf{R} \cdot \hat{\mathbf{z}} = R \cos \theta$, where $R = |\mathbf{R}|$. In Fig. 4.8(b), we show plots of the time-series of $\cos \theta$ for the two filaments shown in panel (a). This time series illustrates the seemingly continuous changes in the orientation of

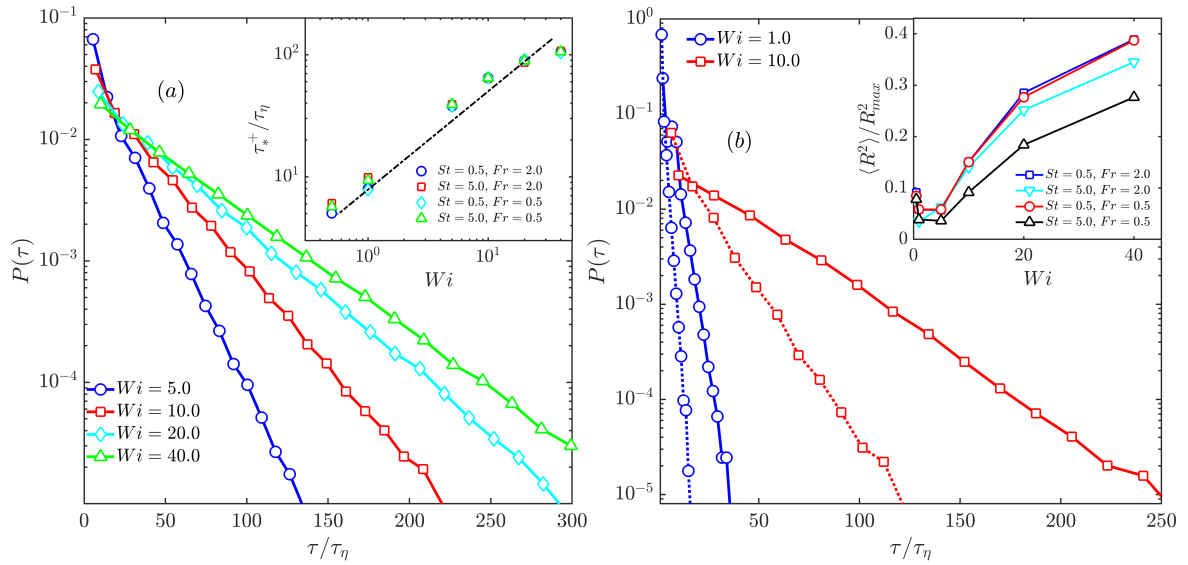


FIGURE 4.9: (a) Probability distribution functions $P^+(\tau)$ of the residence time in the up ($\Psi = 1$) state for filaments with $St = 2.0$, $Fr = 0.5$ and different values of Wi . (Inset) Log-log plot of the characteristic time-scale τ_*^+ versus Wi for different values of St and Fr ; the thick black line indicates a scaling of $Wi^{4/5}$. (b) Conditioned probability distribution functions of time spent in the up ($\Psi = 1$) state, for filaments with relatively small ($\langle R \rangle_+ < \ell_1$; dashed lines) and large ($\langle R \rangle_+ > \ell_2$; solid lines) time-averaged lengths. The values of the thresholds for the two cases are $\ell_1 = 9\eta$, $\ell_2 = 20\eta$ for $Wi = 1$, and $\ell_1 = 40\eta$, $\ell_2 = 65\eta$ for $Wi = 10$. In both cases, $St = Fr = 1.0$. (Inset) Plot of normalised $\langle R^2 \rangle$, versus Wi for different values of St and Fr .

the settling filaments with a suggestion that filaments tumble more frequently as the Wi decreases. Such observations naturally lead us to (i) suitably define the *state* Ψ of the filament as being either “up” or “down” and (ii) to characterise the transitions between these two states.

We define the up and down states as $\Psi = 1$ for $\cos \theta \geq 0$ and $\Psi = 0$ for $\cos \theta < 0$, respectively. The apparently random switching between the two states, clearly illustrated in Fig 4.8(c), is quantified by calculating the pdfs $P^+(\tau)$ ($P^-(\tau)$) of the residence time τ over which the filaments remain up (down). These distributions yield the probability of a filament in an up (or down) state to continue to remain in the same state for a duration of τ . We recall that questions of this sort—the so-called persistence problems—have a special importance in areas of non-equilibrium statistical physics [62–65] and, more recently, have been adapted to understand the geometrical aspects of turbulent flows [66–68]. Such persistence problems in the context of fluid flows, and consequently their direction reversals as a result of thermal convection have also been investigated [69–71].

In Fig. 4.9(a), we show semi-log plots of $P^+(\tau)$ for filaments with $St = 2.0$, $Fr = 0.5$, but different degrees of elasticity. We have confirmed, by varying the range of angles

θ which define an up or down state, that the precise definition of these states does not affect the results qualitatively; furthermore, $P^+(\tau) = P^-(\tau)$ because the problem is symmetric to the transformation $r_j \rightarrow -r_j$ which reverses the end-to-end vector. These distributions clearly show an exponential fall-off: $P^+(\tau) \sim \exp(-\tau/\tau_*^+)$, which indicates that tumbling manifests as a Poisson process (which also characterizes, for example, the escape of particles from vortices [68] and the turbulent entrainment of coarse grains [72]). The characteristic time scale τ_*^+ ($= \tau_*^-$) has a weak dependence on St and Fr , but increases systematically with Wi (see Ref. [61] for single polymers in a shear flow), as seen in the inset of Fig. 4.9(a).

Why do more extensible filaments require longer times to tumble? The answer lies in the connection between the dynamic length of a filament and its tumbling. We expect a highly stretched, long filament that spans multiple flow eddies to have a lower probability of experiencing the sequence of coordinated drag forces required to cause a transition in its orientation. To test this hypothesis, we calculate the average end-to-end length of a filament over each interval of time spent in the up state $\langle R \rangle_+$. When a transition occurs, we record $\langle R \rangle_+$ along with the persistence time τ , which then allows us to obtain the pdf of τ conditioned on the time-averaged length of the filament. Fig 4.9(b) shows these conditioned pdfs for relatively short (dashed line) and long (solid line) filaments, defined as those with $\langle R \rangle_+ < \ell_1$ and $\langle R \rangle_+ > \ell_2$ ($\ell_1 < \ell_2$), where the values of the thresholds depend on Wi and are given in the figure caption (small variations in these values do not affect our conclusions). Two values of Wi are considered, and in both cases we see that when filaments are more stretched they do indeed take a longer time to tumble. Now, as Wi increases, the filaments become more extensible and the distribution of R broadens. This is demonstrated by the inset of Fig. 4.9(b), which presents the variation of $\langle R^2 \rangle$ with Wi . As a result, a larger Wi filament is much more likely to be in a highly stretched state, which explains its tendency to persist in a given orientation for a longer time before tumbling. The consequent increase of τ_*^+ with Wi , shown in the inset of Fig. 4.9(a), appears to follow a power-law (the fitted dashed-line has an exponent of 4/5) for small to moderate Wi , but then begins to level-off at large Wi , as the filament approaches its maximum length.

Interestingly, the tumbling time τ_*^+ is seen to be almost independent of Fr . In fact, we have checked, by running additional simulations, that neutrally buoyant chains ($Fr = \infty$) exhibit the same power law dependence of τ_*^+ on Wi as that seen in the inset of Fig. 4.9(a). This result is closely related to a recent experimental observation made by [37] for rigid, inextensible, neutrally buoyant fibres in isotropic turbulence. They find that the variance of the tumbling rate decreases with the (fixed) length L of

the fibre as a power law, $L^{-4/3}$, which can be derived by assuming that the tumbling rate is determined by the inverse of the turnover time of an inertial range eddy of scale L [37]. In our case of extensible fibres, the situation is more complex, as we have a dynamically varying filament length, with a broad distribution that widens with Wi [cf. Fig. 4.6(b) and the inset of Fig. 4.9(b)].

4.7 Stiff Filaments

How valid are our results when the filaments are *stiff*? Chains with bending stiffness have an energy cost associated with bending, which manifests as an additional force on the beads of the chain. The bending energy is defined using the angles (via the dot product) between successive link vectors, such that a relatively inflexible filament has a larger bending cost and so is more likely to remain in a rod-like configuration. If S is the measure of bending stiffness, then the resulting force acting on the j -th bead is given as [73] :

$$\mathbf{f}_j^B = \frac{S}{r_0} \left[\frac{\alpha_{j-2}}{r_{j-1}} \hat{\mathbf{r}}_{j-2} - \left(\frac{\alpha_{j-2}}{r_{j-1}} \hat{\mathbf{r}}_{j-2} \cdot \hat{\mathbf{r}}_{j-1} + \frac{\alpha_{j-1}}{r_j} + \frac{\alpha_{j-1}}{r_{j-1}} \hat{\mathbf{r}}_{j-1} \cdot \hat{\mathbf{r}}_j \right) \hat{\mathbf{r}}_{j-1} \right. \quad (4.15)$$

$$\left. + \left(\frac{\alpha_{j-1}}{r_j} \hat{\mathbf{r}}_{j-1} \cdot \hat{\mathbf{r}}_j + \frac{\alpha_{j-1}}{r_{j-1}} + \frac{\alpha_j}{r_j} \hat{\mathbf{r}}_j \cdot \hat{\mathbf{r}}_{j+1} \right) \hat{\mathbf{r}}_j - \frac{\alpha_j}{r_j} \hat{\mathbf{r}}_{j+1} \right] \quad (4.16)$$

with

$$\alpha_j = \begin{cases} 0 & \text{if } j \leq 0 \text{ or } j = N_b \\ 1 & \text{otherwise.} \end{cases} \quad (4.17)$$

The characteristic-time associated with the bending force is $\tau_B = \zeta r_0^3 / S$ where ζ is the Stokes drag on the beads and r_0 is the equilibrium length of the elastic links. Similar to the Weissenberg number, we define a dimensionless measure of bending stiffness as the bending Weissenberg number $Wi_B = \tau_B / \tau_\eta$. The filaments become inflexible for small Wi_B , while the limit of fully flexible filaments is attained for large Wi_B .

The equation of motion for the links [Eq. (1.55)] now includes the additional term $\frac{1}{\zeta} (\mathbf{f}_{j+1}^B - \mathbf{f}_j^B)$ on the right hand side to account for bending stiffness. However, because these bending forces are internal to the filaments, they do not affect the motion of the center-of-mass explicitly and so its equation of motion remains identical to that of fully flexible filaments [Eq. (1.56)].

We now simulate these filaments in a turbulent flow using the techniques described in Sec. B; however these additional simulations were performed on a smaller $N^3 = 256^3$ grid and consequently with a smaller Taylor-scale based Reynolds number $Re_\lambda \approx 111$.

Furthermore we use a wide range of the bending Weissenberg number $1.6 \times 10^{-3} < Wi_B < 1.6 \times 10^3$, along with $0.16 < St < 12.72$, $0.8 < Wi < 64$ and $0.5 < Fr < 2$.

Figure 4.10(a) shows a log-log plot of the normalised variance σ versus the settling parameter St/Fr for a wide range of Wi_B . Clearly, the addition of the bending stiffness does not alter the scaling form $\sigma \sim (St/Fr)^{-2}$ (indicated by the thick black line), obtained earlier for fully-flexible filaments. This is not surprising, because the theoretical derivation of the scaling for σ , to leading order, is insensitive to Wi_B . Furthermore, in the inset of Fig. 4.10(a) we show a plot of the settling velocity Δ_V , for different values of Wi_B , which shows the same non-monotonic behaviour with St as seen in Fig. 4.6 for fully flexible chains. However, as Wi_B is decreased, the degree of enhancement of the settling velocity reduces from the value for fully-flexible chains. So, stiffness acts along with elasticity to constrain the motion of the filament and prevent it from preferentially sampling downward moving regions of the flow.

We next consider the effecting of bending stiffness on tumbling. As with the case of fully-flexible filaments, we quantify this through the probability distribution $P^+(\tau)$ ($P^-(\tau)$) of the residence times τ for which our stiff filaments persist in the up (down) orientation. In Fig. 4.10(b), we show representative plots of $P^+(\tau)$ for different values of Wi_B , but for $Fr = 1.0$, $St = 1.26$ and $Wi = 16.0$; in the inset we show how, for a given $Wi_B = 1.6$, $Fr = 1.0$ and $St = 1.26$, these exponential distributions vary with changing Wi . The characteristic tumbling time is seen to be larger for smaller Wi_B , implying that stiffer chains take longer to tumble.

Overall, the results presented here for stiff chains confirm that the central conclusions drawn from studying fully-flexible filaments are unchanged even with the inclusion of bending stiffness. We note that this is consistent with a recent study [34] which showed that the qualitative aspects of the preferential sampling of three dimensional turbulent flows by filaments are unchanged when bending stiffness is included to make such chains more inflexible.

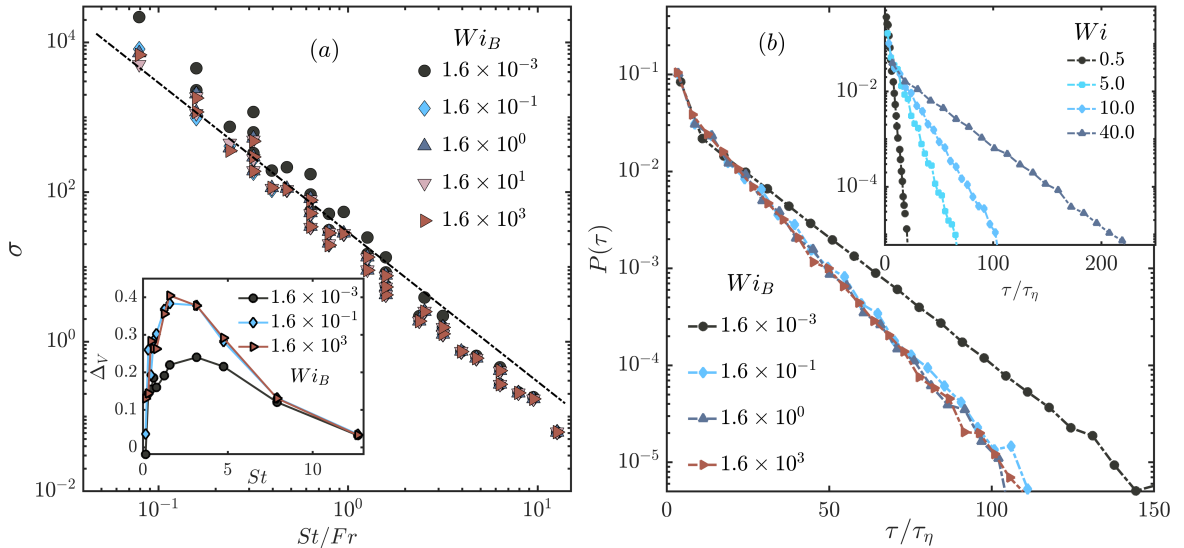


FIGURE 4.10: (a) Log-log plot of the normalized variance σ versus the settling parameter St/Fr for different values of Wi_B ; the thick black line is a guide to the eye indicating a scaling form of $(St/Fr)^{-2}$. In the inset, we show a representative plot of Δ_V vs St for $Fr = 2.0$ and $Wi = 16.0$ and different values of Wi_B . (b) Semi-log plots of $P^+(\tau)$ for filaments with $Fr = 1.0$, $St = 1.26$ and $Wi = 16.0$ and different values of Wi_B ; in the inset we plot the same distributions for stiff ($Wi_B = 1.6$) filaments with the same Stokes and Froude numbers but varying Wi

4.8 Conclusions

To summarise, we have analyzed two complementary aspects of the dynamics of long and heavy, elastic filaments in a turbulent flow: the fluctuating settling velocity, and the transitions in vertical orientation associated with tumbling. For a given turbulent flow, we have found, rather surprisingly, that to leading order the weight of the filament only impacts its settling velocity [via the St dependence of Δ_V and the $(St/Fr)^{-2}$ scaling of σ] while the elasticity and consequent stretching of the filament only affects its tumbling. Furthermore, we perform additional simulations for chains with a bending energy and have found that our central results remain qualitatively unchanged, although stiff filaments settle and tumble slower than fully-flexible ones.

The Poisson distribution of tumbling times brings to mind the Poissonian *back-and-forth* motion of filamentary, motile microorganisms. Such a tumbling-like motion is thought to be an efficient strategy for foraging [26, 27], but given that the Reynolds number of oceanic turbulence [28] is similar to that in our study, it is tempting to consider in future works whether the tumbling of marine filamentary microorganisms are a consequence of active strategy or physical inevitability. Admittedly, these microorganisms are motile and much smaller than our filaments; nevertheless, our results should motivate work on longer marine organisms and their journey as they settle in the ocean.

References

- [1] M. Maxey, *The gravitational settling of aerosol particles in homogeneous turbulence and random flow fields*, *J. Fluid Mech.* **174** (1987) 441–465.
- [2] L.-P. Wang and M. Maxey, *Settling velocity and concentration distribution of heavy particles in homogeneous isotropic turbulence*, *J. Fluid Mech.* **256** (1993) 27–68.
- [3] A. Aliseda, A. Cartellier, F. Hainaux and J. C. Lasheras, *Effect of preferential concentration on the settling velocity of heavy particles in homogeneous isotropic turbulence*, *J. Fluid Mech.* **468** (2002) 77–105.
- [4] S. Ghosh, J. Dávila, J. Hunt, A. Srdic, H. Fernando and P. Jonas, *How turbulence enhances coalescence of settling particles with applications to rain in clouds*, *Proceedings of the Royal Society A: Mathematical, Physical and Engineering Sciences* **461** (2005) 3059–3088.
- [5] O. Ayala, B. Rosa, L.-P. Wang and W. Grabowski, *Effects of turbulence on the geometric collision rate of sedimenting droplets. part 1. results from direct numerical simulation*, *New J. Phys.* **10** (2008) 075015.
- [6] J. Davila and J. Hunt, *Settling of small particles near vortices and in turbulence*, *J. Fluid Mech.* **440** (2001) 117–145.
- [7] J. Bec, H. Homann and S. S. Ray, *Gravity-driven enhancement of heavy particle clustering in turbulent flow*, *Phys. Rev. Lett.* **112** (2014) 184501.
- [8] K. Gustavsson, J. Jucha, A. Naso, E. Lévêque, A. Pumir and B. Mehlig, *Statistical model for the orientation of nonspherical particles settling in turbulence*, *Phys. Rev. Lett.* **119** (2017) 254501.
- [9] P. Anand, S. S. Ray and G. Subramanian, *Orientation dynamics of sedimenting anisotropic particles in turbulence*, *Phys. Rev. Lett.* **125** (2020) 034501.
- [10] P. A. Vaillancourt and M. K. Yau, *Review of Particle-Turbulence Interactions and Consequences for Cloud Physics*, *Bulletin of the American Meteorological Society* **81** (2000) 285–298.

- [11] G. Falkovich, A. Fouxon and M. G. Stepanov, *Acceleration of rain initiation by cloud turbulence*, *Nature* **419** (2002) 151–154.
- [12] R. A. Shaw, *Particle-turbulence interactions in atmospheric clouds*, *Annual Review of Fluid Mechanics* **35** (2003) 183–227.
- [13] E. Bodenschatz, S. P. Malinowski, R. A. Shaw and F. Stratmann, *Can we understand clouds without turbulence?*, *Science* **327** (2010) 970–971.
- [14] R. Monchaux, M. Bourgoin and A. Cartellier, *Analyzing preferential concentration and clustering of inertial particles in turbulence*, *Int. J. Multiph. Flow* **40** (2012) 1 – 18.
- [15] A. J. Baran and P. N. Francis, *On the radiative properties of cirrus cloud at solar and thermal wavelengths: A test of model consistency using high-resolution airborne radiance measurements*, *Quarterly Journal of the Royal Meteorological Society* **130** (2004) 763–778.
- [16] M. W. Gallagher, P. J. Connolly, J. Whiteway, D. Figueras-Nieto, M. Flynn, T. W. Choullarton et al., *An overview of the microphysical structure of cirrus clouds observed during emerald-1*, *Quarterly Journal of the Royal Meteorological Society* **131** (2005) 1143–1169.
- [17] A. K. Pandit, H. S. Gadhavi, M. Venkat Ratnam, K. Raghunath, S. V. B. Rao and A. Jayaraman, *Long-term trend analysis and climatology of tropical cirrus clouds using 16 years of lidar data set over southern india*, *Atmospheric Chemistry and Physics* **15** (2015) 13833–13848.
- [18] G. A. Voth and A. Soldati, *Anisotropic particles in turbulence*, *Annual Review of Fluid Mechanics* **49** (2017) 249–276.
- [19] S. Alben, M. Shelley and J. Zhang, *Drag reduction through self-similar bending of a flexible body*, *Nature* **420** (2002) 479–481.
- [20] B. Marchetti, V. Raspa, A. Lindner, O. du Roure, L. Bergougnoux, E. Guazzelli et al., *Deformation of a flexible fiber settling in a quiescent viscous fluid*, *Phys. Rev. Fluids* **3** (2018) 104102.
- [21] A. A. Banaei, M. Rahmani, D. M. Martinez and L. Brandt, *Inertial settling of flexible fiber suspensions*, *Phys. Rev. Fluids* **5** (2020) 024301.
- [22] F. Lundell, L. D. Söderberg and P. H. Alfredsson, *Fluid mechanics of papermaking*, *Annual Review of Fluid Mechanics* **43** (2011) 195–217.

- [23] D. K. A. Barnes, F. Galgani, R. C. Thompson and M. Barlaz, *Accumulation and fragmentation of plastic debris in global environments*, *Philosophical Transactions of the Royal Society B: Biological Sciences* **364** (2009) 1985–1998.
- [24] M. Stelfox, J. Hudgins and M. Sweet, *A review of ghost gear entanglement amongst marine mammals, reptiles and elasmobranchs*, *Marine Pollution Bulletin* **111** (2016) 6–17.
- [25] L. Lebreton, B. Slat, F. Ferrari, B. Sainte-Rose, J. Aitken, R. Marthouse et al., *Evidence that the great pacific garbage patch is rapidly accumulating plastic*, *Sci. Rep.* **8** (2018) 4666.
- [26] R. H. Luchsinger, B. Bergersen and J. G. Mitchell, *Bacterial swimming strategies and turbulence*, *Biophysical Journal* **77** (1999) 2377–2386.
- [27] R. Stocker, *Reverse and flick: Hybrid locomotion in bacteria*, *Proceedings of the National Academy of Sciences* **108** (2011) 2635–2636.
- [28] J. Jimenez, *Oceanic turbulence at millimeter scales*, *Scientia Marina* **61** (1997) 47–56.
- [29] R. B. Bird, C. F. Curtiss, R. C. Armstrong and O. Hassager, *Dynamics of Polymeric Liquids*. John Wiley and Sons, New York, 1977, [10.1002/pol.1978.130160210](https://doi.org/10.1002/pol.1978.130160210).
- [30] C. Brouzet, G. Verhille and P. Le Gal, *Flexible fiber in a turbulent flow: A macroscopic polymer*, *Phys. Rev. Lett.* **112** (2014) 074501.
- [31] G. Verhille and A. Bartoli, *3d conformation of a flexible fiber in a turbulent flow*, *Exp. in Fluids* **57** (2016) 117.
- [32] J. R. Picardo, D. Vincenzi, N. Pal and S. S. Ray, *Preferential sampling of elastic chains in turbulent flows*, *Phys. Rev. Lett.* **121** (2018) 244501.
- [33] R. Singh, M. Gupta, J. R. Picardo, D. Vincenzi and S. S. Ray, *Elastoinertial chains in a two-dimensional turbulent flow*, *Phys. Rev. E* **101** (2020) 053105.
- [34] J. R. Picardo, R. Singh, S. S. Ray and D. Vincenzi, *Dynamics of a long chain in turbulent flows: impact of vortices*, *Phil. Trans. R. Soc. A.* **378** (2020) 20190405.
- [35] M. E. Rosti, A. A. Banaei, L. Brandt and A. Mazzino, *Flexible fiber reveals the two-point statistical properties of turbulence*, *Phys. Rev. Lett.* **121** (2018) 044501.
- [36] S. Allende, C. Henry and J. Bec, *Stretching and buckling of small elastic fibers in turbulence*, *Phys. Rev. Lett.* **121** (2018) 154501.

-
- [37] T. B. Oehmke, A. D. Bordoloi, E. Variano and G. Verhille, *Spinning and tumbling of long fibers in isotropic turbulence*, *Phys. Rev. Fluids* **6** (2021) 044610.
- [38] S. Jin and L. R. Collins, *Dynamics of dissolved polymer chains in isotropic turbulence*, *New J. Phys.* **9** (2007) 360.
- [39] R. M. Jendrejack, J. J. de Pablo and M. D. Graham, *Stochastic simulations of dna in flow: Dynamics and the effects of hydrodynamic interactions*, *The Journal of Chemical Physics* **116** (2002) 7752–7759.
- [40] C. M. Schroeder, E. S. G. Shaqfeh and S. Chu, *Effect of hydrodynamic interactions on dna dynamics in extensional flow: simulation and single molecule experiment*, *Macromolecules* **37** (2004) 9242–9256.
- [41] M. Cosentino Lagomarsino, I. Pagonabarraga and C. P. Lowe, *Hydrodynamic induced deformation and orientation of a microscopic elastic filament*, *Phys. Rev. Lett.* **94** (2005) 148104.
- [42] X. Schlagberger and R. R. Netz, *Orientation of elastic rods in homogeneous stokes flow*, *Europhys. Lett.* **70** (2005) 129–135.
- [43] I. Llopis, I. Pagonabarraga, M. Cosentino Lagomarsino and C. P. Lowe, *Sedimentation of pairs of hydrodynamically interacting semiflexible filaments*, *Phys. Rev. E* **76** (2007) 061901.
- [44] B. Delmotte, E. Climent and F. Plouraboué, *A general formulation of bead models applied to flexible fibers and active filaments at low reynolds number*, *Journal of Computational Physics* **286** (2015) 14 – 37.
- [45] R. G. Cox, *The motion of long slender bodies in a viscous fluid part 1. general theory*, *J. Fluid Mech.* **44** (1970) 791–810.
- [46] X. Xu and A. Nadim, *Deformation and orientation of an elastic slender body sedimenting in a viscous liquid*, *Physics of Fluids* **6** (1994) 2889–2893.
- [47] M. James and S. S. Ray, *Enhanced droplet collision rates and impact velocities in turbulent flows: The effect of poly-dispersity and transient phases*, *Sci. Rep.* **7** (2017) 12231.
- [48] Y. Dubief and F. Delcayre, *On coherent-vortex identification in turbulence*, *Journal of Turbulence* **1** (2000) N11.

-
- [49] S. I. Abarzhi and K. R. Sreenivasan, *Turbulent mixing and beyond*, *Philosophical Transactions of the Royal Society A: Mathematical, Physical and Engineering Sciences* **368** (2010) 1539–1546.
- [50] K. R. Sreenivasan and J. Schumacher, *Lagrangian views on turbulent mixing of passive scalars*, *Philosophical Transactions of the Royal Society A: Mathematical, Physical and Engineering Sciences* **368** (2010) 1561–1577.
- [51] K. R. Sreenivasan, *Turbulent mixing: A perspective*, *Proceedings of the National Academy of Sciences* **116** (2019) 18175–18183.
- [52] P. K. Yeung and J. Xu, *Effects of rotation on turbulent mixing: Nonpremixed passive scalars*, *Physics of Fluids* **16** (2004) 93–103.
- [53] M. Holzer and E. D. Siggia, *Turbulent mixing of a passive scalar*, *Physics of Fluids* **6** (1994) 1820–1837.
- [54] J. M. Ottino, *Mixing, chaotic advection, and turbulence*, *Annual Review of Fluid Mechanics* **22** (1990) 207–254.
- [55] A. M. Lyapunov, *The general problem of the stability of motion*, *International Journal of Control* **55** (1992) 531–534.
- [56] L. Y. Adrianova, *Introduction to linear systems of differential equations*. American Mathematical Soc., 1995.
- [57] G. Lapeyre, *Characterization of finite-time lyapunov exponents and vectors in two-dimensional turbulence*, *Chaos: An Interdisciplinary Journal of Nonlinear Science* **12** (2002) 688–698.
- [58] P. L. Johnson and C. Meneveau, *Large-deviation joint statistics of the finite-time lyapunov spectrum in isotropic turbulence*, *Physics of Fluids* **27** (2015) 085110.
- [59] J. Bec, L. Biferale, G. Boffetta, M. Cencini, S. Musacchio and F. Toschi, *Lyapunov exponents of heavy particles in turbulence*, *Physics of Fluids* **18** (2006) 091702.
- [60] S. Gerashchenko and V. Steinberg, *Statistics of tumbling of a single polymer molecule in shear flow*, *Phys. Rev. Lett.* **96** (2006) 038304.
- [61] A. Celani, A. Puliafito and K. Turitsyn, *Polymers in linear shear flow: A numerical study*, *Europhys. Lett.* **70** (2005) 464–470.
- [62] S. N. Majumdar, C. Sire, A. J. Bray and S. J. Cornell, *Nontrivial exponent for simple diffusion*, *Phys. Rev. Lett.* **77** (1996) 2867–2870.

- [63] B. Derrida, V. Hakim and R. Zeitak, *Persistent spins in the linear diffusion approximation of phase ordering and zeros of stationary gaussian processes*, *Phys. Rev. Lett.* **77** (1996) 2871–2874.
- [64] S. N. Majumdar, *Persistence in nonequilibrium systems*, *Current Science* **77** (1999) 370–375.
- [65] A. J. Bray, S. N. Majumdar and G. Schehr, *Persistence and first-passage properties in nonequilibrium systems*, *Advances in Physics* **62** (2013) 225–361.
- [66] P. Perlekar, S. S. Ray, D. Mitra and R. Pandit, *Persistence problem in two-dimensional fluid turbulence*, *Phys. Rev. Lett.* **106** (2011) 054501.
- [67] B. Kadoch, D. del Castillo-Negrete, W. J. T. Bos and K. Schneider, *Lagrangian statistics and flow topology in forced two-dimensional turbulence*, *Phys. Rev. E* **83** (2011) 036314.
- [68] A. Bhatnagar, A. Gupta, D. Mitra, R. Pandit and P. Perlekar, *How long do particles spend in vortical regions in turbulent flows?*, *Phys. Rev. E* **94** (2016) 053119.
- [69] K. R. Sreenivasan, A. Bershadskii and J. J. Niemela, *Mean wind and its reversal in thermal convection*, *Phys. Rev. E* **65** (2002) 056306.
- [70] M. Chandra and M. K. Verma, *Dynamics and symmetries of flow reversals in turbulent convection*, *Phys. Rev. E* **83** (2011) 067303.
- [71] P. K. Mishra, A. K. De, M. K. Verma and V. Eswaran, *Dynamics of reorientations and reversals of large-scale flow in rayleigh–bénard convection*, *Journal of Fluid Mechanics* **668** (2011) 480–499.
- [72] M. Valyrakis, P. Diplas and C. L. Dancey, *Entrainment of coarse grains in turbulent flows: An extreme value theory approach*, *Water Resources Research* **47** (2011) .
- [73] E. Gauger and H. Stark, *Numerical study of a microscopic artificial swimmer*, *Phys. Rev. E* **74** (2006) 021907.

Chapter 5

Lagrangian Manifestation of Anomalies in Active Turbulence

We show that Lagrangian measurements in active turbulence bear imprints of turbulent and anomalous streaky hydrodynamics leading to a self-selection of persistent trajectories—Lévy walks—over diffusive ones. This emergent dynamical heterogeneity results in a super-diffusive first passage distribution which could lead to biologically advantageous motility. We then go beyond single-particle statistics to show that for the pair-dispersion problem as well, active flows are at odds with inertial turbulence. Our study, we believe, will readily inform experiments in establishing the extent of universality of anomalous behaviour across a variety of active flows.

This chapter closely follows the work [Singh *et al.*, arXiv:2112.00667 (2021); Phys. Rev. Fluids *in press*].

5.1 Introduction

Flowing active matter, such as dense suspensions of bacteria, has emerged as one of the most intriguing class of problems in complex, driven-dissipative systems which sits at the intersection of non-equilibrium statistical physics, biophysics, soft-matter and of course fluid dynamics [1–4]. What makes such low Reynolds number systems particularly fascinating is the emergence of rich and complex collective patterns at scales much larger than, but driven by, relatively simpler individual dynamics [1, 2, 5, 6] as well as its ubiquity across systems as diverse as bacterial colonies [7, 8], suspensions of microtubules and molecular motors [9–11], or schools of fish [12] and bird flocks [1, 13, 14]. In dense active systems, typically those involving microscopic entities, the interactions between individual agents lead to unorganized, often vortical, dynamics with self-similar distribution of energy across several length scales. This last

aspect, namely the *appearance* of the flow field and the power-laws which emerge in measurements of the kinetic energy across Fourier modes [4, 7, 15, 16], lead to such states being called *active turbulence* in analogy with similar traits of high Reynolds number inertial turbulence [4].

However, there are important distinctions between inertial and active turbulence. The most striking of these being that unlike high Reynolds number flows, experiments suggest non-universal signatures of Lévy walks and anomalous diffusion in measurements of mean-square-displacements (MSDs) in active suspensions [17–20]. These observations were substantiated in a recent theoretical work [21] which showed not only the robustness of the anomalous diffusion and its coincidence with the emergence of novel, *streaky* structures in the flow for optimal activity, but also why in earlier theoretical studies [22] such a scaling regime remained masked.

The fact that trajectories of tracers in such systems show Lévy statistics is consistent with other examples from the natural world where *active agents* Lévy walk or fly [23–27]. Nevertheless, this throws up interesting questions regarding the nature of trajectories and hence, fundamental issues of Lagrangian turbulence in such dense bacterial suspensions. In particular, a consequence of this could well be that while for low activities, trajectories are nearly always meandering (hence diffusive), at higher activities, there is a balance between those which follow Lévy statistics and those which do not. In fact, even for a given tracer it is conceivable that depending on the flow it experiences, its trajectory could either be persistent or random.

We address some of these issues relevant to dense (and dry) bacterial suspensions, by taking a continuum, numerical approach to the problem. The generalized hydrodynamic model (see, also, Refs. [7, 28] for a detailed description), which is essentially a modified version of the Navier-Stokes equation employing terms that lead to pattern formation (similar to Swift-Hohenberg theory [29]) and flocking behaviour (Toner-Tu theory [30, 31]), is used to simulate the evolution of the coarse-grained velocity field \mathbf{u} of bacterial suspensions, and is given as:

$$\partial_t \mathbf{u} + \lambda \mathbf{u} \cdot \nabla \mathbf{u} = -\nabla p - \Gamma_0 \nabla^2 \mathbf{u} - \Gamma_2 \nabla^4 \mathbf{u} - (\alpha + \beta |\mathbf{u}|^2) \mathbf{u} \quad (5.1)$$

where \mathbf{u} satisfies the incompressibility constraint $\nabla \cdot \mathbf{u} = 0$. The parameter $\lambda > 1 (< 1)$ corresponds to pusher (puller)-type bacteria while the higher order derivatives along with the non-linear self-advective term drive the formation of chaotic flow patterns when $\Gamma_0, \Gamma_2 > 0$. A key difference is that the usual diffusion term of the Navier-Stokes equation appears with the opposite sign, and acts towards inducing a turbulence instability in the bacterial system, while the additional bi-Laplacian term aids

dissipation. The last term is a Toner-Tu drive [30, 31], which is effectively a quartic Landau-potential for the velocity, with the activity α taking both positive (friction) and negative (active injection) values, while β is strictly positive for stability and causes most of the momentum dissipation. For driven active systems ($\alpha < 0$), this term leads to global polar ordering with a velocity $v_0 = \sqrt{|\alpha|/\beta}$.

5.2 Simulations

In our simulations, we solve Eq. (5.1) by using a de-aliased, pseudo-spectral algorithm on square, periodic domains of lengths $L \in \{20, 40, 80\}$ which are discretized by using $N^2 \in \{1024^2, 4096^2\}$ collocation points. The simulations are performed for 5×10^5 iterations with time-steps $\delta t = 0.001$ and, in some cases, $\delta t = 0.0002$ for higher temporal resolution (note that a simulation time of ~ 30 is ~ 1 minute of real time [7]). The other parameters of the model are taken to be consistent with earlier studies [21, 32–34], and these were carefully chosen to reproduce the physically observed flow patterns and Eulerian statistics [7]. Here, $\Gamma_0 = 0.045$, which corresponds to $-53 \mu\text{m}^2/\text{s}$, $\Gamma_2 = \Gamma_0^3$ and $\lambda = 3.5$ [7]. The swarming speed of *Bacillus subtilis*, which is linked to the activity, can vary over a wide range of $25 - 100 \mu\text{m}/\text{s}$, depending on the oxygen concentration of the system and the boundary conditions [7, 20, 35, 36]. These velocities in the experiment are associated with the typical velocities which arise in the hydrodynamic description: $v_\Gamma = \sqrt{|\Gamma_0|^3/\Gamma_2}$ or $v_0 = \sqrt{|\alpha|/\beta}$. An empirical comparison between simulations and experiments (see [7], Supporting Information) suggested that $\alpha = -1$ and $\beta = 0.5$ (simulation units) corresponded to $-0.5/\text{s}$ and $4 \times 10^{-4} \text{s}/\mu\text{m}^2$ (physical experimental units), respectively. These physical units correspond to a velocity scale $\sim 35 \mu\text{m}/\text{s}$, with the corresponding simulation velocity scale $v_0 = \sqrt{|\alpha|/\beta} = \sqrt{2}$. However, as was shown in a recent theoretical study [21], phenomena like anomalous diffusion and Lévy walks, that were recently observed in experiments [20], *only* become robust at sufficiently high activity levels in simulations (around $\alpha = -6$). Therefore, while keeping $\beta = 0.5$ fixed, we vary the activity over a wide range $-6 \leq \alpha \leq -1$. We note that the highest value of $\alpha = -6$ yields $v_0 \approx 2.4\sqrt{2}$ (simulation units) or $v_0 \approx 72 \mu\text{m}/\text{s}$ (choosing, for convenience, the average velocity in the range $25 \mu\text{m}/\text{s} - 35 \mu\text{m}/\text{s}$ reported by [7] as reference), which is well within the physically viable range of bacterial velocities [7, 36]. We caution the reader that this mapping of parameters should be seen as a rough guide, since the calibration of coefficients between theory and experiments is largely empirical. Lastly, the flow is seeded with 10^5 randomly distributed tracers which evolve as $d\mathbf{x}/dt = \mathbf{u}(\mathbf{x}(t))$, with $\mathbf{x}(t)$ being the tracer location at time t , after a spinup time of 2×10^4 iterations (when the flow reaches a statistically steady state). We use a fourth-order Runge-Kutta scheme,

along with a bilinear interpolation (see Appendix E) scheme to obtain the fluid velocity at the particle positions $\mathbf{u}(\mathbf{x}(t))$, to evolve the tracers with statistics being stored every 100 iterations.

In Fig. 5.1(a) we show representative trajectories from our simulations with increasing levels of activity. While for suspensions with low activity ($\alpha = -1$), the particle motion is predominantly diffusive with large, *knotted* regions of *random-walk*, the more active fields ($\alpha = -4$) give rise to trajectories which have a persistent motion showing characteristic signatures of Lévy walks; a precise definition of the activity parameter α is given below. However, these Lévy-like, persistent trajectories are only one part of the story. Careful measurements in these simulations indicate that even at higher activity ($\alpha = -6$) it is easy to find in an ensemble trajectories that are persistent (Fig. 5.1(b)) and those that remain predominantly diffusive (Fig. 5.1(c)). (We note that the trajectories were artificially moved to a common center for visualization; in simulations, their origins are distributed randomly at different points in the flow.)

5.3 Quantifying Trajectories

This leads us to critically examine the nature of trajectories in such highly active systems and establish connections between anomalies of the emergent coarse-grained velocity field and its effect on the resultant Lagrangian statistics. As a result we uncover a remarkable dynamical heterogeneity in trajectories, implicit in Fig. 5.1, and its critical role in assisting the swarm for efficient foraging through first-passage statistics. We also show, in a way which is easily amenable to experiments, that such persistent motion are facilitated by the novel, emergent structures in the bacterial field—*streaks*—which have no known counterparts in inertial, high Reynolds number turbulence. We conclude by going beyond single-particle statistics and investigating the pair-dispersion problem in active turbulence.

Trajectories, especially for high activity, often comprise of long walking-segments of varying step-lengths, interspersed with turning points as seen in Figs. 5.1(a) and 5.1(b). Identifying the “turns” [20, 21] is then crucial to segment trajectories into their constituent step-lengths (and waiting-times) for the analysis that follows. This is done by first calculating a turning angle θ at each point along the trajectory at time intervals Δt as $\cos(\theta(t)) = \frac{\Delta \mathbf{r}(t) \cdot \Delta \mathbf{r}(t+\Delta t)}{|\Delta \mathbf{r}(t)| |\Delta \mathbf{r}(t+\Delta t)|}$, where $\Delta \mathbf{r}(t) = \mathbf{r}(t) - \mathbf{r}(t - \Delta t)$; our results are insensitive for a wide range of Δt . Walking-segments and turns can be identified using a threshold $\theta(t) > \theta_c$, which in turn gives the step-lengths d and waiting-times τ of the segments between successive turns. We choose $\theta_c = 30^\circ$ for this study [21] and have checked that our results remain unchanged for $25^\circ \leq \theta_c \leq 45^\circ$.

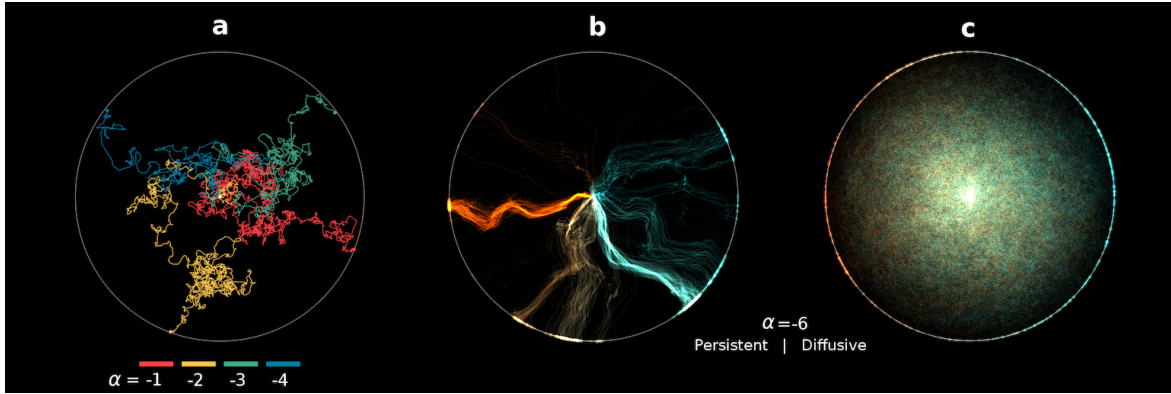


FIGURE 5.1: Representative trajectories for (a) suspensions with different degrees of activity as well as for highly active suspensions showing the (b) fastest 1% tracers, that are persistent and anisotropic and (c) slowest 1% tracers that are diffusive and isotropic. Different trajectories are translated to a common origin for clarity and the color variation is a function of the angle at which they reach the bounding circle while the brightness is proportional to the density of trajectories. (These images, and Fig. 5.3, were generated with Processing [37, 38]).

5.4 Fast and Slow Trajectories and The Role of Emergent Flow Structures

Do tracers in highly active suspensions ($\alpha = -6$) show a bias in the way they sample the relatively weaker and stronger vorticity $\omega = \nabla \times \mathbf{u}$ regions of the flow (Fig. 5.2(a))? The probability distribution function (pdf) of the vorticity field normalised by $\omega' = \sqrt{\langle \omega^2 \rangle}$, where $\langle \cdot \rangle$ denotes spatial averaging, along the Lagrangian trajectories and conditioned on the step-lengths d shows (Fig. 5.2(f)) that trajectories are less likely to have persistent, *directed* motion in regions of strong vorticity: Quiescent regions favour persistent motion (Fig. 5.1(b)).

While this is a useful starting point, it does not capture the two main geometrical effects—vortical and straining regions—which characterise (inertial and active) two-dimensional turbulence. A first approach to this problem is through the Okubo-Weiss parameter $\Lambda = (\omega^2 - \sigma^2)/4\langle \omega^2 \rangle$, where $\sigma^2 = S_{ij}S_{ij}$ is the square of the strain-rate $S_{ij} = (\nabla \mathbf{u} + \nabla \mathbf{u}^T)/2$, measured along individual trajectories: The sign of the Okubo-Weiss criterion [39, 40] determines if the particle is either in a vortical ($\Lambda > 0$) or a straining ($\Lambda < 0$) region as shown in Fig. 5.2(b) for the Eulerian vorticity field of panel (a).

Figure 5.2(g)—the Lagrangian pdf of Λ , measured along particle tracks and conditioned on step-lengths in a manner similar to panel (f)—while clearly showing an overall preferential bias for vortical regions, brings out the inference drawn before more clearly. Tracers are far more likely to move in long, straight segments when they are in regions of the flow where both ω and Λ have a small magnitude. This bias for

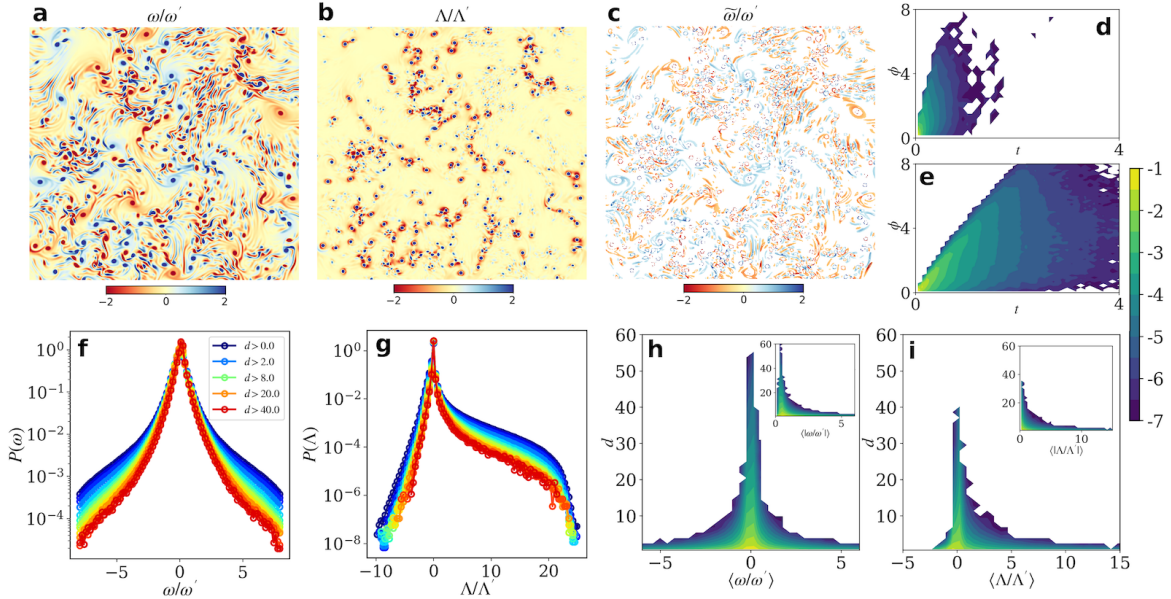


FIGURE 5.2: Pseudocolor plots of the (a) vorticity ω , (b) Okubo-Weiss parameter Λ and (c) masked vorticity $\tilde{\omega}$ fields showing the vortical, straining and streaky patches. Joint-distributions of the residence time and normalised distances of particles (d) within and (e) outside the streaks showing streaks facilitating enhanced displacement in shorter times. Probability distribution functions of the Lagrangian history of (f) vorticity and (g) Okubo-Weiss criterion, conditionally sampled over trajectory segment lengths d , show that persistent segments pass preferentially through quiescent regions of ω and Λ . Joint distributions of the segment lengths d with (h) ω and (i) Λ (insets show the distribution with $|\omega|$ and $|\Lambda|$) further emphasise that the longer trajectory segments mostly occur in quiescent field regions (the colorbar for the joint distributions shows logarithmically spaced decades).

persistent motion in quiescent regions of the flow is further affirmed by the joint distributions of tracer displacements d with ω and Λ as shown in Figs. 5.2(h) and 5.2(i), respectively. The insets in these panels are the same joint distributions but for $|\omega|$ and $|\Lambda|$. These clearly show that large displacements are more probable when both ω and Λ are small: Long straight excursions instead of diffusive meandering occur in these regions.

These distributions, however, cannot trace the *origins* of extremely coherent motion of tracers, illustrated in Fig. 5.1(b), which contribute most to the anomalous diffusive behaviour in highly active suspensions. This is because a simple decomposition of the flow field in terms of vortical and straining regions fails to capture a recently discovered [21] additional emergent *geometrical* feature (with no counterpart in inertial turbulence): *Streaks* which are striped structures with alternate signs of ω as seen in Fig. 5.2(a).

Are streaks the primary cause for persistent Lévy walks seen in our Lagrangian measurements? In fact, the local flow geometry, and how it evolves in time, essentially

governs the fate of a trajectory that passes through it. We demonstrate this in Fig. 5.3, which shows representative close-by trajectories originating in (a) vortical, (b) streaky or (c) quiescent straining regions; the color panels above the trajectories show the vorticity in the small region of the flow where these trajectories originate. This immediately brings out the striking difference in the fate of tracers depending on where they are in the flow. While particles originating in vortical spots (Fig. 5.3(a)) travel diffusively and incoherently, the ones which start in streaky regions (Fig. 5.3(b)) form a coherent bundle with persistent and correlated motions. Trajectories originating in quiescent regions (Fig. 5.3(c)) show elements of both diffusive motion with periods of persistence.

How, then, do we understand this puzzling behaviour? As the underlying field evolves, the trajectories which may have originated in a particular geometry of the flow are likely to encounter a different flow topology in time. This rules out mean-squared-displacements, conditioned on where trajectories originate, as a diagnostic for a couple of reasons. Firstly, such an exercise can be only performed up to short times during which the field remains largely unchanged. Secondly, these short-time MSDs are invariably ballistic, regardless of where they originate. Hence, the subtle correlation between the emergent vagaries of the Eulerian field and the individual trajectories must be found within the Lagrangian history of particle dynamics.

But first, a sharper definition of what is a streak must be made which goes beyond the visual. To that end, careful measurements suggest that streaks coincide with places with (a) relatively moderate values of ω and (b) low magnitudes of Λ . This becomes clear upon comparing the vorticity field, in Fig. 5.2(a), with the Λ field at the same time instance, shown in Fig. 5.2(b). This hints at a criterion, albeit somewhat *ad-hoc*, for identifying the streak regions. We define streaks as regions of the flow where, locally, the vorticity is bounded from below and the Okubo-Weiss criterion is bounded from above, i.e., $\omega \geq \omega_T$ and $\Lambda \leq \Lambda_T$; we choose (and other similar choices give equally consistent results) thresholds $\omega_T = 0.5\omega'$ and $\Lambda_T = 0.1\Lambda'$. This criterion allows us to define a *mask* which, when applied to the vorticity field of active flows, generates a filtered field $\tilde{\omega} = \omega$ in streaks and 0 otherwise. In Fig. 5.2(c) we show $\tilde{\omega}$ for the same flow realisation as in panel (a) to demonstrate the accuracy of this criterion which goes beyond the binary classification of the Okubo-Weiss parameter and picks out the streaky regions.

With the definitions of the flow topologies in place, we can now unambiguously separate trajectories based on the flow regions they encounter. An obvious quantification is the joint distribution of tracer displacements s with residence times t in and out of streak regions. Since the streaky regions occupy a relatively small area-fraction A_f of the

flow, it is useful to look at the effective displacements $\phi \equiv s/\sqrt{A_f}$ within a streak, and conversely $\phi \equiv s/(1 - \sqrt{A_f})$ outside it, to ascertain the relative degree to which streaky and non-streaky regions assist persistent motion.

While streaks form a small fraction ($\sim 12\%$) of the flow resulting in a relatively smaller residence time, tracers inside the (Fig. 5.2(d)) streaks are advected much farther within this short time than those outside (Fig. 5.2(e)). The joint $\phi-t$ distribution is much wider when outside these special structures, indicating that large residence times (in purely vortical and straining patches) do not lead to large displacements. Thus, coherent, persistent motion is intrinsically correlated with the special flow patterns (Fig. 5.2(c)) that a bacterial suspension can spontaneously generate.

5.5 First Passage Problem and Dynamical Heterogeneity

This surprising ability to exploit self-generated patterns and their emergent hydrodynamics to aid persistent motion accords individuals a distinct advantage to reach targets—for nutrition, for example—on much shorter time scales than it would be otherwise possible. While this was certainly implicit in earlier observations of anomalous diffusion through measurements of the mean-square-displacements [21], a direct way of looking at this is to ask how such activity-induced streaks enhance the efficacy of tracers in reaching distances R away. This, of course, is the much studied question in statistical physics of First Passage Problems [41–45], also used to quantify biological motility [46–48]: What is the statistics of the time t_R for tracers to reach (for the first time and be “absorbed” at) the boundary of a circle of radius R as illustrated in Fig. 5.1.

In the context of bacterial suspensions and living systems in general, the first passage characteristics are critical to how efficiently bacteria forage for food and survive. In an active turbulent flow whose evolution is governed by Eq. (5.1), a bacterium foraging for food can be thought of as a point tracer being advected by an active turbulent flow until it reaches the food source at a distance R , at which point the search is concluded.

The probability of a tracer reaching (and being absorbed by) a boundary R at time $t = t_R$ when it starts from $r = 0$ at $t = 0$ is given by the first passage probability distribution $P(R, t_R)$ which is calculated from the (survival) probability $S(t) = \int_0^R p(r, t) 2\pi r dr$ of not reaching the boundary in time t_R via $P(R, t_R) = -\frac{\partial S}{\partial t} \Big|_{t_R}$. The survival probability assumes isotropy of the distribution $p(r, t)$ of tracers which, for low activities, satisfy the diffusion equation [49] with absorbing boundary conditions

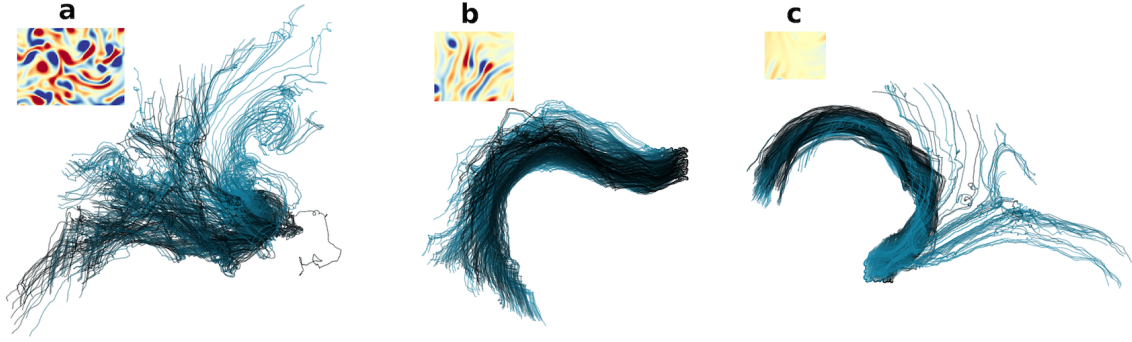


FIGURE 5.3: Representative bundles of trajectories originating in (a) vortical spots, (b) streaks and (c) quiescent regions. While the trajectories spread incoherently in (a) and coherently in (b), there is a mix of both for (c). The trajectories are coloured, varying smoothly from blue (left edge) to black (right edge), based upon their x -coordinates with the colour and gives a sense of mixing vis-à-vis coherence in the trajectory bundles.

$p(R, t) = 0$ and the initial condition $p(r, 0) = \delta(r)/2\pi r$. By using standard techniques and Bessel functions of the first kind, a solution of this diffusion equation and thence the dominant contribution to the first passage distribution via the survival probability yields the well-known result $P(R, t_R) \sim \frac{K_d A}{R^2} e^{-AK_d t_R/R^2}$, where the constant A emerges from the expansion of the Bessel function and K_d the diffusion constant [50] (see Appendix B for details). The first passage distribution can be generalised to the case of anomalous diffusion as $P(R, t_R) \sim e^{-t_R/R^{2/\xi}}$, where the scaling exponent $1 \leq \xi \leq 2$ is a consequence of the anomalous diffusion in the mean-square-displacement $\Delta x^2 \sim t^\xi$ (and which can also be obtained analytically by solving the fractional Fokker-Planck equation [51–55]).

In the inset of Fig. 5.4(a) we show the first passage time distributions for different values of R which collapse on to a unique curve when the first passage times are scaled as t_R/R^2 (Fig. 5.4(a)) consistent with our theoretical prediction for moderately active suspensions. On making suspensions more active, as shown in Fig. 5.4(b), the diffusive t_R/R^2 scaling still remains approximately true but only for large values of R . Indeed, for smaller values of R (Fig. 5.4(b), inset), the distributions collapse only when the first passage times are scaled as $t_R/R^{3/2}$, accounting for the enhanced motility. This is because at such short distances, persistent trajectories contribute to the statistics of first passage overwhelmingly and hence the scaling exponent associated with anomalous diffusion in such systems, $\xi \approx 4/3$ [21], leads to an anomalous form of the first passage distribution.

While the normalized first passage distributions give a statistical sense for an *ensemble* of trajectories, it does not allow us to have a sense of the variations, within an ensemble, of individual trajectories. Since tracers sample the entire phase space, the issue of an

incipient *dynamical heterogeneity* in the flow is a vexing one.

In order to understand this, we take a fraction (10%, for sufficient statistics) of the fastest and slowest trajectories that reach various target radii R , for different values of α . Visually, the fastest and slowest trajectories are different: The former mostly straight and persistent, while the latter convoluted and meandering for *all* levels of activity. However, the Lagrangian history of these tracers, i.e., the Λ values they encounter before hitting their targets, shows, as illustrated in the inset of Fig. 5.4(c) that at mild levels of activity there is no distinction between the underlying Eulerian field sampled by the fastest and slowest tracers. These conditional distributions of the Okubo-Weiss parameter show that the heterogeneity in trajectories, up to intermediate levels of activity, is simply a statistical consequence of the *random* sampling of the flow. However, for highly active suspension, where anomalous diffusion becomes robust, signatures of dynamical heterogeneity, as seen in the clearly different Lagrangian histories of the fastest and slowest trajectories (see Fig. 5.4(c), manifest themselves. Consistent with the findings so far that persistent motion favours quiescent field regions, the fastest tracers sample milder regions of the Okubo-Weiss field, in comparison to the slowest tracers. This distinction, moreover, is starker for smaller R values, while at large values of R , the tracers begin to experience (statistically) similar underlying fields.

This evidence for dynamical heterogeneity in the flow, such that the variation in the nature of trajectories is not *merely* statistical as happens in inertial turbulence [56], is further strengthened by looking at where in the flow do the fastest and slowest tracers originate, for a given value of R . In other words, do trajectories get *lucky* by being at the right place at the right time, which allows them to reach their targets faster than others? This would suggest that for highly active suspensions, the initial locations of these fast, lucky trajectories must be clustered in nearby regions while for less active flows they are more uniformly distributed. In the inset of Fig. 5.4(d), we show a plot of the starting points of the fastest 1% of the trajectories for a target at $R = 15$. We indeed find that for the highly active suspensions ($\alpha = -6$) these points remain strongly clustered, unlike the random and uniform distribution seen for the less active ($\alpha = -1$) case. While confirming a dynamically heterogeneous flow, this also explains the bundling of these trajectories already seen in Fig. 5.1(b), where the fastest tracers (after their initial locations are artificially superimposed at the center of the circle), evolve as coherent *bundles*, arriving at their target circle and forming a very anisotropic distribution around the circumference. This is because the bundles originate clustered together in a few special locations in the flow and hence follow very similar trajectories. We quantify the degree of this clustering by calculating the pair-distribution function

$g(r)$, for the fastest and slowest 1% of the tracers, in Fig. 5.4(d). The $g(r)$ of the origins of the slowest tracers quickly attains a value close to 1, irrespective of activity, corresponding to a uniform (or ideal-gas) distribution of points (albeit with a small overshoot for $\alpha = -6$ at small r , showing weak preferential clustering also for the slowest tracers). The fastest tracer origins for high activity show a pronounced peak in the pair distribution at small values of r , reflecting the presence of these lucky spots. At mild activity, the $g(r)$ for the fastest tracer origins rapidly attains to a value of 1 as well, reflecting the fact that the heterogeneity of trajectories is merely statistical.

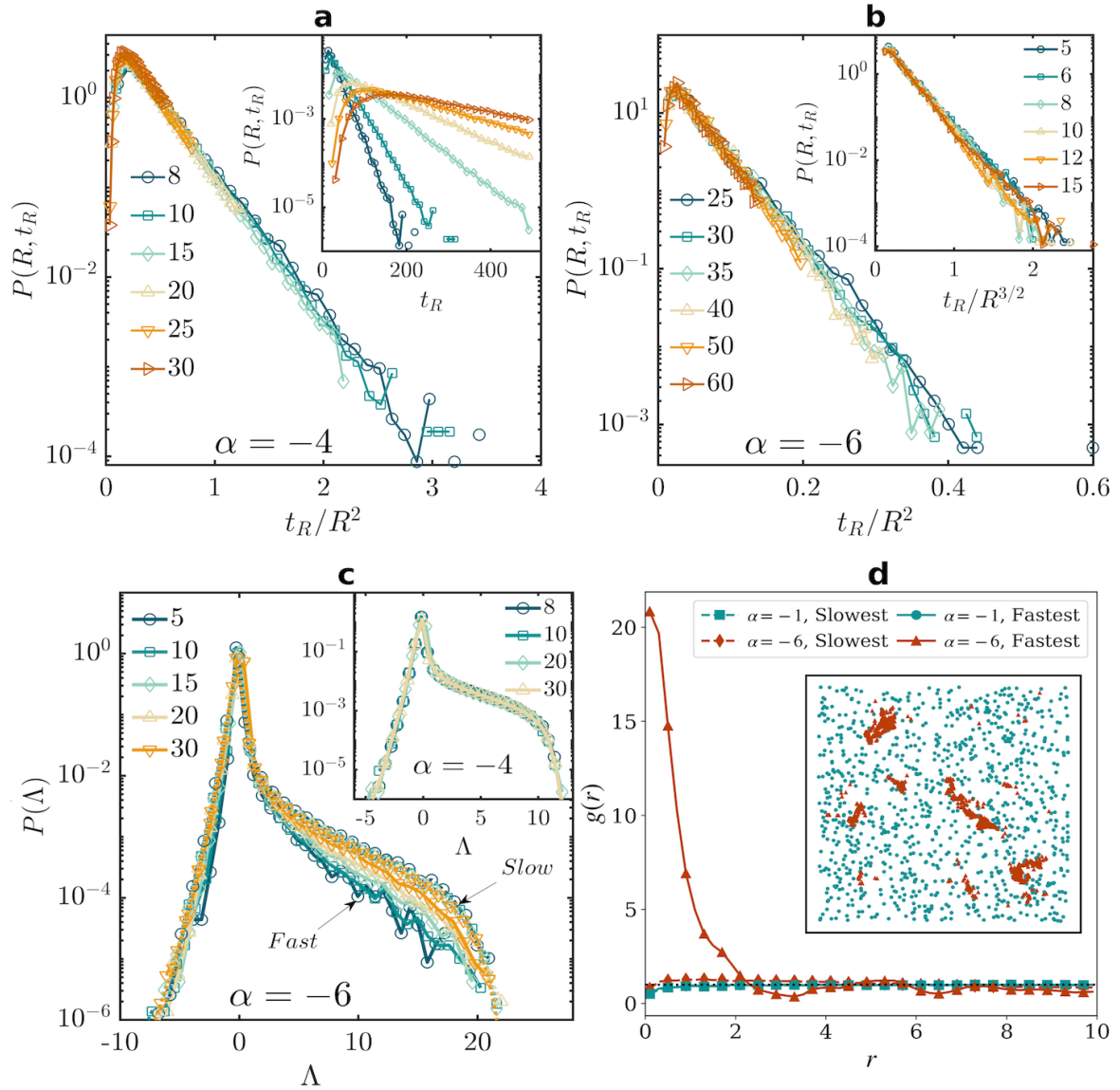


FIGURE 5.4: (a) Semi-log plots of the first passage distributions for mildly active suspensions collapse on a single curve for rescaled time t_R/R^2 corresponding the diffusive transport for different values of R ; the inset shows the same without the rescaling of time. (b) Analogous plots for highly active suspensions show a similar diffusion-driven collapse *only* for large distances and time; for short distance (inset) the curves collapse when time is rescaled as $t_R/R^{3/2}$ which factors in anomalous diffusion. (c) Probability distribution functions of Λ conditioned on the fastest (solid-lines) and slowest (dashed-lines) 10% of tracers for $\alpha = -6$ and $\alpha = -4$ (inset) and for various target radii R . The distributions differ only for the highly active suspension and for small R showing the emergence of a true dynamical heterogeneity. This is visually illustrated in the inset of panel (d) showing that the origins of the fastest 1% tracers for $\alpha = -1$ are randomly distributed whereas those for $\alpha = -6$ are strongly localised suggesting “lucky” spots for efficient motility. This is confirmed in (d) measurements of the pair-distribution function which gives a pronounced peak for the fastest tracer origins for $\alpha = -6$, while rapidly converging to the uniform distribution $g(r) = 1$. Similar measurements for the fastest tracers for lower activity and indeed for the slowest trajectories for all activity show uniform distribution throughout.

5.6 Pair-Dispersion

So far we have focussed our attention on single-particle statistics. But before we conclude, we must consider the implications of these anomalies on the Richardson-Obukhov pair-dispersion problem [57, 58] which informs much of our understanding of inertial turbulence [59]. Pair-dispersion is simply the statistics of separation of particle pairs that originate within a small distance ϵ of each other measured as $\langle r_p^2(t) \rangle = \langle |\mathbf{x}_1(t) - \mathbf{x}_2(t)|^2 \rangle$, where $\mathbf{x}_1(t)$ and $\mathbf{x}_2(t)$ are the positions of a particle pair, with $|\mathbf{x}_1(0) - \mathbf{x}_2(0)| = \epsilon$ being their initial separation, and $\langle \cdot \rangle$ denotes averaging over all particle pairs.

Figure 5.5(a) shows pair-separation for increasingly active suspensions, with $\epsilon = 0.001$. Interestingly, the influence of activity appears to be mild, with only a slight change in the extent of the intermediate scaling; even for $\alpha = -6$, a scaling regime seems to extend only up to a decade. The limited extent of scaling, and its significant deviation from the Richardson prediction $\sim t^3$ for inertial turbulence, may stem from the lack of an inertial range in active turbulence. It has been shown that active turbulence, atleast using the nematohydrodynamic model and other minimal models for wet active nematics [4, 60, 61], does not have an energy cascade resulting from non-linear mode interactions. While, admittedly, our model differs from these, it is likely that a similar situation arises here. In fact, the presence of a particularly wide inertial range and scale separation (effectively, a large Reynolds number) is essential to observe the Richardson scaling regime even in inertial turbulence, despite cascade dynamics, and persistent motion in trajectories (ballistic Lévy walks) can further lead to deviation from Richardson scaling [62]. While there is no natural way to increase scale separation in our system, we tested various domain sizes for $\alpha = -6$, from $L = 20$ (on $N = 1024$) to $L = 80$ (on $N = 4096$), and obtained identical pair-separation curves, without an increase in the extent of scaling. The inset of Fig.5.5(a) shows the influence of the initial separation ϵ on pair-separation for $\alpha = -6$. As ϵ decreases, the slope of the intermediate range increases significantly. This ϵ dependence is consistent with findings from two-dimensional inertial turbulence [63, 64], and the apparent steepening of the slope is a consequence of an exponential initial separation tending to diffusive separation at longer times.

In the absence of robust Richardson scaling, other pair-separation measures have been proposed to quantify dispersion statistics [62, 65]. One such is the probability distribution of pair-separations r_p , at different times during the growth of $\langle r_p^2 \rangle$. Figure 5.5(b) shows the probability distribution of the rescaled (with the variance) pair-separations $s_p = r_p/\sigma$, at various time instances, for trajectories with an initial separation of $\epsilon = 0.001$ and for $\alpha = -6$. The separations s_p collapse to a single stretched-exponential

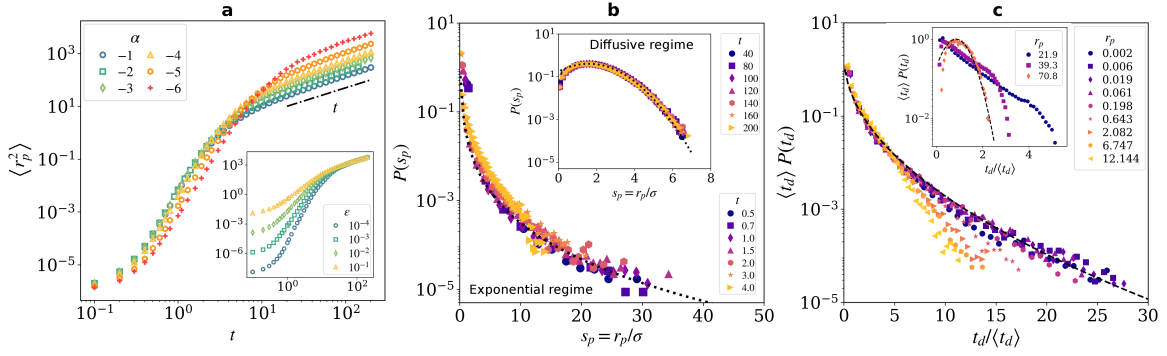


FIGURE 5.5: (a) The dependence of the relative pair separation on α (with $\epsilon = 0.001$) and (inset) on ϵ (for $\alpha = -6$). (b) Probability distribution of the normalized pair separation s_p follows a stretched exponential for times up to diffusive pair-separation, whence (inset) the distribution becomes Gaussian. (c) The probability distribution of pair-separation doubling times t_d are also stretched exponentials at small separations; the curves become steeper with increasing r_p and (inset) converge to a Gaussian distribution for large r_p .

distribution while at very long times, well into the diffusive pair-separation regime $\langle r_p^2 \rangle \sim t$, the s_p distribution becomes Gaussian. All this is consistent with findings from two-dimensional inertial turbulence [63, 65], where a stretched-exponential and Gaussian distribution of rescaled separations is found for the forward enstrophy-cascade and inverse energy-cascade regimes, respectively. This shows that the pair-separation process is self-similar in time, following different distributions during the rapid and (eventually) diffusive growth.

Related to the first passage problem, we consider the distribution of separation doubling-times [62, 63]. This is defined as the time t_d it takes for an initial separation r_p to grow to a scale ρr_p . Here, we can also expect an influence of the persistence in trajectories. Smaller initial separations r_p will lead to longer correlated motion, as trajectory-pairs will sample similar flow geometries (Fig. 5.3). This would lead to relatively longer doubling times, and a wider t_d distribution. At large initial separations, where trajectory-pairs are essentially uncorrelated to begin with, the separation doubling will occur more rapidly. This is precisely what is observed in Fig. 5.5(c) for $\rho = 1.8$; our results are similar for other ρ values that are not too small. The distributions of doubling-times t_d , normalized by the mean doubling time $\langle t_d \rangle$, for small values of r_p , follow a stretched exponential function, similar to two-dimensional inertial turbulence in the enstrophy-cascade range [63]. The distributions become steeper with increasing r_p , reflecting the decorrelation within trajectory pairs. The inset of Fig. 5.5(c) shows that at very large values of r_p , deep into the diffusive pair-separation phase, the distribution of t_d , as anticipated, approaches a Gaussian.

5.7 Conclusions

Anomalous diffusion and Lévy walks are common place in a wide variety of biological systems. However, in dense suspensions of microorganisms, such as bacterial swarms, which are a typical example of flowing active matter and a testing ground for active turbulence, the experimental evidence for such phenomena is only recent [20]. Furthermore, theoretical studies have been unable to go beyond the simple diffusion picture and predict, detect or understand the emergence of such super-diffusive regimes in active turbulence. This issue was resolved by a recent work [21] showing that anomalous Lagrangian statistics manifest only in extremely active suspensions, with $\alpha \sim -6$. Further exploring such highly active suspensions consistently revealed signatures of anomalies in Lagrangian measurements. The streaky flow regions, together with an emergent dynamical heterogeneity, contrive to selectively propel tracers persistently and aid in anomalous first-passage statistics. The results presented in this work should be readily amenable to experimental measurements in super-diffusive bacterial swarms, as well as in a diverse class of active flows. Whether the conjoined emergence of Eulerian streaks at high activity, and their role in promoting persistent motion, is universal, remains to be ascertained, and the true mechanisms for manifesting Lagrangian anomalies may well be system dependent. Notwithstanding, we feel that our results show a biologically crucial aspect of the generalized hydrodynamics model beyond what has been previously observed, extending its applicability to a realm closer to experimental observations. Further, measures like pair-dispersion mirror fundamental quantities like Lyapunov exponents, that characterize chaos in both diverging trajectories and solutions of the hydrodynamic equations. For instance, the flow Lyapunov exponent is known to increase with Reynolds number in inertial turbulence approximately as $\sim \text{Re}^{1/2}$ [66–68]. The analogous effect of activity on Lyapunov exponents in active turbulence remains unknown and is part of ongoing work, both within the Eulerian [66–68] and Lagrangian framework [69, 70], which looks at different aspects of many-body chaos [71] in such systems. Indeed, a complete understanding of the dynamical facets of active turbulence calls for a complete characterization of the skeleton of chaos underlying active flows. It is interesting to note that a recent work [72] on the (Lagrangian) irreversibility in such suspensions shows similar anomalies between active and inertial turbulence. Lastly, our work also lays out a systematic framework for the Lagrangian analysis of active flows, including measures for identifying geometrical structures emerging in the Eulerian fields. Adopting these in future work will not only ascertain the extent of universality of active turbulence anomalies, but also help connect hydrodynamic theories of active matter more closely to the physical picture.

References

- [1] M. C. Marchetti, J. F. Joanny, S. Ramaswamy, T. B. Liverpool, J. Prost, M. Rao et al., *Hydrodynamics of soft active matter*, *Rev. Mod. Phys.* **85** (2013) 1143–1189.
- [2] S. Ramaswamy, *Active matter*, *Journal of Statistical Mechanics: Theory and Experiment* **2017** (2017) 054002.
- [3] A. Doostmohammadi, J. Ignés-Mullol, J. M. Yeomans and F. Sagués, *Active nematics*, *Nature Communications* **9** (2018) 3246.
- [4] R. Alert, J. Casademunt and J.-F. Joanny, *Active turbulence*, *Annual Review of Condensed Matter Physics* **13** (2022) 143–170.
- [5] J. Toner, Y. Tu and S. Ramaswamy, *Hydrodynamics and phases of flocks*, *Annals of Physics* **318** (2005) 170–244.
- [6] J. M. Yeomans, *Playful topology*, *Nature Materials* **13** (2014) 1004–1005.
- [7] H. H. Wensink, J. Dunkel, S. Heidenreich, K. Drescher, R. E. Goldstein, H. Löwen et al., *Meso-scale turbulence in living fluids*, *Proceedings of the National Academy of Sciences* **109** (2012) 14308–14313.
- [8] J. Dunkel, S. Heidenreich, K. Drescher, H. H. Wensink, M. Bär and R. E. Goldstein, *Fluid dynamics of bacterial turbulence*, *Phys. Rev. Lett.* **110** (2013) 228102.
- [9] K.-T. Wu, J. B. Hishamunda, D. T. Chen, S. J. DeCamp, Y.-W. Chang, A. Fernández-Nieves et al., *Transition from turbulent to coherent flows in confined three-dimensional active fluids*, *Science* **355** (2017) .
- [10] T. Sanchez, D. T. N. Chen, S. J. DeCamp, M. Heymann and Z. Dogic, *Spontaneous motion in hierarchically assembled active matter*, *Nature* **491** (2012) 431–434.
- [11] Y. Sumino, K. H. Nagai, Y. Shitaka, D. Tanaka, K. Yoshikawa, H. Chaté et al., *Large-scale vortex lattice emerging from collectively moving microtubules*, *Nature* **483** (2012) 448–452.

- [12] Y. Katz, K. Tunström, C. C. Ioannou, C. Huepe and I. D. Couzin, *Inferring the structure and dynamics of interactions in schooling fish*, *Proceedings of the National Academy of Sciences* **108** (2011) 18720–18725.
- [13] S. Ramaswamy, *The mechanics and statistics of active matter*, *Annual Review of Condensed Matter Physics* **1** (2010) 323–345.
- [14] A. Cavagna, A. Cimarelli, I. Giardina, G. Parisi, R. Santagati, F. Stefanini et al., *Scale-free correlations in starling flocks*, *Proceedings of the National Academy of Sciences* **107** (2010) 11865–11870.
- [15] L. Giomi, L. Mahadevan, B. Chakraborty and M. F. Hagan, *Banding, excitability and chaos in active nematic suspensions*, *Nonlinearity* **25** (2012) 2245–2269.
- [16] R. Alert, J.-F. Joanny and J. Casademunt, *Universal scaling of active nematic turbulence*, *Nature Physics* **16** (2020) 682–688.
- [17] X.-L. Wu and A. Libchaber, *Particle diffusion in a quasi-two-dimensional bacterial bath*, *Phys. Rev. Lett.* **84** (2000) 3017.
- [18] H. Kurtuldu, J. S. Guasto, K. A. Johnson and J. P. Gollub, *Enhancement of biomixing by swimming algal cells in two-dimensional films*, *Proceedings of the National Academy of Sciences* **108** (2011) 10391–10395.
- [19] A. Morozov and D. Marenduzzo, *Enhanced diffusion of tracer particles in dilute bacterial suspensions*, *Soft Matter* **10** (2014) 2748–2758.
- [20] G. Ariel, A. Rabani, S. Benisty, J. D. Partridge, R. M. Harshey and A. Be’Er, *Swarming bacteria migrate by lévy walk*, *Nature Communications* **6** (2015) 8396.
- [21] S. Mukherjee, R. K. Singh, M. James and S. S. Ray, *Anomalous diffusion and lévy walks distinguish active from inertial turbulence*, *Phys. Rev. Lett.* **127** (2021) 118001.
- [22] S. C.P. and A. Joy, *Friction scaling laws for transport in active turbulence*, *Physical Review Fluids* **5** (2020) 024302.
- [23] M. F. Shlesinger, B. J. West and J. Klafter, *Lévy dynamics of enhanced diffusion: Application to turbulence*, *Phys. Rev. Lett.* **58** (1987) 1100–1103.
- [24] P. Dhar, T. M. Fischer, Y. Wang, T. E. Mallouk, W. F. Paxton and A. Sen, *Autonomously moving nanorods at a viscous interface*, *Nano Letters* **6** (2006) 66–72.
- [25] O. V. Bychuk and B. O’Shaughnessy, *Anomalous surface diffusion: A numerical study*, *The Journal of Chemical Physics* **101** (1994) 772–780.

- [26] M. F. Krummel, F. Bartumeus and A. Gérard, *T cell migration, search strategies and mechanisms*, *Nature Reviews Immunology* **16** (2016) 193–201.
- [27] B. J. Cole, *Fractal time in animal behaviour: the movement activity of drosophila*, *Animal Behaviour* **50** (1995) 1317–1324.
- [28] F. Zanger, H. Löwen and J. Saal, *Analysis of a living fluid continuum model*, in *Mathematics for Nonlinear Phenomena: Analysis and Computation: International Conference in Honor of Professor Yoshikazu Giga on his 60th Birthday*, pp. 285–303, Springer, 2015.
- [29] J. Swift and P. C. Hohenberg, *Hydrodynamic fluctuations at the convective instability*, *Physical Review A* **15** (1977) 319.
- [30] J. Toner and Y. Tu, *Long-range order in a two-dimensional dynamical XY model: How birds fly together*, *Phys. Rev. Lett.* **75** (1995) 4326–4329.
- [31] J. Toner and Y. Tu, *Flocks, herds, and schools: A quantitative theory of flocking*, *Phys. Rev. E* **58** (1998) 4828–4858.
- [32] M. James and M. Wilczek, *Vortex dynamics and lagrangian statistics in a model for active turbulence*, *The European Physical Journal E* **41** (2018) 21.
- [33] S. C. P. and A. Joy, *Friction scaling laws for transport in active turbulence*, *Phys. Rev. Fluids* **5** (2020) 024302.
- [34] M. James, D. A. Suchla, J. Dunkel and M. Wilczek, *Emergence and melting of active vortex crystals*, *Nature Communications* **12** (2021) 5630.
- [35] I. M. Jánosi, J. O. Kessler and V. K. Horváth, *Onset of bioconvection in suspensions of bacillus subtilis*, *Phys. Rev. E* **58** (1998) 4793–4800.
- [36] A. Sokolov and I. S. Aranson, *Physical properties of collective motion in suspensions of bacteria*, *Phys. Rev. Lett.* **109** (2012) 248109.
- [37] C. Reas and B. Fry, *Processing: a programming handbook for visual designers and artists*. Mit Press, 2007,
<https://mitpress.mit.edu/books/processing-second-edition>.
- [38] M. Pearson, *Generative art: a practical guide using Processing*. Simon and Schuster, 2011, <https://www.simonandschuster.com/books/Generative-Art/Matt-Pearson/9781935182627>.
- [39] A. Okubo, *Horizontal dispersion of floatable particles in the vicinity of velocity singularities such as convergences*, *Deep Sea Research and Oceanographic Abstracts* **17** (1970) 445–454.

- [40] J. Weiss, *The dynamics of enstrophy transfer in two-dimensional hydrodynamics*, *Physica D: Nonlinear Phenomena* **48** (1991) 273–294.
- [41] S. Chandrasekhar, *Stochastic problems in physics and astronomy*, *Rev. Mod. Phys.* **15** (1943) 1–89.
- [42] A. J. Bray, S. N. Majumdar and G. Schehr, *Persistence and first-passage properties in nonequilibrium systems*, *Advances in Physics* **62** (2013) 225–361.
- [43] S. Redner, *A Guide to First-Passage Processes*. Cambridge University Press, 2001, [10.1017/CBO9780511606014](https://doi.org/10.1017/CBO9780511606014).
- [44] V. Balakrishnan, *Elements of nonequilibrium statistical mechanics*. Springer, 2021, [10.1007/978-3-030-62233-6](https://doi.org/10.1007/978-3-030-62233-6).
- [45] R. Metzler, G. Oshanin and S. Redner, *First-Passage Phenomena and Their Applications*. WORLD SCIENTIFIC, 2014, [10.1142/9104](https://doi.org/10.1142/9104).
- [46] T. Chou and M. R. D’Orsogna, *First passage problems in biology*, in *First-passage phenomena and their applications*, pp. 306–345. World Scientific, 2014.
- [47] K. Bisht, S. Klumpp, V. Banerjee and R. Marathe, *Twitching motility of bacteria with type-iv pili: Fractal walks, first passage time, and their consequences on microcolonies*, *Phys. Rev. E* **96** (2017) 052411.
- [48] H. Teimouri and A. B. Kolomeisky, *Theoretical investigation of stochastic clearance of bacteria: first-passage analysis*, *Journal of The Royal Society Interface* **16** (2019) 20180765.
- [49] H. Risken and T. Frank, *The Fokker-Planck Equation*. Springer, 1996, [10.1007/978-3-642-61544-3](https://doi.org/10.1007/978-3-642-61544-3).
- [50] A. K. Verma, A. Bhatnagar, D. Mitra and R. Pandit, *First-passage-time problem for tracers in turbulent flows applied to virus spreading*, *Phys. Rev. Research* **2** (2020) 033239.
- [51] A. J. F. Siegert, *On the first passage time probability problem*, *Phys. Rev.* **81** (1951) 617–623.
- [52] G. Rangarajan and M. Ding, *First passage time distribution for anomalous diffusion*, *Physics Letters A* **273** (2000) 322–330.
- [53] G. Rangarajan and M. Ding, *Anomalous diffusion and the first passage time problem*, *Phys. Rev. E* **62** (2000) 120–133.

- [54] M. Gitterman, *Mean first passage time for anomalous diffusion*, *Phys. Rev. E* **62** (2000) 6065–6070.
- [55] V. V. Palyulin, G. Blackburn, M. A. Lomholt, N. W. Watkins, R. Metzler, R. Klages et al., *First passage and first hitting times of lévy flights and lévy walks*, *New Journal of Physics* **21** (2019) 103028.
- [56] R. Scatamacchia, L. Biferale and F. Toschi, *Extreme events in the dispersions of two neighboring particles under the influence of fluid turbulence*, *Phys. Rev. Lett.* **109** (2012) 144501.
- [57] L. F. Richardson and G. T. Walker, *Atmospheric diffusion shown on a distance-neighbour graph*, *Proceedings of the Royal Society of London. Series A, Containing Papers of a Mathematical and Physical Character* **110** (1926) 709–737.
- [58] A. Obukhov, *On the distribution of energy in the spectrum of turbulent flow*, *Bull. Acad. Sci. USSR, Geog. Geophys.* **5** (1941) 453–466.
- [59] J. P. Salazar and L. R. Collins, *Two-particle dispersion in isotropic turbulent flows*, *Annual Review of Fluid Mechanics* **41** (2009) 405–432.
- [60] J. Urzay, A. Doostmohammadi and J. M. Yeomans, *Multi-scale statistics of turbulence motorized by active matter*, *Journal of Fluid Mechanics* **822** (2017) 762–773.
- [61] L. N. Carenza, L. Biferale and G. Gonnella, *Cascade or not cascade? energy transfer and elastic effects in active nematics*, *Europhys. Lett.* **132** (2020) 44003.
- [62] G. Boffetta and I. M. Sokolov, *Statistics of two-particle dispersion in two-dimensional turbulence*, *Physics of Fluids* **14** (2002) 3224–3232.
- [63] M. K. Rivera and R. E. Ecke, *Pair dispersion and doubling time statistics in two-dimensional turbulence*, *Phys. Rev. Lett.* **95** (2005) 194503.
- [64] H. Xia, N. Francois, B. Faber, H. Punzmann and M. Shats, *Local anisotropy of laboratory two-dimensional turbulence affects pair dispersion*, *Physics of Fluids* **31** (2019) 025111.
- [65] M.-C. Jullien, J. Paret and P. Tabeling, *Richardson pair dispersion in two-dimensional turbulence*, *Phys. Rev. Lett.* **82** (1999) 2872–2875.
- [66] S. Mukherjee, J. Schalkwijk and H. J. J. Jonker, *Predictability of dry convective boundary layers: An les study*, *Journal of the Atmospheric Sciences* **73** (2016) 2715 – 2727.

-
- [67] G. Boffetta and S. Musacchio, *Chaos and predictability of homogeneous-isotropic turbulence*, *Phys. Rev. Lett.* **119** (2017) 054102.
- [68] A. Berera and R. D. J. G. Ho, *Chaotic properties of a turbulent isotropic fluid*, *Phys. Rev. Lett.* **120** (2018) 024101.
- [69] J. Bec, L. Biferale, G. Boffetta, M. Cencini, S. Musacchio and F. Toschi, *Lyapunov exponents of heavy particles in turbulence*, *Physics of Fluids* **18** (2006) 091702.
- [70] S. S. Ray, *Non-intermittent turbulence: Lagrangian chaos and irreversibility*, *Phys. Rev. Fluids* **3** (2018) 072601.
- [71] S. D. Murugan, D. Kumar, S. Bhattacharjee and S. S. Ray, *Many-body chaos in thermalized fluids*, *Phys. Rev. Lett.* **127** (2021) 124501.
- [72] K. V. Kiran, A. Gupta, A. K. Verma and R. Pandit, *Irreversibility in bacterial turbulence: Insights from the mean-bacterial-velocity model*, *arXiv preprint arXiv:2201.12722* (2022) .

Chapter 6

Anomalous diffusion and Lévy walks distinguish active turbulence

Bacterial swarms display intriguing dynamical states like active turbulence. Using a hydrodynamic model we now show that such dense active suspensions manifest super-diffusion, via Lévy walks, which masquerades as a crossover from ballistic to diffusive scaling in measurements of mean-squared-displacements, and is tied to the emergence of hitherto undetected oscillatory streaks in the flow. Thus, while laying the theoretical framework of an emergent advantageous strategy in the collective behaviour of microorganisms, our study underlines the essential differences between active and inertial turbulence.

This chapter closely follows the work [Mukherjee *et al.*, Phys. Rev. Lett. **127** (11), 118001].

6.1 Introduction

Flowing active matter, resulting from the motility of organisms, cells and particles, forms an intriguing class of non-equilibrium phenomena [1–3]. Biological functions like foraging and evasion, that require active agents to both sample their neighbourhoods and make large jumps to cover ground, become inextricably coupled with collective flow patterns in dense systems [4]. Active flow driven enhanced diffusion and mixing are also essential for feeding of microorganisms [5–7]. Active agents, hence, profit from optimal processes like Lévy motion [8, 9] characterised by long-tailed, self-similar step-size distributions leading to anomalous diffusion [10] and increased encounter rates [11] — all which can emerge from simple generative mechanisms [12]—as opposed to inefficient meandering by random walks limited to classical diffusion. Interestingly, the motion of individual active entities in isolation often differ from when they are in

large numbers [13]: Movements of a single swimming bacteria can be fundamentally different from its motion in a dense, *fluid-like* swarm [14].

A remarkable feature of the collective behaviour of dense active suspensions is the emergence of spatio-temporal structures strongly reminiscent of inertial turbulence [15–20]: Such two-dimensional suspensions are vortical [21], chaotic [16] with non-Gaussian distributions of velocity gradients [21–23] and a power-law kinetic energy spectrum [24, 25]. These facets of low Reynolds number suspensions have led to a new class of phenomena known as *active turbulence* [26].

However, does the similarity between high Reynolds number inertial turbulence and low Reynolds number active turbulence hold even for Lagrangian statistics? This is a fundamentally important question for two reasons. First, while for inertial turbulence, Lagrangian (tracer) trajectories, measured through mean squared displacements (MSD) have a universal behaviour of purely diffusive self-separation [27], experiments in active turbulence suggest non-universal signatures of Lévy walks and anomalous diffusion [14, 28–30]. Secondly, if such effective biological strategies emerge in active suspensions, why have they remained theoretically undetected and experimentally inconclusive so far?

Using a continuum hydrodynamic model we now provide definitive answers to these questions. We show what appears as an *inconsequential* transition (see Fig. 6.1(a)) between the ballistic and diffusive scaling regimes in MSD measurements is really an intermediate, anomalous diffusive regime leveraging the crucial biological advantages of Lévy walks [31]. Thus, while low Reynolds number active suspensions may well share features, at the level of equations and the resultant dynamics, with high Reynolds number inertial turbulence, active turbulence still allows for emergent behaviour consistent with biological systems striving for efficient searching strategies. This, we discover, is facilitated by a synthesis of two basic flow patterns: Novel oscillatory *streaks* responsible for anomalous diffusion and unique to such systems, and vortical features reminiscent of inertial turbulence.

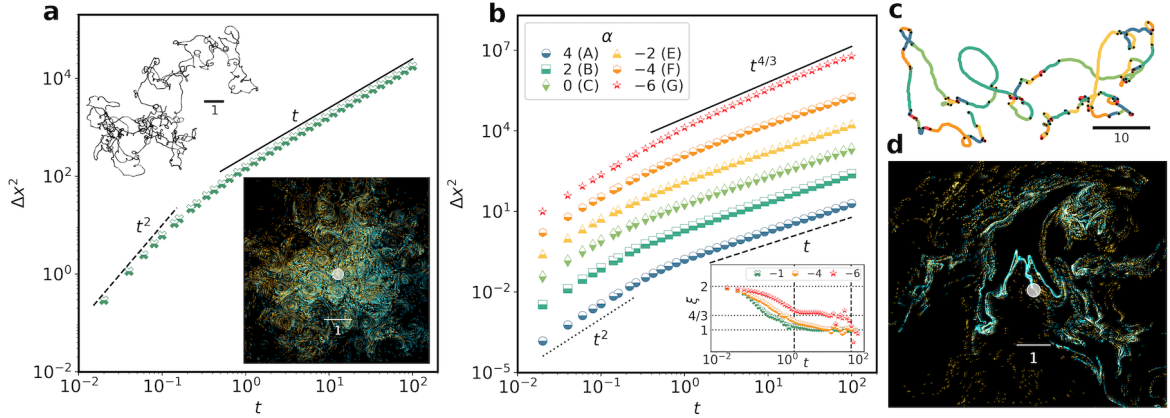


FIGURE 6.1: MSD of Lagrangian trajectories (a) for mild activity and (b) with increasing levels of activity (vertically staggered for clarity). Local slopes (b, inset) of Δx^2 : While ξ continuously decreases from 2 to 1 for $\alpha \leq -4$, it plateaus (between the vertical lines) at $\xi \approx 4/3$ for $\alpha = -6$. Representative trajectories for (a) $\alpha = -1$ (upper inset) and (c) $\alpha = -6$ (see text) reflecting the change from diffusive to anomalous behaviour and also seen in snapshots of particle positions (initially localised within the small white disk) at $t \approx 10$ for $\alpha = -1$ (panel (a), lower inset) and (d) $\alpha = -6$; the brightness of the colours reflects the particle density.

6.2 Generalised Hydrodynamics

Dense, active suspensions lend themselves to a generalized hydrodynamic description, developed for bacterial swarms [16, 32]

$$\partial_t \mathbf{u} + \lambda \mathbf{u} \cdot \nabla \mathbf{u} = -\nabla p - \Gamma_0 \nabla^2 \mathbf{u} - \Gamma_2 \nabla^4 \mathbf{u} - (\alpha + \beta |\mathbf{u}|^2) \mathbf{u} \quad (6.1)$$

where the incompressible velocity field $\mathbf{u}(\mathbf{x}, t)$ (with $\nabla \cdot \mathbf{u} = 0$), is a coarse-grained description of the motility of dense, active (bacterial) suspensions. Here, $\lambda > 0$ corresponds to pusher-type bacteria and the Γ -terms are responsible for quasi-chaotic pattern formation via stress-induced instabilities (when $\Gamma_0, \Gamma_2 > 0$) in the bacterial system [16, 24, 33–35]. The last term adds Toner-Tu drive [36, 37], where β needs to be positive for stability, while the activity α can take both positive (Ekman friction) and negative (active injection) values. In our direct numerical simulations (see Section 5.2), Γ_0 and Γ_2 are fixed according to experimental length and time scales [16], while other parameters are varied to obtain the flow fields explored in this study. The characteristic length and time scales associated with the linear instability in (6.1) are $L_\Gamma = \sqrt{\Gamma_2/\Gamma_0}$ and $\tau_\Gamma = \Gamma_2/\Gamma_0^2$ [16], while the activity length and time scales are given by $1/\sqrt{|\alpha|\beta}$ and $1/|\alpha|$, respectively. In conformity with the previous studies using this model, we present our results in simulation units.

6.3 Simulations

The generalized hydrodynamic model, is solved using a pseudo-spectral method [23]. Simulations are performed on a periodic domain of sizes 1024^2 and 4096^3 grid points, with a physical extent of $L = 20$ and $L = 80$, respectively, for a duration of 5×10^5 iterations, with a time-step of $\delta t = 0.0002$. To be consistent with previous work [16, 23, 38], we set $\Gamma_0 = 0.045$, $\Gamma_2 = \Gamma_0^3$, $\beta = 0.5$, $\lambda = 3.5$. Cases A to G correspond to $\alpha \in \{4, 2, 0, -1, -2, -4, -6\}$. We additionally simulate Case Z, after a parameter search, with $\beta = 22.22$ and $\alpha = -16.66$, which is to exemplify an extreme state dominated by streaks, leading to robust anomalous diffusion.

After a spinup period of 2×10^4 iterations, the flow is seeded with 10^5 tracer particles randomly distributed in the domain, which follow the equation $d\mathbf{x}(t)/dt = \mathbf{u}(\mathbf{x}, t)$, integrated with a 4th-order Runge-Kutta scheme. Field quantities are interpolated to off-grid locations using bilinear interpolation (see Appendix E), and data is stored every 100 iterations to report well-converged statistics.

6.4 Anomalous Diffusion at High Activity

Figure 6.1(a) shows the MSD $\Delta x^2 = \langle \|\mathbf{x}(t) - \mathbf{x}(0)\|^2 \rangle$ (where $\|\cdot\|$ and $\langle \cdot \rangle$ denote the Euclidean norm and ensemble averaging over all particles, respectively) for an active suspension with $\alpha = -1.0$. This scaling behaviour seems consistent with inertial turbulence: A ballistic regime $\Delta x^2 \sim t^2$ crossing over to a diffusive regime $\Delta x^2 \sim t$ [38]. Individual trajectories (upper inset, Fig. 6.1(a)), similarly, show diffusive meandering.

However, some experiments [14, 28] on dense bacterial swarms provide strong evidence of anomalous diffusion $\Delta x^2 \sim t^\xi$, with $1 < \xi < 2$. This raises the question whether what is seen as a crossover from ballistic to diffusive behaviour is *actually* masking an intermediate, anomalous diffusive regime.

To uncover the true behaviour of such suspensions, we perform several simulations (see Section 5.2 for details) on domain sizes $20 \leq L \leq 80$ with $-6 \leq \alpha \leq 4$, seeded with tracers that evolve as $d\mathbf{x}(t)/dt = \mathbf{u}(\mathbf{x}, t)$, and measure the associated MSD as shown in Fig. 6.1(b). For $\alpha \geq 0$, corresponding to an Ekman friction effect, and for modest activity $0 < \alpha \leq -2$ (Cases A – E), we see little evidence of anomalous diffusion. However, as we increase the activity further (Case F), the first signatures of an intermediate regime appear. This observation is validated for Case G where the Δx^2 shows a convincing super-diffusive regime, and local slope analysis (Fig. 6.1(b), inset) gives $\xi = \frac{d\text{Log}\Delta x^2}{d\text{Log}t} = 1.31 \pm 0.08 \approx 4/3$, for close to two decades before giving way to diffusion. This scaling, we recall, is not inconsistent with recent experimental

measurements [14, 28] and simplified model predictions [39, 40] which suggest similar super-diffusion for dense suspensions of motile bacteria. It is important to alert the reader that whether these are indeed non-trivial fixed points in the renormalisation group sense would require an exponent flow [41] or more sophisticated data analysis through asymptotic extrapolation [42–45]; given the high precision data required for such approaches to be beyond speculative, we refrain from this analysis here.

The emergence of anomalous diffusion, as suspensions become more active, ought to carry its signature in Lagrangian trajectories, providing a crucial link in understanding how bacterial colonies forage and avoid hostile environments. In Fig. 6.1(c) we show a representative trajectory of a tracer corresponding to a highly active suspension with $\alpha = -6$ which, in sharp contrast to trajectories in mildly active suspensions (Fig. 6.1(a), upper inset), shows short diffusive behaviour punctuated by long “steps” indicative of anomalous diffusion.

6.5 Quantifying Trajectories

Each trajectory is divided into individual walking segments (as illustrated in the main text) that are identified by a threshold on the turning angle θ at each time t . The angles $\theta(t)$ are calculated along trajectories as

$$\cos(\theta(t)) = \frac{\Delta\mathbf{r}(t) \cdot \Delta\mathbf{r}(t + \Delta t)}{|\Delta\mathbf{r}(t)| |\Delta\mathbf{r}(t + \Delta t)|} \quad (6.2)$$

where $\Delta\mathbf{r}(t')$ is the displacement vector connecting points $\mathbf{r}(t' - \Delta t)$ and $\mathbf{r}(t')$, and Δt is the temporal coarsening, and results were found similar for $\Delta t = 2\delta t, 3\delta t$ and $4\delta t$. Individual segments and turns can be identified using a simple threshold of $\theta(t) > \theta_c$, although the exact segments are rather sensitive to the choice of θ_c . A filtering is done to identify clusters of two or three successive points that are all identified as “turns” (usually occurs during sharp turns), where only the point with the highest turning angle is retained. The waiting time τ is calculated as the time between successive turns. Figure 6.1(c) shows a trajectory divided into segments (shown in different colours), that are identified every time the trajectory turns (points marked in black) by an angle θ greater than a threshold angle θ_c ; we choose $\theta_c = 30^\circ$ for illustration in Fig. 6.1(c). While trajectories evolve mostly with small variations in θ for mild suspensions, increasing activity makes sharper turns more probable. This is seen in Fig. 6.2 which shows the distribution of turning angles with increasing levels of activity.

In Fig. 6.1(d) we show a snapshot of 20,000 particles, initially localised within the small white disk at the center, at time $t \approx 10$ for Case G ($\alpha = -6$); the brightness

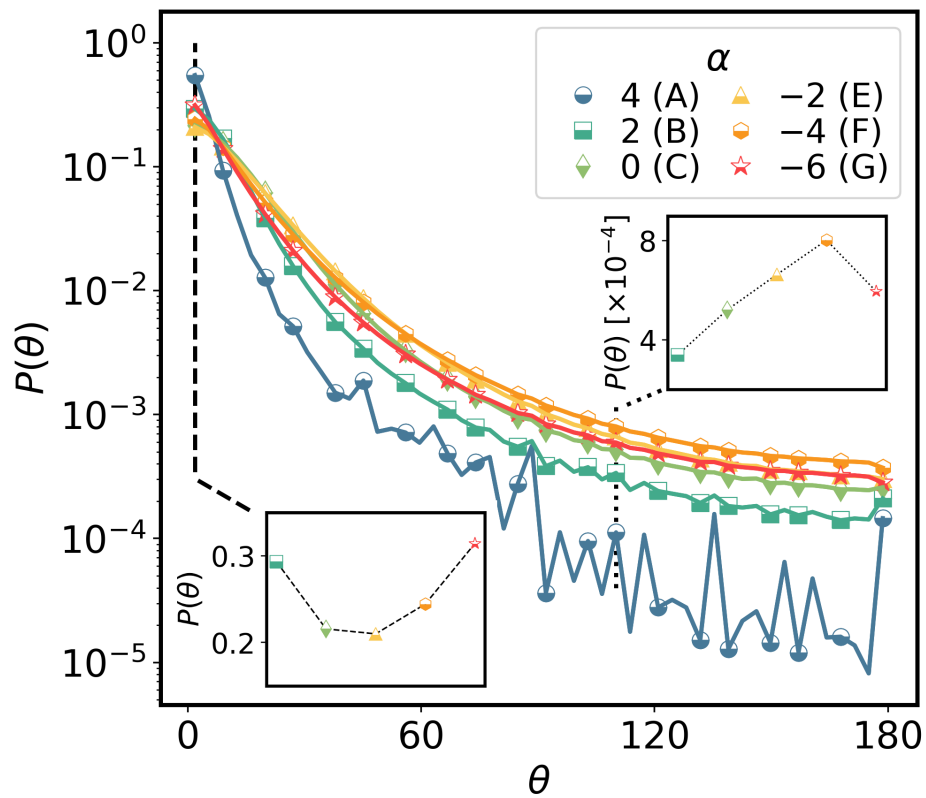


FIGURE 6.2: The probability distributions $P(\theta)$ along trajectories show that activity increases the probability of sharper turns. Moreover, the propensity for small changes in θ (Case A) first decreases with activity (up to Case E), and then increases again (Cases F and G), which, together with the prevalence of sharp turns at higher activity, reflects Lévy walk-like behaviour.

of the colours is a measure of the local density of particles. The evolution of the puff in highly active suspensions is far more “irregular” than what is seen, under identical conditions, at low activity ($\alpha = -1$, Fig. 6.1(a), lower inset) where they spread through diffusion.

6.6 Lévy Walks in Active Turbulence

This inevitably leads to the question whether these visual cues are stemming from *real* Lévy walks, marked by power-law step size and equivalently, because of an approximately constant velocity, waiting time distributions. A convincing argument in favour of Lévy walks is the distribution $p(\tau)$ of waiting times τ , which ought to show a significant range of scaling of the form $p(\tau) \sim \tau^{-\gamma-1}$ for a reasonably large spread in the choice of the threshold angle θ_c which determines a “turn”. Fig. 6.3 confirms the existence of such a power-law and a local slope analysis $\gamma = -1 - \frac{d\text{Log}p(\tau)}{d\text{Log}\tau}$ (Fig. 6.3, lower inset) shows scaling for about a decade with $\gamma = 1.7 \pm 0.3$. Similarly, the probability distribution $p(d)$ of step sizes, for the more active suspensions, follow a scaling $p(d) \sim d^{-\gamma-1}$. Hence, in the same inset, we also show local slopes obtained from $p(d)$ (with the x-axis rescaled to $d/5$ for ease of comparison), showing a comparable extent of scaling, from which we obtain $\gamma = 1.6 \pm 0.2$. Importantly, this scaling exponent $\gamma \approx 5/3$ when coupled with the anomalous MSD exponent $\xi \approx 4/3$, satisfies the Lévy walk constraint $\gamma + \xi = 3$ [46]. Finally, the joint distribution of flight lengths d and waiting times τ between turns in the trajectories for active suspensions (Fig. 6.3, upper inset) shows an almost linear scaling reflecting a constant system velocity. All of these are clear, unambiguous indicators of Lévy walks [47].

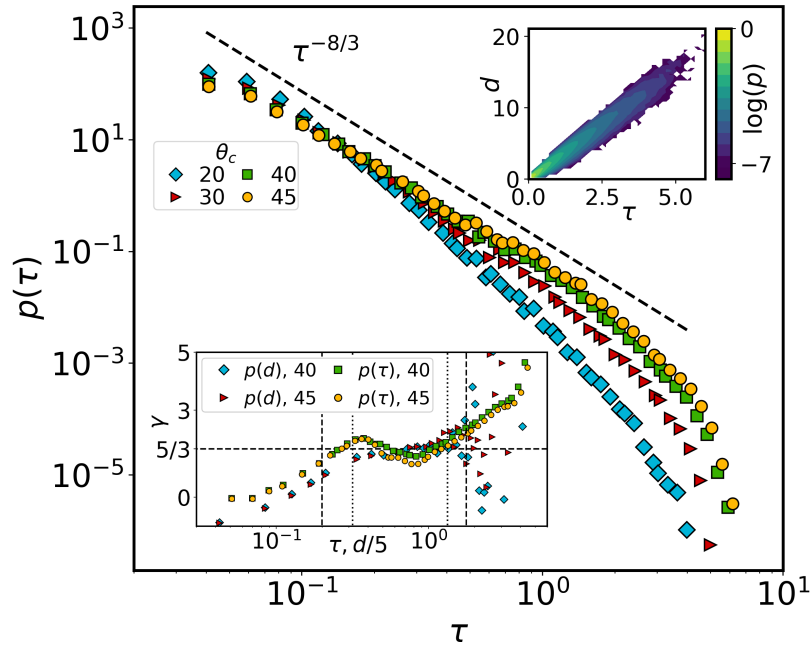


FIGURE 6.3: For highly active suspensions (Case G), probability distributions $p(\tau)$ of the waiting time τ with a $\tau^{-8/3}$ scaling (dashed line), as a guide to the eye, for different θ_c , see Fig. 6.2. (Lower inset) Local slope analysis of $p(\tau)$ and $p(d)$ (x-axis rescaled for visualisation) yields $\gamma = 1.7 \pm 0.3$ and $\gamma = 1.6 \pm 0.2$, respectively, consistent with Lévy walk estimates, showing a scaling range (between dashed ($p(\tau)$) and dotted ($p(d)$) vertical lines) for about a decade. (Upper inset) Joint probability distribution of d and τ confirming a finite velocity through the near linear relationship between the two.

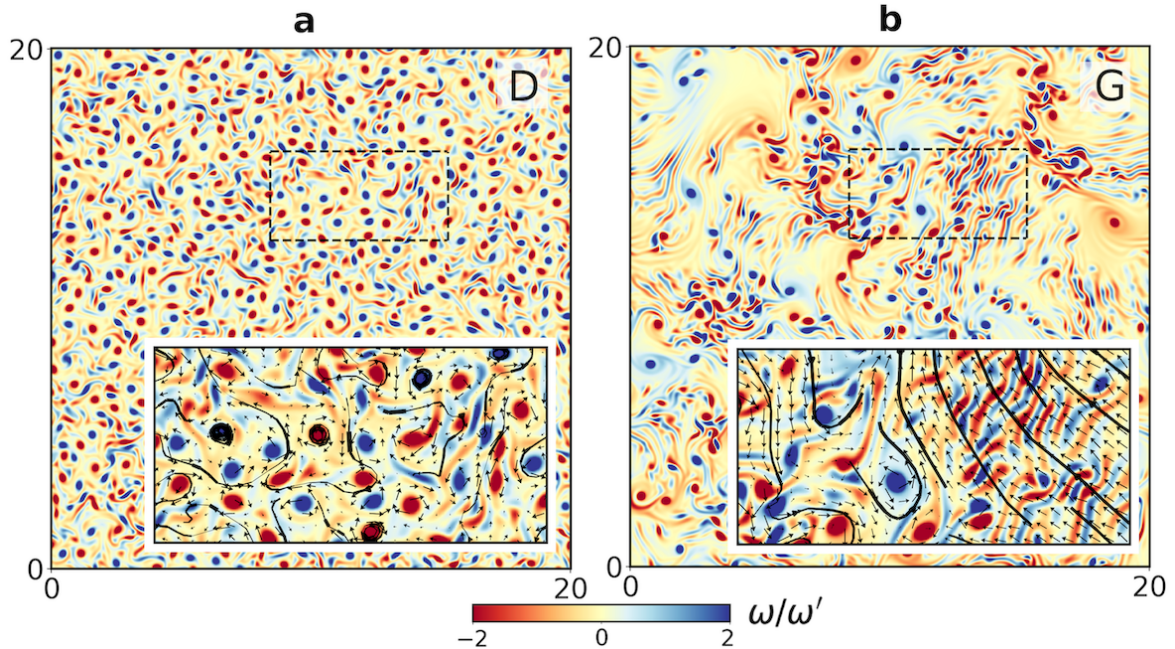


FIGURE 6.4: Representative snapshots of vorticity fields (and their magnified sections with velocity vectors as arrows and instantaneous streamlines as solid lines) for (a) Case D ($\alpha = -1$), and (b) Case G ($\alpha = -6$). In the latter, highly active suspensions a new feature shows up: The vorticity field is now populated by oscillatory *streaks* (see also Fig. 6.5).

6.7 Emergent Streaks

Does the emergence of (Lagrangian) anomalous scaling carry tell-tale signs in the vorticity field $\boldsymbol{\omega} = \nabla \times \mathbf{u}$? Figure 6.4 shows slices of the vorticity field, for Cases D and G. While the vorticity fields appear, overall, *disorganized*—active turbulence—a closer inspection reveals a pattern hitherto undetected. With increasing activity, the dense packing of diffused vortices, which mainly appear as *spots*, gives way to *sharper* spots with trailing wisps of vorticity *streaks* (Case D). For highly active suspensions (Case G), there is an equal preponderance of spots and streaks. Curiously, these streaks appear with alternating signs in a periodic fashion with a characteristic length scale δ .

The probability distribution of vorticity $p(\omega)$ is non-Gaussian (similarly to inertial turbulence) with fat tails which fall-off as a power-law, becoming more pronounced with increasing activity (see Fig. 1.4). This analogy with inertial turbulence extends to the energy spectrum scaling as $k^{-5/3}$ scaling at high activity (see Fig. 1.4).

Is there a causal link between the alternating *streaks* and the anomalous diffusion that we observe? Careful measurements certainly suggest so. While a definitive answer is beyond the scope of this work, the instantaneous, jet-like velocity and elongated streamlines, orthogonal to the streaks, (Fig. 6.4 insets) would in the absence of dynamics ensure the persistence of trajectories, often over lengths $\mathcal{O}(L/2)$ (consistent with the scaling extent in $p(d)$), while the vortical patches serve to reorient trajectories. Naively, this suggests streak regions as origins of anomalous diffusion, while their absence (low activity) leads to classical diffusion. Importantly, these streaks are distinct from the “laning” phenomena in some active suspensions [48]. In order to further test the role of streaks, we push the system to an *extreme* case (with $\alpha = -16.66$ and $\beta = 22.22$), which shows that the emergence of more distinct, pattern forming streaks (Fig. 6.5(a), with a magnified view in panel (b)) is accompanied by a robust super-diffusive $\Delta x^2 \sim t^{4/3}$ regime (Fig. 6.5(c)). Unsurprisingly, the trajectories reflect this anomalous diffusion through clear Lévy walks (see inset in Fig. 6.5(c)), and are also found to have power-law distributions of d and τ . Thus, we show that active systems are actually super-diffusive and what may be mistaken as a cross-over from ballistic to diffusive behaviour masks the most important and non-trivial aspects of such systems.

While the origin of the oscillatory streaks remains to be established, it seems reasonable to assume that the length scale δ , determining the alternating pattern of streaks, is influenced by the activity which sets the characteristic velocity for global polar ordering $v_0 = \sqrt{|\alpha|/\beta}$ [16]. Since the dominant time-scale is set by activity, $\delta \simeq 1/\sqrt{|\alpha|\beta}$.

Given the heuristic nature of this argument, we made careful measurements of the “wavelength” of the oscillations for a range of parameters and found that they are in reasonable agreement with our conjectured estimate. Why the system senses this length scale will perhaps be found when the origins of these oscillatory streaks are systematically known, and the question of universality (or not) of such oscillatory patterns for different classes of active systems is an important one. While the specific model [49] studied in this work seems to allow for an instability that triggers spatio-temporal chaotic states with bands of opposite polarities which show up as spots and streaks [50], the precise mechanisms involved are left for future work.

6.8 Conclusions

Nature exploits Lévy movements and anomalous diffusion, across scales, ranging from the microscopic to ecological [51], and across taxa, from systems comprising individual agents like midge swarms [52], migrating metastatic cancer cells [53], living cancer cells [54] and intracellular DNA transport [55], foraging marine predators [56] and expanding colonies of seemingly immobile beach grasses [57], to dense systems with collective flow states like swimming bacteria [14]. Yet, detecting Lévy walks theoretically in active turbulence has remained elusive, despite some experimental results strongly suggestive of their existence. While recent work using a particle-based active model [31] reconciles some of these findings, the lack of consistency with the most general hydrodynamic framework to describe active suspensions is surprising. We uncover why this is, showing that while it is true that anomalous diffusion is hardly detectable (though incipient in the light of our results) for mildly active suspensions, such systems exhibit distinct Lévy walks and super-diffusion when nudged to higher levels of activity.

Our observations of the vorticity spots and streaks, a basis of future theories of emergent anomalous diffusion, provide a template for clearly identifiable structures experimentally. Thus experiments would be able to probe how universal these patterns are, aiding a more robust understanding of why they emerge and whether they are central to the super-diffusive behaviour of such systems. Recent works, which derive the hydrodynamic model presented here from microswimmer dynamics, show that the activity is related, among other factors, to their individual motility [58, 59]. Thus high activity might be achieved by tuning the motility. A potential candidate for an experiment is a spermatozoa suspension [60], which also exhibit a turbulent phase [61] and whose motility can be controlled by changing the ambient temperature [62].

Finally, we underline what sets active turbulence apart from inertial fluid turbulence

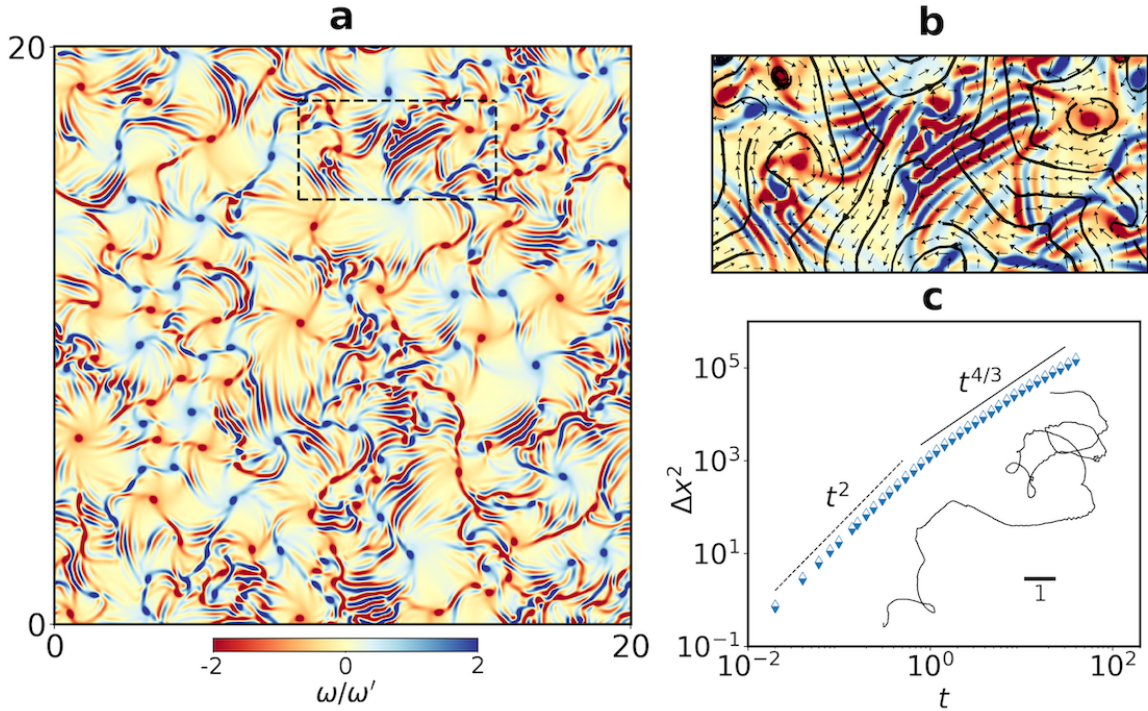


FIGURE 6.5: Extremely active suspensions shows that (a) the vorticity field is dominated by *streaks* interspersed with fewer vortical *spots* (magnified view in panel (b) with velocity vectors as arrows and instantaneous streamlines as solid lines) and is associated with (c) robust anomalous diffusion $\Delta x^2 \sim t^{4/3}$, reflected in a representative trajectory (inset).

and thus the limitations of drawing equivalences between the two. The Lagrangian picture, arising from our work, marks a crucial departure in the analogy in a rather counter-intuitive way. This is because for Eulerian statistics, increasing activity results in a *more intermittent* vorticity field and accompanying power-laws of energy spectra (6.6) like in two-dimensional fluid turbulence. However, this “*increasingly turbulent state*” in active systems is paradoxically accompanied by *persistent* super-diffusion, Lévy walks and structural changes in the vorticity field which have no known counterparts in inertial turbulence. It would be interesting, however, to see how this distinction manifests itself in other measurements such as pair-particle dispersion [63].

Before concluding, we recall that our MSD exponent $\xi \approx 4/3$ (at high activity) is consistent with those predicted for 1D Hamiltonian systems [64]. Whether this suggests a possible underlying universality is unclear. Recent theoretical studies of the walk time distribution [65, 66] show that local dynamics are central to super-diffusion with $\gamma = 3/2$. While we detect $\gamma \approx 5/3$, it is possible that this exponent is one of an intermediate asymptotics (in α) which may converge to $3/2$ for sufficiently high activity and diffusive behaviour appears as a pre-asymptotic correction to the asymptotic super-diffusive regime [67] that we report.

Our work suggests that activity is geared for manifesting optimality: Yet another way

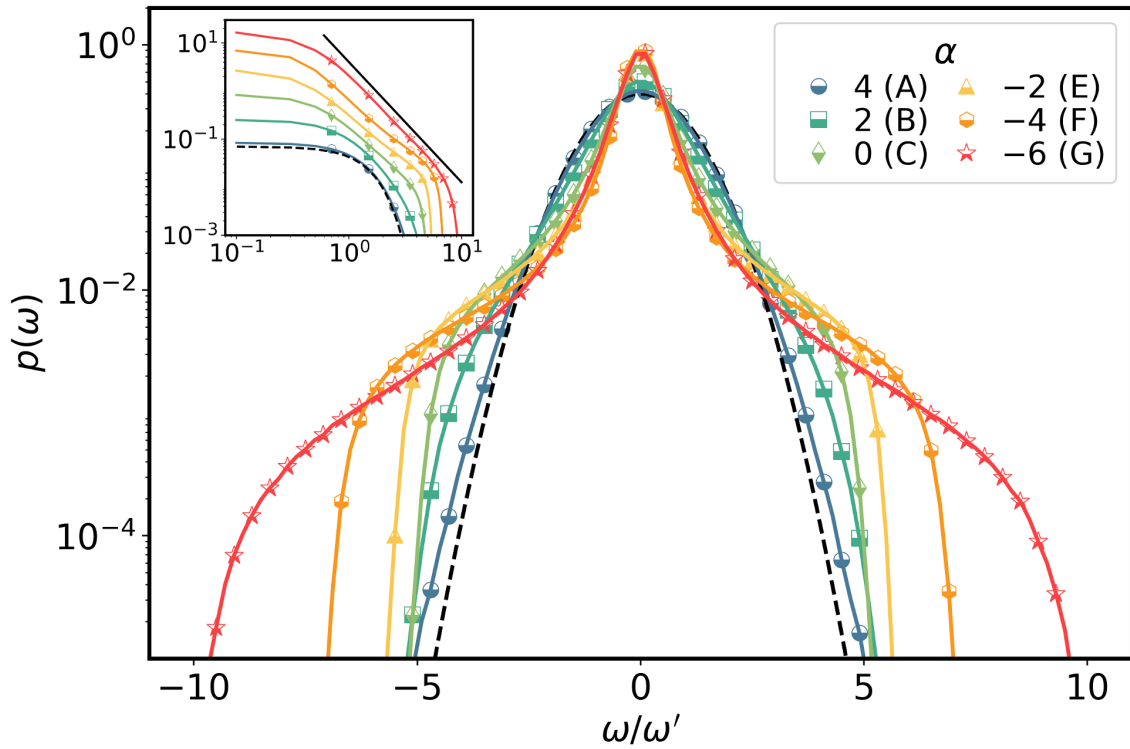


FIGURE 6.6: The statistics of the ω field is quantified by the probability density function $p(\omega)$ and it shows non-Gaussian, fat tails with power-laws (see inset, where the curves have been vertically staggered for clarity) as suspensions become more active. This increasing intermittency with higher activity is analogous to the effect of increasing Reynolds number in inertial turbulence.

biological systems continue to defy bounds on inanimate matter, now in a turbulence-like flow state. This gives new direction to the assessment of what is truly turbulent, and universal, in low Reynolds number active flows.

References

- [1] M. C. Marchetti, J.-F. Joanny, S. Ramaswamy, T. B. Liverpool, J. Prost, M. Rao et al., *Hydrodynamics of soft active matter*, *Reviews of Modern Physics* **85** (2013) 1143.
- [2] S. Ramaswamy, *Active matter*, *Journal of Statistical Mechanics: Theory and Experiment* **2017** (2017) 054002.
- [3] A. Doostmohammadi, J. Ignés-Mullol, J. M. Yeomans and F. Sagués, *Active nematics*, *Nature communications* **9** (2018) 1–13.
- [4] A. Shellard and R. Mayor, *Rules of collective migration: from the wildebeest to the neural crest*, *Philosophical Transactions of the Royal Society B* **375** (2020) 20190387.
- [5] S. Humphries, *Filter feeders and plankton increase particle encounter rates through flow regime control*, *Proceedings of the National Academy of Sciences* **106** (2009) 7882–7887.
- [6] K. C. Leptos, J. S. Guasto, J. P. Gollub, A. I. Pesci and R. E. Goldstein, *Dynamics of enhanced tracer diffusion in suspensions of swimming eukaryotic microorganisms*, *Physical Review Letters* **103** (2009) 198103.
- [7] A. Lagarde, N. Dagès, T. Nemoto, V. Démery, D. Bartolo and T. Gibaud, *Colloidal transport in bacteria suspensions: from bacteria collision to anomalous and enhanced diffusion*, *Soft Matter* **16** (2020) 7503–7512.
- [8] N. E. Humphries, N. Queiroz, J. R. Dyer, N. G. Pade, M. K. Musyl, K. M. Schaefer et al., *Environmental context explains lévy and brownian movement patterns of marine predators*, *Nature* **465** (2010) 1066–1069.
- [9] G. Volpe and G. Volpe, *The topography of the environment alters the optimal search strategy for active particles*, *Proceedings of the National Academy of Sciences* **114** (2017) 11350–11355.
- [10] J. Klafter and I. M. Sokolov, *Anomalous diffusion spreads its wings*, *Physics world* **18** (2005) 29.

- [11] F. Bartumeus, J. Catalan, U. Fulco, M. Lyra and G. Viswanathan, *Optimizing the encounter rate in biological interactions: Lévy versus brownian strategies*, *Physical Review Letters* **88** (2002) 097901.
- [12] A. Reynolds, *Liberating lévy walk research from the shackles of optimal foraging*, *Physics of life reviews* **14** (2015) 59–83.
- [13] D. Knebel, C. Sha-Ked, N. Agmon, G. Ariel and A. Ayali, *Collective motion as a distinct behavioral state of the individual*, *Iscience* **24** (2021) 102299.
- [14] G. Ariel, A. Rabani, S. Benisty, J. D. Partridge, R. M. Harshey and A. Be’Er, *Swarming bacteria migrate by lévy walk*, *Nature communications* **6** (2015) 1–6.
- [15] C. Dombrowski, L. Cisneros, S. Chatkaew, R. E. Goldstein and J. O. Kessler, *Self-concentration and large-scale coherence in bacterial dynamics*, *Physical Review Letters* **93** (2004) 098103.
- [16] H. H. Wensink, J. Dunkel, S. Heidenreich, K. Drescher, R. E. Goldstein, H. Löwen et al., *Meso-scale turbulence in living fluids*, *Proceedings of the National Academy of Sciences* **109** (2012) 14308–14313.
- [17] J. Dunkel, S. Heidenreich, K. Drescher, H. H. Wensink, M. Bär and R. E. Goldstein, *Fluid dynamics of bacterial turbulence*, *Physical Review Letters* **110** (2013) 228102.
- [18] S. Zhou, A. Sokolov, O. D. Lavrentovich and I. S. Aranson, *Living liquid crystals*, *Proceedings of the National Academy of Sciences* **111** (2014) 1265–1270.
- [19] K.-T. Wu, J. B. Hishamunda, D. T. Chen, S. J. DeCamp, Y.-W. Chang, A. Fernández-Nieves et al., *Transition from turbulent to coherent flows in confined three-dimensional active fluids*, *Science* **355** (2017) .
- [20] B. Martínez-Prat, J. Ignés-Mullol, J. Casademunt and F. Sagués, *Selection mechanism at the onset of active turbulence*, *Nature Physics* **15** (2019) 362–366.
- [21] L. Giomi, *Geometry and topology of turbulence in active nematics*, *Physical Review X* **5** (2015) 031003.
- [22] M. James, W. J. Bos and M. Wilczek, *Turbulence and turbulent pattern formation in a minimal model for active fluids*, *Physical Review Fluids* **3** (2018) 061101.
- [23] M. James and M. Wilczek, *Vortex dynamics and lagrangian statistics in a model for active turbulence*, *The European Physical Journal E* **41** (2018) 1–6.

-
- [24] V. Bratanov, F. Jenko and E. Frey, *New class of turbulence in active fluids*, *Proceedings of the National Academy of Sciences* **112** (2015) 15048–15053.
- [25] R. Alert, J.-F. Joanny and J. Casademunt, *Universal scaling of active nematic turbulence*, *Nature Physics* **16** (2020) 682–688.
- [26] R. Alert, J. Casademunt and J.-F. Joanny, *Active turbulence*, *arXiv preprint arXiv:2104.02122* (2021) , [2104.02122].
- [27] H. Xia, N. Francois, H. Punzmann and M. Shats, *Lagrangian scale of particle dispersion in turbulence*, *Nature communications* **4** (2013) 1–8.
- [28] X.-L. Wu and A. Libchaber, *Particle diffusion in a quasi-two-dimensional bacterial bath*, *Physical review letters* **84** (2000) 3017.
- [29] H. Kurtuldu, J. S. Guasto, K. A. Johnson and J. P. Gollub, *Enhancement of biomixing by swimming algal cells in two-dimensional films*, *Proceedings of the National Academy of Sciences* **108** (2011) 10391–10395.
- [30] A. Morozov and D. Marenduzzo, *Enhanced diffusion of tracer particles in dilute bacterial suspensions*, *Soft Matter* **10** (2014) 2748–2758.
- [31] K. Kanazawa, T. G. Sano, A. Cairoli and A. Baule, *Loopy lévy flights enhance tracer diffusion in active suspensions*, *Nature* **579** (2020) 364–367.
- [32] J. Dunkel, S. Heidenreich, M. Bär and R. E. Goldstein, *Minimal continuum theories of structure formation in dense active fluids*, *New Journal of Physics* **15** (2013) 045016.
- [33] J. Swift and P. C. Hohenberg, *Hydrodynamic fluctuations at the convective instability*, *Physical Review A* **15** (1977) 319.
- [34] R. A. Simha and S. Ramaswamy, *Hydrodynamic fluctuations and instabilities in ordered suspensions of self-propelled particles*, *Physical review letters* **89** (2002) 058101.
- [35] M. Linkmann, M. C. Marchetti, G. Boffetta and B. Eckhardt, *Condensate formation and multiscale dynamics in two-dimensional active suspensions*, *Physical Review E* **101** (2020) 022609.
- [36] J. Toner and Y. Tu, *Long-range order in a two-dimensional dynamical XY model: How birds fly together*, *Phys. Rev. Lett.* **75** (Dec, 1995) 4326–4329.
- [37] J. Toner and Y. Tu, *Flocks, herds, and schools: A quantitative theory of flocking*, *Phys. Rev. E* **58** (Oct, 1998) 4828–4858.

- [38] S. C.P. and A. Joy, *Friction scaling laws for transport in active turbulence*, *Physical Review Fluids* **5** (2020) 024302.
- [39] G. Ariel, A. Be'er and A. Reynolds, *Chaotic model for lévy walks in swarming bacteria*, *Phys. Rev. Lett.* **118** (Jun, 2017) 228102.
- [40] G. Ariel and J. Schiff, *Conservative, dissipative and super-diffusive behavior of a particle propelled in a regular flow*, *Physica D: Nonlinear Phenomena* **411** (2020) 132584.
- [41] D. Panja, G. T. Barkema and R. C. Ball, *Complex interactions with the surroundings dictate a tagged chain's dynamics in unentangled polymer melts*, *Macromolecules* **48** (Mar, 2015) 1442–1453.
- [42] J. van der Hoeven, *On asymptotic extrapolation*, *Journal of Symbolic Computation* **44** (2009) 1000–1016.
- [43] W. Pauls and U. Frisch, *A borel transform method for locating singularities of taylor and fourier series*, *Journal of Statistical Physics* **127** (Jun, 2007) 1095–1119.
- [44] C. Bardos, U. Frisch, W. Pauls, S. S. Ray and E. S. Titi, *Entire solutions of hydrodynamical equations with exponential dissipation*, *Communications in Mathematical Physics* **293** (Jan, 2010) 519–543.
- [45] S. Chakraborty, U. Frisch, W. Pauls and S. S. Ray, *Nelkin scaling for the burgers equation and the role of high-precision calculations*, *Phys. Rev. E* **85** (Jan, 2012) 015301.
- [46] V. Zaburdaev, S. Denisov and J. Klafter, *Lévy walks*, *Reviews of Modern Physics* **87** (2015) 483.
- [47] There are of course examples of more generalised Lévy walks, such as those seen in the anomalous diffusion of cold atoms in optical lattices, where this linear relation fails [? ?].
- [48] H. H. Wensink and H. Löwen, *Emergent states in dense systems of active rods: from swarming to turbulence*, *Journal of Physics: Condensed Matter* **24** (oct, 2012) 464130.
- [49] L. Chen, C. F. Lee and J. Toner, *Mapping two-dimensional polar active fluids to two-dimensional soap and one-dimensional sandblasting*, *Nature Communications* **7** (Jul, 2016) 12215.
- [50] A. Maitra. Private Communication, 2021.

- [51] A. M. Reynolds, *Current status and future directions of lévy walk research*, *Biology open* **7** (2018) .
- [52] A. M. Reynolds and N. T. Ouellette, *Swarm dynamics may give rise to lévy flights*, *Scientific reports* **6** (2016) 1–8.
- [53] S. Huda, B. Weigelin, K. Wolf, K. V. Tretiakov, K. Polev, G. Wilk et al., *Lévy-like movement patterns of metastatic cancer cells revealed in microfabricated systems and implicated in vivo*, *Nature communications* **9** (2018) 1–11.
- [54] N. Gal and D. Weihs, *Experimental evidence of strong anomalous diffusion in living cells*, *Phys. Rev. E* **81** (Feb, 2010) 020903.
- [55] A. Muralidharan, H. Uitenbroek and P. E. Boukany, *Intracellular transport of electrotransferred dna cargo is governed by coexisting ergodic and non ergodic anomalous diffusion*, *bioRxiv* (2021) .
- [56] D. W. Sims, E. J. Southall, N. E. Humphries, G. C. Hays, C. J. Bradshaw, J. W. Pitchford et al., *Scaling laws of marine predator search behaviour*, *Nature* **451** (2008) 1098–1102.
- [57] V. C. Reijers, K. Siteur, S. Hoeks, J. van Belzen, A. C. Borst, J. H. Heusinkveld et al., *A lévy expansion strategy optimizes early dune building by beach grasses*, *Nature communications* **10** (2019) 1–9.
- [58] S. Heidenreich, J. Dunkel, S. H. Klapp and M. Bär, *Hydrodynamic length-scale selection in microswimmer suspensions*, *Physical Review E* **94** (2016) 020601.
- [59] H. Reinken, S. H. Klapp, M. Bär and S. Heidenreich, *Derivation of a hydrodynamic theory for mesoscale dynamics in microswimmer suspensions*, *Physical Review E* **97** (2018) 022613.
- [60] M. James, D. A. Suchla, J. Dunkel and M. Wilczek, *Emergence and melting of active vortex crystals*, *arXiv preprint arXiv:2005.06217* (2020) , [2005.06217].
- [61] A. Creppy, O. Praud, X. Druart, P. L. Kohnke and F. Plouraboué, *Turbulence of swarming sperm*, *Physical Review E* **92** (2015) 032722.
- [62] S. M. H. Alavi and J. Cosson, *Sperm motility in fishes. i. effects of temperature and ph: a review*, *Cell biology international* **29** (2005) 101–110.
- [63] G. Boffetta and A. Celani, *Pair dispersion in turbulence*, *Physica A: Statistical Mechanics and its Applications* **280** (2000) 1–9.

-
- [64] H. Spohn, *Nonlinear fluctuating hydrodynamics for anharmonic chains*, *J Stat Phys* **154** (2014) 1191.
- [65] A. Miron, *Universality in the onset of superdiffusion in lévy walks*, *Phys. Rev. Lett.* **124** (Apr, 2020) 140601.
- [66] A. Miron, *Origin of universality in the onset of superdiffusion in lévy walks*, *Phys. Rev. Research* **2** (Aug, 2020) 032042.
- [67] A. Miron. Private Communication, 2021.

Chapter 7

Conclusions and Outlook

In this Chapter we summarise the central results of this thesis as well as discuss briefly possible outcomes which stem from these studies.

As we stressed in the introductory chapter, this thesis is in two parts: In the first, properties of filaments in classical, high Reynolds number inertial turbulence was studied while the second dealt with problems in low Reynolds number active turbulence. The central theme which connects these two, perhaps disparate, halves is the use of techniques to understand the Lagrangian aspects of these systems.

The study, theoretical and experimental, of extended—beyond the dissipation scale of the flow—filaments and fibers in turbulent flows is fairly recent. In this thesis, we adapt the bead-spring model to incorporate inertial drag, elasticity and bending stiffness to model elastic filaments and immerse them in fully developed turbulent flows in two and three dimensions.

In the absence of inertia, such filaments are known to preferentially sample the vortical regions of the flow unlike an *ensemble* of tracers without elastic interactions which distribute themselves homogeneously. This novel and somewhat dramatic behaviour was first noted by Picardo *et al.* [Picardo, Vincenzi, Pal and Ray, Phys. Rev. Lett. **121**, 244501 (2018)] in a two-dimensional turbulent flow which has the advantage of long-lived vortical structures where such chains can coil up and remain trapped. In this thesis, we examined if such preferential sampling still holds in three-dimensional flows where the vortex tubes can cause rapid stretching of the chains as opposed to the coiling mechanism which dominates when filaments are trapped in the vortices of two-dimensional turbulence. We showed that indeed a similar preferential sampling is seen when inertia-less, elastic filaments are carried by a three-dimensional turbulent flows. However, the mechanism and the origin of this is completely different from what compels preferential sampling in two dimensions: In two dimensions, a filament coils and shrinks and thence gets trapped inside a vortex while in three dimensions,

they align themselves along tubular vortices and remain stretched inside them. The latter is a consequence of the vortex stretching mechanism in three-dimensional flows. Furthermore, stiffness of the filaments play a marginal role in determining its dynamics.

Elasticity is the dominant mechanism for filaments formed from a string of tracers connected with elastic springs. However, for a more realistic model, we make our beads inertial while factoring in the Stokesian drag on such spheres. This now becomes a model where the competing and contrasting effects of inertia and elasticity can be studied systematically: For example, in a two-dimensional flow, the inertia of the beads would lead to their centrifugal expulsion from vortices while, as discussed above, the elasticity of the springs would tend to keep them trapped. We first studied this interplay of inertia and elasticity in two-dimensional turbulent flows which results in a non-trivial sampling of the flow as discussed in the thesis. Furthermore, these studies were conducted both for filaments with uniformly distributed mass and those which had a heavy head attached to an inertia-less, elastic tail. A more detailed study of this phenomenon was carried out in three-dimensional turbulent flows including the chaotic nature of the trajectories of individual filaments through standard Lagrangian techniques.

Our model of inertial filaments are perhaps the simplest prototype for marine debris with additional degrees of freedom. Hence, the final problem that was investigated in this thesis was the how such filaments tend to settle under gravity, in a three-dimensional turbulent flow, and the influence of elasticity and inertia on one hand (which leads to a non-trivial sampling of the flow field) and the competition between turbulent accelerations and that due to gravity on the other. We investigate the dynamics of these long, elastic, inertial filaments in 3D turbulence as they settle under gravity in Chapter 4. We find that the settling of filaments under gravity and the complicated tumbling motion they undergo as they settle are complementary to each other: Fluctuations in the settling velocity of a filament, up to the leading order, is determined only by its weight (inertia coupled with gravity) whereas the rate of tumbling is determined only by elasticity and the consequent stretching of the filament. We also show that for filaments with bending stiffness our central results remain qualitatively unchanged, although stiff filaments settle and tumble slower than fully-flexible ones.

Through our work in this thesis it is clear that inertia and elasticity are characteristics that are critical in determining the dynamics of long filaments in turbulent flows. In this thesis, we considered a minimal model of a filament that incorporates only inertia and elasticity and disregards effects such as intra-chain and inter-chain hydrodynamic interactions, excluded volume interactions or their back reaction to the

turbulent flow. The effects of these on the dynamics of our filaments still remains to be investigated and is crucial for more realistic modelling of chains and filaments. Furthermore, our filaments can be used to model active, filamentary (micro) organisms in marine environments which are self-propelled and whose motion is influenced by the strong fluctuations in the carrier turbulent flow as well as served as a basis for complex models of fibres with a non-uniform mass distribution.

The second half of this thesis dealt with problems in extremely low Reynolds number flows. Indeed, the emergent fluid behaviour of two-dimensional, dense suspensions of motile bacteria is susceptible to a wide range of dynamical phases making their characterisation quite distinct from our more accustomed understanding of (classical) inertial fluids. Amongst the different dynamical phases, in this thesis we investigated the Lagrangian properties of the active turbulence regime by using a coarse-grained hydrodynamic description of such suspensions.

Whilst staying true to the observed activities in experiments, we showed that highly active suspensions are fundamentally different from moderately active ones. In particular, our work reveals that for extreme activity these flows display anomalous diffusion in measurements of mean-square-displacements of single Lagrangian particles. The anomalous diffusion in such flows, while having some experimental validation, has been a subject of some debate. In this thesis we showed not only the robustness of this prediction but also the accompanying Lévy walks which characterise the motion of these tracers. Furthermore, the persistent nature of Lagrangian trajectories in such systems lead to anomalous transport which reflect in more accustomed measures of pair dispersion and first passage times. We also identified (and characterised) that at the heart of anomalous transport in active turbulence is the emergence of novel structures, christened *streaks* and hitherto unseen in both high and low Reynolds number flows, which propels tracers in a coherent and persistent manner. It is this which causes passive tracers in the flow to superdiffuse via Lévy walks rather than undergoing simple diffusion.

Our work underlines features that distinguish active and classical inertial fluid turbulence. Critically, it also points to a possible asymptotic state for extremely active turbulent flows. On the theoretical side, it remains to be seen if there is indeed a crossover or critical degree of activity where such states emerge. And if there is one, the issue of universality and intermittency of such states need to be investigated in future studies. Indeed, it is conceivable that the non-universality of the spectral exponent [Bratanov, Jenko, and Frey, PNAS **112**, 15048 (2015)] in active turbulence is perhaps valid only at low values of activity and the arguments leading to such a conclusion no longer holds under extreme activity. This thesis also stops short of investigating the

precise mechanisms which gives rise to the streaks. Starting with the coarse-grained hydrodynamic description used in these studies, the theory of why such streaks appear remains to be worked out. In parallel to these open, theoretical questions, the work suggests precise experimental measurements. We hope that this thesis provides the necessary impetus to develop experiments—in-house or elsewhere—which will focus on the new emergent states of active turbulence as identified from our Lagrangian studies.

Appendix A

Variance of the Settling Velocity

For our filaments transported by a turbulent flow under gravity, we have in the settling regime, that $\langle a_z \rangle = \langle \ddot{x}_z \rangle = 0$. We also have using Eq. (4.2) that:

$$\begin{aligned} \langle v_z \rangle &= \frac{1}{N_b} \left\langle \sum_{j=1}^{N_b} u_z(\mathbf{x}_j) \right\rangle + \frac{A}{N_b} \left\langle \sum_{j=1}^{N_b} \xi_{z,j} \right\rangle - \tau_p g \\ \Rightarrow \langle v_z \rangle &= \langle \bar{u}_z \rangle - \tau_p g ; \quad \bar{u}_z = \frac{1}{N_b} \sum_{j=1}^{N_b} u_z(\mathbf{x}_j) \end{aligned} \quad (\text{A.1})$$

which using the definition of enhancement in settling velocity $\Delta_V = \langle v_z \rangle / \tau_p g - 1 = -\langle u_z \rangle / \tau_p g$ gives:

$$\langle v_z \rangle = \langle \bar{u}_z \rangle - \tau_p g = -(1 + \Delta_V)(\tau_p g) \quad (\text{A.2})$$

The variance in settling velocity is defined as $\langle v_z^2 \rangle - \langle v_z \rangle^2$. We obtain the expression for the variance using Eq. (4.2) as below:

$$\begin{aligned} \tau_p^2 \langle a_z^2 \rangle &= \langle (\bar{u}_z - v_z)^2 \rangle + \tau_p^2 g^2 + A^2 \langle \bar{\xi}_z^2 \rangle - 2\tau_p g \langle \bar{u}_z - v_z \rangle + 2A \langle \bar{\xi}_z (\bar{u}_z - v_z) \rangle \\ &= \langle \bar{u}_z^2 + v_z^2 - 2\bar{u}_z v_z \rangle - \tau_p^2 g^2 + A^2 \langle \bar{\xi}_z^2 \rangle - 2A \langle \bar{\xi}_z v_z \rangle \\ &= \langle \bar{u}_z^2 + v_z^2 \rangle - \tau_p^2 g^2 + A^2 \langle \bar{\xi}_z^2 \rangle - 2\langle (\bar{u}_z + A\bar{\xi}_z) v_z \rangle \\ &= \langle \bar{u}_z^2 + v_z^2 \rangle - \tau_p^2 g^2 + A^2 \langle \bar{\xi}_z^2 \rangle + 2\langle (\bar{u}_z + A\bar{\xi}_z)(\tau_p a_z - \bar{u}_z - A\bar{\xi}_z + \tau_p g) \rangle \\ \Rightarrow \langle v_z^2 \rangle &= \tau_p^2 \langle a_z^2 \rangle + \langle \bar{u}_z^2 \rangle + \tau_p^2 g^2 + A^2 \langle \bar{\xi}_z^2 \rangle + 4A \langle \bar{\xi}_z \bar{u}_z \rangle \\ &\quad - 2\tau_p \langle a_z (\bar{u}_z + A\bar{\xi}_z) \rangle - 2\tau_p g \langle \bar{u}_z \rangle \end{aligned} \quad (\text{A.3})$$

where overbars denote averaged values over a filament and $\langle \cdot \rangle$ denotes ensemble averages and average over time. We note that ξ 's are zero-mean, independent, white Gaussian noises with unit variance. So, the terms with $\langle \bar{\xi}_z \rangle$ drop out. And we obtain

the mean-square contribution from noise as

$$\begin{aligned}\langle \bar{\xi}_z^2 \rangle &= \frac{1}{N_b^2} \sum_{j=1}^{N_b} \sum_{k=1}^{N_b} \langle \xi_{j,z}(t) \xi_{k,z}(t') \rangle \\ &= \frac{1}{N_b^2} \sum_{j=1}^{N_b} \sum_{k=1}^{N_b} \delta_{j,k} \delta(t-t') = \frac{1}{N_b} \delta(t-t') = C \delta(t-t')\end{aligned}\quad (\text{A.4})$$

The normalized variance $\sigma = (\langle v_z^2 \rangle - \langle v_z \rangle^2) / \langle v_z \rangle^2 = \langle v_z^2 \rangle / \langle v_z \rangle^2 - 1$. We have using (A.2), (A.4) in Eq. (A.3):

$$\begin{aligned}\langle v_z^2 \rangle &= \tau_p^2 \langle a_z^2 \rangle + \langle \bar{u}_z^2 \rangle + \tau_p^2 g^2 + CA^2 - 2\tau_p \langle a_z (\bar{u}_z + A\bar{\xi}_z) \rangle + 2\Delta_V (\tau_p g)^2 \\ \Rightarrow \frac{\langle v_z^2 \rangle}{\langle v_z \rangle^2} - 1 &= \frac{\tau_p^2 \langle a_z^2 \rangle + \langle \bar{u}_z^2 \rangle + CA^2 - 2\tau_p \langle a_z (\bar{u}_z + A\bar{\xi}_z) \rangle - \Delta_V^2 (\tau_p g)^2}{[(1 + \Delta_V) \tau_p g]^2}\end{aligned}\quad (\text{A.5})$$

Using $\Delta_V < 1$ and assuming $\tau_p \langle a_z (\bar{u}_z + A\bar{\xi}_z) \rangle$ has a very small contribution:

$$\sigma \approx \frac{\tau_p^2 \langle a_z^2 \rangle + \langle \bar{u}_z^2 \rangle + CA^2}{(\tau_p g)^2} = \left[\frac{\langle \bar{u}_z^2 \rangle + CA^2}{(a_\eta \tau_\eta)^2} + St^2 \frac{\langle a_z^2 \rangle}{a_\eta^2} \right] \left(\frac{St}{Fr} \right)^{-2}\quad (\text{A.6})$$

Appendix B

First Passage Time Distribution

We begin by writing the Fokker-Planck (diffusion) equation:

$$\partial_t p(r, t) = K_d \nabla^2 p(r, t) \quad (\text{B.1})$$

We assuming a solution of the form $p(r, t) = u(r)f(t)$ yields separate differential equations for the temporal and radial parts:

$$\frac{1}{K_d} \frac{f'}{f} = -C^2 = \frac{u''}{u} + \frac{u'}{ru}$$

which have solutions of the form:

$$f(t) = f_0 e^{-C^2 K_d t}; \quad u(s) = J_0(s) = \sum_{n=0}^{\infty} \frac{(-1)^n}{(n!)^2} \left(\frac{s}{2}\right)^{2n}$$

where $f_0 = f(t)|_{t=0}$, $s = Cr$ and J_0 is the Bessel function of the first kind and order zero. The absorbing boundary condition $u(R, t) = 0$ yields the equation

$$J_0(CR) = \sum_{n=0}^{\infty} \frac{(-1)^n}{(n!)^2} \left(\frac{CR}{2}\right)^{2n} = 0 \quad (\text{B.2})$$

If h_i be zeros of Bessel J_0 , where $i = 1, 2, 3, \dots$, we have constants $C_i = h_i/R$ that solve Eq. (B.2). Thus, the general solution is given by the linear combination of all possible solutions:

$$u(r) = \sum_{i=0}^{\infty} J_0(C_i r) = \sum_{i=0}^{\infty} J_0\left(\frac{h_i r}{R}\right) \quad (\text{B.3})$$

The distribution $p(r, t)$ is now given as:

$$p(r, t) = f_0 \sum_{i=1}^{\infty} e^{-K_d h_i^2 t / R^2} J_0\left(\frac{h_i r}{R}\right) \quad (\text{B.4})$$

Now, we use the initial condition to set the constant f_0 in the temporal part $f(t)$:

$$\begin{aligned}
2\pi f_0 \int_0^R p(r, 0) r dr &= 1 \\
\Rightarrow 2\pi f_0 \sum_{i=0}^{\infty} \int_0^R J_0(C_i r) r dr &= 1 \\
\Rightarrow 2\pi f_0 \sum_{i=0}^{\infty} \frac{R}{C_i} J_1(C_i R) &= 1 \\
\Rightarrow f_0 &= \frac{1}{2\pi R^2 \left(\sum_i \frac{J_1(h_i)}{h_i} \right)}
\end{aligned}$$

where we have used $C_i = h_i/R$ and J_1 is the Bessel function of first kind and order one. We, thus, have the probability distribution of tracers as:

$$p(r, t) = \frac{1}{2\pi R^2 \left(\sum_i \frac{J_1(h_i)}{h_i} \right)} \sum_i J_0\left(\frac{h_i r}{R}\right) e^{-h_i K_d t / R^2}; \quad (\text{B.5})$$

Now, the probability $S(t)$ that a tracer survives being absorbed by the boundary R until time t is total probability of tracers being in the region $(0, R)$:

$$S(t) = \int_0^R p(r, t) 2\pi r dr = \sum_i e^{-h_i K_d t / R^2} \frac{J_1(h_i)}{h_i} \quad (\text{B.6})$$

The probability that a tracer hits the boundary at R for the first time at $t = t_R$ is simply the probability that it survives until time t_R but is absorbed in an interval dt after that:

$$\begin{aligned}
P(R, t_R) dt &= [S(t) - S(t + dt)] \Big|_{t=t_R} \\
\Rightarrow P(R, t_R) &= -\frac{\partial S}{\partial t}
\end{aligned} \quad (\text{B.7})$$

The first passage time distribution $P(R, t_R)$ is then directly obtained using the expression for the survival probability from (B.6):

$$P(R, t_R) = -\partial_t S|_{t=t_R} = \frac{K_d}{R^2} \sum_i e^{-h_i K_d t_R / R^2} J_1(h_i) \quad (\text{B.8})$$

The dominant contribution to the first passage distribution comes from the smallest $h_i (= h_i^*)$: $P(R, t_R) \sim \frac{K_d}{R^2} e^{-h_i^* K_d t_R / R^2}$.

Appendix C

The Adams-Bashforth Method

In this Appendix we outline the numerical scheme used for time integration of the Navier-Stokes equation. (1.1) in 3D. For clarity let us consider the following ordinary differential equation (ODE):

$$\frac{df}{dt} = -\alpha f + h(t). \quad (\text{C.1})$$

For an ODE of the form above, we have the identity :

$$e^{\alpha(t+\delta t)} f(t + \delta t) - e^{\alpha t} = \int_t^{t+\delta t} e^{\alpha s} h(s) ds. \quad (\text{C.2})$$

The slaved scheme is obtained by first writing down the equation for $q(t)$ and $q(t - \delta t)$; we then add the two to obtain :

$$f(t + \delta t) = e^{-2\alpha\delta t} f(t - \delta t) + \int_{t-\delta t}^{t+\delta t} e^{-\alpha(t+\delta t-s)} h(s) ds. \quad (\text{C.3})$$

It is now reasonable to approximate $h(s)$ by either replacing $h(s)$ by $h(t)$ (the slaved-frog scheme) or by making the substitution $f(s) = (3/2)f(t) - (1/2)f(t - \delta t)$. The former yields the solution

$$f(t + \delta t) = e^{-2\alpha\delta t} f(t - \delta t) + \frac{1 - e^{-2\alpha\delta t}}{\alpha} h(t); \quad (\text{C.4})$$

the latter yields the slaved Adams-Bashforth scheme

$$f(t + \delta t) = e^{-2\alpha\delta t} f(t - \delta t) + \frac{1 - e^{-2\alpha\delta t}}{\alpha} \left[\frac{3}{2} h(t) - \frac{1}{2} h(t - \delta t) \right] \quad (\text{C.5})$$

Appendix D

Algorithm for the Eulerian Code

We discuss the pseudo-spectral algorithm used in our thesis to solve two- and three-dimensional, inertial turbulence and two-dimensional active turbulence. For simplicity, we consider the Navier-Stokes equation in 2D with periodic boundary conditions. We work in the vorticity (ω) – stream function (ψ) formulation. The velocity \mathbf{u} is a function of the x and y coordinates only. The pseudo-scalar vorticity is given by Eq. (1.32) which we rewrite for completeness:

$$\omega \equiv \nabla \times \mathbf{u}. \quad (\text{D.1})$$

The incompressibility constraint

$$\partial_x u_x + \partial_y u_y = 0 \quad (\text{D.2})$$

ensures that the velocity is uniquely determined by the stream-function via

$$\mathbf{u} \equiv (-\partial_y \psi, \partial_x \psi). \quad (\text{D.3})$$

The Navier-Stokes equation, in the $\omega - \psi$ formulation, can be written as follows :

$$\partial_t \omega - J(\psi, \omega) = \nu \nabla^2 \omega + f; \quad (\text{D.4})$$

$$\nabla^2 \psi = \omega; \quad (\text{D.5})$$

here

$$J(\psi, \omega) \equiv (\partial_x \psi)(\partial_y \omega) - (\partial_x \omega)(\partial_y \psi). \quad (\text{D.6})$$

Our pseudospectral DNS proceeds along the following lines :

We first write the Navier-Stokes equation in the following equivalent form :

$$\hat{\psi} = -\frac{1}{k^2} \hat{\omega}; \quad (\text{D.7})$$

$$\partial_t \omega + \partial_x(u_x \omega) + \partial_y(u_y \omega) = \nu \nabla^2 \omega + f, \quad (\text{D.8})$$

where u_x and u_y are, respectively, the x and y component of the velocity vector \mathbf{u} . f is the source function or the forcing. The spatial Fourier transform of this equation is

$$\partial_t \hat{\omega} = i(k_x \widehat{u_x \omega} + k_y \widehat{u_y \omega}) - \nu k^2 \hat{\omega} \quad (\text{D.9})$$

where carets denote Fourier transforms. Our algorithm proceeds via the following steps:

1. Start with $\hat{\omega}$ in Fourier space.
2. Evaluate the stream function $\hat{\psi}$ and from it the velocities in Fourier space \hat{u}_x and \hat{u}_y :

$$\hat{\psi} = -\frac{1}{k^2} \hat{\omega}; \quad (\text{D.10})$$

$$\hat{u}_x = ik_y \hat{\psi}; \quad (\text{D.11})$$

$$\hat{u}_y = -ik_x \hat{\psi}. \quad (\text{D.12})$$

$$(\text{D.13})$$

3. Inverse Fourier Transform (IFT) $\hat{\omega}$ to real space ω . IFT $\hat{u}_x \rightarrow u_x$ and $\hat{u}_y \rightarrow u_y$.
4. Evaluate ωu_x and ωu_y in real space.
5. Fourier Transform (FT) $\omega u_x \rightarrow \widehat{\omega u_x}$ and $\omega u_y \rightarrow \widehat{\omega u_y}$. Let us define

$$\hat{\mathcal{N}} = i(k_x \widehat{u_x \omega} + k_y \widehat{u_y \omega}). \quad (\text{D.14})$$

Then the evolution eqn. (D.9) becomes:

$$\partial_t \hat{\omega} = \hat{\mathcal{N}} - \nu k^2 \hat{\omega}. \quad (\text{D.15})$$

6. We now solve this equation by using the second-order Runge–Kutta scheme. Eq. (D.15) can be written as

$$\partial_t (e^{\nu k^2 t} \hat{\omega}) = e^{\nu k^2 t} \hat{\mathcal{N}}. \quad (\text{D.16})$$

This suggests the following scheme

$$\hat{\omega}_* = e^{-\nu k^2 \delta t / 2} \left\{ \hat{\omega}_n + \frac{\delta t}{2} \hat{\mathcal{N}}[\hat{\omega}_n] \right\}; \quad (\text{D.17})$$

$$\hat{\omega}_{**} = e^{-\nu k^2 \delta t} \hat{\omega}_n + \delta t e^{-\nu k^2 \delta t / 2} \hat{\mathcal{N}}[\hat{\omega}_*]; \quad (\text{D.18})$$

$$\hat{\omega}_{n+1} = \hat{\omega}_{**}. \quad (\text{D.19})$$

Appendix E

Lagrangian Particle Tracking

In this Appendix, we describe the Lagrangian tracking of a tracer particle transported by a (turbulent) flow. For simplicity, we discuss this problem for two-dimensional flows. Let us assume that the tracer particle is at a point (x, y) where (x, y) does not lie on the Eulerian grid and resides inside a square whose vertices are the Eulerian grid points (x_i, y_j) , (x_{i+1}, y_j) , (x_i, y_{j+1}) , and (x_{i+1}, y_{j+1}) . To know the position of the particle at the next time step, we need first to know the velocity of the particle at its present position; then we use Newton's laws to update the particle position at the next time step. Thus, if (u_x, u_y) is the Eulerian velocity at the point (x, y) , then, after a time step δt , the particle will be in the new position (x', y') , where

$$\begin{aligned}x' &= x + u_x \delta t; \\y' &= y + u_y \delta t.\end{aligned}\tag{E.1}$$

Therefore, to track a particle efficiently it is important to interpolate the velocity field at an off-grid position from the known velocities at the neighbouring grid points. In two-dimensions, the bilinear-interpolation method gives the following interpolation formula for each component of $u(x, y)$:

$$\begin{aligned}u(x, y) &= u(x_i, y_j) \frac{(x_{i+1} - x)(y_{j+1} - y)}{(x_{i+1} - x_i)(y_{j+1} - y_j)} + u(x_{i+1}, y_j) \frac{(x - x_i)(y_{i+1} - y)}{(x_{i+1} - x_i)(y_j + 1 - y_j)} \\ &+ u(x_i, y_{j+1}) \frac{(x_{i+1} - x)(y - y_j)}{(x_{i+1} - x_i)(y_{j+1} - y_j)} + u(x_i, y_{j+1}) \frac{(x - x_i)(y - y_j)}{(x_{i+1} - x_i)(y_{j+1} - y_j)}\end{aligned}\tag{E.2}$$